Tailoring solid catalysts for the ethene oligomerization reaction

Dissertation for the Degree of Philosophiae Doctor

Mustafa Sæterdal Kømurcu

Department of Chemistry
Faculty of Mathematics and Natural Sciences
University of Oslo

February 2021

Series of dissertations submitted to the
Faculty of Mathematics and Natural Sciences, University of Oslo
No. 2392

ISSN 1501-7710

Cover: Hanne Baadsgaard Utigard.
Print production: Reprosentralen, University of Oslo.

Preface

The work presented in this thesis was carried out between February 2017 and February 2021 and finalizes the research carried out during this four-year Ph. D. scholarship at the Department of Chemistry, University of Oslo.

The level of research conducted over the last four years as a Ph. D. student would not be possible without commitment and unwavering support from others and I would like to acknowledge a list of people.

I am very grateful to Prof. Unni Olsbye for allowing me to perform this work and for her guidance and support throughout the project. A special thanks is given to Dr. Elisa Borfecchia for her guidance on XAS and for her continuous support. I would also like to thank Dr. Rasmus Y. Brogaard for his collaboration to bring together my experimental and his theoretical work. Furthermore, I would like to express my sincere thanks to Prof. Gloria Berlier and Prof. Silvia Bordiga for fruitful collaborations and scientific discussions.

I would also like to acknowledge the whole CONFINE team, especially Andrea Lazzarini and Gurpreet Kaur for fruitful collaborations and Emil Sebastian Gutterød and Carlo Buono for good discussion and valuable feedback on the project. I am also grateful to the entire catalysis group for providing a good professional and social environment.

Finally, I would like to dedicate a special thanks to my wife Kristina, my parents Durmus and Nilgun and a list of friends that is too long to list here for their unyielding support and faith in me. This list cannot be complete without mentioning my four months old daughter Nora for motivating me and my cat Kedi for keeping me company, both day and night, in these corona times.

List of abbreviations used in this thesis

^{1}H-NMR	Proton nuclear magnetic resonance
BA	Benzoic acid
BAS	Brønsted acid site
H_2bdc	Benzene-1,4-dicarboxylic acid
H_2bpdc	Biphenyl-4,4′-dicarboxylic acid
H_2bpydc	[2,2'-bipyridine]-5,5'-dicarboxylic acid
DFT	Density functional theory
DFT-MD	Density functional theory based molecular dynamics
DSC	Differential scanning calorimetry
EDS	Energy-dispersive X-ray spectroscopy
EXAFS	Extended X-ray absorption fine structure
FA	Formic acid
FID	Flame-ionization detector
f.linker	Functional linker
FTIR	Fourier-transformed infrared spectroscopy
GC	Gas chromatography
H_2bndc	[1,1'-binaphthalene]-4,4'-dicarboxylic acid
H_2bpdc-(NH_2)	2-amino-[1,1'-biphenyl]-4,4'-dicarboxylic acid

H_2bpdc-$(NH_2)_2$	2,2'-diamino-[1,1'-biphenyl]-4,4'-dicarboxylic acid
H_2bpdc-$(OH)_2$	2,2'-dihydroxy-[1,1'-biphenyl]-4,4'-dicarboxylic acid
LAO	Linear alpha olefins
LAS	Lewis acid site
LCF	Linear combination fit
LNT	Liquid nitrogen temperature
MAO	Methyl alkylaluminoxane
MCR	Multivariate curve resolution
MCT	Mercury Cadmium Telluride
MFC	Mass flow controllers
MOF	Metal-organic framework
MS	Mass spectrometer
MP-AES	Microwave plasma atomic emission spectrometer
PXRD	Powder X-ray diffraction
S_{BET}	Specific surface area
SEM	Scanning electron microscopy
SHOP	Shell higher olefin process
STC	Standard reaction conditions
TGA	Thermogravimetric analysis

TOF	Turnover frequency
TOS	Time on stream
H_2tpdc	P-terphenyl-4,4″-dicarboxylic acid
UiO	University of Oslo
wt. %	Weight percent
WHSV	Weight hourly space velocity
XANES	X-ray absorption near-edge structure
XAS	X-ray absorption spectroscopy
XPS	X-ray photoelectron spectroscopy

Table of contents

List of publications

I. Ethene oligomerization on nickel microporous and mesoporous-supported catalysts: Investigation of the active sites. Henry, R.; Kømurcu, M.; Ganjkhanlou, Y.; Brogaard, R. Y.; Li Lu.; Jens, K. J.; Berlier, G.; Olsbye, U. *Catal. Today*. **2018**, *299*, 154– 163

II. Ethene Dimerization on Zeolite-Hosted Ni Ions: Reversible Mobilization of the Active Site. Brogaard, R. Y.; Kømurcu, M.; Dyballa, M. M.; Botan, A.; Van Speybroeck, V.; Olsbye, U.; De Wispelaere, K. *ACS Catal.* **2019**, *9*, 5645– 5650

III. Cocatalyst free ethene dimerization over Zr-based metal-organic framework (UiO-67) functionalized with Ni and bipyridine. Kømurcu, M.; Lazzarini, A.; Kaur, G.; Borfecchia, E.; Øien-Ødegaard, S.; Gianolio, D.; Bordiga, S.; Lillerud, K. P.; Olsbye, U. *Catalysis Today*. **2020**

Author's contribution

I. Performed all catalytic experiments and related data analysis. Performed TGA, N_2-adsorption, SEM imaging, elemental characterization and PXRD measurements. The author was strongly involved in planning the work, interpretation of the results and in preparation of the manuscript.

II. Performed Ni functionalization, XRD, N_2-adsorption and elemental characterization and related data analysis. Planned and conducted all the catalytic experiments and analyzed related data. Participated in the preparation of manuscript, specifically the part related to catalytic testing.

III. Performed all catalytic experiments and related data analysis. Performed TGA, N_2-adsorption, SEM imaging and PXRD measurements and data analysis. Participated in XAS beam time application and measurements. The author was strongly involved in planning the work, interpretation of the results and in preparation of the manuscript.

Conference contributions

Ethene oligomerization over Ni-containing beta zeolite. Kømurcu, M.; Olsbye, U.; et al. Poster presentation at the 3rd KAUST Research Conference: New Challenges in Heterogeneous Catalysis, 29th – 31st January 2018, Kaust, Kingdom of Saudi Arabia.

Ethene dimerization over Zr-based metal-organic framework (UiO-67) functionalized with Ni and bipyridine. Kømurcu, M.; Olsbye, U. et al. Poster presentation at the 21st National Chemistry Meeting, 16th – 18th October 2018, Lillestrøm, Norge

Ethene dimerization over Zr-based metal-organic framework (UiO-67) functionalized with Ni and bipyridine. Kømurcu, M.; Olsbye, U.; et al. Oral presentation at the 14th EuropaCat 2019, 18th – 23rd August, Aachen, Germany.

Scope

The scope of this Ph. D. thesis was to identify the active site, asses the role of the support and gain mechanistic and kinetic insight on the ethene oligomerization reaction over Ni functionalized heterogeneous catalysts. Two types of porous heterogeneous catalysts, Ni-zeolites and Ni-MOFs have been investigated in this work. Ethene dimerization and oligomerization with heterogeneous catalysts has been studied for several decades but has received increased attention in the past decade with the increased availability of ethene. Furthermore, the possibility to produce ethene from renewable biomass has made ethene dimerization and oligomerization for petrochemical production even more attractive.

The first goal of this work consisted of studying the ethene oligomerization reaction over Ni functionalized micro and mesoporous aluminosilicates. Experimental results show that butene formation on microporous Ni catalyst have higher reaction order in ethene pressure compared to mesoporous Ni catalyst. This observation suggests that the surrounding molecules can have a significant influence on ethene dimerization over these two types of catalysts. The detailed study over Ni-zeolites generated a new understanding on how Ni dynamically crosses the border between homogeneous and heterogeneous catalysis throughout the dimerization reaction.

The second goal of this thesis, which constituted most of the thesis, was to investigate Ni functionalized metal-organic frameworks (MOF) for the cocatalyst free ethene dimerization reaction. In recent years, MOFs have demonstrated promise as catalysts for ethene dimerization and oligomerization. Most of these catalysts show high activities and selectivities for butenes, especially 1-butene, but require the use of activators or cocatalyst in large excess and the presence of solvents as a bulk liquid phase. A series of Ni functionalized MOFs were prepared and investigated. Significant effort was directed towards understanding active site formation and identifying the active site in these cocatalyst free Ni-MOF catalysts.

1 Introduction

1.1 Catalysis

Catalysts are used extensively in nature, in laboratories, in most industrial chemical processes, and thus have a strong significance in our lives. For example, the Haber-Bosch process, a nitrogen fixation process where N_2 is catalytically reduced by H_2, is the main industrial process for production of ammonia, a critical component in chemical fertilizer manufacture. It is estimated that in 2008, chemical fertilizers were responsible for feeding 48 % of the world's population [1]. Catalysts also play a vital role in achieving cleaner environment through *e.g.* pollution prevention by increasing the yield of the desired product and reducing the formation of unwanted byproducts or by removing and destruction of pollutants [2, 3].

A catalyst is a substance that can increase the rate of reaction without itself being consumed. It does so by creating an alternative, energetically favorable reaction pathway compared to the non-catalytic reaction. A catalytic reaction is generally more complex than the non-catalytic reaction and involves more steps as the catalyst must interact (*e.g.* form and break bonds) with the reactants and products. However, it is important to note that a catalyst does not affect the overall energy change of the reaction, *i.e.* the position of the equilibrium remains unaltered. Figure 1 show a hypothetical potential energy diagram where these two processes are illustrated.

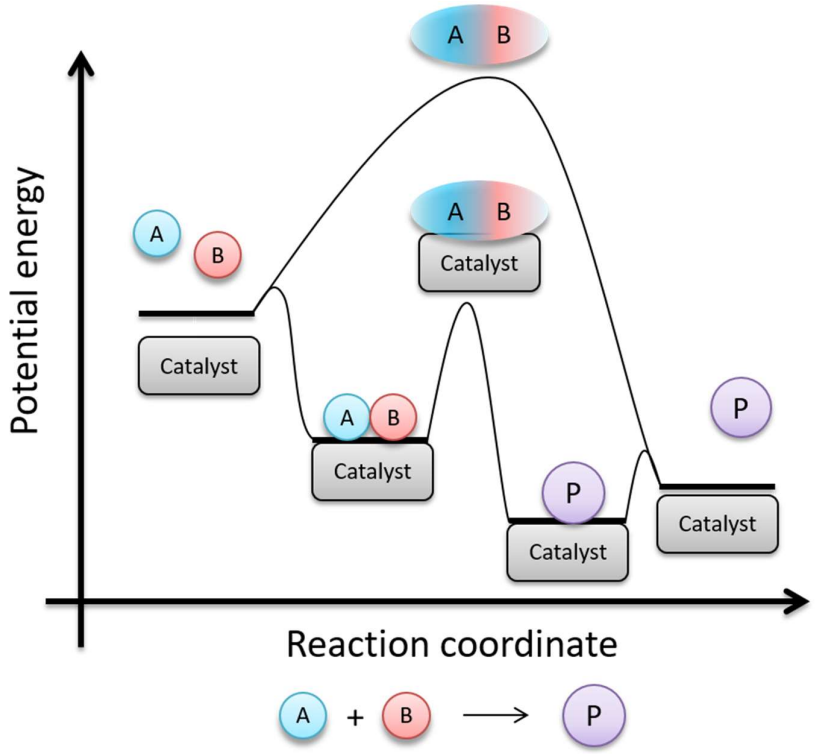

Figure 1: Potential energy diagram of the catalytic and non-catalytic reaction (A + B → P) are illustrated. The energy barrier of the catalytic reaction is lower than the barrier of the non-catalytic reaction, which leads to an increased rate for the catalyzed reaction. Adapted from [4].

The form of a catalyst ranges from atoms and molecules to larger structures such as particles and enzymes. It is customary to categorize catalysts into three classes: homogeneous catalysis, heterogeneous catalysis and biocatalysis. Catalysts are classified as homogeneous if both the reactant and catalyst is present in the same phase, *e.g.* a catalyst present as solute in liquid reaction mixture. A heterogeneous catalyst is present in a different phase from that of the reactants, usually, the catalyst is solid, and the reactants are either in liquid or gas phase. Biocatalysis is often considered as a third category.

This thesis focuses on the heterogeneous catalysis of gas phase ethene over zeolite and metal-organic framework catalysts.

1.2 Zeolites

Zeolites are naturally occurring crystalline aluminosilicate minerals. The primary building units of the zeolites are TO_4, where T refers to silicon or aluminum atoms. These tetrahedral units assemble together such that adjacent tetrahedra share corners via a common oxygen atom, forming a well-ordered, microporous three-dimensional framework [5]. Examples of how the primary building units can assemble to form unique frameworks is illustrated in Figure 2:. Each framework type is assigned a three-letter code which defines a unique channel system, and its corresponding pore and cavity dimensions [6]. Other atoms such as phosphorus can also be incorporated in the framework. These materials, referred to as zeotypes, will not be covered in detail in this thesis. At the time of writing (January 2021), there is a total of 253 zeolite structures recognized by the International Zeolite Association [7].

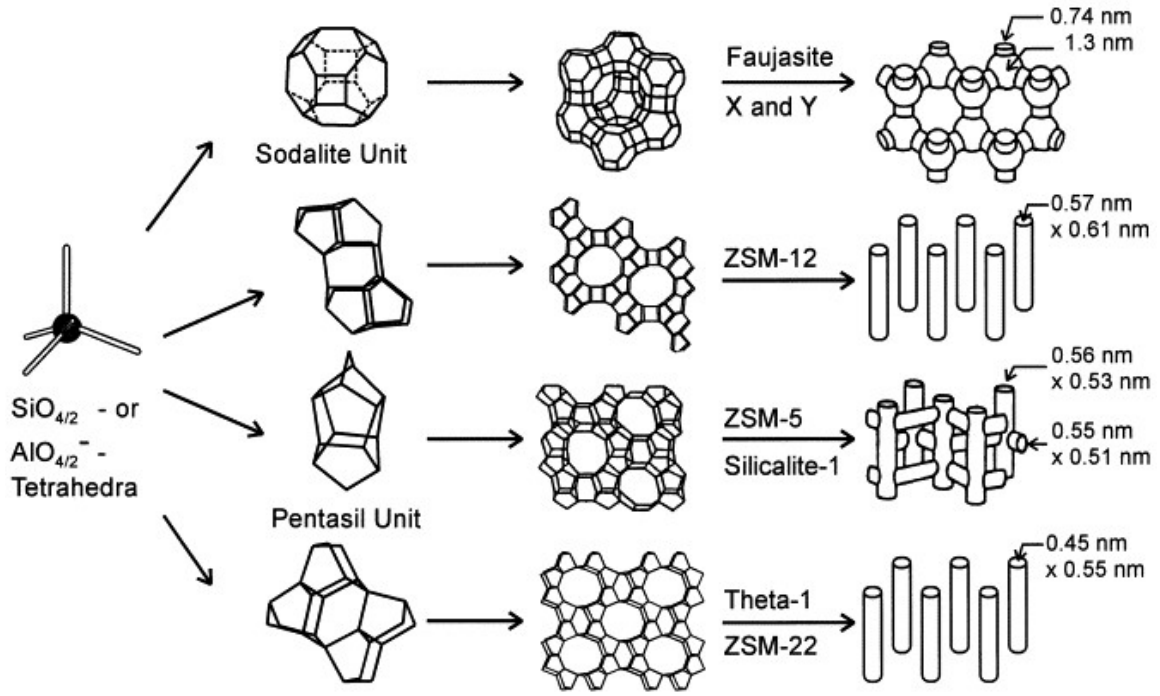

Figure 2: Examples of how the tetrahedral TO_4 primary building units can assemble in order to form different zeolite structures with different micropore systems and dimensions. Reproduced from [8] with permission.

The molecular dimension of the pores allow zeolites to act as molecular sieves, *i.e.* allow small molecules to diffuse in and out of the pores while excluding larger molecules [9]. As illustrated in Figure 2, the pore system of zeolites can extend in one, two or three dimensions. Zeolites are often categorized according to their pore size, typically characterized by the number of TO_4 units forming the ring opening. The most common pore sizes contain 8, 10, 12 or more than 12 TO_4 units and zeolites containing these are referred to as, small, medium, large, and ultra large pore zeolites. The effective pore width of 8, 10 and 12 rings are approximately 4.1, 5.5. and 7.4 Å, respectively [10]. Most zeolite have pores smaller than 20 Å and fall within IUPACs classification as microporous materials [11].

The chemical composition of a zeolite can be represented with the following formula $M_{\frac{x}{n}}^{n+}\,[Si_{1-x}Al_xO_2] * mH_2O$. A framework consisting of only SiO_4 tetrahedra will be electrically neutral. Substituting Si with Al creates a net negative charge in the framework because of the lower valency of Al (trivalent) compared to Si (tetravalent). All such framework charges must be neutralized by cations (M^{n+}), typically, sodium, ammonium, or proton. These cations are mobile and easily exchangeable and give rise to the ion-exchange capabilities of zeolites. In fact, the use of zeolites as ion-exchangers in detergents, to soften the washing water by exchanging calcium and magnesium ions for sodium ions, represents their largest market in terms of tonnage [12].

Although zeolites naturally have molecular sieving and ion-exchange properties, additional functionalities are required to make zeolites a good catalyst. Substituting the charge balancing cations M^{n+} with protons will create Brønsted acid sites (BAS) that can catalyze a variety of reactions involving hydrocarbons such as cracking, isomerization and dehydrogenation [13]. Furthermore, exchanging the cations with transition metals will create redox active sites. The ability to create BAS and redox active sites together with well-defined structure, extensive internal surface area, high thermal stability, ease of reactant and product separation inherent to heterogeneous catalysts and their ability to affect product selectivity by shape selectivity is among the main factors that has made zeolites into successful catalysts.

Shape selectivity is a result of the molecular dimensional pores present in the zeolite framework and is usually divided into three types: reactant, product and transition state shape selectivity [14], as illustrated in Figure 3.

Reactant selectivity is based upon size exclusion. Molecules that are too bulky to diffuse into the pore system are prevented from interacting with the active site and are therefore not converted into products. Product selectivity occurs when the products formed inside the pores have different rate of diffusion. Molecules too large to diffuse out of the pores undergo secondary reactions to form less bulky molecules, or alternatively remain retained inside the catalyst pores. Transition state selectivity takes place when certain transition states are inhibited due to the confinement of the active site and constraints imposed by the surroundings on the active site.

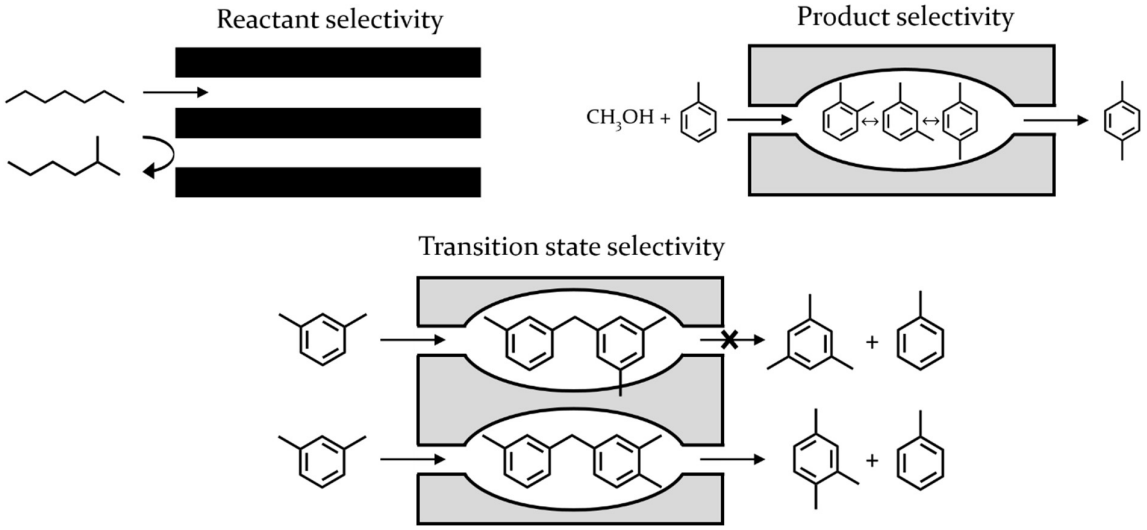

Figure 3: The three types of shape selectivity in zeolites. Adapted from [5].

Two of the zeolite catalysts employed in this work was SSZ-24 and Beta zeolite which belong to the AFI and BEA* framework topology, respectively (Figure 4). The AFI framework topology consists of one-dimensional twelve-ring straight channels. These almost circular channels have dimensions of 7.3 Å x 7.3 Å. Beta zeolite with BEA* framework topology is a disordered structure made of intergrown polymorphs that form

a three-dimensional system made from two orthogonal and intersecting twelve-ring channels. The framework has two types of twelve membered rings with pore diameters of 7.7 Å x 6.6 Å and 5.6 Å x 5.6 Å [7].

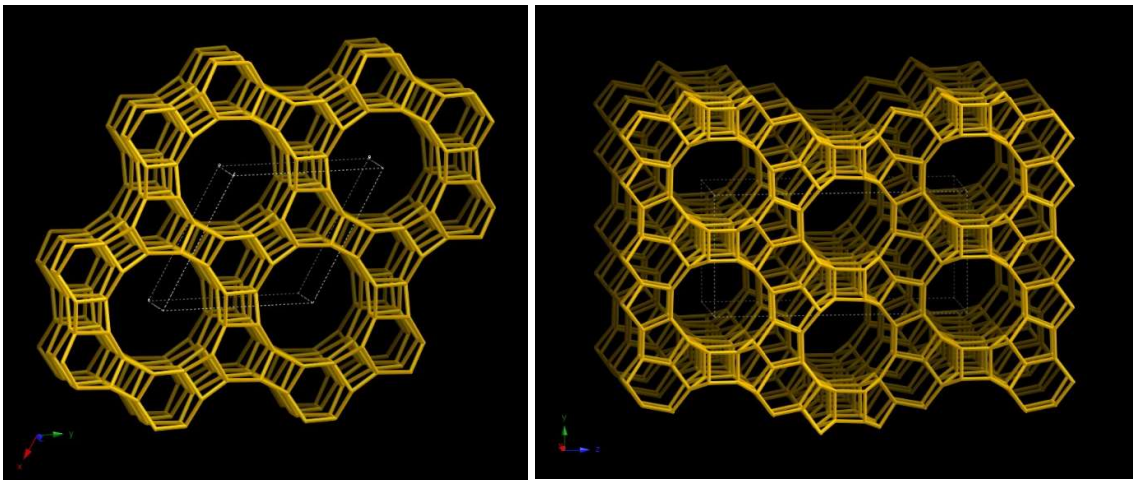

Figure 4: Illustrations of the AFI (left) and BEA* (right) topology [7].

1.3 MOFs

Another class of porous materials that share some common features with zeolites are metal–organic frameworks (MOFs). MOFs are crystalline, porous materials where the framework consists of inorganic nodes linked together by organic molecules to form a two- or three-dimensional network. The inorganic constituents of MOFs are typically either individual metal ions or small clusters for example, single Zn atom in ZIF-8 [15], four Zn atoms in MOF-5 [16] or six Zr atoms in UiO-66 [17]. The organic ligands (*i.e.* linkers) are relatively rigid molecules with multiple functional groups that connect the inorganic clusters. These coordinating moieties are typically carboxylate groups, but could also be imidazolates or amines [18].

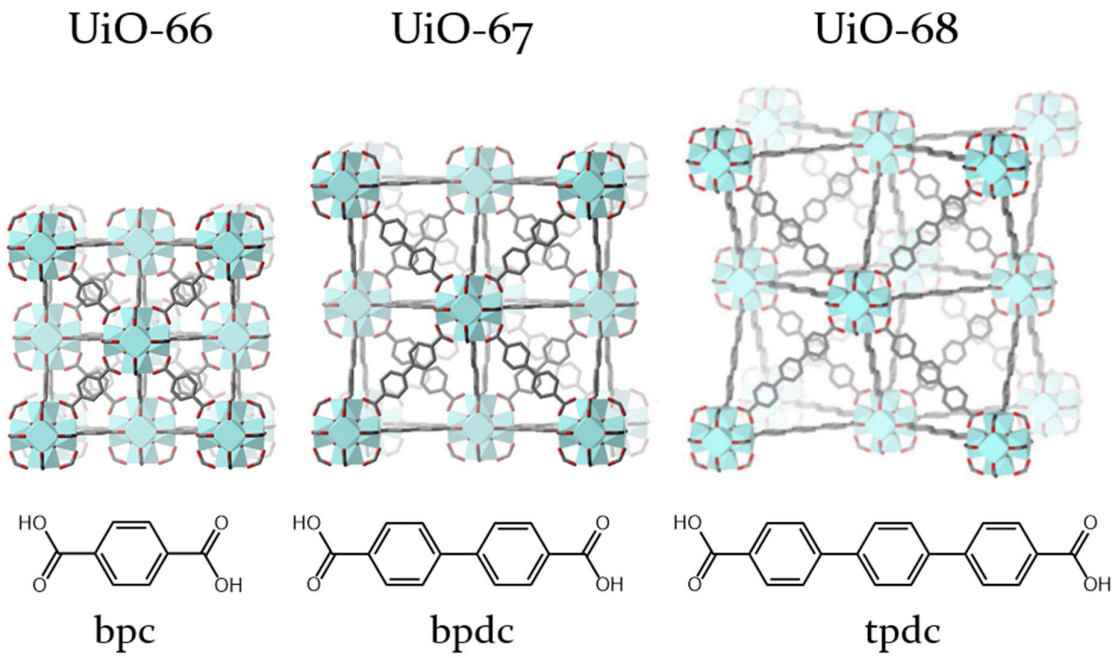

Figure 5: UiO-66, UiO-67 and UiO-68 MOFs constructed from $[Zr_6(\mu^3\text{-}O)_4(\mu^3\text{-}OH)_4]^{12+}$ clusters and linear dicarboxylic acid linkers, benzene-1,4-dicarboxylic acid (H_2bdc), biphenyl-4,4′-dicarboxylic acid (H_2bpdc) and p-terphenyl-4,4″-dicarboxylic acid (H_2tpdc), respectively. Zr atoms are shown as green square antiprisms, C atoms as grey and O atoms as red sticks. H atoms are omitted for clarity. Adopted from [19].

The approach by which MOFs are designed and assembled is termed reticular synthesis and is based upon how the inorganic and organic constituents come together to form a

"net" [20]. This gave rise to the term 'isoreticular MOFs'; MOFs where the nature and size of the linkers can be varied while maintaining the topology. One notable example and relevant to this thesis is the UiO (University of Oslo) series. The UiO MOFs consist of 12 coordinated $[Zr_6(\mu^3\text{-}O)_4(\mu^3\text{-}OH)_4]^{12+}$ clusters connected by H_2bdc, H_2bpdc and H_2tpdc linkers for the isoreticular UiO-66, UiO-67 and UiO-68 MOFs, respectively [17] (Figure 5). Substituting the linker from H_2bdc (UiO-66) to a longer linker such as H_2bpdc (UiO-67) leads to symmetric expansion of the framework, resulting in bigger tetrahedral and octahedral cages in UiO-67 compared to UiO-66 (Figure 6, left). Another unique feature of MOFs is the possibility to build the framework with more than one isostructural linker. The organic linkers can be modified to accommodate additional functional groups such as hydroxyl, amino and (bi)pyridine groups (Figure 6, right). Depending on the MOF, the concentration of functionalized linker can be varied from 0 % to 100 % while still maintaining porosity and crystallinity [21]. However, a large concentration of functionalized linker may have a negative impact on thermal and chemical stability and is not always favorable. Thus "mixed linker MOFs" with a small concentration of functionalized linkers are often a good compromise.

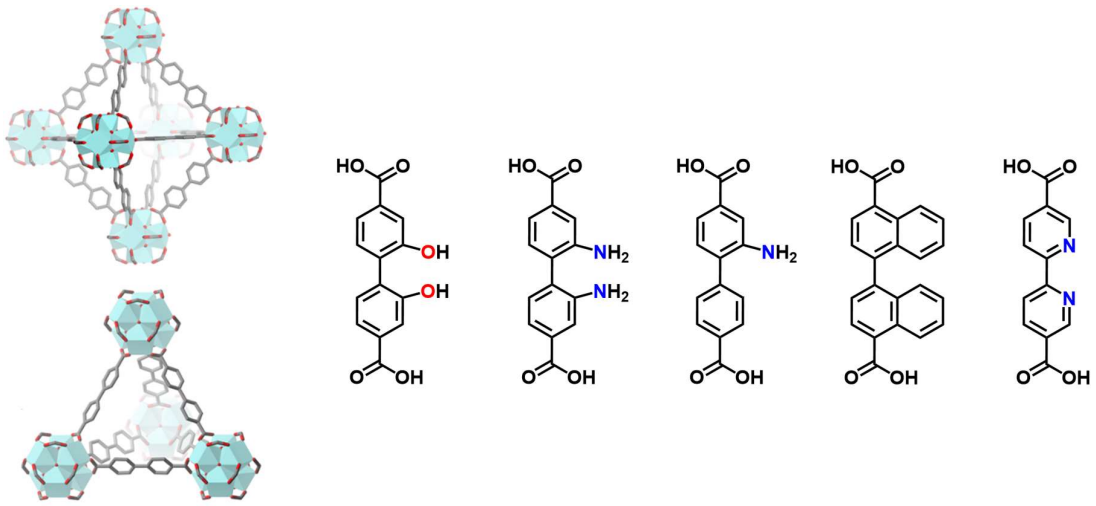

Figure 6: Representation of the tetrahedral and octahedral cages in UiO-67. Adopted from [22] (left). Structure of some of the isostructural linkers that can be exchanged with the bpdc linkers in UiO-67. From left to right: 2,2'-dihydroxy-[1,1'-biphenyl]-4,4'-dicarboxylic acid (H_2bpdc-$(OH)_2$), 2,2'-diamino-[1,1'-biphenyl]-4,4'-dicarboxylic acid (H_2bpdc-$(NH_2)_2$), 2-amino-[1,1'-biphenyl]-4,4'-dicarboxylic acid (H_2bpdc-(NH_2)), [1,1'-binaphthalene]-4,4'-dicarboxylic acid (H_2bndc) and [2,2'-bipyridine]-5,5'-dicarboxylic acid (H_2bpydc) (right).

Due to MOFs exceptional porosity and flexibility in its chemical composition, a wide range of potential uses have been reported including gas storage [23, 24], gas separation [25] and catalysis [18, 26, 27]. Although MOFs share some of the relevant features of zeolites such as large surface areas and uniform pore size and channels, they also differ in many ways. As zeolites are purely inorganic materials, they are mechanically robust and thermally stable and are therefore well suited for operation under extreme reaction conditions. Some MOFs show good thermal stability, but unlike zeolites, MOFs contain organic components which limits their operating temperature. They are also more prone to chemical reaction with guest molecules, which may cause degradation.

Regardless, MOFs have attracted the attention of many researchers as catalyst candidate because they offer opportunity for catalyst design, as it is in principle possible to rationally design the active site and the environment around it [28]. There are several methods to introduce catalytic sites into the MOF. The catalytic function can be implemented at both the linkers [29, 30] and metal clusters [31]. Alternatively, the MOF can be used to encapsulate metal particles [32, 33] or to install well-known homogeneous catalyst on the linkers or metal clusters [34-37]. Specific examples related to ethene dimerization and oligomerization will be presented in chapter 2.4.

2 Ethene oligomerization

2.1 Ethene production

Ethene (C_2H_4) is the simplest of alkenes and among the most important base organic chemicals with an annual consumption exceeding 150 million in 2017 [38]. It is raw material for a wide range of products; reactions of ethene include polymerization, oxidation, oligomerization and many more. Ethene is primarily produced through steam cracking of hydrocarbons via gas-phase radical reactions at high temperatures [39]. Typically, naphtha fraction of crude oil has been the major raw material, but following the 'shale gas revolution', stream crackers especially in North America, have shifted to lighter feedstock [40]. However, ethene is not the sole product of naphtha reforming, other valuable co-products such as propene, butadiene, benzene, and xylenes are obtained in the process. Figure 7 compares the products obtained per unit of ethene from shale-gas derived ethane or naphtha [41]. The industrial transition from naphtha to ethane as feedstock for ethene production has led to a shorter supply of propene and butene conventionally produced from oil [42]. This change has inspired the search for alternative production processes for propene, butenes and butadiene.

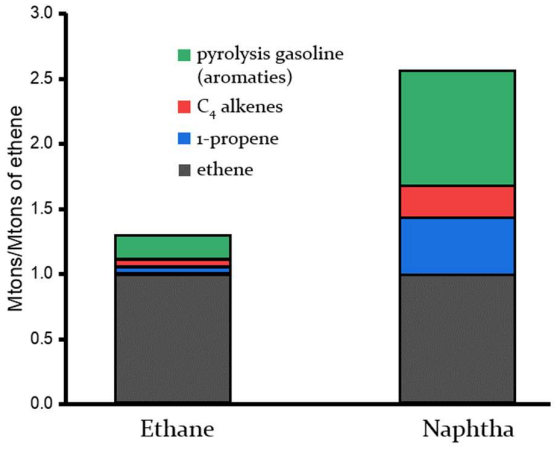

Figure 7: Products composition obtained per unit of ethene produced from shale-gas derived ethane or naphtha. Adapted from [41].

2.2 Environmental considerations

Petrochemicals are part of the fabric of our societies, found across a vast range of modern products such as clothing, digital devices, packaging, medical equipment, and countless other everyday items. In 2018, the petrochemical feedstock accounted for 12 % of global oil demand and it is expected to increase significantly over the next decades driven by the increasing demand for plastics, fertilizers and other products [43]. The pursuit of sustainable energy, fuel and chemicals production is becoming a more urgent and pressing matter. Nonrenewable sources face eventual depletion and with growing awareness of the detrimental environmental effects related to its use and production, researchers have directed their attention to alternative resources and various options are currently studies such as wind-based, photosynthetic, geothermal and biomass based energy sources [44].

Chemicals and fuel produced from biomass can, in principle, be CO_2 neutral and contribute to a solution of the environmental concerns [45]. One of these resources is bioethanol, which is mainly associated with its use as biofuel to substitute fossil-based fuels. Bioethanol has become the largest biofuel with an estimated worldwide production of 110 billion liters in 2019 and the demand is expected to increase [46]. However, bioethanol also holds great promise as a bio-based building block for the chemical industry. If sustainably produced, assessment show that it can become a major renewable source for bio-based ethene, among other platform chemicals [41, 47-50]. Ethene produced from biomass is a so called 'drop in' replacement, as it is identical to and can directly replace ethene from fossil-based sources and take advantage of the already existing infrastructure and contribute to the development of a cyclic economy [51].

There are several commercial processes for bioethanol to ethene currently in operation [52], but current industrial processes utilize easily fermentable sugars extracted from sugarcanes or obtained via hydrolysis of starchy materials such as corn and grains. Thus, bioethanol production from these sources are considered unsustainable because of the

potential stress it places on food commodities [53]. However, various options are being explored to produce bioethanol from nonedible biomass more efficiently [49-53].

There are numerous industrial processes for olefin production. In selective dehydrogenation processes, alkanes are converted to their corresponding alkenes. UOP's Oleflex where C_3 and C_4 alkanes are converted to alkenes is an example for this process [54]. Syngas is a mixture of CO and H_2 which can be obtained from coal, natural gas and biomass and can be utilized to form olefins via a direct and indirect routes such as the Fischer-Tropsh-to-olefins [55] and methanol-to-olefins [56], respectively.

2.3 Ethene oligomerization

Among these different routes, ethene oligomerization has since the mid-1970s been the main route for linear alpha olefins (LAO, even-carbon numbered olefins between C_4-C_{30}) production [57]. The LAOs are valuable building blocks for a range of industrial and consumer products, including co-monomers for polyethylene production, oxo-alcohols used in plasticizers and detergents and for production of synthetic lubricants [58]. Oligomerization and polymerization are often reviewed together because of their close mechanistic relation. Some versatile catalysts can even catalyze the former or the latter reaction depending on process condition and ligand coordination. A similar approach will be employed in the following sections.

The basis of the technology that is used to produce LAOs and polyethylene from ethene lie with the discovery by Ziegler in 1950s that titanium and zirconium alkoxides, in combination with alkylaluminum compounds, react with ethene [59]. The technology is currently referred to as Ziegler-Natta catalysis and the mechanism of this process was first described by Cossee [60, 61]. Not long after, a different mechanism, metallacycle mechanism, was proposed for catalysts that exclusively produced short chain LAOs [62]. In homogeneous catalysis, the mechanism of ethene oligomerization have been extensively investigated and the metallacycle and Cossee-Arlman mechanism are now widely recognized [63-65].

2.3.1 Cossee-Arlman mechanism

Scheme 1 shows a representation of this mechanism starting from $[M\text{-}H\text{-}ethene]^+$ sites. The first step involves the 1,2-migratory insertion of ethene into a Ni-H bond followed by ethene coordination and a second 1,2-migratory insertion of ethene into a Ni-alkyl bond. In this stage of the cycle, the alkyl species can undergo β-H elimination after coordination of another ethene molecule to form 1-butene or it can undergo a series of ethene insertions to form longer chain LAOs such as 1-hexene, 1-octene or even polyethylene. The chain transfer reaction has been proposed to occur via a direct β-H transfer from alkyl to the ethene [66, 67] or through a step-wise substitution of alkene by ethene *i.e.* an associative mechanism [68, 69]. In both cases, the transition state is similar and involves an ethene, alkyl chain and hydride species with the olefins in axial positions. Note that both pathways concur with the observation that steric hindrance in the axial positions of the metal-ligand plane by surrounding ligands lead to decreased rate for chain transfer and yield longer chained products and even polymers [70]. For the associative mechanism, retardation of chain transfer was ascribed to a slow displacement of the alkyl chain due to hindrance of incoming ethene by bulky substituents in the axial positions. Similarly for the direct β-H transfer route, an increase in barrier (destabilization of transition state) with increasing bulk in axial positions was suggested [70].

According to the Cossee-Arlman mechanism, the formal oxidation state of the metal is +2 and remains unchanged throughout the catalytic cycle. The oligomer distribution, *i.e.* the product chain lengths, depend on the relative rates of propagation and termination, which are typically independent of chain length. Internal isomers can also be formed as primary reaction products by a parallel isomerization pathway where the initially formed 1-butene can undergo a 2,1-reinsertion with subsequent β-H elimination to form cis-2-butene and trans-2-butene. Another characteristic of this mechanism is that the oligomer distribution can be described by an exponential decay function, a Schulz-Flory distribution, where the probability of chain growth and the probability of termination is expressed as α and 1 – α, respectively [71]. For a given α, the mole fraction (x_n) of an

oligomer comprising n monomer units (n = 1 for ethene, n = 2 for butene etc.) can be computed using the standard Schultz-Flory formula, $x(n) = (1 - \alpha)\alpha^{n-1}$ [72].

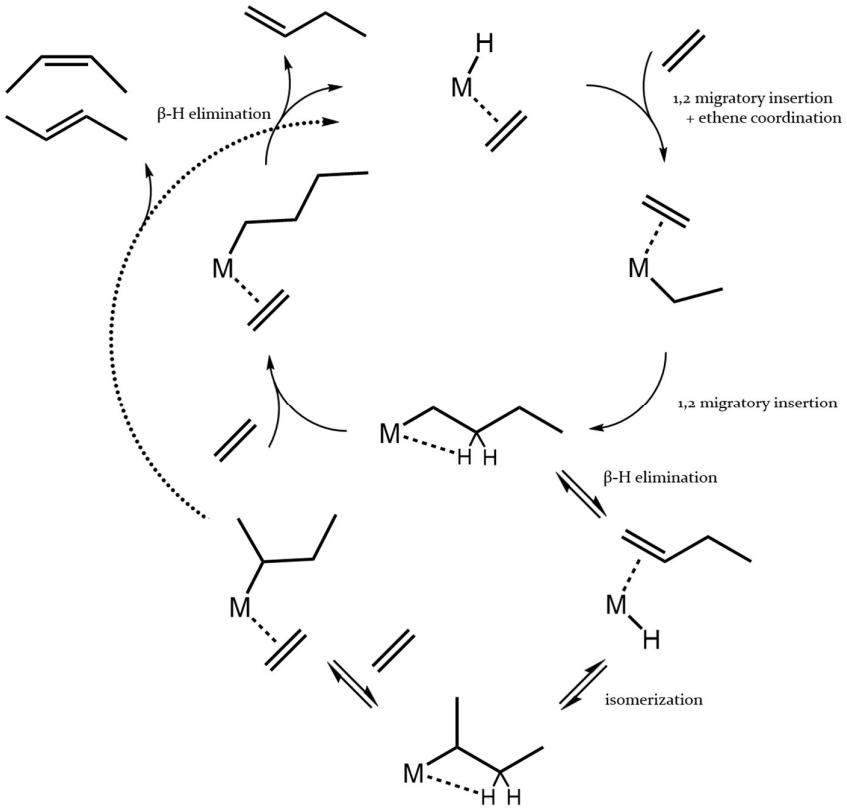

Scheme 1: Cossee-Arlman mechanism for ethene dimerization and oligomerization at [Ni(II)-H-ethene]$^{+}$ active sites.

2.3.2 Metallacycle mechanism

Metallacycloalkane compounds are an important and extensively studied class of organometallic compounds [73-75], which are known to be key intermediates in several reactions, especially in ethene trimerization [76] and tetramerization [77] reactions.

The metallacycle mechanism (Scheme 2) start with coordination of two ethene molecules followed by oxidative addition of the two ethene molecules to the metal site to produce a metallacyclopentane species. This metallacyclopentane species is susceptible to further ethene insertion to produce larger metallacycle rings, while decomposition at any point will produce linear α–olefins. The hydride shift can occur through a stepwise process, β-

H elimination followed by reductive elimination or through a concerted 3,5-hydrogen shift [65]. The latter process has been thought to be difficult for metallacyclopentanes due to the constrained geometry of this species [78].

The key differences between the metallacycle and Cossee-Arlman mechanism is that the Cossee-Arlman mechanism is often based on a metal–alkyl species formed from a cocatalyst such as alkylaluminum halide or methylaluminoxane (MAO) compounds, while catalyst operating with the metallacycle mechanism does not require a cocatalyst. Furthermore, catalysts following the metallacycle mechanism selectively produce 1-alkenes and this mechanism does not account for the formation of internal alkenes such as trans-2-butene and cis-2-butene as primary products, as illustrated for the Cossee-Arlman mechanism in Scheme 1. Finally, unlike the Cossee-Arlman mechanism, the metal undergoes a redox cycle where the oxidation state of the metal change by $\delta + 2$.

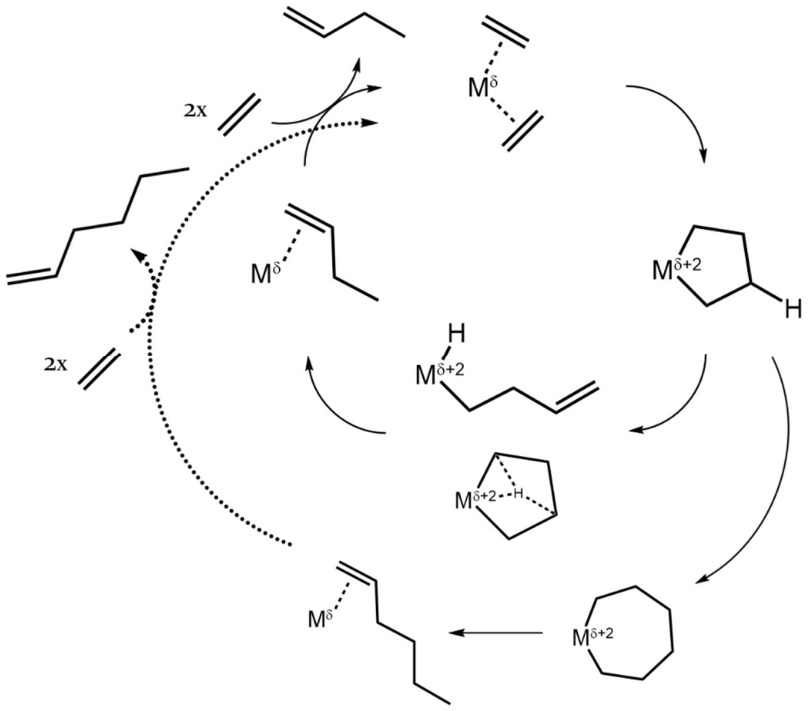

Scheme 2: Metallacycle mechanism for ethene oligomerization.

2.3.3 Ethene oligomerization with homogeneous nickel catalysts

Since its discovery, the ethene oligomerization reaction has kept its importance as a key industrial reaction. Today, the production of LAOs is predominately carried out in organic solvents using transition metal (Shell higher olefin process, SHOP) and aluminum (CPChem or INEOS) catalysts. These 'full-range processes' produce a broad range of olefins (C_4 – C_{20+}) in nearly fixed ratio with a Schulz-Flory distribution (SHOP and CPChem) or a Poisson distribution, stoichiometric ethene oligomerization that depends solely on the rate of occurrence and without any chain-end influence on the ethene insertion reaction, (INEOS) [58, 65, 79, 80]. Important work has been devoted into catalysts design and to the study of their activity and selectivity as well as investigating the electronic and steric effects of the ligands on the reaction. Due to its industrial importance, a vast number of articles have been published in the field of ethene oligomerization with homogeneous catalysts and it is still subject of many studies in both academia and industry.

A number of transition metals such as Ti, Co, Fe, Ni and Pd etc. have been utilized for olefin oligomerization and a review of all of these catalysts with their corresponding linker combinations in their respective reaction conditions is beyond the scope of this work. Since nickel has been the transition metal in focus in this thesis, a brief introduction will be presented with focus on trends rather than discussing individual catalysts.

The major breakthrough of nickel in ethene oligomerization reaction began with the accidental discovery of Erhard Holzkamp, a student of Karl Ziegler, who observed that nickel salts alter the AlR_3 catalyzed ethene oligomerization reaction to yield dimers only, a phenomenon referred to as the "nickel effect" in the literature [81]. It was later determined that late transition metals, relative to the early transition metals, generally exhibited a reduced activity for ethene insertion such that β-hydride elimination competed with chain growth, resulting in dimers and oligomers. This generalization has been changed, around the 1990s, upon the discovery by Brookhart et al. that Ni(II) α-diimine complexes mixed with MAO were highly active for ethene oligomerization and

polymerization. Since then, substantial amount of work has been put into development of new nickel catalysts for both ethene oligomerization and polymerization, some with great success *e.g.* the SHOP.

It should be noted that for homogeneous catalysts employed in the ethene oligomerization and polymerization reactions, the term catalyst often refers to the catalyst precursor and there is generally only limited direct information on the exact nature and the structure of the active species.

The ligand coordination chemistry for organometallic compounds is rich and examples of nickel catalyst with mono to tridentate chelating ligands can be found in the literature [82]. The ligands have several key roles over the nickel metal complex in the ethene oligomerization reaction: 1) control coordination geometry, 2) control oxidation state and 3) steric protection of the active site and influence selectivity. Studies of nickel catalysts for ethene oligomerization and polymerization have primarily been focused on monoanionic and neutral bidentate ligand systems with N,N, N,O, P,O, P,N chelating ligands [64, 82, 83].

The nickel catalysts can generally be divided into two groups: cationic Ni(II) complexes of neutral ligands (Scheme 3, type 1) and neutral Ni(II) complexes of monoanionic bidentate ligands (Scheme 3, type 2) [84]. The catalytically active cationic complexes are coordinatively unsaturated and highly electrophilic and are based on Ziegler-Natta type systems where a nickel precursor and an activator such as MAO are mixed to generate an ion pair ($[L_nMR]^+ \ldots [X]^-$) [85, 86].

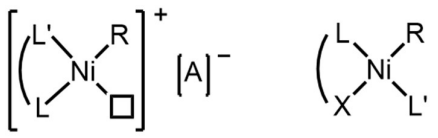

Type 1 Type 2

X = anionic
L, L' = electron donor
R = alkyl or H

Scheme 3: General structure of cationic (type 1) and neutral (type 2) Ni(II) complexes for ethene oligomerization and polymerization.

One example for a cationic catalyst is Ni(II) dihalide complexes with α-diimine ligands. The easily varied steric and electronic properties combined with their versatility and the ease of synthesis made these ligands system very popular [82]. Upon activation of precursors **1** with MMAO, turnover frequencies (TOF) up to $1.3 \cdot 10^5$ h^{-1} with LAO selectivities up to 95 % with Schulz-Flory distribution is observed [87]. Depending on the nickel precursor, several methods can be employed to generate the cationic species [88]. Here, the role of the cocatalyst is twofold: anionic ligand abstraction and metal center alkylation to form the active cationic species [89].

A novel discovery with these complexes is that they serve as oligomerization or polymerization catalysts depending on the steric bulk of the surrounding ligands (steric bulk of the ortho-aryl substituents bound to the nitrogen atoms, Figure 8). Bulky isopropyl groups located above and below the square-planar coordination plane retards chain transfer (See 2.3.1) and lead to polymerization *e.g.* over **2**. While substituting the bulky group with a sterically less demanding H atom yields a highly active ethene to LAO catalyst [87, 89, 90].

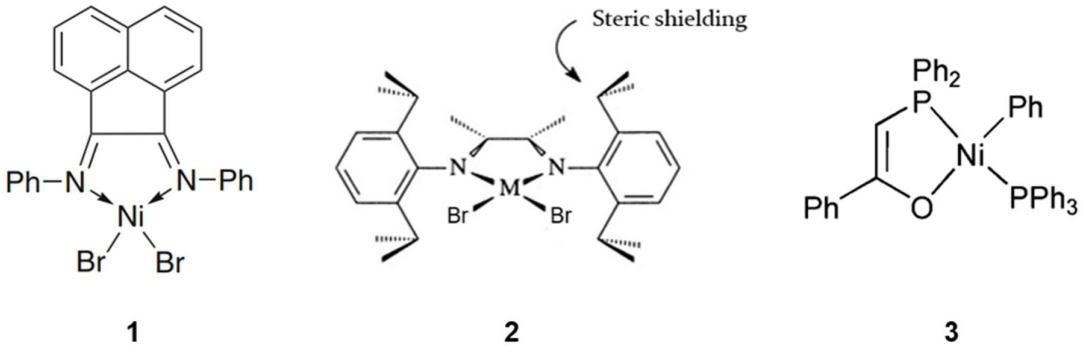

Figure 8: Ni(II) α-diimine ethene oligomerization and polymerization precursors (left and center, respectively) and SHOP-type catalyst (right). Active catalyst for Ni(II) α-diimine complexes are generated after reaction with a Lewis acid such as MMAO. Adapted from [84].

The use of neutral Ni(II) catalyst in SHOP for the manufacture LAO represents a prominent example for the utility of these complexes for ethene oligomerization. Developed by Keim et al. in the 1960 and 70s, SHOP in which catalyst of type 2 (Scheme 3) were utilized for production of LAO, constitute one of the most significant processes of homogeneous transition-metal catalysis [91]. Unlike the cationic Ni(II) catalysts, the neutral Ni(II) catalysts do not necessarily require an alkylating agent and the active nickel species can be formed *in situ* after reaction with ethene. The product composition can be modified depending on the reaction conditions or by fine-tuning electronic and steric properties of the ligands. For example, increasing the basicity of the L' increases its coordination strength to Ni and consequently favors short LAO. Similar to Ni(II) α-diimine catalysts, these oligomerization catalysts are also capable of producing polyethylene under certain conditions. At 50 °C under 50 bar ethene in toluene, **3** affords LAO with 98 % selectivity with activity close to $1.0 \cdot 10^4$ h^{-1}. While in n-hexane or with a phosphine scavenger (or with a more labile L' such as pyridine), the same catalyst form linear polyethylene [92]. The impact of several parameters on these types of catalyst are discussed in depth elsewhere [93].

The accepted mechanism for both type of Ni(II) catalysts is Cossee-Arlman type mechanism and the distribution of olefins is essentially a Schulz-Flory distribution. However, around 50 % of LAOs produced are used as co-monomers for the production of linear low-density polyethylene and high-density polyethylene, which utilize the 1-butene, 1-hexene and 1-octene fractions [63]. The continuous increase in demand for short chain LAO (C_4 – C_8), which is increasing faster than for the longer ones (C_{10+}) [64], has led to a growing interest in selective oligomerization of ethene to C_4–C_8 products and several on-purpose industrial processes were developed.

AlphaButol process developed by IFPEN and SABIC utilize a titanium-based homogeneous catalyst with an alkylaluminum cocatalyst for 1-butene production through ethene dimerization. TOF up to $1 \cdot 10^6$ h^{-1} and 1-butene selectivity up to 93 % is reported. In the Phillips trimerization system (not to be confused with Phillips catalyst for

polymerization), 1-hexene is produced selectively through ethene trimerization with a homogeneous chromium catalyst with an alkylaluminum cocatalyst [58, 63, 65, 76].

Over the last decades, significant effort has been put into the development of heterogeneous catalysts for the ethene dimerization reaction, as the heterogeneous process offer a continuous throughput, easy separation of products, reusability and a more environmentally friendly alternative by avoiding the use of toxic solvents.

Several solid catalysts such as solid acids, Ni complexes immobilized on polymers and oxides, metal organic framework and nickel supported on inorganic porous materials have been investigated for ethene dimerization and oligomerization under both batch and continuous flow conditions. Two recent reviews by Finiels et al. (2014) [94] and Hulea (2018) [47] provides an overview on the Ni-based heterogeneous catalysts for ethene oligomerization. The reader is referred to these two articles for an excellent and thorough review. At the time of writing, a comprehensive review on ethene oligomerization over homogeneous and heterogeneous Ni catalysts have been published by Olivier-Bourbigou et al. [95]. Here, a brief introduction of ethene dimerization and oligomerization over heterogeneous catalysts will be presented.

2.3.4 Solid acids

Ethene oligomerization over various solid acid and zeolitic materials, which is considered the most promising candidate among the solid acids, have been subject of many investigations [96]. In these materials, several reaction mechanism for ethene oligomerization involving Lewis or Brønsted acid sites have been proposed, simplified schemes are illustrated in Figure 9 [97]. In the case of Brønsted acid sites, two mechanisms have been suggested: the carbenium ion mechanism and surface alkoxy mechanism. The main difference between the two mechanisms is that the first mechanisms is suggested to lead to the formation of branched oligomers, while the second mechanism is suggested to lead to linear oligomers [98, 99]. In the cationic intermediate mechanism, the reaction

is initiated by Lewis acid sites (LAS) in the lattice and the main products are branched oligomers.

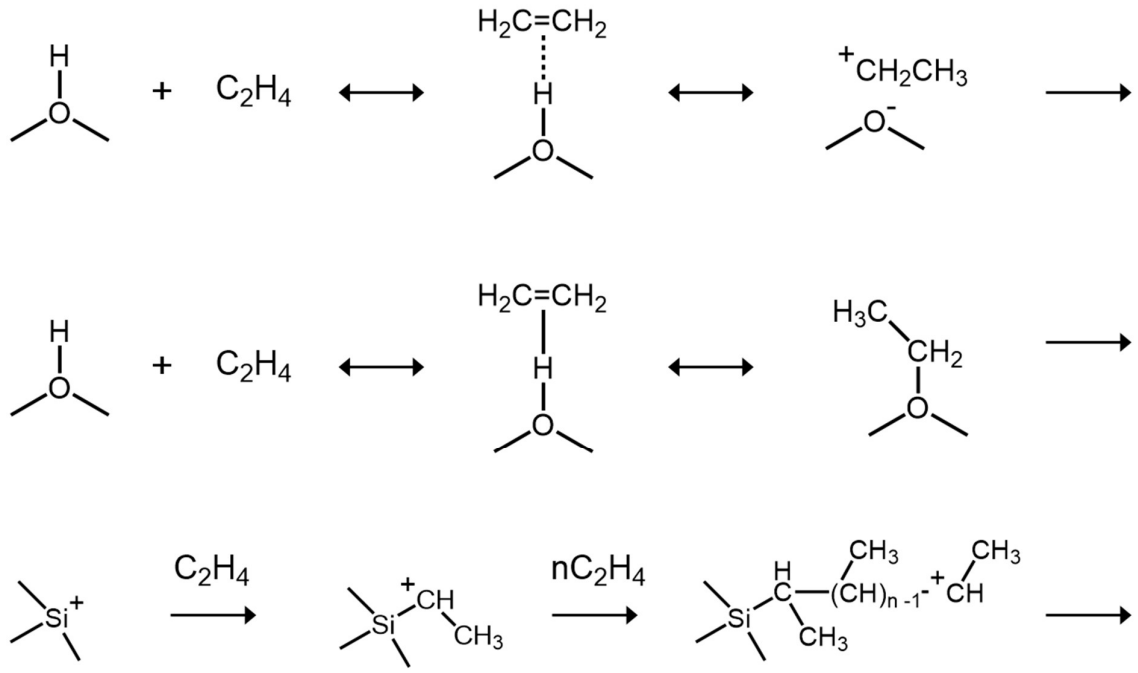

Figure 9: Reaction mechanisms proposed for ethene oligomerization over solid acids; (top) carbenium ion mechanism, (middle) surface ethoxy mechanism and (bottom) cationic mechanism. Adapted from [100]

Ethene, having only two carbon atoms, can only form primary carbocation and inherently have lower reactivity than other light alkenes, *i.e.* the products, that can readily form more stable secondary and tertiary carbocations. Generally, high activity can be achieved at elevated temperatures, but other reactions besides oligomerization such as isomerization, cracking, hydrogen transfer and aromatization becomes important and a broad range of products and coke is formed [100].

2.3.5 Nickel complexes supported on oxides

In this approach, complexes, and model compounds well known from homogeneous catalyst for ethene dimerization/oligomerization are typically supported on materials such as zeolites, silica, and silica-alumina.

Peuckert et al. [101] impregnated silica and silica-alumina with two Ni complexes considered model compounds for the SHOP process (**4** and **5**, Figure 10) that produced LAOs with 99 % selectivity in liquid phase testing. The catalysts were successfully heterogenized and tested for ethene oligomerization in fixed-bed continuous flow reactor at 50 °C and P_{ethene} between 60 – 68 bar. Catalysts supported on acidic silica-alumina showed one to two order magnitude higher activity compared to the catalysts supported on silica, but poorer selectivity (~50 %) to LAOs as the acidic support also enhanced double bond isomerization and branching. Pore blocking due to wax and polymer formation was also observed.

Angelescu et al. [102] studied Ni(4,4-bipyridine)Cl_2 (**6**, Figure 10) complexes activated with Et_2AlCl supported on various molecular sieves such as zeolites (Y, Mordenite and L), mesoporous MCM-41 and on amorphous silica alumina. Tested under mild reaction conditions (25 °C and 12 bar ethene pressure), the supported complex catalysts showed higher TOF than the unsupported catalyst. However, the conversion varied only slightly with respect to the unsupported catalyst (7 ± 5 %), except MCM-41 based catalyst that was up to 5 times more active, partially due to secondary reactions and formation of C_{5+}. Comparing selectivities under similar conversion level, butene selectivity remained almost unaltered whilst the 1-butene selectivity reduced by 25 – 50 % compared to the unsupported catalyst.

Similarly, Rossetto et al. anchored nickel-β-diimine complexes of the type **7** (Figure 10) on silica [103] and MCM-41 [104] with the aim to heterogenize these homogeneous ethene dimerization catalysts. Both the homogeneous and heterogeneous complexes were tested under identical reaction conditions, in batch mode in toluene at 10 °C and 15 bar P_{ethene} using alkylaluminum cocatalyst to start the reaction. The heterogeneous complexes were less active but showed similar 1-butene selectivity (> 90 %) to their homogeneous analogues.

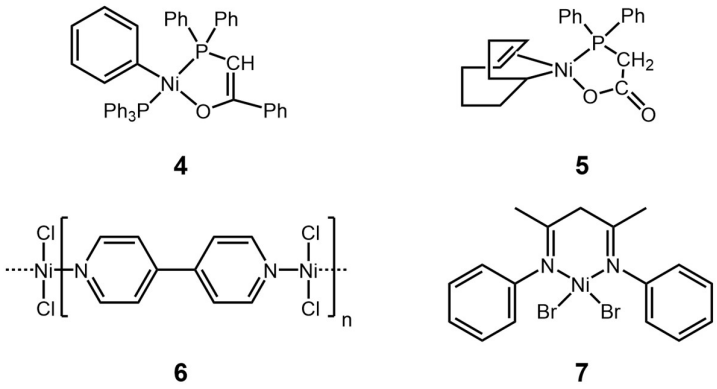

Figure 10: Structures of selected nickel complexes supported on inorganic support for ethene dimerization and oligomerization.

2.4 Metal-organic frameworks

Several MOF-based catalysts have been tested for ethene oligomerization. One strategy for MOF functionalization for ethene oligomerization involves anchoring well-known homogenous catalyst into the MOF linkers (or employing catalytically active metalloligands). Starting from (Fe)MIL-101-NH_2, Canivet et al. created N,N-chelating centers for nickel in the MOF linkers (Figure 11, top left) [34]. These catalysts with pyridine-imine type complexes were suspended in heptane and exposed to 15 – 30 bars of ethene at 0 – 40 °C in the presence of Et_2AlCl. High activity and selectivity were reported where the best result reported was obtained at 25 °C and 30 bar ethene (TOF ~ $1.1 \cdot 10^4$ h^{-1} and 95 % 1-butene selectivity).

Gonzales et al. [35] utilized Ni^{2+} and H_2bpydc functionalized UiO-67 for ethene oligomerization (Figure 11, top right). The biphenyl linkers of UiO-67 were reported to be exchanged with H_2bpydc linkers and functionalized with Ni^{2+}. This catalyst was active for ethene oligomerization ($3.6 \cdot 10^4$ h^{-1}) in cyclohexane and Et_2AlCl under 59 bar ethene at 55 °C and products ranging from C_4 – C_{18} was observed. Deviation from Schulz – Flory distribution and enhancement of selectivity towards shorter alkenes was ascribed to the confinement effect of the active site inside pores. Control experiments showed that Ni^{2+} functionalized UiO-67 was active for ethene oligomerization reaction, without the bpy-

Ni^{2+} moiety, with TOFs in the same order of magnitude. The authors suggested that the activity originated most likely from excess nickel coordinated to water and hydroxide ligands on the zirconium cluster. In addition to oligomers, significant amount of polyethylene was formed during reaction, 80 wt. % in the worst case. The authors ascribed this reactivity towards polyethylene to the steric bulk in the axial position near the active sites, similar to what was observed over Ni α-diimine catalysts (Figure 8).

In contrast to the linkers as anchoring sites, a different approach was employed by Madrahimov et al. where Ni-bpy was grafted on the free Zr-OH sites in the NU-1000 cluster (Figure 11, bottom left) [37]. Treatment with Et_2AlCl yielded active catalyst in liquid (in heptane, 15 bar ethene at 21 °C, TOF ~ 1.1 – $6.0 \cdot 10^3$ h^{-1}) and gas phase (15 bar ethene, RT, TOF ~ $1.5 \cdot 10^3$) ethene dimerization reaction under batch conditions. Analysis of the catalyst after each catalytic run revealed that crystalline polyethylene formed during the reaction led to catalyst deactivation.

Another method to utilize the MOF clusters as grafting site was demonstrated by Li et al [105]. Using atomic later deposition technique, Ni ions were uniformly installed on the clusters of NU-1000. Investigated at 45 °C and 2 bar ethene under continuous flow conditions, the catalyst became active for ethene oligomerization with TOF of ~$1.1 \cdot 10^3$ after mixing with Et_2AlCl. The main products were C_4 and C_8 with selectivities approximately 50 % for both fractions. Deactivation with time on stream (TOS) was attributed to polymer formation.

Differently from the two methods mentioned above which utilized the clusters as anchoring points, Metzger et al. prepared a catalytically active material, Ni-MFU-4l, by modifying the cluster of the MOF [31]. Exchanging one of the five Zn^{2+} ions in the MOF cluster with Ni^{2+} by mild cation exchange yielded isolated Ni(II) sites (Figure 11, bottom right) and this catalyst was investigated under the following reaction conditions: 5 – 50 bar ethene, 0 – 50 °C and 50 – 500 equivalents of MAO. Under optimized reaction conditions, the highest TOF was close to $4.2 \cdot 10^4$ h^{-1} with 98 % butene and 95 % 1-butene selectivity with C_6 alkenes as the only byproduct. However, catalysts with high metal

loading produced trace amount of polyethylene and suffered from deactivation due to reductive demetalation. The authors recognized the challenges associated with the scalability and cost of MFU-4l and synthesized a more cost effective and scalable MOF, Ni-CFA-1, for the selective dimerization of ethene to 1-butene. These two MOFs are not isoreticular, but the nodes are structurally homologous. Tested under similar reaction conditions to Ni-MFU-4l, but with MMAO instead of MAO, TOFs of $3.1 \cdot 10^4$ h^{-1} with 90 % 1-butene selectivity were obtained [106].

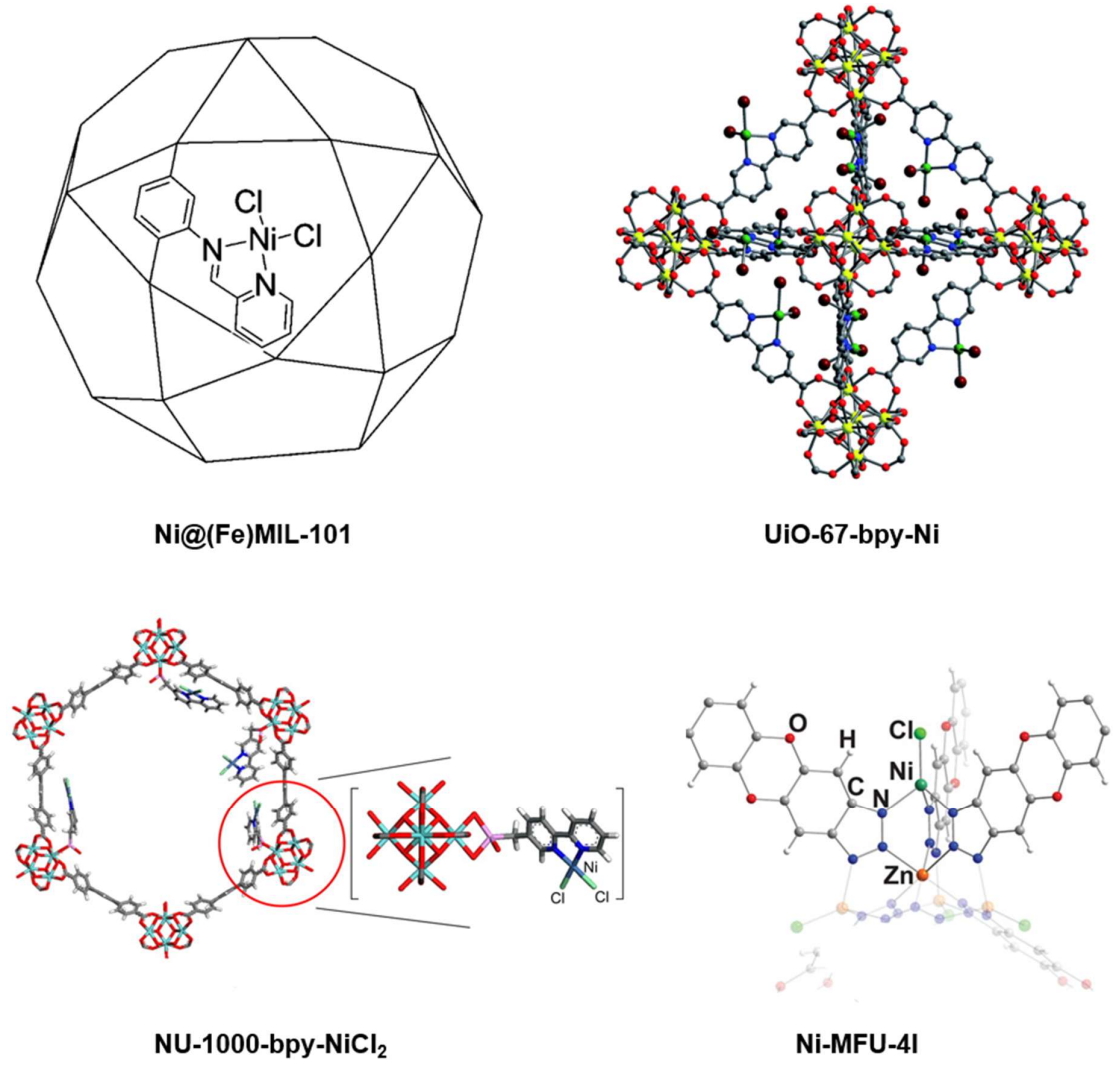

Figure 11: Simplified structures and the different methods to introduce catalytic site into the MOFs for ethene oligomerization reaction. For the catalysts in the top row, Ni@(Fe)MIL-101 [34] and UiO-67-bpy-Ni [35], functional linkers are utilized to graft Ni. For the catalysts in the bottom row, the cluster is (1) utilized by using it as anchoring

point to coordinate well known homogeneous catalyst [37] and (2) modified by exchanging one of the Zn^{2+} ions with Ni^{2+} [31].

One notable cocatalyst free ethene dimerization MOF catalyst is (Ru)HKUST-1. A series of ligand and thermal engineered defective (Ru)HKUST-1 yielded catalytically active species after thermal activation in inert or inert/H_2 mixture. Operated under continuous flow in gas-phase reactor at 60 °C and 42 bar ethene, TOF of 200 h^{-1} with 99 % 1-butene selectivity was reported. Operated under intrapore ethene condensation regime, the catalyst was resistant to deactivation. Whilst outside this regime, irreversible binding of oligomers formed from secondary reactions lead to catalyst deactivation, which could nonetheless be regenerated by oligomer hydrogenation in H_2 at 150 °C to recover the initial rates.

Importantly, most Ni-MOF catalysts published to date are tested as liquid-phase oligomerization catalysts where the use of solvent and cocatalyst, such as diethylaluminum chloride (Et_2AlCl) or MAO, is required in large excess. These compounds are highly flammable and avoiding their use would have strong impact on process safety. There are no explicit reports on how the active sites are formed in MOF catalysts, which is another challenge and drawback associated with the use of activators. The formation of active Ni(II) sites are adopted from what has been reported for their homogeneous Ni counterparts (Ziegler-Natta catalysts), where cocatalyst is used to generate the active metal-alkyl intermediate and oligomerization proceeds by insertion of ethene into a metal-alkyl bond.

Thus, like their homogeneous Ni analogues that require cocatalyst, the Ni-MOFs are suggested to operate through the Cossee-Arlman mechanism. In a separate work dedicated to mechanistic studies, Metzger et al. investigated the mechanism of ethene dimerization in Ni-MFU-4l utilizing a combination of techniques such as isotopic labeling studies, mechanistic probes and DFT calculations and demonstrated that this catalyst operated via the Cossee-Arlman mechanism [107]. To the best of the authors' knowledge, the only Ni-MOF that has been reported as ethene oligomerization catalyst without a cocatalyst is Ni-CPO-27 [108]. This catalyst was tested using a continuous flow fixed-bed

reactor and was active for propene and ethene dimerization at 5 bar and 180 °C. The two major drawbacks of Ni-CPO-27 were the low conversion and the rapid deactivation (conversion < 1 % for propene and 2 % for ethene after 400 min TOS, reaction condition: 5 bar propene, 453 K, WHSV = 64 h^{-1}).

2.5 Aluminosilicates

Ni-aluminosilicates have long been considered the most promising heterogeneous ethene oligomerization catalyst. While the first MOF catalyst for ethene oligomerization was discovered in the last decade, the first nickel based heterogeneous ethene oligomerization catalyst, NiO on silica, was first reported by Morikawa in 1938 [109]. These catalysts dimerize ethene to butene at ambient temperature, but the silica support became absolute with the discovery that incorporation of Al on silica increased the activity of these catalysts for ethene oligomerization. Sohn et al. investigated activity over $NiSO_4$ on SiO_2 and on SiO_2-Al_2O_3 at 20 °C and ~ 0.4 bar ethene. Under the same reaction conditions, the activity over the latter catalyst was up to six times higher with respect to the SiO_2 support [110]. Similar observation was reported for aluminum incorporated mesoporous materials such as Ni-MCM-41 and Ni-AlMCM-41 [111].

The four main classes of inorganic supports that gained attention are Ni(II) grafted zeolites, amorphous SiO_2-Al_2O_3, Al_2O_3 and mesoporous materials such as AlMCM-41 and AlSBA-15. These catalysts are bifunctional in the sense that they mainly contain two different types of active sites: Brønsted (and Lewis) acid and nickel sites. In contrast to solid acids that only contain Brønsted acid sites and require high temperature (see 2.3.4), the nickel functionalized catalysts showed interesting properties at low temperature. Heveling et al. [112] identified two separate temperature regions for high activity over nickel exchanged NaY, one at low temperature (120 °C) and one at high temperature (300 °C). Only even-numbered products were observed at low temperature, while at high temperature acid site catalyzed reactions contributed to the product spectrum and both even and odd-numbered products were identified. A blank run with NaY demonstrated that the support alone becomes active only at temperatures higher than ~ 250 °C, proving

that these two sites are operating with different mechanism and have distinct activity and selectivity in the ethene oligomerization reaction.

Among other properties of the catalysts, porosity has been reported to have the most crucial role for the activity and lifetime of the catalyst. The mesoporous catalysts are reported to perform better than microporous catalysts in terms of activity and stability. Hulea et al. compared the catalytic activity of various Ni-exchanged aluminosilicate catalysts with different topologies and porosities under similar reaction conditions (150 °C, 35 – 40 bar ethene, batch mode) [47]. As shown in Figure 12, the average activity increased strongly with an increase in pore size. Another drawback of microporous catalyst is that they typically suffer from rapid deactivation due to blocking of micropores by reaction products. In contrast, the large pores in mesoporous catalysts facilitate the diffusion of the products resulting in a low deactivation rate [113]. An exception to this is the nanocrystalline Ni-H-Beta zeolite, which was resistant to deactivation under the investigated conditions (120 °C and P_{ethene} = 26 bar) [114].

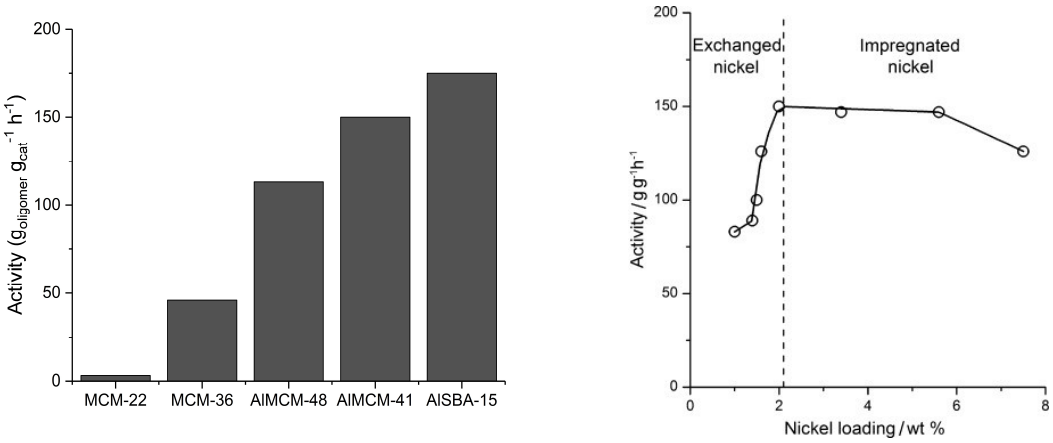

Figure 12: Left: Average activity over micro- and mesoporous Ni-exchanged aluminosilicate catalysts. Reaction conditions: 150 °C, 35 – 40 bar ethene, batch mode. Adapted from [47]. Right: Activity of Ni-MCM-41 catalysts in ethene oligomerization reaction as a function of Ni loading. Reaction conditions: 150 °C, 35 bar ethene, batch mode. Adopted from [115].

The nickel containing aluminosilicates are usually prepared by ion exchange or impregnation with Ni(II) salts. Nanocrystalline Ni-H-Beta (Si/Al = 12) [114] and Ni-

AlMCM-41 (Si/Al = 9) [115] prepared by these two methods show increased activity with increasing nickel loading reaching a plateau followed by a decrease in activity (Figure 12). In both cases, the increase in activity was ascribed to an increase in Ni^{2+} concentration as charge-compensating cation. Further increase in Ni concentration, after the saturation of the exchange sites, did not lead to an increase in conversion. In the contrary, it led to a decrease in activity at which was explained by partial blocking of the pores by formation of bulk NiO particles.

Despite almost a century since the discovery of Ni catalyzed ethene oligomerization reaction, the nature of the active nickel site, how it is formed and where it is placed is not unambiguously agreed upon in literature. The important upsides of Ni-aluminosilicate catalysts compared to the traditional homogeneous Ni-complexes and Ni-MOFs is that they do not require a cocatalyst and that they can be regenerated by heating in an oxidative atmosphere at elevated temperature to burn off eventual reaction products deposited on the catalyst [47, 94]. This highlights the crucial role of the support in the ethene oligomerization reaction.

Mechanistic and spectroscopic studies on Ni-based aluminosilicates are in part complicated because residual Brønsted acid sites are present in the Ni functionalized catalyst, in part because Ni can adopt a number of oxidation states and lastly because it can bind to several distinct sites on the aluminosilicate support. Monovalent Ni^{+} (**8**, Figure 13) on silica-alumina [116], zeolite Y [117] and MCM-41 [111] and divalent Ni^{2+} (**9**, Figure 13) on Beta zeolite [114] and MCM-41 [118] on the ion-exchanged sites have been suggested as active species. Recently, Iglesia et al. proposed isolated $[Ni\text{-}OH]^{+}$ grafted onto exchange sites (**10**, Figure 13) as active sites on the basis that the presence of two nearby H^{+} is unlikely for AlMCM-41 with high Si/Al, this was supported by the observation that dimerization rate increased with Ni content up to saturation exchange stoichiometries (1 Ni exchanged per H^{+})[119].

In parallel, Martinez et al. proposed the Ni^{2+} species interacting with the weakly acidic surface hydroxyl groups (*i.e.* silanols and aluminols) and under-coordinated Ni^{2+} on the

surface of sub-5 nm NiO nanoparticles on Ni-AlMCM-41 and Ni-Siralox-30 (silica-doped alumina) as the main active species [120]. In a later study focusing on nanocrystalline Ni-H-Beta, isolated Ni^{2+} grafted onto acidic silanols (**11**, Figure 13), rather than Ni^{2+} on ion-exchange sites, were proposed as the main active sites based on time- and temperature resolved *operando* FTIR [121].

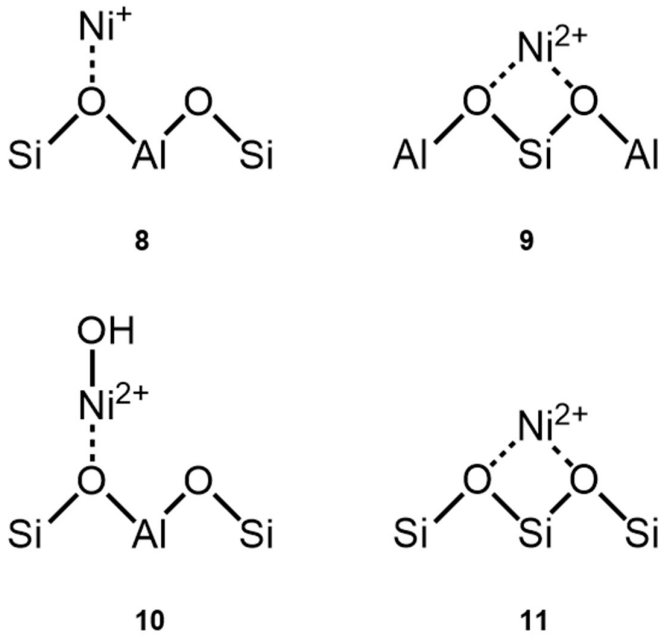

Figure 13: Proposed Ni species formed over aluminosilicates after Ni functionalization. Ni species are defined as monovalent Ni^{+} (**8**), Ni^{2+} exchanged on two H^{+} sites (**9**), hydroxylated Ni^{2+} (**10**) and Ni^{2+} grafted onto acidic silanols (**11**).

Since Ni-aluminosilicates do not require a cocatalyst, the reaction mechanism have proven difficult to determine and both metallacycle and Cossee-Arlman mechanism have been suggested [122-125]. However, recent experimental and theoretical investigations further support the Cossee-Arlman type mechanism and the ion-exchanged Ni^{2+} sites as the active sites.

Specifically, Brogaard et al. [122] performed density functional theory (DFT) calculations of ethene oligomerization in microporous zeolite-based catalyst, Ni-SSZ-24, and compared the free energy profiles of Cossee-Arlman, metallacycle and a new proton-

transfer mechanism on Ni^0, Ni^+ and Ni^{2+}. Based on these results, the Cossee-Arlman mechanism on Ni^{2+} at ion exchange positions were found to be most probable. Next, the authors suggested two mechanisms for the formation of Cossee-Arlman active sites ([Ni-ethene-H]$^+$] species) from Ni^{2+} ions. According to the first pathway, a stoichiometric reaction starting from [Ni-(ethene)$_2$] can take place to form [Ni-ethene-H]$^+$ active sites, generating 1,3-butadiene and a Brønsted acid site as 'by-product' in the process. The second pathway considers the formation of the active site from isolated [Ni-OH]$^+$ species (**10**, Figure 13). Unlike the first mechanism, the second mechanism does not lead to the formation of 1,3-butadiene or a Brønsted acid site, but to the formation of a vinyl alcohol (ethenol).

Gounder et al. [126] evaluated the ethene dimerization activity of Ni^{2+} sites in Ni-Beta zeolite (0.01–1 kPa, 453 K, WHSV = 0.01–10 h^{-1}) after suppressing contributions from the H^+ sites on the support. An induction period was observed at low P_{ethene} (< 0.4 kPa), which decreased with increasing ethene pressure until (> 0.4 kPa) or in the presence of H_2. Based on H/D isotopic scrambling experiments, co-feeding H_2 was proposed to facilitate the formation of [Ni(II)-H]$^+$ sites and their concentration was quantified based on H_2 – D_2 isotopic exchange experiments. *In-situ* X-ray absorption spectroscopy showed that Ni retained its +2 oxidation state during reaction with ethene. Continued formation of 2-butenes on Ni^{2+} -derived active sites, together with ethene assisted formation of [Ni(II)-H]$^+$ intermediates, the results were found to be consistent with the Cossee-Arlman mechanism taking place over Ni^{2+} located on the ion-exchange sites.

Martinez et al. [121] studied the nature of the active site and its formation in Ni-H-beta catalyst by temperature resolved *operando* FT-IR. Starting from – 100 °C, the catalyst was heated under constant ethene pressure (0.0015 bar) up to 120 °C and the products were simultaneously analyzed with a mass spectrometer. Formation of both H_2 and alkanes and appearance of IR peak assigned to [Ni-H]$^+$ (1814 cm^{-1}) after the catalyst was exposed to ethene, show that ethene readily undergoes C-H bond dissociation even at sub-ambient temperature. Concurrently with the appearance of IR peaks for [Ni-alkyl]$^+$ (3015, 1411, 1602 cm^{-1}) at– 33 °C, gaseous butene products were detected. Based on the observation that

detection of butene in the gas phase correlated best with formation of $[Ni\text{-}alkyl]^+$ species, the authors ascribed only minor, if any, contribution from $[Ni\text{-}H]^+$ species to the overall reaction.

In contrast to what has been proposed over Ni-silica-alumina, where Ni^0 and Brønsted acid site was suggested to combine to form $[Ni\text{-}H]^+$ active species during activation [127], here the authors excluded this mechanism based on the observation that $[Ni\text{-}H]^+$ formed only after the catalyst came in contact with ethene. The absence of 1,3-butadiene in the gas phase and lack of IR peaks at 3610 and 3640 cm^{-1} for the eventual formation of new Brønsted acid site with ethene, was used to rule out one of the pathways proposed by Brogaard et al. [122]. Furthermore, FTIR in the OH stretching region of the activated sample only showed three peaks belonging to Brønsted acid sites, silanols and extra framework aluminum species and no additional peaks for $[Ni\text{-}OH]^+$ species expected around 3630 cm^{-1}, thus questioning whether $[Ni\text{-}OH]^+$ species participate in the dimerization reaction or formation of the active site.

Nevertheless, formation of $[Ni\text{-}alkyl]^+$ and $[Ni\text{-}H]^+$ species are consistent with the Cossee-Arlman type mechanism. However, the authors suggested a redox type catalytic cycle where one ethene molecule coordinate to Ni^{2+} on silanols (**11**, Figure 13) followed by oxidative addition to form [Ni^{2+}-ethenyl-H] species where the formal oxidation state of Ni becomes +4.

It is important to note that kinetic studies on ethene dimerization and oligomerization reactions over heterogeneous catalysts is scarce. These measurements are often complicated by contributions from side reactions occurring at Brønsted acid sites and by rapid deactivation of the catalyst. Unless specified otherwise, all the reported kinetic parameters are derived under pseudo steady state conditions *i.e.* after the initial rapid deactivation observed over the investigated catalysts. In some cases, the pseudo steady-

state rate is only a fraction of those measured at initial reaction times, which means that only a fraction of the total active sites is being probed during the experiments.

Creaser et al. studied NiNaY zeolite in the temperature range 50 – 70 °C and ~ 7 bar – 41 bar ethene. Ethene pressure and temperature variation experiments carried after the initial deactivation (~ 20 % of the initial activity under pseudo steady-state conditions), revealed a reaction order of 1.09 ± 0.29, 1.16 ± 0.12 and 1.20 ± 0.92 with respect to rate of ethene consumption at 50, 60 and 70 °C, respectively, and an apparent activation energy of 42.1 kJ/mol [128]. Espinoza et al. employed a different approach to account for deactivation for similar studies over Ni functionalized silica-alumina [129]. Instead of measuring the rate at pseudo steady-state, they measured the activity over the catalyst at a set condition (varied between 120 – 380 °C and 1.6 – 21.4 bar ethene) after 60 min TOS. The catalyst was then regenerated in air at 500 °C and the activity measured under another set of conditions. The apparent activation energy was determined to be 37 kJ/mol while the reaction order with respect to ethene consumption was close to first order (~ 1.1).

Combining experimental observations and single-event microkinetic modeling, Toch et al. investigated the ethene oligomerization over Ni-exchanged silica-alumina between 170 – 230 °C and 1.5 – 3.5 bar ethene [123]. The catalyst was resistant to deactivation during 480 min on stream and due to the absence of strong acid sites, low space-time and low ethene partial pressure, the catalytic activity was ascribed solely to the nickel ions. The rate of reaction increased linearly with ethene partial pressure and the reaction was found to be first order on ethene consumption. The catalyst showed a Schulz-Flory type product distribution with about 90% selectivity towards butenes, while thermodynamic distribution was observed among the linear butenes. Parameters fitted in a single-event microkinetic model, on the assumption that the catalyst operated through the Cossee-

Arlman mechanism, successfully described the experimental results. However, the authors did not definitely exclude the metallacycle mechanism.

Alkene dimerization rates has also been investigated on mesoporous Ni-MCM-41 catalyst under transient deactivation (gas-phase reaction) and steady-state conditions (the catalyst was resistant to deactivation when operated under intrapore ethene condensation regime)[119]. Steady-state rates obtained at -30 and -20 °C and pseudo steady-state rates obtained at 175 °C showed a second order dependency on ethene fugacity and pressure, respectively, where P_{ethene} was varied between 5 –25 bar. The authors suggested the second order dependence in ethene pressure and fugacity was consistent with the C-C bond formation between a gaseous and a bound ethene present at low coverages on Ni centers.

3 Experimental methods

3.1 Materials

While Ni functionalization was carried out by the author, the materials used in this work were either commercially available or have been synthesized by other members of the group.

3.1.1 Aluminosilicates

The microcrystalline NH_4-Beta zeolite (Si/Al = 19) was obtained from Zeolyst (CP-814C). Nanocrystalline Na-Beta zeolite (Si/Al = 13) was obtained from PQ. The SSZ-24 zeolite was synthesized by Dr. Michael Martin Dyballa as described in detail in **Paper II**. SiO_2-Al_2O_3 and γ-Al_2O_3 supports impregnated with an aqueous solution of nickel sulfate was prepared by Dr. Lu Li, as described here [130].

Functionalization of Beta zeolite and SSZ-24 are described in detail in **Paper I** and **II**.

3.1.2 Metal-organic frameworks

The H_2bpdc and H_2bpydc mixed-linker MOFS, referred to as UiO-67-bpy, was synthesized by Dr. Gurpreet Kaur as described here in **Paper III**. The other mixed-linker MOFs were synthesized and characterized by Dr. Gurpreet Kaur as described in her Ph. D dissertation [131]. The post synthetic metalation of various mixed-linker UiO-67 MOFs was carried out in EtOH with nickel(II) acetate tetrahydrate ($Ni(OAc)_2{\cdot}4H_2O$, 99.9 % Sigma-Aldrich) and nickel(II) nitrate hexahydrate ($Ni(NO_3)_2{\cdot}6H_2O$, 99.9 % Sigma-Aldrich) where the amount of precursor was adjusted to produce materials with Ni:functional linker molar ratio ~2.4 and ~1.2, respectively.

For UiO-67-$bpy_{11\%}$ and UiO-67-$bpy_{4\%}$ series reported in **Paper III**, the metalation was carried out with 20 % excess of what was required for Ni:bpy (mol/mol) ratio of 0.5, 1 and 2, i.e. Ni:bpy molar ratio = 0.6, 1.2 and 2.4, respectively. For UiO-67-$bpy_{11\%}$, Ni functionalization was also carried out with nickel(II) chloride hexahydrate ($NiCl_2{\cdot}6H_2O$,

99.9 % Sigma-Aldrich) $Ni(NO_3)_2 \cdot 6H_2O$ and nickel(II) acetylacetonate ($Ni(acac)_2$) with 20 % excess of what was require for Ni:bpy (mol/mol) ratio of 2. All MOFs were dried at 196 °C in air prior to metalation. The required amount of Ni salt for various Ni:bpy (mol/mol) ratios was dissolved in EtOH (10 mL EtOH/$g_{cat,}$ except for $Ni(acac)_2$ where the liquid to solid ratio was 20 mL) and mixed with the catalyst in a HDPE bottle. The slurry was sonicated for 30 min, capped, and heated overnight at 65 °C. The resulting slurry was washed three times with 10 mL EtOH/g_{cat} and dried in air overnight at 65 °C.

Two of the mixed-linker MOFs, (2.2)Ni-UiO-67-$(bpdc(OH)_2)_{5.1\%}$ and (2.3)Ni-UiO-67-$(bpdc(NH_2)_2)_{6.9\%}$, required two additional washing steps to get rid of unreacted $Ni(acetate)_2 \cdot 4H_2O$ that was deposited as green powder on top of the MOF powder.

The Ni-CPO-27 material was provided by Dr. Sachin Chavan and was synthesized following a recipe reported in literature [22].

3.2 Catalyst characterization

Powder X-ray diffraction

Powder X-ray diffraction (PXRD) was used to identify the phase purity and crystallinity of the materials. For this purpose, a Bruker D8 Discover diffractometer with Cu Kα radiation (λ = 1.5406 Å) was employed.

Thermogravimetric analysis

The stability of the catalysts in synthetic air, as well as the amount of retained hydrocarbons after reaction was determined by thermogravimetric analysis (TGA) on a Netzsch STA 449 F3- Jupiter instrument. Approximately 20 mg of catalyst was heated under a flow of synthetic air (25 mL/min) to 800 °C at a rate of 5 °C/min.

^{1}H-NMR

The relative concentrations of organic compounds in the MOF catalysts was determined by liquid-phase proton nuclear magnetic resonance (^{1}H-NMR), after digestion of the MOF in a NaOH/ D_2O solution. 20 mg of dry sample was weighed in a centrifuging tube and 1 mL of 1M NaOH (in D_2O) was added. The tube was shaken properly to obtain a homogeneous suspension and kept overnight for digestion. After centrifuging the digested suspension for 15 min, 600 µL solution was pipetted to an NMR tube. Liquid ^{1}H NMR spectra were obtained with a Bruker AVII 400 NMR Spectrometer (400 MHz). The relaxation delay (d1) was set to 20 seconds with 64 scans. The H-NMR analysis was carried out by Dr. Gurpreet Kaur.

Scanning electron microscopy

Scanning electron microscopy (SEM) was performed on all materials in order evaluate particle size, morphology and to estimate nickel distribution. The instrument used was a Hitachi SU8230 microscope. Additionally, the elemental composition of the catalysts, especially for MOFs, were determined by energy-dispersive X-ray spectroscopy (EDS) at 10 kV accelerating voltage utilizing a X-flash 6|10 detector.

The Ni wt. % of the catalysts were determined by assuming the stoichiometric formula $Zr_6O_4(OH)_4(bpdc)_x(Functional\ linker)_yBA_zFA_w6Ni/Zr$, where BA and FA is benzoate and formate, respectively, and x, y, z and w were determined from ^{1}H-NMR and TGA.

N_2 adsorption

The textural properties of the samples were derived from N_2 adsorption isotherms, measured at –196 °C, liquid nitrogen temperature (LNT), using a BELSORP-mini II instrument. Unless specified otherwise, all samples were outgassed in vacuum for 60 min at 80 °C and 180 min at 300 °C, and then measured. The catalyst pore volumes and surface areas were determined using the t-plot and BET methods.

Elemental analysis

The Si, Al and Ni content in the zeolites were quantified using an Agilent 4100 microwave plasma atomic emission spectrometer (MP-AES). Prior to the element analysis, the concentration of the elements was estimated with EDS analysis and calibration solutions were made with Si, Al, and Ni standards in estimated concentration range. Approximately 20 mg of zeolite was dissolved in 1 mL 15 wt. % HF in a Teflon container. After 45 min, the

mixture was transferred to a 50 mL polypropylene flask containing boric acid to neutralize the remaining unreacted hydrofluoric acid and filled with deionized water.

Analysis of the retained hydrocarbon species

Analysis of hydrocarbons retained in the catalyst after reaction was done by dissolving the zeolite with HF, liberating the molecules trapped inside the pores. Approximately 15 mg of tested zeolite was dissolved in Teflon vials using 1 mL ~15 wt. % HF and the hydrocarbons extracted with 1 mL CH_2Cl_2 with ortho-chloro-toluene as internal standard. The organic mixture was analyzed on an Agilent 7890/5975 GC/MS with a HP5-MS column (60 m x 0.25 mm x 0.25 μm).

Fourier-transformed infrared spectroscopy

Fourier-transformed infrared spectroscopy (FTIR) was employed to investigate the acidic properties of the zeolitic catalysts and to investigate the nature of the active sites of both zeolitic and MOF catalysts. The measurements were performed in transmission mode on a Bruker Vertex 80 instrument with a Mercury Cadmium Telluride (MCT) detector. For this purpose, a quartz cell with KBr windows was employed. Catalysts were prepared as thin wafers supported in a gold envelope.

The concentration of acid sites was investigated with FTIR spectroscopy using pyridine as probe molecule. The catalysts were pretreated in vacuum (<10–5 mbar) for 180 min: 60 min at 150 °C followed by 120 min at 300 °C. The adsorption of pyridine was done by exposing the pellets to pyridine vapor. After equilibration at room temperature, the catalysts were degassed at 200 °C for 2 h. The final spectrum was recorded at RT and the integrated area of the bands at 1545 cm^{-1} and 1455 cm^{-1} with molar extinction coefficients

of 0.73 and 0.64 were used to determine the amounts of Brønsted and Lewis acid sites, respectively.

The nature of the active sites in MOF catalysts were investigated by Dr. Andrea Lazzarini in the University of Oslo using CO as probe molecule. The catalysts were pretreated in vacuum at 250 °C for 3 h. The probe molecule was dosed to the sample at RT and cooled down using liquid N_2. Afterwards, CO was gradually removed by applying vacuum while IR spectra were collected at each step of desorption.

The nature of the active sites in zeolitic catalysts were investigated by Dr. Berlier et al. in the University of Turin. Detailed description of the experimental procedure is reported in **Paper I**.

X-ray photoelectron spectroscopy

X-ray photoelectron spectroscopy (XPS) was performed to investigate the fraction of Ni free and Ni coordinated bpy. The measurements were carried with a Kratos Axis UltraDLD instrument using a monochromatic AlKa radiation (hν = 1486.6 eV) at 15 kV and 10 mA. Charge neutralization was necessary to acquire the spectra and the pass energies for the survey and high-resolution scans were 160 and 20 eV, respectively. The pressure in the chamber was maintained below of 6×10^{-9} Torr during the acquisition. Analysis was performed using Casa XPS software, version 2.3.18. PR1.0. The binding-energy values were corrected with reference to C1s = 284.6 eV.

Dr. Maria Evangelou Kalyva is acknowledged for carrying out the experiments and data analysis.

X-ray absorption spectroscopy

X-ray absorption spectroscopy (XAS) was utilized to probe the active sites and determine the oxidation state and local environment of the Ni species present in the MOF catalysts. The Ni K-edge XAS data reported in this work was acquired in two different beamlines over the same catalysts from an identical batch: (1) B18 beamline of the Diamond Light Source, UK [132] and (2) SuperXAS beamline at the Swiss Light Source, Switzerland.

In Diamond Light Source: Ni-functionalized MOF samples, in their as-prepared state and recovered after catalytic tests were measured at RT in air, in the form of self-supporting pellets, with optimized weights in the 80–90 mg for 1.3 cm^2 area pellets. Selected model compounds (NiO, $Ni(OH)_2$, $Ni(OAc)_2(H_2O)_4$, $Ni(OAc)_2(H_2O)_2(bpy)$) were also measured in the form of self-supporting pellets, with optimized weights for transmission-mode XAS, using BN as diluent when necessary to obtain a robust enough pellet. All the XAS spectra were normalized to unity edge jump and aligned in energy using the Athena software from the Demeter package [133]. A more in-depth description is reported in **Paper III**

Spectrometer operation at the synchrotron and the final X-ray absorption fine structure (EXAFS) and X-ray absorption near-edge structure (XANES) refinements were performed by Dr. Elisa Borfecchia and Dr. Diego Gianolio.

In Swiss Light Source: *In situ* time-resolved Ni *K*-edge XAS measurements were performed at SuperXAS beamline of Swiss Light Source [134, 135]. For the measurements, the Ni-MOF catalysts were pressed, crushed, and sieved to 150 – 100 μm grain size. Approximately 5 mg catalyst was loaded in a quartz capillary reactor and fixed from both sides by quartz wool. The diameter of the capillaries was 1.5 or 2.0 mm depending on the Ni loading in the samples. The reactor was connected to a gas-flow setup and activated *in situ* at 300 °C for 360 min in a flow of 10 % O_2 in N_2 (total flow of 17 mL/min). The temperature was controlled using a heat gun, based on calibration with a thermocouple placed next to the reactor. The heating and cooling were always performed using a rate of $\pm$ 5 °C/min. The feed was then switched to N_2, reactor cooled to 250 °C and total pressure was increased to

15 bar, monitored and controlled by a back pressure controller (Bronkhorst P-702CV). The ethene oligomerization reaction was carried out at 15 bar ethene with a total flow of 10 mL/min.

The raw experimental data were processed by ProXAS software [136] to obtain normalized μ(E) data. The spectra were then averaged over 30-180 s to improve signal-to-noise ratio preserving the sufficient time-resolution. To extract the characteristic spectra related to independent species, multivariate curve resolution (MCR) approach was applied using pyMCR module [137]. The extracted components (i.e. spectra) were analyzed in EXAFS region within the standard first-shell approach in Demeter software [133], while for XANES spectra, the machine learning based procedure of pyFitIt was applied [138]. In the latter approach, a set of starting geometries was suggested at the first step with a set of geometry modifiers (e.g. bond lengths, bond angles, etc.) defined for each structure. Then, a big number (100 – 1000, depending on the number of modifiers) of structures with different geometries according to the defined modifiers was generated and a XANES spectrum was calculated *ab initio* for each structure within the full potential finite difference approach of FDNMES code [139, 140]. The obtained spectral library was used to train the machine-learning algorithm, which was then able to provide the geometry yielding the best agreement between theory and a given experimental spectrum.

Spectrometer operation at the synchrotron and the final XANES and EXAFS refinements together with the multivariate curve resolution analysis were performed by Dr. Aram Bugaev

3.3 Catalytic testing

Catalytic testing set-up

The schematics of the fixed-bed flow set-up for catalytic testing used in this thesis is shown in Figure 14. The set-up is comprised of five Broonkhorst El-Flow Select series mass flow controllers (MFC). The gases used on each MFC and their flow range in mL/min is shown below. Almost all the tubes and valves were Swagelok and was 316 stainless steel with 1/8" or 1/16" dimensions. One exception is the two four-way Valco GC valves located before the reactor and that was controlled with a microelectronic actuator. The pressure was controlled by a back pressure regulator (Bronkhorst P-702CV) and monitored at several locations with electronic pressure transducers.

The set-up is controlled via LabView interface developed by Senior Engineer Terje Grønås at the Department of Chemistry, University of Oslo

All the catalytic tests were carried out in a continuous flow, fixed bed, stainless steel reactor (i.d. 8.3 mm) with a quartz sinter and wool in the middle upon which the catalyst powder was placed. A thermocouple placed on top of the catalyst bed was utilized to monitor the operating temperature. Before each experiment, the catalyst was pressed, crushed, and sieved with particle size between 240 – 420 µm. The reactor was first loaded with catalyst and was activated in-situ. After the pre-treatment, the reactor was cooled to the desired reaction temperature and the pressure increased with helium.

A small portion of the reactor effluent, about 10 mL/min, was led through heated and insulated lines (in red in Figure 14) (~ 200 °C) to an online gas chromatograph. This allowed for the online analysis of all effluent products simultaneously without the need to condense the heavy products. To prevent condensation of hydrocarbons in the pressure controller, which was held at RT, a cylinder filled with silicon oil was placed upstream to trap heavy hydrocarbon products that might have formed during the reaction.

The effluent was analyzed by an online GC-TCD-FID (Agilent 7890B) equipped with three columns: CP-Molsieve5A (50 m·0.53 mm·50µm) connected to thermal conductivity detector, GS-Gaspro (60 m·0.32 mm) and DB-1 (40m·0.10 mm·0.20µm) both connected to flame-ionization detector (FID). He was used as carrier gas in the first two columns while H_2 was used for the last column. The three channels were used for detection of Ne, light hydrocarbons up to butenes and heavier hydrocarbons, respectively. The presence of Ne (10 % Ne in He) as an internal standard allowed for calibration to obtain accurate mass balances.

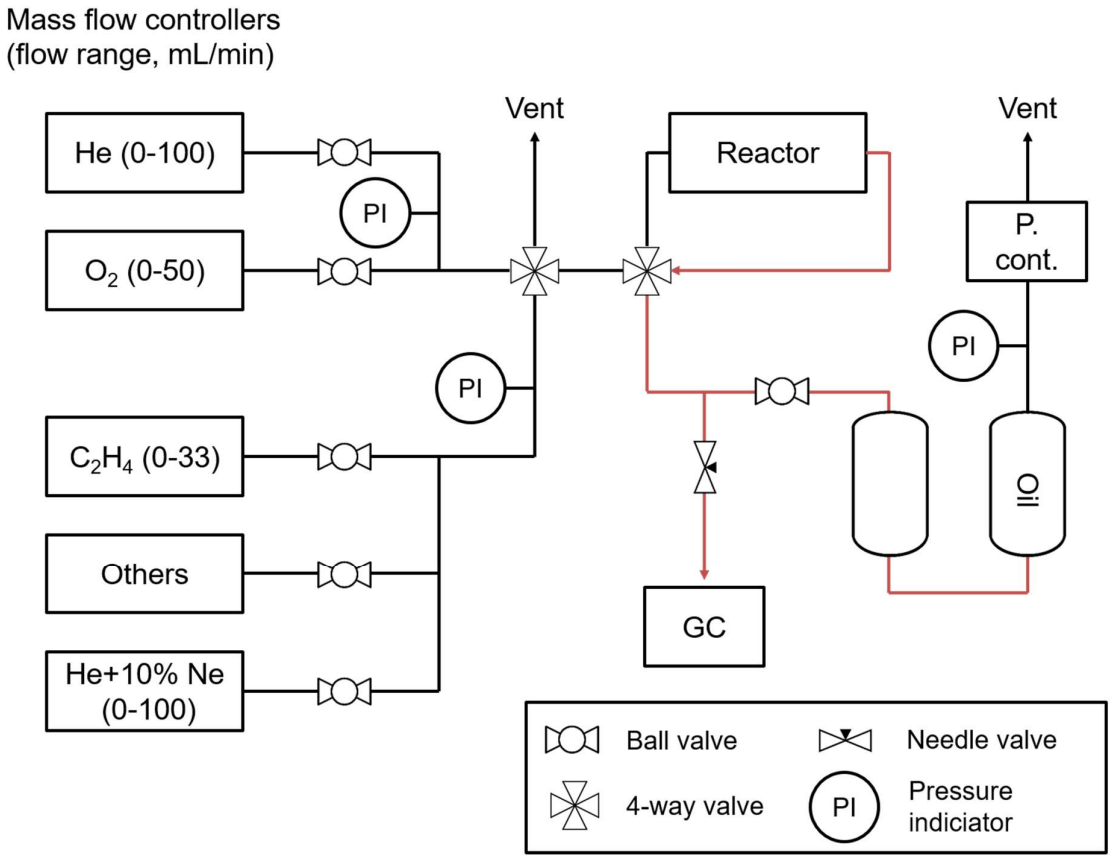

Figure 14: Schematic diagram of the set-up employed for catalytic testing in this work.

Experimental procedure

Due to the wide variety of activation and reaction conditions used in this work, the reader is referred to the experimental section in **Paper I**, **II** and **III** for specific experimental details. Generally, the catalyst was pressed (0.5 – 1.0 bar), crushed and sieved with particle size between 240 – 420 μm. The reactor was first loaded with catalyst and was activated in-situ. After the pre-treatment, the reactor was cooled to the desired reaction temperature and the pressure increased with helium.

Deactivation correction

Due to long chain alkenes formed during alkene oligomerization, the microporous zeolites have been reported to suffer from rapid deactivation. This was also the case over the catalysts tested in this thesis. To assure that the catalyst was at the same state before varying a reaction parameter and to correct for deactivation, each experiment was started under the standard reaction conditions (STC). STC was also run for several hours between each change of conditions. The results obtained under STC was then used to simulate a deactivation model to correct for deactivation. A more in-depth explanation and examples are shown in "Supporting info" in **Paper I** and **II**

4 Synopsis of results

The aim of this work was to identify the active site, asses the role of the support and gain mechanistic and kinetic insight on the ethene oligomerization reaction over Ni functionalized heterogeneous catalysts. Two types of porous heterogeneous catalyst, Ni-zeolites and Ni-MOFs was investigated in this work.

In **Paper I**, we presented a kinetic study of nickel containing mesoporous (Al_2O_3 and SiO_2-Al_2O_3) and microporous (micro and nanocrystalline) Beta zeolite coupled with CO FTIR to investigate the nature of the active sites. **Paper II** describes studies of ethene dimerization over Ni-SSZ-24 using DFT-based molecular dynamics (DFT-MD) simulations at operating condition corroborated by continuous-flow experiments.

In **Paper III**, we investigated a series of cocatalyst free Ni and H_2bpydc functionalized UiO-67 catalyst with continuous-flow experiments together with *ex situ* XAS and CO FTIR spectroscopy to investigate the active site. However, it was observed that the active site was generated *in situ* after the catalysts were exposed to ethene. Identification of the active site and developing mechanistic understanding of their operation are fundamental and crucial for the ongoing cocatalyst free catalyst development. In addition to published results, Ch. 4.2 contains unpublished work following **Paper III** based on kinetic investigations and *operando* XAS, under relevant working conditions, of Ni-UiO-67-bpy.

The following chapter summarizes the main findings obtained during this work. The synopsis is divided into two subtopics, one for Ni-aluminosilicates and the other for Ni-MOF catalysts.

4.1 Ni-aluminosilicates

In the following chapter, the results obtained over Ni-SSZ-24 are separated from results obtained over Ni-Beta and mesoporous supports because the aim of the two studies were different. Furthermore, the reaction conditions employed in each study was slightly different, making it difficult to present the data in a fashionable manner.

The type of aluminosilicate support in focus in this part of the work was Beta zeolite. In contrast to other microporous supports, the Ni functionalized nanocrystalline Beta zeolite investigated at 120 °C and 26 bar ethene was resistant to deactivation [114] making it a good candidate for further catalytic and spectroscopic investigations. Four years ago, the time these investigations started, discussions were still ongoing regarding the oxidation state of Ni, its location, number of active sites and the reaction mechanism for the oligomerization reaction, for the most part discussed between metallacycle and Cossee-Arlman type mechanism.

Experimental results show that butene formation on microporous Ni catalyst have higher reaction order in ethene pressure compared to mesoporous Ni catalyst. This observation suggests that the surrounding molecules can have a significant influence on ethene dimerization over these two types of catalysts.

In the following chapter, some aspects of these topics have been investigated and the findings are reported herein. The chapter starts with CO FTIR spectroscopy to investigate the types of Ni surface sites before moving onto general characterization and catalytic testing results obtained over Ni-Beta and Ni-(Al_2O_3)-SiO_2.

4.1.1 Ni species: active and spectator species

Infrared spectroscopy of CO adsorbed at LNT (approx. –196 °C) was utilized to investigate the different types of Ni surface sites available on Ni-H-Beta(m) before and after ethene contact. For the sake of brevity, only the spectra measured at relatively low CO coverage (θ_{CO}) are reported and discussed, since they provide most information about the nature

of Ni sites. These are reported in Figure 15 for Ni-H-Beta(m) after activation in inert (3 h at 300 °C in He) and contact with ethene (30 min at 150 °C, P_{ethene} = 0.29 bar) or activated catalyst only (top and middle, respectively) and for only activated H-Beta(m) as reference (bottom).

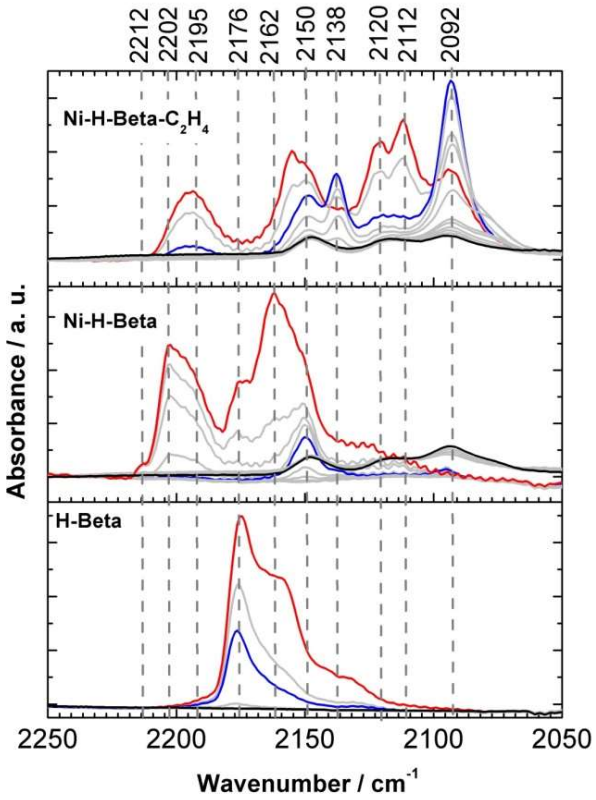

Figure 15: Low coverage CO spectra measured at LNT on: top) Ni-H-Beta(m) sample activated in ethene flow at 150 °C after activation in He; middle) Ni-H-Beta(m) sample activated in He flow for 180 min at 300 °C and bottom) H-Beta(m) sample activated in He flow for 180 min at 300 °C. Red curves correspond to the highest CO pressure (0.1 mbar), blue curves to intermediate coverage allowing to appreciate spectra evolution (0.01-0.005 mbar), black spectra were measured under dynamic vacuum (residual pressure 1 10^{-4} mbar).

Concentrating on He activated Ni-H-Beta(m) sample (middle panel), bands are observed at high frequency at 2212 (weak), 2202 and 2195 cm^{-1} (shoulder), which gradually decrease with θ_{CO}. These are in the typical region of CO adducts on Ni^{2+} sites and were assigned to complexes formed on two distinct Ni^{2+} counterions (2212 and 2202 cm^{-1}) and on grafted Ni^{2+} sites (2195 cm^{-1}) [141-144]. Moving to lower frequency, the band at 2150 cm^{-1},

disappearing upon θ_{CO} decrease, was observed upon CO adsorption on low surface area NiO particles, suggesting the presence of small (XRD silent but observed with SEM, Figure 16) nickel oxide particles [145]. Saturation of the ion-exchange sites for Ni^{2+} functionalized zeolite catalysts is expected when the Ni/Al ratio reaches 0.5, *i.e.* when each Ni(II) replaces two Brønsted acid sites. However, Ni can also bind to existing defects and in some cases form NiO particles, as it can be observed for Ni-H-Beta(m). For catalysts with high Si/Al, $[Ni\text{-}OH]^{+}$ on ion-exchange sites has also been suggested as major species [119].

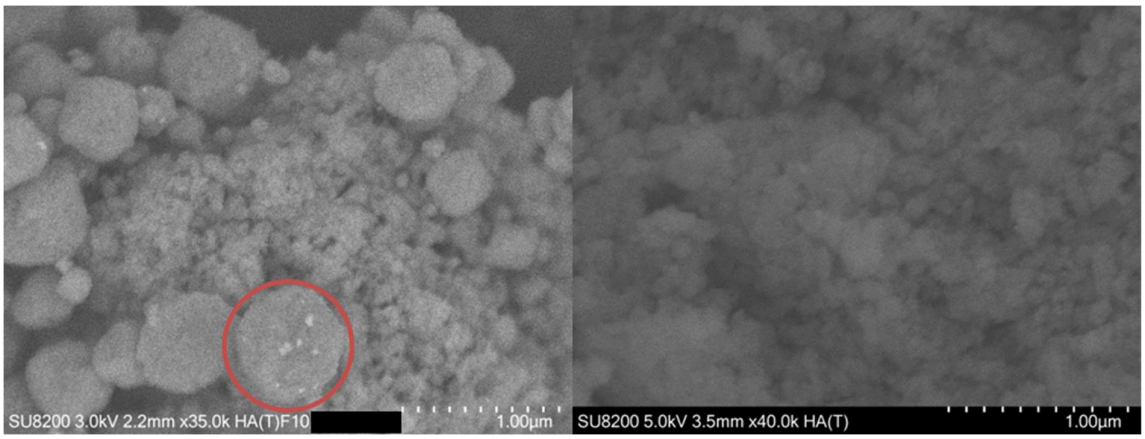

Figure 16: Backscattered electron image of Ni-H-Beta(m) (left) and Ni-H-Beta(n)(2) (right). The bright spots (highlighted with red circle) on the surface of Ni-H-Beta(m) crystals are assigned to NiO particles.

Bands at lower frequency are in the spectral region typical of CO adducts on Ni^{+} and Ni^{0} particles [114, 144, 146, 147]. More in detail, at intermediate coverage (blue spectrum) very weak features are observed at 2138 and 2095 cm^{-1}. Under dynamic vacuum (black curve) broad bands are formed with maxima at 2148, 2116 and 2092 cm^{-1}, with a broad tail extending to lower wavenumbers, indicating some reduction of Ni^{2+} upon activation in inert, as observed elsewhere [144].

Focusing next on CO spectra measured in similar conditions on Ni-H-Beta(m) sample after ethene contact (Figure 15, top panel). First, note the decrease in intensity of the bands at 2176 and 2162 cm^{-1}, related to CO adducts on BAS and silanols, indicating an interaction of ethene with these sites. Concerning the bands assigned to Ni ions, the bands related to Ni^{2+} counterions (2202 and 2215 cm^{-1}) are no longer present, as opposed

to those related to grafted Ni^{2+} sites and NiO particles. Additionally, an increase in the intensity of the bands related to reduced Ni sites (2157, 2138, 2120, 2112 and 2092 cm^{-1}) is observed. The reported results clearly show a reductive effect of ethene, with formation of highly coordinatively unsaturated Ni^{+}, which are thus likely to be present as counterions. Noticeably, even if a small amount of $Ni^{+}(CO)_2$ complexes could be inferred on activated catalyst (middle panel, blue curve, bands at 2138 and 2092 cm^{-1}), it was not possible to exclude the formation of Ni^{0} particles, as suggested by the broad tail below 2100 cm^{-1}, increasing when reducing CO pressure, as often observed in the presence of metal particles [146].

It remains elusive how ethene reduces Ni^{2+} to Ni^{+} and it is insufficient to explain the reduction of Ni^{2+} to Ni^{+} in ethene by an electron transfer from ethene to Ni, as it does not take into account how the excess zeolite framework charge is compensated for. Based on the theoretical work of Brogaard and Olsbye [24], the reduction of Ni^{2+} counterions to Ni^{+} ions is suggested to be related to the reduction of the active $[Ni\text{-alkene-alkyl}]^{+}$ to Ni^{+} when the cell is evacuated and excess ethene and alkyl groups are removed, analogously to how $[Cu(II)\text{-}OH]^{+}$ is reduced to Cu^{+} in vaccuum [148]. It is acknowledged that the spectator and active species cannot be derived on these basis alone. However, this hypothesis may provide a coherent mechanistic explanation of the results.

4.1.2 Influence of support morphology and topology

One of the aims of **Paper I** was to compare the performance of Ni-functionalized catalysts based on zeolite supports and dense, mesoporous supports, under similar reaction conditions. For this purpose, microcrystalline and nanocrystalline Ni-Beta catalysts and $NiSO_4$ functionalized SiO_2 and SiO_2-Al_2O_3 was prepared. The main physical properties of the catalysts are summarized in Table 1.

Table 1: Textural properties and elemental composition of the parent and Ni-aluminosilicate catalysts.

Sample	S_{BET} (m^2/g)	V_{micro} (cm^3/g)	V_{meso} (cm^3/g)	Si/Al	Ni/Al	Ni (wt. %)	BAS mmol/g	LAS mmol/g
H-Beta(m)	677	0.28	0.08	19.0	-	-	0.55	0.49
Ni-H-Beta(m)	651	0.28	0.17	23.1	0.5	2.2	0.19	0.92
Na-Beta(n)	712	0.27	0.76	13.0	-	-		
H-Beta(n)	677	0.19	0.80		-	-	0.65	0.68
Ni-H-Beta(n)	570	0.18	0.58	16.8	0.4	2.1	0.29	1.20
Ni-H(Na)-Beta(n)(2)	616	0.23	0.73	16.9	0.8	4.2	0.42	1.37
Ni-H-Beta(n)(2)	620	0.22	0.69	15.2	0.8	4.6	0.26	1.41
$NiSO_4$-Al_2O_3	193	0.01	0.66	-	-	2.0	-	-
$NiSO_4$-SiO_2-Al_2O_3	454	0.03	0.55	-	-	2.0	-	-
H-SSZ-24	430	0.14	0.11	75	-	-	-	-
Ni-SSZ-24	412	0.15	0.12	80	0.3	0.4	-	-

Initial ethene conversion rates obtained over the Ni-containing catalysts under standard conditions (120 °C, P_{ethene} = 25.1 bar) are plotted versus TOS in Figure 17. The zeolite catalysts showed rapid initial deactivation, followed by a period of slower deactivation. Such behavior is typical of processes where product deposition is responsible for catalyst deactivation [149]. The lower conversion rate of Ni-H-Beta(m) compared to Ni-H-Beta(n) is mainly ascribed to the particle size (100 – 700 nm and < 50 nm, respectively) as the amount of nickel, BAS and LAS is similar in the two materials (Table 1). Larger crystallites of Ni-H-Beta(m) present a longer diffusion path compared to Ni-H-Beta(n) and transport of the reactant and products between the active sites and the surface is limited [150], leading to build-up of larger products inside the pores and deactivation (**Paper I**).

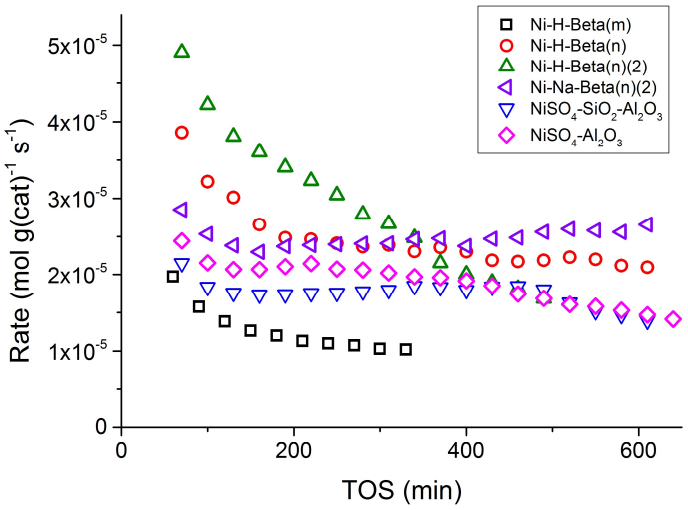

Figure 17: Rate of ethene oligomerization versus time on stream for all catalysts. Reaction conditions: 29 bar total pressure where P_{ethene} = 25.1 bar and P_{inert} = 3.9 bar, T = 120 °C and m_{cat} = 0.100 g for nanocrystalline Beta zeolites and 0.200 g for microcrystalline Beta zeolite and mesoporous catalysts, contact time = 3.4 and 6.8 mg_{cat}·min·mL^{-1}, respectively.

Comparing the activity over Ni-H-Beta(n) with 2 wt. % Ni to Ni-H-Beta(n)(2) and Ni-H(Na)-Beta(n)(2) with 4 wt. % Ni, show that the conversion rate is almost unaffected by the doubling in nickel concentration. This result confirms that different nickel species are present in the catalysts and that only nickel in certain configuration is active for ethene oligomerization, as previously reported by Martinez et al. [114]. Although, detailed characterization of the surface species for the nanocrystalline catalysts are lacking, for catalysts with Ni/Al ratio above 0.5, an increase in concentration of grafted Ni species and NiO, is expected. Considering that the Ni/Al ratio doubled from 0.4 for Ni-H-Beta(n) to 0.8 for Ni-H-Beta(n)(2) while the activity remained unchanged, is best in accordance with Ni^{2+} on ion-exchange sites as the active site in these catalysts.

Next considering the mesoporous catalysts ($NiSO_4/Al_2O_3$ and $NiSO_4/SiO_2$-Al_2O_3), after a short period of deactivation, the activity increased for several hours before subsequently decreasing again. Such behavior is typical of systems where active sites are initially formed or gradually become accessible for the reactants at a higher rate than the rate of deactivation, until deactivation dominates, in this case after approximately 200 and 500

min on stream for $NiSO_4/Al_2O_3$ and $NiSO_4/SiO_2$-Al_2O_3, respectively. This pattern has already been observed in propene oligomerization by Mlinar et al. [151]. In that work, the authors argue that the activation period is due to the migration of nickel ions in the lattice of faujasite; this interpretation cannot be directly applied to the $NiSO_4$-containing catalysts used in this study, as they do not present the same microporous structure. Another possible explanation is that the initiation period is due to the slow build-up of active sites, which may involve formation of Ni-C bond and breakage of Ni-O bond [122, 152]. Deactivation over mesoporous catalysts may appear contradictory to what was written in the introduction (Ch. 2.5, Figure 12), however, majority of those results were obtained over Ni^{2+} functionalized mesoporous catalysts, operated under milder conditions where the reaction was operated in batch mode. These results demonstrate the importance of comparing ethene dimerization catalysts under similar operating conditions.

All catalysts showed high linear butene selectivity (Figure 18) and only traces of alkanes and odd carbon number products were formed, indicating that acid-catalyzed side reactions such as cracking were not occurring to a significant extent. Furthermore, no trace of iso-butene was observed. It should be noted that even though the linear butene selectivity was 95 % in the gas phase, not all products formed were gaseous: some carbon-containing products were not detected by GC-FID, but were quantified from mass balance (denoted retained hydrocarbons, R-HC). Small amounts of gaseous hexene (below 5 % selectivity) were also detected; for clarity, this amount was lumped with the R-HC fraction. The hydrocarbons R-HC retained in Ni-H-Beta(n) were characterized and were found to consist of long chained even-numbered alkenes. The absence of odd numbered products in R-HC further supports that the acid sites are not active to a significant degree.

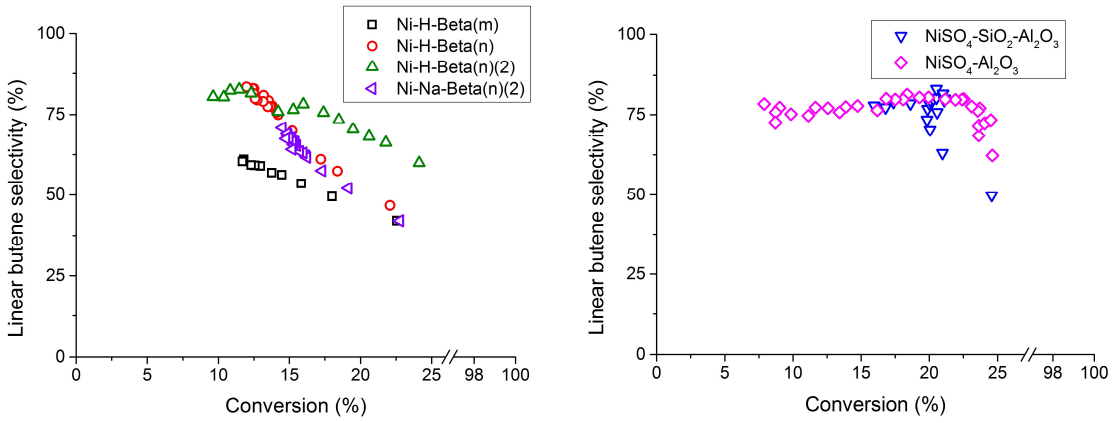

Figure 18: Linear-$C_4^=$ selectivity versus ethene conversion for microporous (left) and mesoporous (right) catalysts. Reaction conditions: 29 bar total pressure where P_{ethene} = 25.1 bar and P_{inert} = 3.9 bar, T = 120 °C and m_{cat} = 0.100 g for nanocrystalline Beta zeolites and 0.200 g for microcrystalline Beta zeolite and mesoporous catalysts, contact time = 3.4 and 6.8 mg_{cat}·min·mL^{-1}, respectively.

Concentrating first on the four zeolite-based catalysts (Figure 18, left panel), butene selectivity steadily increased with a decrease in conversion. This result may suggest that not only ethene, but also product butene and possibly higher alkenes, may adsorb and be converted on the active sites of the catalyst. However, it could also mean that the active sites are changing with deactivation. At any given conversion, butene selectivity was lower for microcrystalline Ni-H-Beta(m) than for nanocrystalline Ni-H-Beta(n), hence the selectivity towards heavier products, including R-HC, is higher. This difference may be explained again by the difference of particle size. Because of the longer diffusion path in larger particles (Ni-H-Beta(m)), the transport of the primary product, butene, from the active sites to the external bulk phase is hindered [153]; this longer residence time in the pores likely favors secondary reactions and formation of longer chains. The longest of these secondary products are permanently stuck in the pores, as the relatively fast deactivation rate and the GC-MS analyses of the spent catalyst suggest. Secondly, larger particles (Ni-H-Beta(m)) have significantly lower external surface, and the selectivity of the external nickel sites may differ from those inside the pores.

Concentrating next on the mesoporous catalysts (Figure 18, right panel), a different pattern was observed: an increase in butene selectivity was observed during the activation

period for each catalyst. This observation suggests that not only the amount, but also the nature of the active sites change during the activation period [154]. During the subsequent period of deactivation, no change in butene selectivity was observed upon decreasing conversion. This result is in accordance with data published by Toch et al. for a Ni/SiO_2-Al_2O_3 catalyst [123]. They observed that product selectivity is independent of ethene conversion, leading to Anderson-Schulz-Flory product distribution [71].

Furthermore, it was observed that the selectivity among linear butenes varied with conversion during the initiation phase. The evolution of yields as a function of ethene conversion, obtained by contact time variation under steady state conditions, can give us a better insight into the primary and secondary products, as well as into the potential presence of different active sites. A new series of experiments was therefore carried out with Ni-H-Beta(m), Ni-H-Beta(n), Ni-H-Beta(n)(2) and Ni-H(Na)-Beta(n)(2) at lower ethene partial pressure (P_{ethene} = 17.4 bar and P_{inert} = 11.6 bar, T = 120 °C) after the catalysts were tested for 500 min at 25.1 bar ethene. 1-butene and 2-butenes selectivities during the initial deactivation period (insets) and in steady state (main plots) is shown in Figure 19.

Overall, the trends are very similar among the four catalysts. The initial performance for all catalysts changed in a similar manner as observed in the tests at P_{ethene} = 25.1 bar: 1-butene yield increases with deactivation, which may suggest that the nature of the active sites changes through time, or that some secondary reaction sites producing 2-butenes from 1-butene, such as Brønsted acid sites, deactivate. The latter hypothesis is in agreement with CO FTIR results where bands at 2176 cm^{-1} (Figure 15, top panel) for BAS disappeared after 30 min at 150 °C under 0.29 bar ethene, suggesting that they are interacting with ethene.

On the other hand, the steady state plots suggest that all butene yields follow a straight line going through the origin. This indicates that all three linear butenes are primary products; hence, only one type of active site is involved in the conversion of ethene to butenes, at least after the first deactivation period. This observation is in best agreement with the Cossee-Arlman mechanism, which accounts for the formation of 2-butenes. In

contrast to the metallacycle mechanism, typical of homogeneous Ni catalysts [64], the Cossee-Arlman mechanism enables isomerization of the formed butyl species before desorption from the active site.

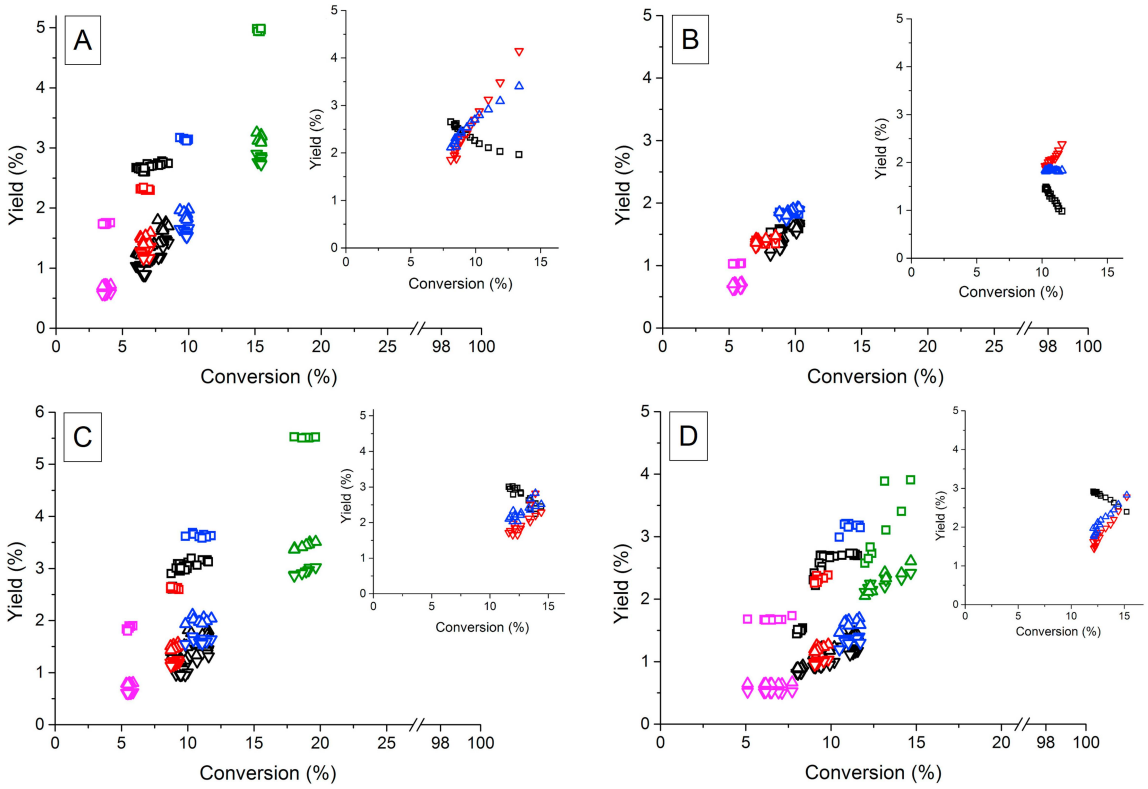

Figure 19: Yield (%) (square: 1-butene, up triangle: cis-2-butene, down triangle: trans-2-butene) as a function of conversion for a) Ni-H-Beta(m), b) Ni-H-Beta(n), c) Ni-H-Beta(n)(2), d) Ni-H(Na)-Beta(n)(2). Reaction conditions: 29 bar total pressure where P_{ethene} = 17.4 bar and P_{inert} = 11.6 bar, T = 120 °C. Contact time varied between 2 – 8 and 4 – 16 mg_{cat}·min·mL^{-1} for nanocrystalline and microcrystalline catalysts, respectively. The results from each contact time measurement are represented by a different color.

To further elucidate the effect of catalyst topology, the five catalysts were subjected to ethene partial pressure variation tests at 120 °C to derive the reaction order of ethene in the rate of consumption of ethene. Distinct differences were observed between the microporous and mesoporous catalysts. The ethene oligomerization reaction was second order over the microporous catalysts, while it was closer to one (1.2 and 1.4) over the mesoporous catalysts. The latter agrees reasonably well with previous work of Toch et al,

who observed a first order dependency on P_{ethene} on Ni/SiO_2-Al_2O_3, for P_{ethene} between 1.5 – 3.5 bar [123].

Table 2: Reaction order with respect to ethene for ethene consumption and for the rate of production of butenes, for the investigated catalysts. Reaction conditions: T = 120 °C, 29 bar total pressure where P_{ethene} = 25.1–11.6 bar and P_{inert} = 3.9–17.4 bar.

Sample	Ethene consumption	Butene formation
Ni-H-Beta(m)	2.0	2.0
Ni-H-Beta(n)	2.0	2.0
Ni-H(Na)-Beta(n)(2)	2.0	2.0
$NiSO_4$–Al_2O_3	1.2	1.5
$NiSO_4$–SiO_2–Al_2O_3	1.4	1.7

Focusing next on the reaction order of ethene in the rate of production of butenes (Table 2). It is instructive to consider the mechanistic implication of the reaction order depending on the catalyst topology. Considering first the Cossee-Arlman mechanism (Scheme 1), theoretical work from Brogaard and Olsbye found that $[Ni\text{-alkene-alkyl}]^+$ species have quite similar stability in the SSZ-24 microporous zeolite [24]. This means that in the Cossee-Arlman mechanism, the resting state of the catalyst can easily change from $[Ni\text{-ethene-ethyl}]^+$, giving a reaction order of 0, to a $[Ni\text{-alkene-alkyl}]^+$ species resulting in a reaction order of 2 in ethene for the rate of butene production. It is reasonable to expect a higher reaction order in the microporous zeolites, where alkyl chains are significantly stabilized, than on mesoporous catalysts where such stabilization is significantly less. This is consistent with the higher reaction orders obtained experimentally with the Beta zeolites, around 2, than on the $NiSO_4$-containing materials, between 1.5 and 1.7 (the uncertainties being high, as the conversion at P_{ethene} = 11 bar is below 2 %). However, a similar change in reaction order could also be consistent with the metallacycle mechanism for the same reason. Longer alkenes adsorb on the Ni sites in the micropores leading to a second order dependence in ethene for butene production, which

could decrease towards first (zeroth) order on a catalyst without stabilization from pores, having a Ni-ethene (dimer) species as resting state. It is acknowledged that these correlations are best made and supported by results obtained from a microkinetic model, which was not carried out in this work. However, this simple analysis may provide an explanation for the second order reaction over the microporous catalysts.

One of the most elegant methods to differentiate between metallacycle and Cossee-Arlman mechanism and widely employed in homogeneous ethene oligomerization catalysts, is based on analyzing the isotopomer distribution from co-oligomerization of a 1:1 mixture of ethene and perdeuteroethene (C_2D_4) [155, 156]. As the metallacycle mechanism leads to no H/D scrambling, only C_4H_8, $C_4H_4D_4$ or C_4D_8 isotopomers should be observed. Conversely, for a Cossee-Arlman based mechanism, H/D scrambling (because of β-hydride elimination) should yield isotopomers containing odd numbers of hydrogen and deuterium. Similar study has also been carried over Ni-MFU-4l, heterogeneous dimerization catalysts, where the authors found the product distribution best in accordance with the Cossee-Arlman mechanism [107].

To differentiate between the two mechanisms, experiments were carried out with C_2D_4 under relevant reactions conditions (120 °C, 7 bar C_2D_4, P_{total} = 10 bar). Preliminary results obtained over Ni-H-Beta(n) by exposing the catalyst first to ethene, followed by perdeuteroethene before switching back to ethene again show that the catalysts suffers from irreversible deactivation in C_2D_4, making it difficult to further investigate the mechanism with this method (Figure 20). Under these reaction conditions, the product selectivity differed significantly from what was observed at 26 bar ethene. In addition to near thermodynamic distribution among the linear butenes (11:54:31 %, 1-, cis and trans-2-butene, respectively), propene, butane and iso-butene was detected in small concentrations (< 0.5 % selectivity in total), suggesting minor contribution to the overall reaction from the remaining Brønsted acid sites. Based on online MS analysis, H/D scrambling among the linear butenes were detected, however, considering that the Brønsted acid sites were still active, this effect could not be ascribed solely to the Ni sites. Furthermore, it was not possible to single out the operating mechanism based on

deactivation as the irreversible deactivation observed under C_2D_4 can be accounted for by both mechanisms, considering that the rate of β-hydride elimination/hydride shift reaction may decrease significantly changing from H to D, leading to increased rate for C-C coupling and eventually deactivation.

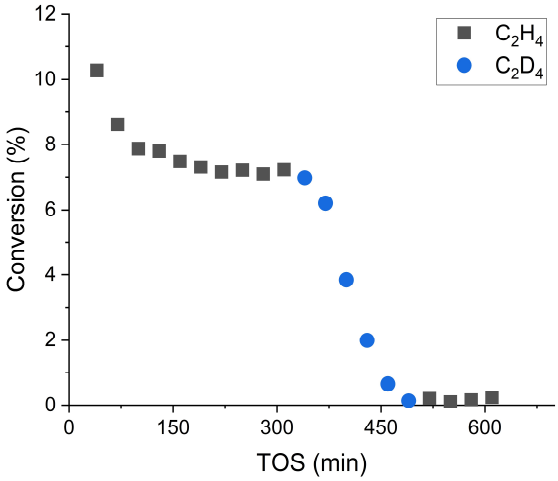

Figure 20: Ethene and perdeuteroethene dimerization over Ni-H-Beta(n) as a function of TOS. Reaction condition: m_{cat} = 0.150 mg, P_{ethene} = 10 bar, T = 120 °C and contact time = 15 mg_{cat}·min·mL^{-1}.

4.1.3 Reversible mobilization of the active sites

The different reaction order with respect to ethene observed over the aluminosilicate catalysts suggest that surrounding molecules may have a significant influence on alkene oligomerization reaction. The novel part of this work was the molecular simulations mimicking operating conditions carried out by Dr. Rasmus Y. Brogaard, while the experiments were performed to test the computational findings. The primary focus of this section will be the experimental results because the author of this dissertation was in charge of the catalytic testing and characterization part of **Paper II**.

In short, the DFT-MD simulations (120 °C and 25 bar ethene) predict that both ethene dimerization and trimerization are catalyzed by mobile $[(ethene)_2Ni\text{-}alkyl]^+$ species *i.e.* $[(ethene)\text{-}Ni\text{-}alkyl]^+$ species mobilized by ethene coordination. The transition states involved in butene formation are slightly lower in free energy than that for hexene formation, indicating a preference toward butene over higher oligomers. Indeed, when employing the free-energy profiles in a microkinetic model (120 °C, 25 bar ethene and assuming 5 % conversion), the rate of formation of 1-butene is two orders of magnitude higher than that of hexene (see **Paper II** for details).

The main physical properties of (microcrystalline) H-SSZ-24 and Ni-SSZ-24 are summarized in Table 1. It is worth noting that the Ni-SSZ-24 had significantly higher Si/Al ratio and thus lower Ni wt. % compared to the Beta zeolite with similar Ni/Al ratio. A total of 13 experiments were carried out in the temperature range from 408 to 438 K, ethene partial pressure from 4 to 26 bar and contact time from 4 – 20 $mg_{cat}\cdot min\cdot mL^{-1}$. Ni-SSZ-24 tested under the standard reaction conditions (26 bar ethene and 150 °C) showed a rapid initial deactivation before reaching steady state. Under all conditions reported in this work, the main product were linear butenes with selectivity higher than 98 %, in agreement with the computational result where the production rate of butene was predicted to be two orders of magnitude higher than that of hexene, as a representative of higher oligomers. The remaining products were mainly longer chain alkenes, denoted C_{6+}, with selectivities less than 2 %. Iso-butene and butane was also observed in some

cases (both less than 0.1 % selectivity), however their selectivity reduced to 0 % after 1000 min TOS (**Paper II**, supporting info).

Figure 21 shows that the rate of butene (and hexene) formation is second order in ethene pressure and that the apparent activation energy is virtually pressure-independent. These findings strongly suggest that the oligomerization mechanism is the same over a wide pressure range. The observed reaction order agrees with microkinetic modeling based on the free-energy profiles based on DFT-MD simulations, where oligomerization occurs on mobile active sites. Note that a second order is only obtained from the model when [ethyl-Ni-alkene]$^+$ species are the most abundant adsorbates *i.e.* the model supports the claim that *if* the anchored adsorbates of the form [ethyl-Ni-butene]$^+$ are prevalent, in accordance with XAS data which indicate that Ni is in tetrahedral coordination with oxygen in the first shell coordination [126], the mobile active sites can indeed explain a second order reaction in ethene pressure.

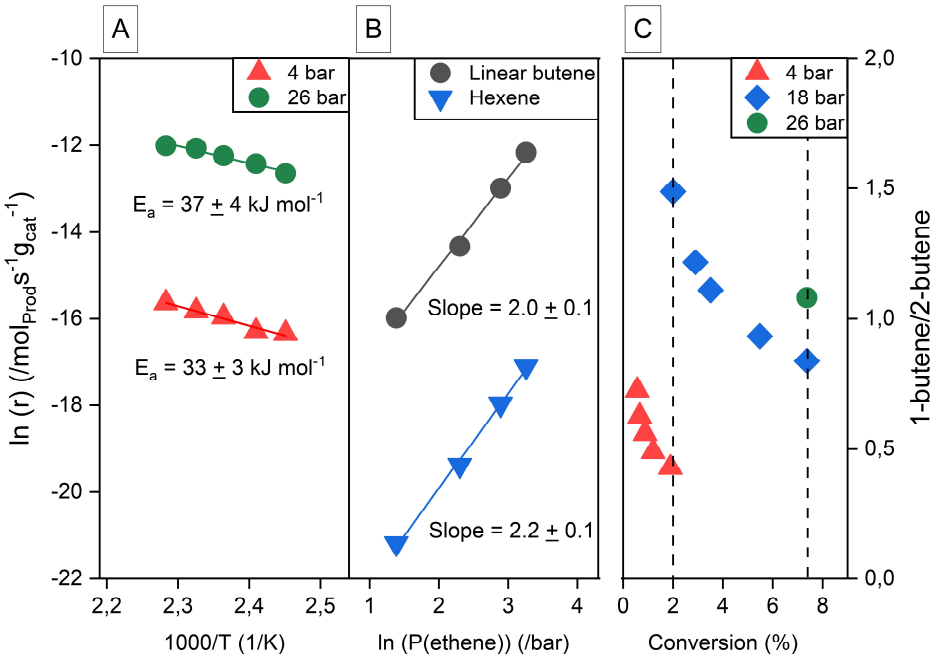

Figure 21: Results from continuous-flow experiments on ethene oligomerization in Ni-SSZ-24. A) Arrhenius plot for butene formation (T = 230 – 270 °C). B) reaction order of butene and hexene in ethene pressure (P_{ethene} = 4 – 26 bar)

and C) 1-butene/2-butene ratio at 150 °C. Reaction conditions: m_{cat} = 0.200 g, contact time: 4–20 mg_{cat}·min·mL^{-1} ethene at STP, T = 135–165°C and P_{total} = 30 bar where P_{ethene} = 4–26 bar and P_{inert} = 26–4 bar.

The experimental results indicate that both 1- and 2-butenes are primary products (Figure A 1), as was also observed on Ni-Beta (*vide supra*). This supports the Cossee–Arlman mechanism, as the [ethyl-Ni-butene]$^+$ species can isomerize between 1- and 2-butene through β-hydrogen elimination on the Ni site prior to desorption, analogously to homogeneous catalysts [82]. Furthermore, the non-equilibrated butene distribution and their dependence on P_{ethene} reflect kinetic control over the production distribution. The increase in 1-butene/2-butene ratio with P_{ethene} is hypothesized to be due to faster substitution of 1-butene at higher ethene partial pressures, thus limiting double bond isomerization on Ni sites.

It is also interesting to consider the impact of this work on the discussion over Ni-Beta and Ni-(SiO_2)-Al_2O_3 catalysts. The computational results show that 1-butene desorption barrier decreases with ethene coordination. The low 1-butene selectivity over the mesoporous catalysts may be due to the lack of assistance from ethene, as ethene facilitate butene desorption over further oligomerization and isomerization, similar to what was demonstrated over Ni-MCM-41 when operated under subambient temperatures when ethene condenses in the mesopores [119]. Furthermore, the lack of the influence from surrounding ethene molecules *e.g.* during CO FTIR, may affect the behavior of the active sites significantly and result in different mechanisms that are in play under the vastly different conditions, such as reduction of Ni^{2+} counterions to Ni^+ on Ni-Beta during evacuation for CO FTIR measurements.

The Si/Al ratio of SSZ-24 zeolite is significantly higher than the Beta zeolite, approx. 80 and 20, respectively. While the proximity of two H^+ is probable for the Beta zeolite, the formation of Ni^{2+} on ion-exchange sites compensating two negative charges on the framework (**9**, Figure 13) is unlikely for SSZ-24. It is plausible that there are several ways to form the active site and to account for this discrepancy, a new mechanism for formation of the Cossee-Arlman site ([Ni-ethene-alkyl)] from [Ni(II)-OH]$^+$ species was proposed based on the previous work of Brogaard et al. [122].

It is also interesting to note that Ni-SSZ-24 did not form nearly as many retained hydrocarbons as micro (and nanocrystalline) Ni-Beta zeolite catalysts. Whilst the mass of Ni-SSZ-24 only increased by 30 mg, the mass of Ni-Beta doubled from 200 mg to 400 mg, indicating significantly more product deposition on the latter catalyst. Furthermore, liquid hydrocarbon on particle surfaces, on the quartz wool and on the sinter below the catalyst was observed.

Although the microcrystalline SSZ-24 and Beta catalysts have similar crystal size, activity and selectivity comparison between the two to gain insight on *e.g.* the effect of topology and morphology (three-dimensional vs one-dimensional channels and round vs cylindrical crystals, respectively) is complicated in part because of the difference in reaction conditions and in part because of the difference in Si/Al ratio, where the acidity of the support have been reported to effect both the activity and stability of the aluminosilicate catalysts [94].

4.2 Ni-functionalized MOFs

In recent years, metal-organic frameworks have demonstrated promise as catalysts for ethene dimerization and oligomerization (Ch. 2.4). These catalysts show high activities and selectivities for butene formation but require the use of activators or cocatalyst in large excess and the presence of solvent as a bulk liquid phase.

To the best of the author's knowledge, the only Ni-MOF that has been reported active for ethene oligomerization without a cocatalyst is Ni-CPO-27 [108]. Ni-CPO-27 has one-dimensional channels with diameter of ~ 10.3 Å where the metal nodes are coordinated to five oxygen atoms of the linker. The solvent occupying the sixth position can be removed with thermal treatment, generating coordinatively unsaturated metal centers. This catalyst was tested using a continuous flow fixed-bed reactor and was active for ethene and propene dimerization at 5 bar and 180 °C after pretreatment overnight at 180 °C in inert. The two major drawbacks of Ni-CPO-27 were low conversion and rapid deactivation. The authors hinted towards the positive effect of higher partial pressure of ethene to increase the rate of dimerization and yield a more active catalyst [94].

A natural starting point for this work was investigating the Ni-CPO-27 catalyst. The activity of Ni-CPO-27 for the dimerization reaction was evaluated at 180 °C under constant total pressure (30 bar) but different ethene partial pressure (3, 10 and 26 bar), after activation in inert at 180 °C for 360 min (Figure A 2). The highest conversion and slowest deactivation were observed under 3 bar ethene, suggesting that the deactivation is related to the rate of reaction where higher rate, expected at increasing ethene partial pressure, leads to faster deactivation. It is hypothesized that the first measurement after 40 min TOS takes place after the activity maxima, where deactivation dominates, justifying the lower observed rate at higher partial pressure of ethene. N_2-adsorption measurements revealed that the S_{BET} of the spent catalyst tested at 26 bar ethene decreased almost two order of magnitude from 774 to 10 m^2/g, suggesting that pores of the tested catalyst are blocked and inaccessible to N_2.

These results confirmed that Ni-CPO-27 possess inherent downside for further studies such as rapid deactivation and low conversion. The focus of this study was hence shifted towards Zr(IV)-based MOFs; specifically Ni functionalized UiO MOFs, recognized for their exceptional chemical and thermal stability. Several cocatalyst activated Ni functionalized Zr-MOFs have been studied in batch mode for ethene oligomerization reaction (see Ch. 2.4) and presented a good starting point for this work. Initially, the aim was to graft Ni on the nodes of UiO-66 and UiO-67 to produce coordinatively unsaturated Ni^{2+} sites coordinated to oxygen atoms on the Zr-nodes. The reason for this was to 1) produce Ni-MOFs where Ni is coordinated to oxygen atoms, similar to Ni in aluminosilicates and Ni-CPO-27 which are active for the ethene oligomerization reaction without cocatalyst, and 2) produce materials with identical coordination site for Ni, while varying the octahedral and tetrahedral cage size to investigate the confinement effect imposed by the support. However, Ni grafted UiO-66 and UiO-67 showed poor performance for the ethene oligomerization reaction under the investigated conditions (*vide infra*).

Next, Ni functionalized mixed-linker MOFs were prepared to produce homogeneously distributed single Ni sites in the MOF framework. The linkers used to partially exchange the H_2bpdc linkers in the UiO-67 framework and investigated here were, from left to right in Figure 22, H_2bpdc-$(OH)_2$, H_2bpdc-$(NH_2)_2$, H_2bpdc-(NH_2), H_2bndc and H_2bpydc. The two linkers considered exceptionally promising was H_2bpdc-$(OH)_2$ and H_2bpydc. The Ni-bpy system, have been proven to be active for ethene oligomerization, both as homogeneous catalyst and incorporated in MOFs, under batch conditions after activating with a cocatalyst [35]. For the dihydroxy system, the aim was to again mimic aluminosilicates where it was hypothesized that coordination of Ni to the dihydroxy linker would result in deprotonation and coordination of oxygen to the metal to yield coordinatively unsaturated Ni^{2+}-sites similar to Ni in aluminosilicates. The two amino functionalized linkers provided basis for comparison. Finally, the confinement effect was investigated by substituting the H_2bpdc linkers with the larger H_2bndc linkers.

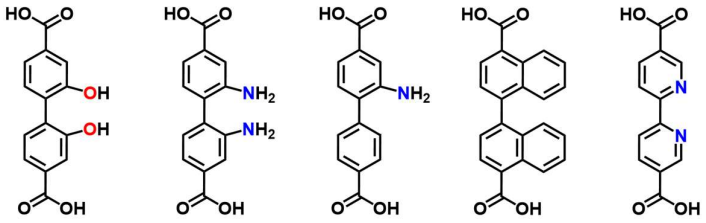

Figure 22: Structure of the isostructural linkers that was exchanged with the bpdc linkers in UiO-67. From left to right: H_2bpdc-$(OH)_2$, H_2bpdc-$(NH_2)_2$, H_2bpdc-(NH_2), H_2bndc and H_2bpydc.

4.2.1 Ni functionalized mixed-linker MOFs

The materials were successfully synthesized with ~ 10 % functional linker (f.linker) incorporation, except the mixed-linker MOF prepared with H_2bpdc-$(OH)_2$ which resulted in 5 % incorporation, and characterized with N_2-adsorption, TGA and ^{1}H-NMR by Dr. Gurpreet Kaur as described in detail in her Ph. D. dissertation [131]. In summary, all of the materials were stable to temperatures up to ~ 500 °C in air (Figure A 3) and the S_{BET} of the materials were closely related to UiO-67 synthesized under similar conditions (Table 3). The samples are denoted UiO-67-f.linker$_y$, where y stands for the mol % f.linker relative to (f.linker + bpdc) determined by ^{1}H-NMR.

Table 3: The specific surface area and defectivity of the parent mixed-linker MOFs. The ideal linker:Zr node ratio for UiO MOFs is 6:1. Linker:node and (linker+modulator):node represents the amount of linker and linker + modulator per Zr node in mol, respectively.

Sample	S_{BET} (m^2/g)	Linker:node	(Linker+modulator):node
UiO-67	2350	5.40	5.71
UiO-67-$bpy_{11\%}$	2431	5.26	5.83
UiO-67-$(bpdc(OH)_2)_{5\%}$	2405	5.27	5.75
UiO-67-$(bpdc(NH_2))_{12\%}$	2311	5.44	5.94
UiO-67-$(bpdc(NH_2)_2)_{12\%}$	-	5.47	6.04
UiO-67-$(bndc)_{91\%}$-$bpy_{9\%}$	1439	5.88	5.88

The ideal linker:Zr node ratio for UiO MOFs is 6:1, but prior investigations on UiO-66 and 67 revealed that synthesis conditions (such as type and concentration of modulator, time and temperature) affect this ratio leading to missing cluster or missing linker defects. The missing linker defects may be capped by modulators, anions of precursor salt, solvent or OH^-/H_2O pairs [157-161]. Combination of solution ^{1}H-NMR and TGA measurements of the parent materials showed that the linker:Zr node ratios for the materials, except UiO-67-$(bndc)_{91\%}$-$bpy_{9\%}$, was close to 5.3, *i.e.* on average, 2-4 Zr coordination sites per Zr node were not connected to a linker (Table 3). Furthermore, the (linker + modulator):Zr node ratio was < 6 for several of the investigated materials, indicating that in addition to benzoic acid (BA) and formic acid (FA), both materials contained Cl^- or OH^-/H_2O pairs. The OH^-/H_2O groups are particularly important, as various metals such as Ni, Al and Zn have been shown to coordinate to these groups in the Zr-cluster of NU-1000[105] [162].

Nickel functionalization was carried out using $Ni(OAc)_2{\cdot}4H_2O$ and $Ni(NO_3)_2{\cdot}6H_2O$ where the amounts used corresponds to Ni:f.linker molar ratio of ~2 and ~1 in the solution, respectively. Concentrating first on $Ni(OAc)_2{\cdot}4H_2O$ functionalized materials, the S_{BET}, Ni

wt. % and Ni:f.linker molar ratio are shown in Table 4. The samples were denoted xNi-UiO-67-f.linker$_y$, where x is the Ni wt. % determined by EDS analysis.

Table 4: Sample characterization of $Ni(OAc)_2{\cdot}4H_2O$ functionalized mixed-linker MOFs. Ni:f.linker represent the amount of Ni relative to the amount of functional linker that was present in the parent material.

Sample	S_{BET} (m^2/g)	Ni (wt. %)	Ni:f.linker (mol/mol)
(2.0)Ni-UiO-67	1540	2.0	-
(3.2)Ni-UiO-67-bpy$_{11\%}$	1549	3.2	2.0
(2.2)Ni-UiO-67-(bpdc(OH)$_2$)$_{5\%}$	2100	2.3	3.0
(2.8)Ni-UiO-67-(bpdc(NH$_2$))$_{12\%}$	1697	2.9	1.5
(2.3)Ni-UiO-67-(bpdc(NH$_2$)$_2$)$_{12\%}$	1677	2.3	1.3
(1.7)Ni-UiO-67-(bndc)$_{91\%}$-bpy$_{9\%}$	1113	1.7	1.4

TGA in dry synthetic air for the Ni functionalized materials show that the decomposition temperature decreased from ~ 500 °C in the parent materials to ~ 400 °C, indicating reduced stability (Figure A 3). Furthermore, Ni functionalization of the mixed-linker MOFs resulted in a significant reduction in S_{BET} compared to their respective parent material. The catalysts were further analyzed with SEM (Figure 23), which show particle deposition on top of the mixed-linker MOFs suggesting that the nickel acetate is either not diffusing into the pores or diffused towards the outer surface during drying. The deposits may then block the pore mouths leading to reduced S_{BET}. The only exception was MOFs containing bpy, where no deposits were observed on the surface. Considering that (3.2)Ni-UiO-67-bpy$_{11\%}$ had the highest Ni wt. % and second highest Ni:f.linker ratio, suggests that bpy plays a key role in directing and retaining nickel in the pores.

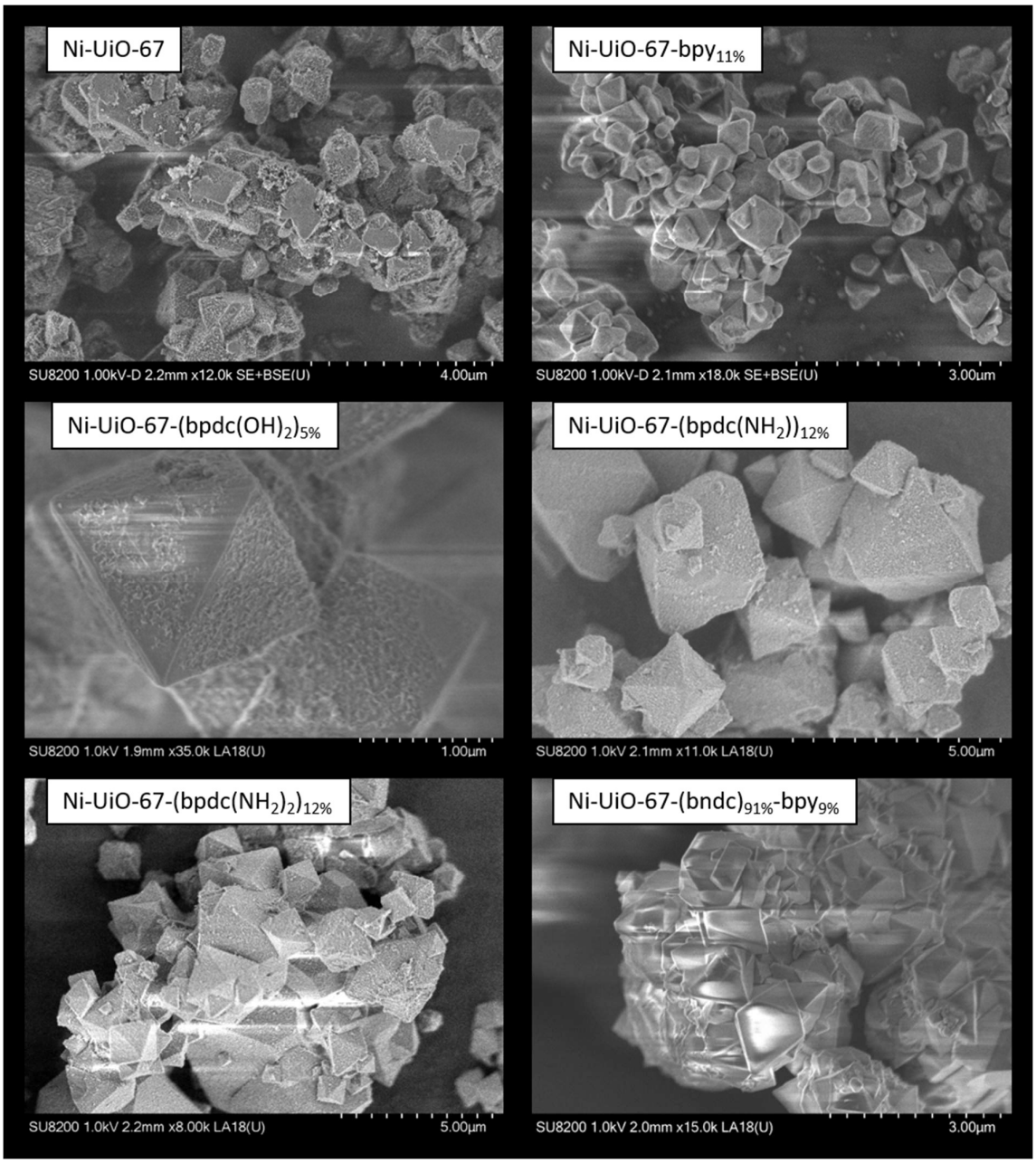

Figure 23: SEM images of pristine Ni functionalized mixed-linker MOFs.

The Ni functionalized mixed-linker MOFs were subjected to ethene dimerization reaction under standard reaction conditions (250 °C, 26 bar ethene and 4 bar He) after activation for 360 min at 300 °C in 10 % O_2 in He and the evolution of ethene dimerization activity with TOS is presented in Figure 24. All catalysts, except (2.0)Ni-UiO-67 (conversion < 0.1 %), show significant activity for the ethene dimerization reaction and exhibit > 96 %

selectivity to linear butenes with longer alkenes denoted C_{6+} as the only detected byproduct (Figure A 4). The transient behaviors among the catalysts differed where (3.2)Ni-UiO-67-bpy$_{11\%}$, (2.3)Ni-UiO-67-(bpdc(NH$_2$)$_2$)$_{12\%}$ and (1.7)Ni-UiO-67-(bndc)$_{91\%}$-bpy$_{9\%}$ show an initiation period followed by a gradual deactivation. On the other hand, (2.2)Ni-UiO-67-(bpdc(OH)$_2$)$_{5\%}$ and (2.8)Ni-UiO-67-(bpdc(NH$_2$))$_{12\%}$ show rapid initial deactivation, followed by a period of slower deactivation, before reaching pseudo steady-state.

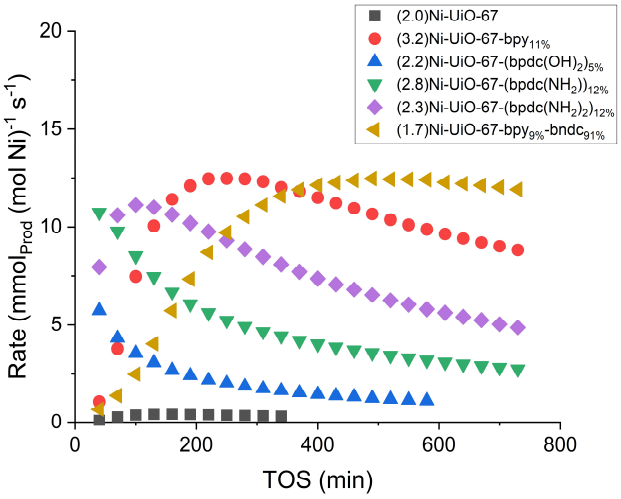

Figure 24: Ethene dimerization rate vs TOS for mixed-linker MOFs functionalized with Ni(OAc)$_2$·4H$_2$O. Reaction conditions: m_{cat} = 0.150 g, 30 bar total pressure where P_{ethene} = 26 bar and P_{inert} = 4 bar, temperature = 250 °C and contact time = 5.0 mg_{cat}·min·mL^{-1} at STP.

The negligible activity observed over (2.0)Ni-UiO-67 suggests that Ni(OAc)$_2$ deposited on MOF crystal surfaces and eventually Ni species coordinated to defect sites cannot be the main active sites. Up to 50 times higher activity over the other catalysts that exhibited similar defect concentration on their respective parent materials (Table 3) further support this hypothesis.

To avoid deposition of Ni precursor on the mixed-linker MOFs, the functionalization was carried out using a more easily EtOH soluble Ni precursor, Ni(NO$_3$)$_2$·6H$_2$O, aiming for Ni:f.linker ratio ~1. Interestingly, EDS analysis showed that only materials containing bpy

retained Ni, while Ni was not detected on the other mixed-linker MOFs (Figure A 5). Removal of all Ni during the washing step in these mixed-linker MOFs suggests that the metal was not covalently bonded but interacted only weakly with the MOF, similar to $Ni(acac)_2$ on UiO-66-NH_2 [163]. On the other hand, UiO-67-$bpy_{11\%}$ functionalized with $Ni(NO_3)_2{\cdot}6H_2O$ resulted in difference in material properties and in the catalytic activity compared to UiO-67-$bpy_{11\%}$ functionalized with $Ni(OAc)_2{\cdot}4H_2O$.

As the bpy mixed-linker MOFs proved to be the best catalyst in terms of activity, did not display $Ni(OAc)_2$ deposits on the crystal surface and retained Ni after washing, further studies were focused on UiO-67-bpy catalysts. Several parameters such as effect of bpy concentration and Ni concentration, counter anion and pore size was studied, and the active and spectator species was identified based on spectroscopic investigations.

4.2.2 Material characterization

To investigate the influence of Ni and bpy concentration, a new series of catalyst with 4 % bpy, in addition to 0 % and 11 % bpy (*vide supra*), was prepared. $Ni(OAc)_2{\cdot}4H_2O$ was subsequently grafted onto the three parent materials with varying concentration and the main physical properties of the catalysts are presented in Table 5. The Ni content in the UiO-67-$bpy_{11\%}$ series varied between 0.9 - 3.2 wt. % corresponding to Ni:bpy molar ratios from 0.5 to 2.0. Two catalysts with 0.8 and 1.2 Ni wt. % were prepared for the UiO-67-$bpy_{4\%}$ series, corresponding to Ni:bpy mole ratios of 1.3 and 1.9, respectively. (2.0)Ni-UiO-67 without bpy was used as reference catalyst.

To elucidate the effect of the charge balancing anion, a series of Ni-UiO-67-$bpy_{11\%}$ catalysts using $Ni(OAc)_2{\cdot}4H_2O$, $Ni(NO_3)_2{\cdot}6H_2O$, $NiCl_2{\cdot}6H_2O$ and $Ni(acac)_2$ as Ni precursors were prepared. The chemical composition and main physical properties of the catalysts are also gathered in Table 5. In this series of materials, all investigated samples were originally aimed to be prepared with Ni:bpy ratio of 2.4. Only UiO-67-$bpy_{11\%}$ functionalized with $Ni(OAc)_2{\cdot}4H_2O$ resulted in Ni:bpy molar ratio $\geq$ 2, while UiO-67-

$bpy_{11\%}$ functionalization with the other Ni precursors all resulted in Ni:bpy molar ratio ~ 1.5.

Table 5: Physicochemical properties of the Ni functionalized catalysts

Sample	S_{BET} (m^2/g)	V_{micro} (cm^3/g)	V_{meso} (cm^3/g)	Nickel (wt. %)	Ni:bpy (mol/mol)
(2.0)Ni-UiO-67 - $Ni(OAc)_2$	1540	0.62	0.10	2.0	-
(0.9)Ni-UiO-67-$bpy_{11\%}$ - $Ni(OAc)_2$	2146	0.83	0.07	0.9	0.5
(1.9)Ni-UiO-67-$bpy_{11\%}$ - $Ni(OAc)_2$	1834	0.75	0.10	1.9	1.2
(3.2)Ni-UiO-67-$bpy_{11\%}$ - $Ni(OAc)_2$	1549	0.68	0.10	3.2	2.0
(0.8)Ni-UiO-67-$bpy_{4\%}$ - $Ni(OAc)_2$	2281	0.91	0.09	0.8	1.3
(1.2)Ni-UiO-67-$bpy_{4\%}$ - $Ni(OAc)_2$	2156	0.88	0.09	1.2	1.9
(2.3)Ni-UiO-67-$bpy_{11\%}$ - $NiCl_2$	1852	0.75	0.10	2.3	1.5
(2.3)Ni-UiO-67-$bpy_{11\%}$ - $Ni(acac)_2$	1944	0.83	0.07	2.3	1.5
(2.0)Ni-UiO-67-$bpy_{11\%}$ - $Ni(NO_3)_2$	1868	0.77	0.10	2.0	1.3

TGA of the 0 %, 4 % and 11 % bpy UiO-67 parent materials show very similar stability with a decomposition temperature ~ 500 °C (Figure A 6). For $Ni(OAc)_2$ functionalized catalysts, the decomposition temperature decreased with increasing Ni concentration, independent of bpy concentration where the decomposition temperature was ~ 420 °C for the catalyst with highest concentration of Ni. TGA for the Ni-UiO-67-$bpy_{11\%}$ - $Ni(X)_2$ series (Figure A 7) show that the decomposition temperature was lowered to ~ 450 °C, irrespectively of Ni precursor used. The reduced stability of all Ni functionalized UiO-67-$bpy_{y\%}$ materials could result from strain induced by Ni coordination to bpy linkers [164]. However, Ni might also catalyze the combustion of organic linkers, in line with the reduced stability of (2.0)Ni-UiO-67.

The XRD patterns show that both the parent and Ni functionalized materials have the UiO-67 structure (Figure A 8 and Figure A 9) and no additional crystalline phase was identified. Particularly, the absence of diffraction peaks corresponding to NiO or Ni metal particles suggests that Ni is highly dispersed in the samples.

The S_{BET} in the Ni-UiO-67-bpy$_{11\%}$ and Ni-UiO-67-bpy$_{4\%}$ series were found to decrease gradually with increasing Ni loading. Similarly, S_{BET} of all the materials in Ni-UiO-67-bpy$_{11\%}$ - Ni(X)$_2$ series decreased to ~ 1850 m^2/g. There was no appreciable increase in mesopore volume for any of the materials, showing that the Ni-functionalization did not partially destroy the crystals to create mesopores.

Molecular dynamics simulations were performed on Ni-UiO-67-bpy$_{11\%}$ to investigate whether the loss of S_{BET} with increasing Ni concentration could result from the formation of [bpy-Ni(OAc)$_2$] or [bpy-Ni$_2$(OAc)$_4$] species inside the pores, rendering the pores inaccessible for N_2 during measurement. Simulations show that the loss of S_{BET} was insignificant (Figure A 10) compared to what was observed experimentally suggesting that the loss of S_{BET} cannot be ascribed to the formation of such species. This is in agreement with prior contributions that only reported a slight decrease in S_{BET} for (2.3)Ni-UiO-67-bpy$_{14\%}$, (Ni:bpy molar ratio = 1) [35] and for (1.5)Pt-UiO-67-bpy$_{5\%}$ (Pt:bpy molar ratio = 0.6) [33] in these (near) defect free materials.

On the other hand, the materials used in this work are not defect free (Table 6). In a more recent publication by Gutterød et al. [165] on (2.4)Pt-UiO-67-bpy$_{11\%}$ (Pt:bpy molar ratio = 0.5, the same batch of parent UiO-67-bpy$_{11\%}$ that was used in this work) a reduction in S_{BET} to 2089 m^2/g was reported. This value is in good agreement with S_{BET} of (0.9)Ni-UiO-67-bpy$_{11\%}$ (Ni:bpy molar ratio = 0.5) that show similar reduction to that of Pt functionalized UiO-67-bpy$_{11\%}$. The exact reason for the loss of S_{BET} in catalysts with Ni:bpy molar ratio < 1 remains unclear, but as also observed for Pt functionalized UiO-67-bpy$_{11\%}$ that was reported to primarily contain isolated [Pt^{2+}-bpy] species. The decrease may occur due to local distortions in the material with gradual formation of [Ni^{2+}-bpy] species, probably due to defects present in the materials.

Table 6: Defectivity of UiO-67, UiO-67-bpy$_{4\%}$ and UiO-67-bpy$_{11\%}$ estimated from solution state ^{1}H-NMR and TGA. (BA = benzoic acid and FA = formic acid).

Sample	bpdc: node	bpy: node	BA: node	FA: node	Linker: node	(Linker+modulator):node
UiO-67	5.40	0	0.31	0	5.40	5.71
UiO-67-bpy$_{4\%}$	4.90	0.22	0.83	0.05	5.12	6.00
UiO-67-bpy$_{11\%}$	4.70	0.56	0.48	0.09	5.26	5.83

In the series of catalyst prepared with different precursors and with a large excess of Ni precursor compared to bpy, the overlap in Ni wt. %, S_{BET} and decomposition temperature, together with the ability to remove larger part of the excess nickel, except when using $Ni(OAc)_2{\cdot}4H_2O$, suggests that Ni form similar complexes in all catalysts. Furthermore, a consistent Ni:bpy molar ratio > 1 suggests that there are additional binding sites for Ni in approximately the same concentration in all materials. The defect sites are considered the most likely coordination site for Ni, after the bpy sites.

In a perfect, defect free UiO-67-bpy$_{11\%}$, a Ni:bpy molar ratio of 1 would correspond to 1.8 wt. % Ni. Assuming that new defect sites are not generated during metalation and that Ni can coordinate to defect sites present in the parent material (expected $(OH^-$ - $H_2O)$/Zr node ratio of ~ 0.2, Table 6), corresponds to a Ni/Zr node molar ratio of 0.2 or 0.6 wt. % Ni, *i.e.* one out of every five Zr node has a Ni coordinated to the defect sites.

For catalysts with Ni:bpy molar ratio of 1.5, summing up the theoretical concentration from bpy coordinated and defect coordinated Ni (1.8 wt. % and 0.6 wt. %, respectively) yields a total Ni wt. % of 2.4, in good agreement with the total Ni wt. % of 2.3 observed in these materials (Table 5). Thus, in these materials, Ni is suggested to coordinated to both bpy and the cluster.

Similar analysis carried out for UiO-67 and UiO-67-bpy$_{4\%}$ suggest that the concentration of Ni coordinated to defects are ~ 0.9 wt. % and ~ 0 wt. %, respectively. The lower

concentration of defect coordinated Ni on UiO-67-bpy$_{4\%}$ is in accordance with the less pronounced reduction in S_{BET} compared to Ni-UiO-67-bpy$_{11\%}$ where a significantly lower S_{BET} was observed for catalyst with similar Ni wt. % and Ni:bpy molar ratio (Table 5). This difference is suggested to be related to the defectivity in the materials, as UiO-67-bpy$_{4\%}$ does not contain uncapped Zr node (Linker+modulator:node = 6.00, Table 6), it is affected less by coordination of Ni on bpy.

Particularly for catalysts with Ni:bpy molar ratio > 1, it is evident that Ni form other complexes in addition to the isolated [Ni^{2+}-bpy] complex. Reduction in S_{BET} due to deposition of $Ni(OAc)_2$, formation of small $Ni(OAc)_2$ multimers or NiO and Ni^0 particles cannot be neglected. Additionally, Ni coordinated to defects can be present either as $Ni(OAc)_2$ weakly interacting with the cluster or directly bonded by replacing one or both OAc anions, similar to what was reported for Ni coordinated to the Zr cluster on NU-1000 [105]. To further investigate the different Ni species present in the catalysts XAS, XPS and FTIR spectroscopy was employed. It is worth noting that spectroscopic studies were only carried over samples prepared with $Ni(OAc)_2{\cdot}4H_2O$.

4.2.3 FT-IR, XAS and XPS: Nature of the Ni sites

Ni K-edge XAS provided information on the average Ni-speciation and local coordination environment in as-prepared $Ni(OAc)_2{\cdot}4H_2O$ functionalized MOF catalysts. Two reference samples, $Ni(OAc)_2{\cdot}4(H_2O)$ and $Ni(OAc)_2(H_2O)_2$(bpy), show good agreement in both XANES and EXAFS with two of the investigated catalysts, (2.0)Ni-UiO-67 and (0.9)Ni-UiO-67- bpy$_{11\%}$, respectively (Figure 25).

The intense white line in XANES spectra of (2.0)Ni-UiO-67 closely resemble what is observed in $Ni(OAc)_2{\cdot}4(H_2O)$ [166]. Small deviations in XANES and FT-EXAFS between the model compound and (2.0)Ni-UiO-67 suggests that the MOF could play an active role – although to a minor extent in the absence of bpy - in directing the incorporation of Ni-species from the $Ni(OAc)_2{\cdot}4(H_2O)$ precursor. $Ni(OAc)_2{\cdot}4(H_2O)$ deposits at the outer crystal surfaces is suggested to coexist with different Ni^{2+} moieties inside the MOFs scaffold, possibly interacting with defects at the UiO-67 nodes.

Conversely, (0.9)Ni-UiO-67- $bpy_{11\%}$,(Ni:bpy molar ratio = 0.5), provides a large excess of bpy linkers with respect to Ni ions, resulting in almost exclusive presence of bpy-coordinated Ni^{2+} moieties inside the MOF scaffold. Comparing the (0.9)Ni-UiO-67- $bpy_{11\%}$ XAS data with the ones obtained for a series of well-characterized bpy-(OAc) Ni^{2+} complexes, we found the best agreement in both the XANES and EXAFS region with a $Ni(OAc)_2(H_2O)_2(bpy)$ model complex, structurally characterized by single crystal XRD (Figure 25).

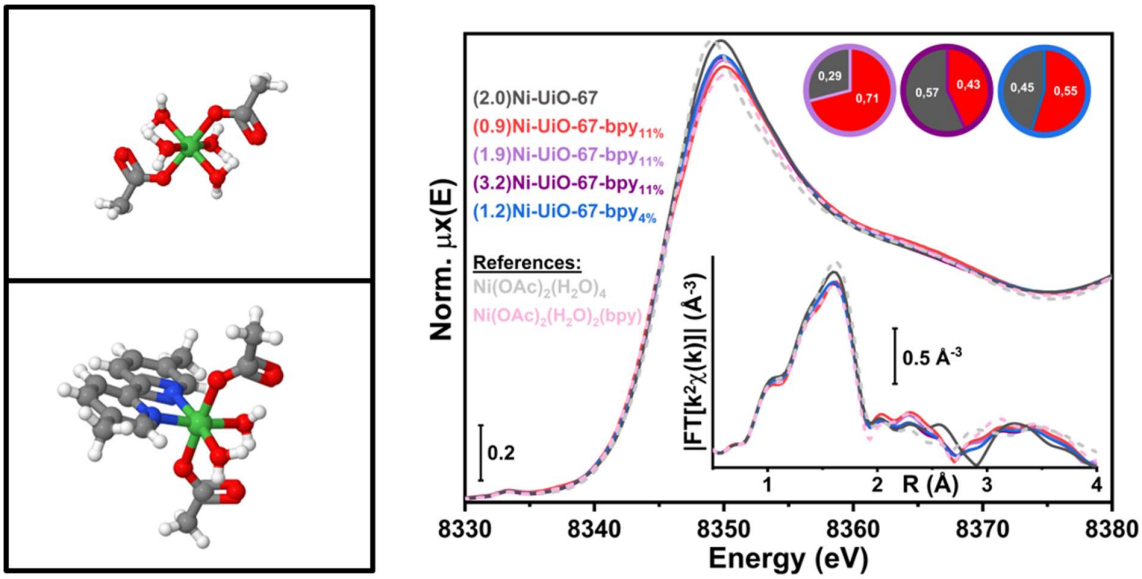

Figure 25: The structure of $Ni(OAc)_2{\cdot}4(H_2O)$ (top left) [166] and $Ni(OAc)_2(H_2O)_2(bpy)$ (bottom left) reference compounds. Right: Ni K-edge XANES of as-prepared Ni-functionalized MOF catalysts. The bottom inset shows the corresponding phase-uncorrected FT-EXAFS spectra, obtained transforming the k^2-weighted $k^2\chi(k)$ curves in the 2.4-14.0 $Å^{-1}$ range. Pie charts illustrate normalized Ni-speciation in samples (1.9)Ni-UiO-67-$bpy_{11\%}$ (light purple), (3.2)Ni-UiO-67-$bpy_{11\%}$ (purple) and (1.2)Ni-UiO-67-$bpy_{4\%}$ (blue) estimated from XANES linear combination fit (LCF) analysis using as references the spectra of the (2.0) Ni-UiO-67 (grey) and (0.9) Ni-UiO-67- $bpy_{11\%}$ (red), representative of Ni^{2+} species incorporated into bpy-free UiO-67 and Ni^{2+} species coordinated to bpy linkers in UiO-67-bpy MOFs, respectively. LCF errors on reported Ni fractions are of ± 0.02 in all cases. XANES and FT-EXAFS spectra of relevant model compounds are also reported as dashed lines, including $Ni(OAc)_2(H_2O)_4$ (light grey) and $Ni(OAc)_2(H_2O)_2(bpy)$ (pink).

The compositional characteristics of these two samples were used to rationalize the Ni speciation in the materials: (2.0)Ni-UiO-67 is representative of Ni^{2+} ions incorporated in the UiO-67 MOF environment in the absence of privileged anchoring points at bpy-

linkers, on the other hand, (0.9)Ni-UiO-67-bpy$_{11\%}$ is representative of bpy coordinated Ni. The XANES of the remaining three catalysts, namely (1.9)Ni-UiO-67-bpy$_{11\%}$, (3.2)Ni-UiO-67-bpy$_{11\%}$ and (1.2)Ni-UiO-67-bpy$_{4\%}$, was modeled as linear combinations of the spectra collected for (2.0)Ni-UiO-67 and (0.9)Ni-UiO-67- bpy$_{11\%}$, optimizing the weights for each component through linear combination fit (LCF) analysis.

As illustrated by the pie charts in Figure 25, an increased Ni:bpy ratio translates in the progressive increase of bpy-free Ni^{2+} moieties. From Figure 25 it is also clear that no large metallic or oxidic aggregates are detectable in the as-prepared catalysts and that the Ni-speciation is dominated by well-dispersed Ni^{2+} species.

Table 7 show the concentration of bpy coordinated and bpy free species based on the XANES LCF analysis. Surprisingly, this analysis suggests that not all bpy is Ni coordinated both in (1.9)Ni-UiO-67-bpy$_{11\%}$ and (3.2)Ni-UiO-67-bpy$_{11\%}$ (expected Ni wt. % for [Ni^{2+}-bpy] is 1.8 wt. %, see p. 71). Conversely, for (1.2)Ni-UiO-67-bpy$_{4\%}$, all bpy is suggested to be coordinated to Ni as the expected Ni concentration for a Ni:bpy molar ratio of 1 for a defect free Ni-UiO-67-bpy$_{4\%}$ equals 0.6 Ni wt. %. It is worth noting that the differences between the samples in the XANES region is small and the concentrations derived from the XANES LCF analysis has uncertainty of ~ 10 % of total Ni wt. %.

Table 7: Concentration of bpy coordinated and bpy free Ni based on XANES LCF analysis.

Sample	[Ni^{2+}-bpy] (wt. %)	[bpy free Ni] (wt. %)
(1.9)Ni-UiO-67-bpy$_{11\%}$	1.35	0.55
(3.2)Ni-UiO-67-bpy$_{11\%}$	1.38	1.82
(1.2)Ni-UiO-67-bpy$_{4\%}$	0.66	0.54

A XPS study of Ni-UiO-67-bpy$_{11\%}$ provided complementary information to XAS: The XPS N1s spectrum of the UiO-67-bpy$_{11\%}$ consists of one peak at BE (N1s: 398.9 eV), corresponding to N atoms of the bpy in the structure of the UiO-67-bpy [167]. The XPS

N1s spectra of (0.9)Ni-UiO-67-bpy$_{11\%}$ and (1.9)Ni-UiO67-bpy$_{11\%}$ consist of one peak at BE (N1s: 398.9 eV) and one contribution at higher BEs (N1s: 400.5 eV) while (3.2)Ni-UiO-67-bpy$_{11\%}$ only show one peak at higher BE (Figure 26). The shift of the peak for N1s toward higher BE can be attributed to a decrease in the electron density of N, indicating a strong coordination of nitrogen atoms to Ni, similar to what has been observed over Pd and Pt functionalized UiO-67-bpy [167, 168]. In agreement with the XANES LCF analysis, the XPS study show that not all bpy is coordinated to Ni in (1.9)Ni-UiO67-bpy$_{11\%}$, (Ni:bpy molar ratio 1.2) whilst all bpy is Ni coordinated in (3.2)Ni-UiO-67-bpy$_{11\%}$., in contrast to what is suggested based on XANES LCF analysis.

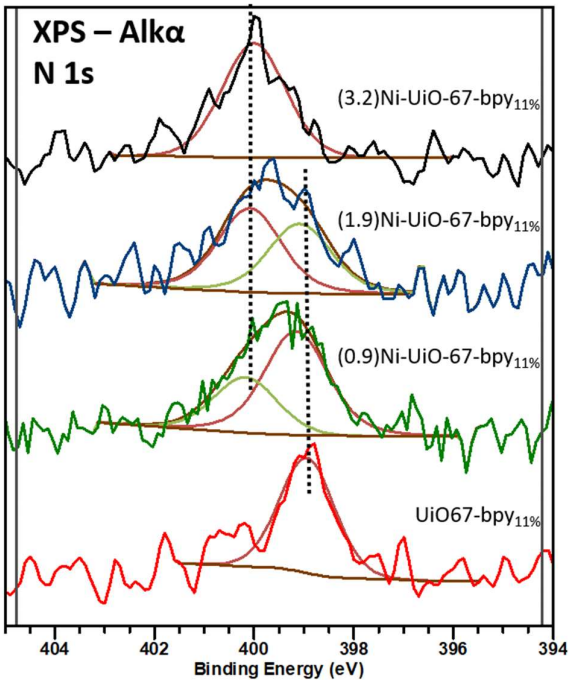

Figure 26: XPS peaks N1s of pristine 0.9, 1.9 and (3.2)Ni-UiO 67-bpy$_{11\%}$. The peaks at BE 398.9 eV and 400.5 eV are shown with dotted lines.

The discrepancy between the two methods could be related to the different conditions employed for the XAS and XPS measurements, atmospheric and ultra-high vacuum (UHV), respectively, most probably resulting in dehydrated Ni species in UHV compared to hydrated species during atmospheric XAS measurement. Regardless of the discrepancy and the difference in surface and bulk sensitivity of the two methods and considering the

error margins of the experiment and data treatment, both results point toward an increase in concentration of bpy coordinated to Ni with increasing Ni:bpy molar ratio.

Finally, *in-situ* XAS investigations of (3.2)Ni-UiO-67-bpy$_{11\%}$ during activation in oxidative (10 % O_2), reductive (10 % H_2) or inert (He) conditions using identical temperature program to what was employed for activation before catalytic testing, did not result in appreciable differences between the samples and only Ni in oxidation state +2 was observed (Figure A 11). Especially, the absence of Ni^0 particles during H_2 activation suggests that the Ni species are not prone to reduction.

Focusing next on FTIR of activated (10 % O_2 in He, 6h at 300 °C) Ni-UiO-67 and Ni-UiO-67-bpy$_{11\%}$ materials (Figure 27A), it can be observed that the samples maintain the same chemical bonding typical to UiO-67 MOFs: a tiny sharp band at 3670 cm^{-1}, related to the residual Zr-μ_3OH at the cornerstones remaining after the thermal treatment for water removal [22, 169]. (C-H_{arom}) stretching, belonging to the biphenyl and bipyridine linkers are arising in 3200-3000 cm^{-1} interval [22, 169]. The region in which ν(C=O) from carboxylates is present (1600-1250 cm^{-1}) is excluded since the signal is out of scale. In the region between 1250 and 700 cm^{-1} all the different bending modes from C-H_{arom} of the linkers are present.

The presence of the band at 3670 cm^{-1} for Zr-μOH before thermal treatment (Figure A 13), without any perturbation, is indicative of that Ni is not covalently bonded to the Zr cluster where the cluster acts as a counterion. Contrary to what was observed for Ni on NU-1000 and Au^+ on UiO-67 covalently bonded to the OH^-/H_2O pair and cornerstone μ_3-OH groups in the Zr cluster, respectively [105, 170, 171]. However, it is not possible to eliminate the possibility of Ni covalently bonded to the Zr cluster based on this alone.

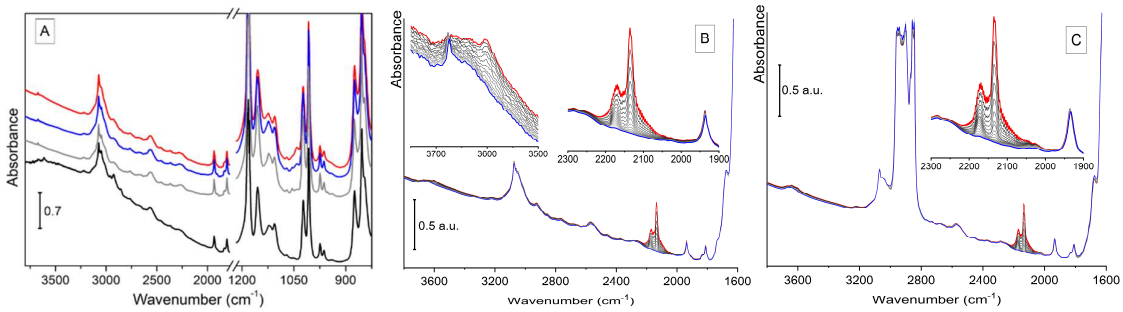

Figure 27: A) FT-IR spectra of UiO-67-bpy$_{11\%}$ samples with different Ni(OAc)$_2$ content (0.9 wt. % - grey curve; 1.9 wt. % - blue curve; 3.2 wt. % - red curve) and of (2.0)Ni-UiO-67 (black curve) after activation for 360 min at 300 °C in 10% O_2. The carboxylates spectral region (1700-1250 cm^{-1}) is excluded since it is out of scale. CO FTIR spectra at LNT of (3.2)Ni-UiO-67-bpy$_{11\%}$ (B) activated in 10 % O_2 for 360 min at 300 °C and (C) tested for 720 min collected while outgassing CO from maximum (red curve) to minimum (blue curve) coverage.

CO FTIR at LNT of (3.2)Ni-UiO-67-bpy$_{11\%}$ (Figure 27B) after activation in 10 % O_2 for 360 min at 300 °C show three evident IR bands: I) an intense band at 2135 cm^{-1}, assigned to CO physisorbed inside the material porosities [172-174]; II) a signal at 2150 cm^{-1}, due to the interaction of CO with the residual hydroxyls terminating the Zr clusters in the MOF [174]; III) a feature centered at 2170 cm^{-1}, ascribable to carbon monoxide interacting with Ni^{2+} moieties [173, 175, 176]. Gradually decreasing θ_{CO} did not show the formation of new bands suggesting that only Ni in oxidation state +2 is present after activation. The absence of bands at frequency lower than the band due to physisorbed carbon monoxide, testify the lack of metal nanoparticles, for which we could expect components between 2100 and 2000 cm^{-1} [174, 177-179], in accordance with the XAS results.

Although there is a good correlation between the band at 2170 cm^{-1} and Ni concentration over the materials (Figure A 12), it is suspected that CO FTIR is probing only a fraction of the Ni^{2+} sites available in the Ni-MOFs. This becomes evident when comparing the CO FTIR of activated only and 720 min tested (3.2)Ni-UiO-67-bpy$_{11\%}$ (Figure 27B and C, respectively). The tested catalyst show very high intensity (out of scale) for hydrocarbons at around 2900 cm^{-1} and a reduction in S_{BET} from 1525 to 503 m^2/g ascribed to product deposition and pore blocking, regardless of this fact, CO FTIR show the same amount of Ni is probed in each case.

Activating Ni-UiO-67-bpy$_{11\%}$ is suggested to dehydrate the Ni species to four-coordinated species regardless of their location on: bpy, Zr cluster or $Ni(OAc)_2$ weakly interacting with the MOF framework. The band at 2170 cm^{-1} is best in correlation with the total Ni concentration (Figure A 12) and the lack of an intense signal suggests that there are not any coordinatively unsaturated Ni^{2+} present in the material. This result is also in accordance with the absence of Ni coordinatively bonded to the cluster, as this process is expected to yield a coordinatively unsaturated Ni^{2+} species, similar to what has been observed for Cu coordinated to defects in Cu-UiO-66 [180].

On the other hand, in other heterogeneous catalysts where CO FTIR was employed to identify the Ni sites *e.g.* Ni exchanged zeolites, the coordinatively unsaturated Ni^{2+} and Ni^{+} in Ni-ZSM-5 have been reported to coordinate up to two and three CO molecules, respectively [141]. CO FTIR applied to a similar material studied in this work, (1.8)Cu-UiO-67-bpy$_{10\%}$, show that Cu interacts with CO, however, Cu^{2+} grafted on bpy ([bpy-Cu(OH)Cl]) is for the most part reduced to Cu^{+} ([bpy-CuCl]) after thermal treatment at 300 °C in N_2. The three coordinated Cu^{+} species, with empty coordination sites, are the main Cu species probed in this catalyst [181]. It is also worth noting that the band for the [bpy-Cu(CO)Cl) species at 2095 cm^{-1} was at a lower wavenumber compared to Cu^{+} in zeolites (~2155 cm^{-1}) as the electrostatic interaction was suggested to be stronger in the latter material due to a higher coordinative unsaturation and the absence of a large, negatively charged Cl^{-} ligand.

It is suggested that the four-coordinated Ni^{2+} species in Ni-UiO-67-bpy is less prone to interact strongly with CO and that only a fraction of Ni^{2+} is probed under the investigated conditions. The adsorption equilibrium is suggested to be far to the gaseous CO side, resulting in same amount of Ni^{2+} being probed on activated and deactivated catalyst. Nonetheless, the conclusions drawn based on the absence of metal nanoparticles, Ni^{+} species or coordinatively unsaturated Ni^{2+} on the Zr cluster on activated catalyst are considered valid since the MOF is porous (based on N_2-adsorption, Table 5) and CO can in principle coordinate to the coordinatively unsaturated Ni^{+} and Ni^{2+} species or nanoparticles eventually present in the material.

The different Ni species present in the MOF during activation and testing will be discussed further based on *operando* XAS. However, the testing results obtained over the Ni-MOF catalyst will be presented prior to *operando* XAS results because they provide useful information for the XAS discussion.

4.2.4 Influence of Ni and bpy concentration

Concentrating first on the influence of Ni and bpy concentration, the evolution of catalyst turn-over rates for ethene dimerization with TOS under standard reaction conditions (250 °C, 26 bar ethene and 4 bar He) is shown in Figure 28A. Figure 28B and Figure 28C highlight the influence of Ni:bpy ratio and bpy content in the catalysts on the ethene dimerization rate after 360 min on stream. Focusing first on Figure 28B, UiO-67-bpy without Ni showed no conversion under the conditions used, clearly pointing to Ni as the active site. Similarly, the UiO-67-Ni catalyst without bpy linker (Ni:bpy = ∞) showed negligible conversion rate (Figure 28B-C), hence demonstrating once again the essential role of bpy linkers for grafting and activation of the $Ni(OAc)_2$ complex. It is worth pointing out once more that based on the negligible activity observed over the Ni functionalized UiO-67, defect coordinated $Ni(OAc)_2$ hypothesized to be present on UiO-67-bpy in significant concentration, are suggested to not be the active sites on these catalysts.

Concentrating next on the time evolution of reaction rate in catalysts that contained both Ni and bpy and focusing first on the Ni-UiO-67-$bpy_{11\%}$ series, the catalysts showed an initiation period where the rate of reaction increased with TOS. This observation is consistent with a rather slow formation of the active catalyst state after the on-set of reaction. Within the Ni-UiO-67-$bpy_{11\%}$ series, the initiation period was shortest for the catalyst with high Ni content and the duration increased with decreasing Ni amount. Furthermore, the more active (3.2)Ni-UiO-67-$bpy_{11\%}$ catalyst deactivated gradually with TOS after 360 min on stream, whereas the less active catalysts had not yet reached their activity maximum after 360 or 720 min on stream, respectively.

Moving next to the Ni-UiO-67-bpy$_{4\%}$ catalysts, it is very interesting to note that the transient behavior after on-set of reaction, as well as the turn-over rate per Ni in the catalyst at a given TOS, were generally very similar for catalysts having the same Ni:bpy ratio. While total Ni and bpy content individually had less impact on catalyst performance (Figure 28 A-C), Figure 28B clearly shows that the activity per Ni site increased with increasing Ni:bpy ratio. Interestingly, we observed a very similar fractional distribution among bpy-free and bpy-coordinated Ni^{2+} species in as-prepared (3.2)Ni-UiO-67-bpy$_{11\%}$ and (1.2)Ni-UiO-67-bpy$_{4\%}$ (Figure 25), close in both cases to 50 % total Ni for each component: this falls in line with the equivalent rates observed for the ethene dimerization reaction over the two catalysts.

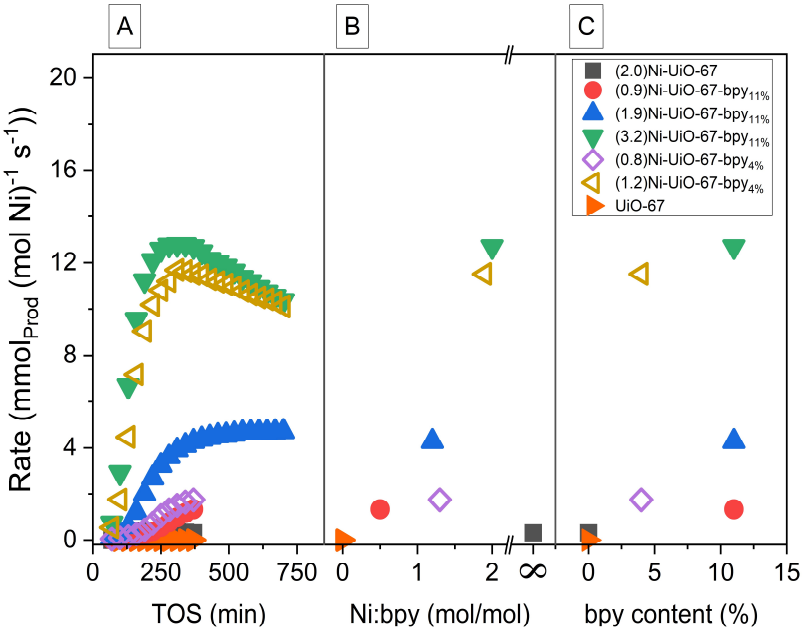

Figure 28: A) Ethene dimerization rate vs TOS. B) Ethene dimerization rate vs Ni:bpy molar ratio and C) vs bpy content (%) after 370 min TOS. The conversion at 370 min TOS for each catalyst shown in the legend was 0.1 %, 0.2 %, 1.1 %, 5.8 %, 1.9 %, 0.2 %, in descending order, respectively. Reaction conditions: m_{cat} = 0.150 g, 30 bar total pressure where P_{ethene} = 26 bar and P_{inert} = 4 bar, temperature = 250 °C and contact time = 5.0 mg_{cat}·min·mL^{-1} at STP.

At first glance, this result suggests that the presence of two adjacent $Ni(OAc)_2$ complexes either facilitates the formation of the active Ni species or creates a particularly active Ni site. However, the XPS study suggests that not all bpy is coordinated to Ni in (1.9)Ni-

UiO67-bpy$_{11\%}$, (Ni:bpy molar ratio 1.2), and only at higher Ni:bpy molar ratios does all of the bpy coordinate to Ni (Figure 26). One possible explanation of higher rate with increasing bpy free Ni is that although the *fraction* of [bpy-Ni(OAc)$_2$] decrease with increased Ni loading (Figure 25), the net concentration increase with increasing Ni:bpy molar ratio and highest rate is observed over the catalysts where all of the bpy is coordinated to Ni. It is worth noting that although not all bpy is suggested to be Ni coordinated on (3.2)Ni-UiO-67-bpy$_{11\%}$ according to the XANES LCF analysis (Table 7), identical evolution in reaction rate per Ni over (3.2)Ni-UiO-67-bpy$_{11\%}$ and (1.2)Ni-UiO-67-bpy$_{4\%}$ where all bpy is suggested to be Ni coordinated in the latter catalyst based on the same analysis, are in accordance the XPS results and points towards [bpy-Ni^{2+}] as the active site.

Ni nanoparticles were detected on (3.2)Ni-UiO-67-bpy$_{11\%}$ with *ex-situ* CO FTIR after 720 min TOS (Figure A 15). The spectrum of the only activated and 100 min tested catalyst did not display any sign of Ni or NiO nanoparticles. Considering that nanoparticles were not observed on the other catalysts and observed on (3.2)Ni-UiO-67-bpy$_{11\%}$ only after 720 min TOS, Ni and NiO nanoparticles can be ruled out as the active site, leaving Ni^{2+} as the most likely active site for ethene dimerization.

Turning next to product selectivity, linear butenes represented 99 % of the products in the reactor effluent, over all tested catalysts, in the studied conversion range (≤ 6 % conversion). Longer chained alkenes, denoted C_{6+}, with selectivity ~ 1 % were also identified. Considering the $C_4^=$ product distribution, the 1-butene:trans-2-butene:cis-2-butene ratio was 41:26:32. Importantly, the distribution was very similar in all catalysts, irrespective of conversion level, and far from the equilibrium distribution at the reaction temperature (12:57:31 %).

Similar to what was discussed for zeolites (*vide supra*), the butene isomer distribution could be primary, because of butyl isomerization on the active site before desorption of the 1- or 2-butene product, or it could be secondary, due to isomerization at the Ni site or at a support site, after re-adsorption of a butene molecule. In zeolites, isomerization can

be catalyzed by Brønsted acid sites in the zeolite lattice or by Ni [100, 114, 182]. Here, possible interference on the isomerization reaction from remaining μ_3-OH sites on the Zr nodes in UiO-67-bpy was investigated by feeding 1-butene over UiO-67-bpy$_{11\%}$ at 250 °C and 1 bar total pressure. No conversion to the 2-butene isomers (or to other products) was observed (Table A 1).

The rate of a secondary reaction is expected to depend on the concentration of the primary product. We observe that the product distribution was unaffected by change in ethene conversion. Together, the test data suggest that the butene isomer distribution is primary in nature, resulting from butyl isomerization on the Ni site before desorption of the butene products. The high butene selectivity and non-equilibrated butene isomer distribution point to shape selectivity as a dominant parameter in the Ni-UiO-67-bpy catalysts.

These results are in accordance with the Cossee-Arlman (degenerate polymerization) mechanism, as previously suggested for other heterogeneous Ni-based ethene oligomerization catalysts [34, 35, 107, 183]. In contrast to the metallacycle mechanism, typical of homogeneous Ni catalysts [64], the Cossee-Arlman mechanism enables isomerization of the formed butyl species before desorption from the active site. As a final note, the similar product selectivity observed for all Ni-UiO-67-bpy catalysts in this study, points to a single Ni active site, positioned in a similar, well-defined, confined environment, being responsible for the activity of all catalysts.

Thermogravimetric analysis of the pristine and used (3.2)Ni-UiO-67-bpy$_{11\%}$ showed that the mass of tested catalyst increased by approximately 15 % compared to the pristine catalyst, suggesting that product deposition is a cause for deactivation (Figure A 14). In accordance with this result, the N_2 adsorption isotherm of pristine, activated, and tested catalyst shows that the S_{BET} of the catalyst was not notably changed after activation (1525 m^2/g). Conversely, the spent catalyst had a substantially lower S_{BET} (503 m^2/g) , which is best explained by pore blocking or by MOF decomposition- X-ray diffractograms of pristine, activated and tested catalyst showed that the MOF catalyst was crystalline in all

stages of the experiment and that the MOF framework was intact after testing (Figure A 14). Hence, pore blocking by hydrocarbon deposits is suggested to be the main cause for deactivation of (3.2)Ni-UiO-67-bpy$_{11\%}$.

Next, we focus on elucidating the role of the charge balancing anions on activity and active site formation through kinetic investigation of Ni-UiO-67-bpy$_{11\%}$ catalysts prepared with various Ni precursors.

4.2.5 Ni precursor variation

The Ni-UiO-67-bpy$_{11\%}$ functionalized with various Ni precursors were subjected to ethene dimerization reaction under standard reaction conditions (250 °C, 26 bar ethene and 4 bar He) and the evolution of ethene dimerization activity with TOS is presented in Figure 29. All catalysts, except (2.3)Ni-UiO-67-bpy$_{11\%}$ - $NiCl_2$ (conversion < 0.05 %), show significant activity for the ethene dimerization reaction and exhibit ~ 99 % selectivity to linear butenes with longer alkenes denoted C_{6+} as the only byproduct detected. Although the transient behaviors differ, all catalysts show an initiation period where the activity increase with TOS, followed by a gradual deactivation.

Comparing the activities after the catalysts reached pseudo-steady state shows that the ethene dimerization activity increase in the following order: 0 ~ (2.3)Ni-UiO-67-bpy$_{11\%}$ - $NiCl_2$ < (1.9)Ni-UiO-67-bpy$_{11\%}$ - $Ni(OAc)_2$ < (3.2)Ni-UiO-67-bpy$_{11\%}$ - $Ni(OAc)_2$ < (2.0)Ni-UiO-67-bpy$_{11\%}$ - $Ni(NO_3)_2$ ~ (2.3)Ni-UiO-67-bpy$_{11\%}$ - $Ni(acac)_2$.

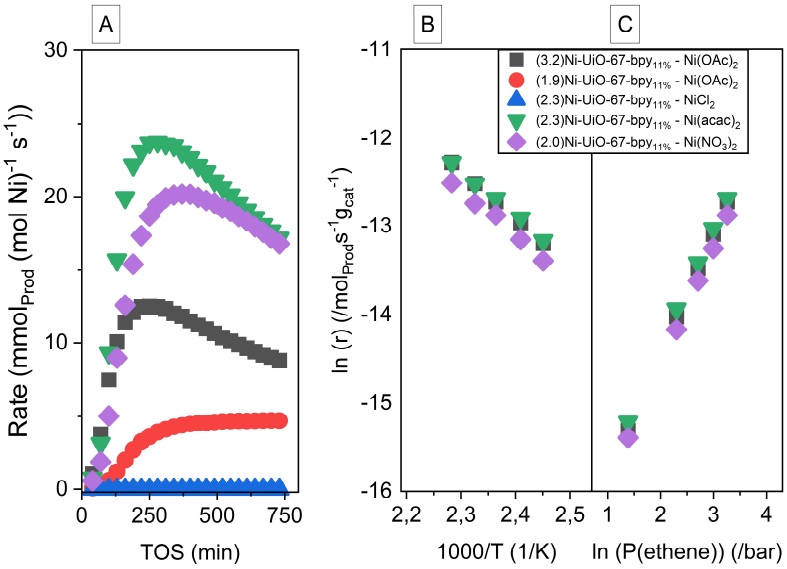

Figure 29: A) Ethene dimerization rate vs TOS. Reaction conditions: m_{cat} = 0.150 g, 30 bar total pressure where P_{ethene} = 26 bar and P_{inert} = 4 bar, temperature = 250 °C and contact time = 5.0 mg_{cat}·min·mL^{-1} at STP. B) Arrhenius plot for butene formation (T = 230 – 270 °C). C) Reaction order of butene in ethene pressure (P_{ethene} = 4 – 26 bar).

Considering the linear butene distribution, similar trends and selectivities, irrespective of conversion level, were observed over all catalysts. During the first ~ 100 min TOS *i.e.* the initiation period, there were small shift (~ 2 %) among the linear butene selectivities. Importantly, the selectivities stabilized for all catalysts after reaching pseudo-steady state at 41 %, 26 % and 32 % ± 2 %, far from thermodynamic equilibrium (12:57:31 %), for 1-butene, trans-2-butene and cis-2-butene, respectively. The high butene selectivity and non-equilibrated isomer distribution suggests that the butene isomer distribution is primary in nature. These results are best in accordance with the Cossee-Arlman mechanism, as previously reported in this thesis (*vide supra*) and in literature for other Ni based heterogeneous catalysts [35, 37, 107].

Keeping charge balance in mind, the formation of a [Ni-alkyl-alkene]$^+$ species characteristic to the Cossee-Arlman mechanism from [Ni(X)$_2$-bpy·yH$_2$O] (X = charge balancing monodentate anion) would require the removal of one anion. Assuming that the active species are of the type [Ni(X)-alkyl-alkene-bpy]$^+$, changing the chemical nature

of the charge balancing anion is likely to affect the active site and result in observable changes in activity and selectivity for the ethene dimerization reaction. Furthermore, similar observable changes are expected if the active sites are dimeric, small oligomers docked near bpy or Zr clusters, where the nature of the anion represent an important active site parameter.

Kinetic parameters derived from ethene partial pressure and temperature variation tests were determined to investigate the effect of the anions on the active site. The apparent activation energy and reaction order of ethene in the rate of production of butenes for the three most active catalysts are determined to be very similar, 50 ± 2 kJ/mol and 1.4 ± 0.1, respectively (Figure 29B-C). Taken together, almost identical selectivity, apparent activation energy and reaction order suggests that the reaction takes place through common intermediates, reaction mechanism and occur on the same active site over these catalysts. Surprisingly, this either suggests that the electronic and steric properties of the anion is irrelevant for the active site or more likely that the [$Ni(X)_2$-bpy·yH_2O] species transform to an intermediate species that acts as a precatalyst and form over all active catalysts during pretreatment. Thus, the differences in rate per mol Ni during the transient and pseudo-steady state is suggested to be related to the rate of active site formation rather than the formation of a different, more reactive site on (2.0)Ni-UiO-67-$bpy_{11\%}$ - $Ni(NO_3)_2$ and (2.3)Ni-UiO-67-$bpy_{11\%}$ - $Ni(acac)_2$.

To examine if a common Ni species may form over these catalysts during thermal treatment, we refer to literature studies showing thermal decomposition of the Ni precursors used to prepare the Ni MOFs. Studies of $Ni(OAc)_2(H_2O)_4$ carried out in air, helium or hydrogen showed that the salt first undergoes dehydration around 110 °C followed by formation of an intermediate basic acetate $(1 - x)Ni(CH_3COO)_2 \cdot xNi(OH)_2$, where $x \sim 0.1$, and finally decomposition around 350 °C [184, 185]. Formation of basic Ni ($Ni(NO_3)_2 \cdot 2Ni(OH)_2 \cdot 4H_2O$) have been observed for $Ni(NO_3)_2 \cdot 6H_2O$ around 200 °C when heated in air [184], while basic Ni species was not observed for $NiCl_2 \cdot 6H_2O$ before 600 °C when heated in N_2 [186].

Although the activation conditions differ slightly from what has been employed here, the trends are in line with the activities observed over Ni-UiO-67-bpy$_{11\%}$ catalysts. MOFs functionalized with precursors that undergoes transformation to basic Ni species during thermal treatment are active for ethene dimerization. While no significant activity was observed over (2.3)Ni-UiO-67-bpy$_{11\%}$ - $NiCl_2$, likely because majority of Ni is present only as inactive [$NiCl_2$-bpy] species. Formation of basic Ni species has not been reported on $Ni(acac)_2$. However, while some authors reported only a single decomposition process at around 320 °C [187], others reported of another processes occurring at around 200 °C, in 4 % O_2 in He [188].

It is hypothesized that similar processes may take place over [$Ni(X)_2$-bpy·yH_2O] species when heated to 300 °C in 10 % O_2, resulting in a small concentration of [$Ni(OH)_2$-bpy] species that can act as a precatalyst. Regrettably, similar decomposition studies could not be conducted here because of interference from the organic constituents of the MOF lattice. CO FTIR at LNT conditions was shown to not probe all the Ni sites and is deemed unsuitable for detecting and differentiating between [$Ni(OAc)_2$-bpy] and [$Ni(OH)_2$-bpy]. Another possibility of identifying [Ni^{2+}-$(OH)_2$] species, would arrive from the careful observation of the ν_{OH} stretching region (3700-3600 cm^{-1}) in the FTIR spectra (Figure A 13), analogous to what was observed on Cu-zeolites [189]. Although no spectral evidence was found for [Ni^{2+}-$(OH)_2$] species on the activated catalysts, the aim of *ex-situ* FTIR was to differentiate between different Ni species and detect any nanoparticles formed with CO as probe molecule and was not optimized to detect low abundance OH groups.

Circumstantial evidence supports the claim of a precatalyst formed during activation. Such as the observation that a longer activation period over (3.2)Ni-UiO-67-bpy$_{11\%}$ lead to a more rapid increase and a higher maximum in activity (Figure A 16), suggested to be due to increased precatalyst concentration with longer activation time. Another observation that is in accordance with this hypothesis is that (3.2)Ni-UiO-67-bpy$_{11\%}$ activated in inert at 150 °C for 360 min was inactive for the reaction, suggesting that only dehydrating the Ni species does not yield active sites and that it requires a chemical transformation.

4.2.6 Pore size

Substituting the bpdc linker in UiO-67 with bndc linker results in a UiO-67 MOF, as its crystal structure is identical to that of UiO-67, but with reduced pore size due to the large naphthyl rings, potentially inducing confinement effects on the active sites. The pore size in bndc-UiO-67 is varying because of rotation and disorder in the MOF, but since the crystal structures are identical, the pore size should correlate well with pore volume, which is significantly smaller in the bndc-UiO-67.

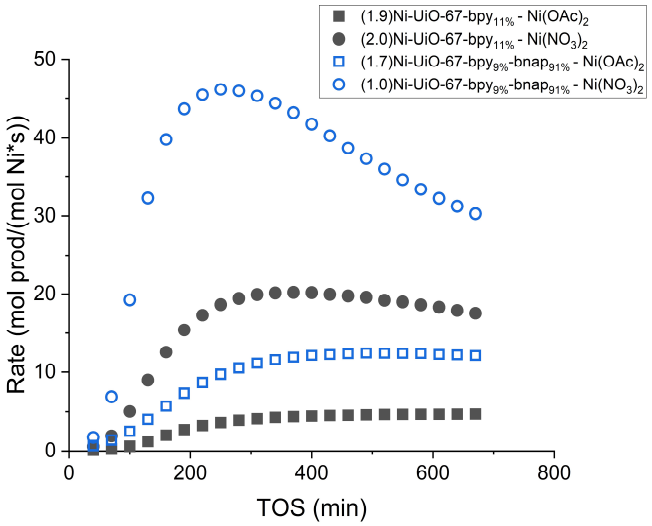

Figure 30: Ethene dimerization rate vs TOS for Ni functionalized UiO-67-bpy$_{11\%}$ and UiO-67-bndc-bpy$_{9\%}$ catalysts. Reaction conditions: m_{cat} = 0.150 g, 30 bar total pressure where P_{ethene} = 26 bar and P_{inert} = 4 bar, temperature = 250 °C and contact time = 5.0 mg_{cat}·min·mL^{-1} at STP.

Comparing the rate of the Ni-UiO-67-bndc-bpy$_{9\%}$ to Ni-UiO-67-bpy$_{11\%}$ catalyst with similar Ni:bpy molar ratio and Ni precursor it is apparent that Ni-UiO-67-bndc-bpy catalyst perform better. However, the product distribution, apparent activation energy and reaction order with respect to ethene was identical to the previously investigated catalysts, suggesting that the confinement effect is not influencing the kinetics of the reaction. The higher rate over the Ni-UiO-67-bndc-bpy can be explained by considering that the steric shielding of the carboxylate and μ-OH groups in the clusters by naphthyl groups [190] may inhibit significant interaction with bpy free Ni and mainly result in bpy

coordinated Ni. Similarly, the more confined space may favor formation of Ni-bpy species rather than $Ni(OAc)_2$ loosely interacting with the framework. This is supported by observing that the Ni:bpy molar ratio is significantly lower in UiO-67-$bndc_{91\%}$-$bpy_{9\%}$ compared to UiO-67-$bpy_{11\%}$ regardless of the fact that they were prepared with excess Ni (Ni:bpy molar ratio of 2.4 in solution) and had similar defectivity (Linker+modulator:Zr node ~5.80, Table 3). These results are in accordance with the hypothesis of isolated Ni-bpy as the only active site in these catalysts.

Table 8: Physicochemical properties of the Ni-containing and bndc functionalized UiO-67 catalysts.

Sample	S_{BET} (m^2/g)	Ni:bpy (mol/mol)	Pore volume ($cm^3(STP)\ g^{-1}$)
(1.9)Ni-UiO-67-$bpy_{11\%}$ - $Ni(OAc)_2$	1834	1.2	452
(2.0)Ni-UiO-67-$bpy_{11\%}$ - $Ni(NO_3)_2$	1868	1.3	452
(1.7)Ni-UiO-67-$bndc_{91\%}$-$bpy_{9\%}$ - $Ni(OAc)_2$	1133	1.4	256
(1.0)Ni-UiO-67-$bndc_{91\%}$-$bpy_{9\%}$ - $Ni(NO_3)_2$	-	0.9	-

4.2.7 Evolution of active Ni-sites

To investigate the nature of the active sites, we performed the ethene dimerization reaction over (1.9)Ni-UiO-67-$bpy_{11\%}$ and (3.2)Ni-UiO-67-$bpy_{11\%}$ under relevant reaction conditions (250 °C and 15 bar ethene), while monitoring the average electronic and structural properties around Ni ions by XAS. Based on the test data, we consider that the results obtained here are also valid and representative for the other catalysts.

To demonstrate the importance of high P_{ethene} on the active site formation, the activity over (3.2)Ni-UiO-67-$bpy_{11\%}$ obtained at atmospheric conditions (1 bar ethene) and under 10 bar and 26 bar ethene (where P_{total} = 30 bar) is shown in Figure A 17. Under atmospheric conditions, the conversion was negligible and stabilized around 0.04 %. A higher partial pressure of ethene led to a more rapid increase in activity, however, the activity converged around 4 % after 700 min TOS under both conditions. This indicates that high P(ethene)

is crucial for the generation of active site. Thus, to avoid complicating the analysis by deactivation observed at 26 bar ethene and to obtain significant conversion, we carried out the XAS measurements under 15 bar ethene.

Through all stages of the XAS experiment, no large metallic or oxidic aggregates were detected. Only Ni in 2+ oxidation state was observed, suggesting again that Ni speciation is dominated by well-dispersed Ni^{2+} species under activation and reaction conditions.

MCR analysis, structure refinement by means of machine learning-based algorithm implemented in PyFitIt code [138], related figures and results were provided by Dr. Aram Bugaev. Significant effort has been put into identifying all the Ni species present in the materials. However, the spectral differences between the various Ni species were small due to their high similarity in both coordination number and geometry making it difficult to distinguish between the Ni species with XAS. This chapter of the dissertation is part of a work in progress and only the preliminary results obtained over (1.9)Ni-UiO-67-$bpy_{11\%}$ will be presented in the following chapter while efforts are ongoing to extend the analysis to (3.2)Ni-UiO-67-$bpy_{11\%}$.

MCR analysis show that every spectrum from the whole set of XAS data, containing several thousand spectra, can be represented by a linear combination of three independent spectra, which correspond to Ni species with different local structure resulting in statistically relevant differences in the XAS spectra (mainly in XANES region). The MCR-retrieved XANES and Fourier-transformed (FT) EXAFS are shown in parts (A) and (B), respectively, of Figure 31, while their related concentration profiles for (1.9)Ni-UiO-67-$bpy_{11\%}$ are shown in (C), as function of TOS during activation (left) and reaction (right).

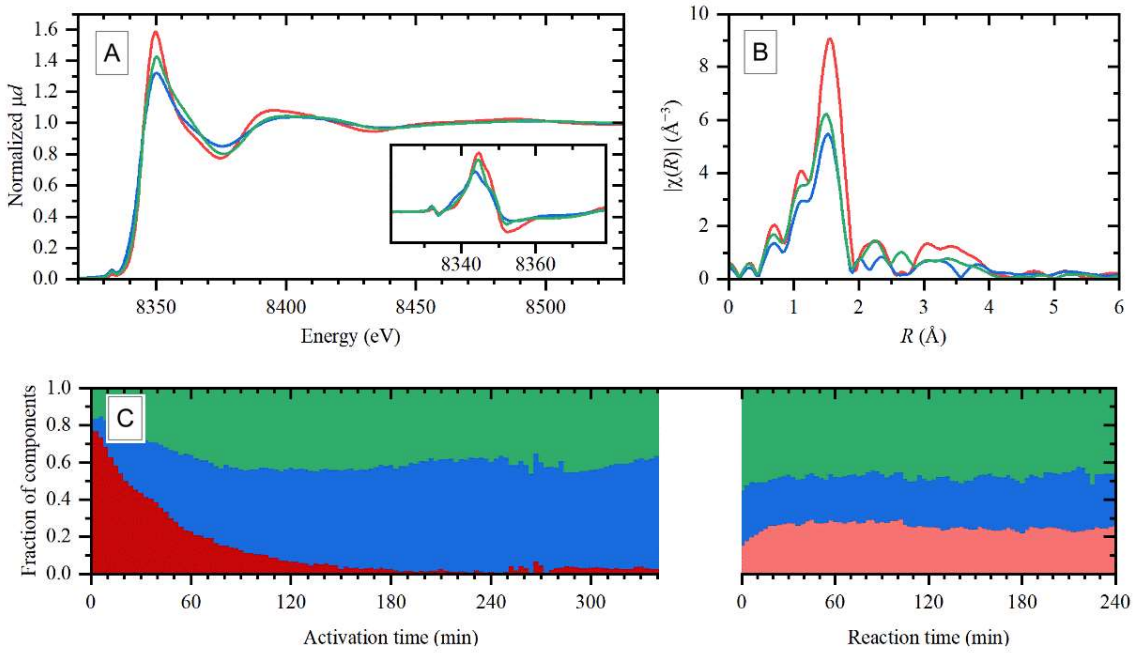

Figure 31: Representative XANES (A), first derivative XANES (inset in part a) and FT-EXAFS (B) spectra extracted from the whole XAS dataset by MCR approach, their concentration profiles during the activation (left parts) and under reaction conditions (right parts) for (1.9)Ni-UiO-67-bpy$_{11\%}$ (C). Activation conditions: From RT to 300 °C, 5°C/min, and kept under isothermal conditions for 340 min in 10 % O_2 in N_2. Reaction conditions: 250 °C, 15 bar ethene.

It is worth reminding once more that within the experimentally observed convolution, different structures with similar local geometry may result in highly similar XANES spectra. In particular, this is the case for the Ni species in dark and light red shown in Figure 31C where the XANES for these two *different* Ni species obtained during activation conditions (oxidative) and reaction conditions (reductive) were identical.

Furthermore, although there is significant amount of bpy free Ni species present (Figure 25 and Figure 26), the three independent spectra obtained from MCR analysis are plausibly representative of more than a single Ni species each, including both bpy coordinated and bpy free Ni (*vide infra*). These results support the fact that the bpy free Ni is very similar to the bpy coordinated Ni species in terms of both coordination number and geometry, especially in their first-shell coordination environment. Thus, making it difficult to distinguish the bpy coordinated and bpy free Ni by analysis method employed here.

Concentrating first on the pristine catalysts, first-shell EXAFS analysis (Table A 2) revealed the dominant presence of a 6-coordinated Ni species (represented in red, Figure 31). In addition, minor contributions are observed from two additional species, depicted in blue and green in Figure 31. First-shell EXAFS analysis links the blue species to 4-coordinated Ni species. The first-shell intensity in the EXAFS of the green species closely resemble the EXAFS for blue species, suggesting that it is also a 4-coordinated species. However, best fit on the EXAFS was achieved using a 6-coordinated species, yet with a substantially increased Debye-Waller factor. The green specie is suspected to be distorted and have a coordination number between 4 and 6 but is treated as a 6-coordinated species in the discussion below.

Concentrating next on the activation period under 10 % O_2 in N_2, a decrease in the concentration of the 6-coordinated red species and an increase in 4-coordinated blue and 6-coordinated green species with increasing temperature from RT to 300 °C can be observed. This trend continued under the isothermal conditions, reached after 60 min TOS, and stabilized at around 180 min TOS. The decrease in red species is rationalized by dehydration of two distinct 6-coordinated species, $[Ni(OAc)_2(H_2O)_2\text{-}(bpy)]$ and $Ni(OAc)_2{\cdot}4H_2O$, resulting in 4-coordinated $[Ni(OAc)_2\text{-}(bpy)]$ and $Ni(OAc)_2$, respectively. Furthermore, a small fraction of $[Ni(OAc)_2(H_2O)_2\text{-}(bpy)]$ is hypothesized to transform to $[Ni(OH)_2\text{-}bpy]$ species.

Turning next to the evolution of Ni species during ethene dimerization with TOS, the XANES and EXAFS of the blue and green species remained identical to those observed during activation, suggesting that $[Ni(OAc)_2\text{-}bpy]$ type species are unreactive towards ethene. The formation of a new 6-coordinated (light) red species that increase in concentration before reaching a plateau can be observed in Figure 31C. The fraction of green species remained unaltered and the red species increase in expense of the blue species suggesting that a portion of the 4-coordinated species transforms to a new 6-coordinated species after reacting with ethene. This is in agreement with the hypothesis that $[Ni(OAc)_2\text{-}bpy]$ and $[Ni(OH)_2\text{-}bpy]$ are both generated during the activation period

and that [$Ni(OH)_2$-bpy] reacts further to form the active site while [$Ni(OAc)_2$-bpy] remains unreactive for the dimerization reaction.

It appears that the induction time observed over (1.9)Ni-UiO-67-$bpy_{11\%}$ is much shorter here (~ 30 min, Figure 31C) compared to during catalytic testing (~ 300 min, Figure 28A). Regrettably, due to technical difficulties with the mass spectrometer, the effluent from the reactor was not analyzed and it was not possible to determine the time products started to form over the catalyst. The discrepancy between the induction times could be related to the difference in the experimental setup and other external factors such as degree of temperature control. However, it is also possible that ethene coordinates to *e.g.* [$Ni(OAc)_2$-bpy] species to form unreactive 6-coordinated [$Ni(OAc)_2(C_2H_4)$-bpy] species, thus contributing to the premature formation of the 6-coordinated species.

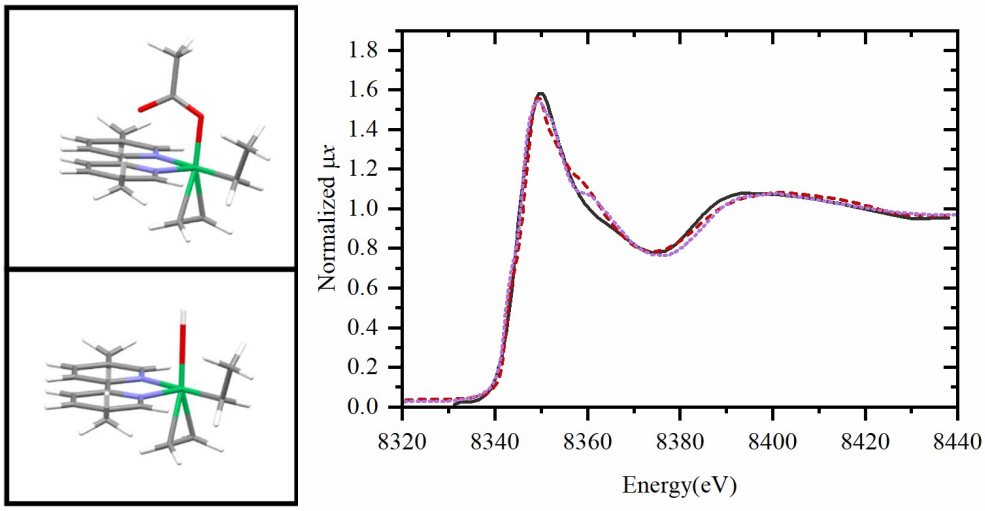

Figure 32: The structures of [Ni(OAc)-alkyl-alkene-bpy] (top left) and [Ni(OH)-alkyl-alkene-bpy] (bottom left) species obtained from DFT calculations. Experimental XANES of the 6-coordinated red species during ethene flow (solid black) and theoretical spectra of [Ni(OAc)-alkyl-alkene-bpy] (dashed red) and [Ni(OH)-alkyl-alkene-bpy] (dotted purple) obtained from DFT calculations (right).

Model structure of [Ni(OH)-alkyl-alkene-bpy] and [Ni(OAc)-alkyl-alkene-bpy], obtained from DFT calculations fit well to the experimental XANES of the 6-coordinated species during ethene flow (Figure 32). Although the two species generate almost indistinguishable XANES spectra, this type of Ni active site is typical for and in agreement

with the Cossee-Arlman type mechanism. Drawing parallel from Ni-aluminosilicates, it is hypothesized that the formation of the active species may take place similar to what has been proposed for Ni-zeolites (Scheme 4, **Paper II**, supporting info) .

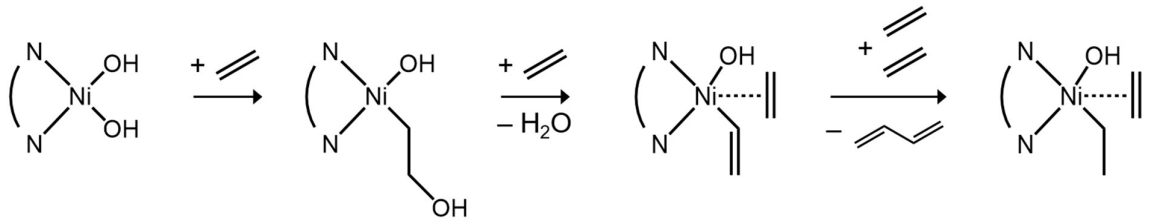

Scheme 4: Cossee-Arlman site formation from $[Ni(OH)_2$-bpy] species inspired from and similar to what has been proposed over Ni-zeolites (**Paper II**, supporting info).

5 Main conclusions

- Significant differences were identified between the mesoporous and microporous Ni functionalized catalysts in terms of activity, selectivity, and reaction order in ethene. The zeolite catalyst showed rapid initial deactivation followed by a period of slower deactivation while the activity over the mesoporous catalyst first decreased, then increased before subsequently decreasing again. Linear butenes were the main product over both types of catalysts, but 1-butene selectivity was up to two times higher over the microporous catalysts.

- The initial change in product selectivity during deactivation of the Ni-zeolite catalysts indicated that they initially had more than one active site, but only one active site remained after pseudo-steady state was reached. Based on contact time variation experiments (120 °C, 17.4 bar ethene and 2 – 16 $mg_{cat}{\cdot}min{\cdot}mL^{-1}$), all three linear butenes were found to be primary products and originated from a single active site, in accordance with the Cossee-Arlman mechanism.

- FTIR spectroscopy confirmed the presence of a variety of Ni species in Ni-H-Beta(m), including two distinct Ni^{2+} counterions, grafted Ni^{2+}, small NiO particles and possibly a very small amount of Ni^{0} particles. Measurements carried out to probe the sites accessible to the CO probe after interaction with ethene showed that only ion exchanged nickel, under +II oxidation state, and Brønsted acid sites allow adsorption and reaction of ethene (30 min at 150 °C and 0.29 bar ethene).

- The results of the DFT-MD simulations at operating conditions show that ethene molecules can reversibly mobilize the active site as they exchange with the zeolite as ligands on Ni during reaction, generating mobile $[(ethene)_2Ni\text{-}alkyl]^+$ species. A microkinetic model that was constructed based on calculated free-energy profiles was tested against experimental data and successfully reproduced the experimentally observed relative production rate of butene compared to higher oligomers and the second-order rate dependence on ethene pressure.

- Several Ni and functional linker functionalized UiO-67 was investigated for the cocatalyst free ethene oligomerization reaction. SEM images revealed that only materials containing H_2bpydc retained Ni inside the pores while $Ni(OAc)_2$ deposits were observed on the other functionalized MOFs. The Ni and H_2bpydc functionalized UiO-67 MOF catalyzed the ethene dimerization reaction cocatalyst free after activation at 300 °C in 10 % O_2. Upon activation, TOF up to 90 h^{-1} with butene selectivities up to 99 % was observed.

- bpy coordinated Ni was identified as the active site and Ni speciation was found to consist of bpy coordinated and defect coordinated Ni. All bpy was found to be fully coordinated to Ni only when Ni was in excess compared to bpy, explaining the higher rate observed with increasing bpy free Ni over these catalysts.

- Kinetic investigation of Ni-UiO-67-$bpy_{11\%}$ prepared with various Ni precursors and *operando* XAS was employed to gain insight on active site formation. Reaction order for butene formation on P_{ethene} and apparent activation energy over the active catalysts, irrespective of Ni precursor used, was 1.4 $\pm$ 0.1 and 50 $\pm$ 2 kJ/mol, respectively. The results were found be in accordance with the formation of a common precatalyst and [Ni-alkyl-alkene-bpy]$^+$ type active site, characteristic to the Cossee-Arlman mechanism.

6 Suggestions for further work

- Although there is an increasing consensus on the oxidation state of the active site (Ni^{2+}), how the insertion-coordination active site forms remain unclear. Considering that several types of Ni^{2+} have been proven to be active for the ethene oligomerization reaction, experiments targeting to elucidate the formation of a specific active site should be carried out. Several DFT based pathways have been proposed, testing, and validating those mechanism is a step forward in understanding how the active site in cocatalyst free Ni-zeolites form.

- A positive identification of the mobile active species formed from interaction with ethene is best investigated under *operando* conditions. *Operando* XAS and EXAFS analysis may validate or disregard the mobile active site model.

- Fixing material properties such as Si/Al and Ni/Al ratio and isolating parameters to investigate the effect of topology and morphology will provide more reliable results.

- The material and mechanistic understanding presented in this work can help design Ni-MOFs catalysts for ethene dimerization reaction. The important upside of MOFs is their versatility and catalyst with N,N chelating, and plausibly N,O, P,O chelating linkers, with additional functionality such as electron donating/withdrawing groups can be screened for the reaction and the electronic and steric effects can be elucidated.

- The very strong geometric and compositional similarity between the bpy coordinated and bpy free Ni significantly complicates spectroscopic analysis. To simplify data analysis and avoid possible interferences, studies should focus on a perfect (defect free) MOF. *Operando* XAS measurements under reaction conditions can be repeated on a catalyst that displays highest activity at Ni:bpy molar ratio = 1.

- Dedicated FTIR studies can be carried out to determine the precatalyst and active site.

- Computational work targeting reaction mechanism and active site formation, similar to what has been carried over Ni-zeolites, can provide insight on designing the active site in these highly tunable MOFs.

References

1. Erisman, J.W., et al., *How a century of ammonia synthesis changed the world.* Nature Geoscience, 2008. **1**(10): p. 636-639.
2. Atkins, O., Rourke, Weller, Armstrong, *Inorganic Chemistry*. 2009: OUP Oxford.
3. P. Atkins, J.D.P., *Physical chemistry*. 2010: Oxford university press.
4. I. Chorkendorff, J.W.N., *Concepts of Modern Catalysis and Kinetics*. 2006: Wiley-VCH.
5. Dyer, A., *An Introduction to Zeolite Molecular Sieves*. 1988: John Wiley & Sons Ltd.
6. Ch. Baerlocher, L.B.M., D.H. Olson 6th ed., *Atlas of zeolite framework types*. 2007, Amsterdam 2007: Elsevier.
7. McCusker, C.B.a.L.B. *Database of Zeolite Structures*. Available from: http://www.iza-structure.org/databases/.
8. Weitkamp, J., *Zeolites and catalysis.* Solid state ionics, 2000. **131**: p. 175 - 188.
9. Maesen, T., *Chapter 1 - The Zeolite Scene – An Overview*, in *Studies in Surface Science and Catalysis*, J. Čejka, et al., Editors. 2007, Elsevier. p. 1-12.
10. Jiří Čejka, H.v.B., Avelino Corma and Ferdi (eds), *Studies in Surface Science and Catalysis 3rd ed.* **2007**: Elsevier.
11. A. D. McNaught, A.W., *IUPAC. Compendium of chemical terminology, 2nd ed. (the "Gold Book")*. 1997, Oxford: Blackwell Scientific Publications.
12. Koohsaryan, E., M. Anbia, and M. Maghsoodlu, *Application of zeolites as non-phosphate detergent builders: A review.* Journal of Environmental Chemical Engineering, 2020. **8**(5): p. 104287.
13. Corma, A., *Inorganic Solid Acids and Their Use in Acid-Catalyzed Hydrocarbon Reactions.* Chemical Reviews, 1995. **95**(3): p. 559-614.
14. Berend Smit, T.L.M.M., *Towards a molecular understanding of shape selectivity.* Nature, 2008. **451**: p. 671-678.
15. Banerjee, R., et al., *High-Throughput Synthesis of Zeolitic Imidazolate Frameworks and Application to CO₂ Capture.* Science, 2008. **319**(5865): p. 939.
16. Li, H., et al., *Design and synthesis of an exceptionally stable and highly porous metal-organic framework.* Nature, 1999. **402**(6759): p. 276-279.
17. Cavka, J.H., et al., *A New Zirconium Inorganic Building Brick Forming Metal Organic Frameworks with Exceptional Stability.* Journal of the American Chemical Society, 2008. **130**(42): p. 13850-13851.

18. Furukawa, H., et al., *The Chemistry and Applications of Metal-Organic Frameworks.* Science, 2013. **341**(6149): p. 1230444.

19. Øien-Ødegaard, S., *Preparation, structure and reactivity of functionalized zirconium metal-organic frameworks*. 2016, Oslo.

20. Rowsell, J.L.C. and O.M. Yaghi, *Metal–organic frameworks: a new class of porous materials.* Microporous and Mesoporous Materials, 2004. **73**(1): p. 3-14.

21. Fei, H. and S.M. Cohen, *A robust, catalytic metal–organic framework with open 2,2′-bipyridine sites.* Chemical Communications, 2014. **50**(37): p. 4810-4812.

22. Chavan, S., et al., *H2storage in isostructural UiO-67 and UiO-66 MOFs.* Physical Chemistry Chemical Physics, 2012. **14**(5): p. 1614-1626.

23. Suh, M.P., et al., *Hydrogen Storage in Metal–Organic Frameworks.* Chemical Reviews, 2012. **112**(2): p. 782-835.

24. Furukawa, H., et al., *Ultrahigh Porosity in Metal-Organic Frameworks.* Science, 2010. **329**(5990): p. 424.

25. Li, J.-R., J. Sculley, and H.-C. Zhou, *Metal–Organic Frameworks for Separations.* Chemical Reviews, 2012. **112**(2): p. 869-932.

26. Lee, J., et al., *Metal–organic framework materials as catalysts.* Chemical Society Reviews, 2009. **38**(5): p. 1450-1459.

27. Mueller, U., et al., *Metal–organic frameworks—prospective industrial applications.* Journal of Materials Chemistry, 2006. **16**(7): p. 626-636.

28. Goesten, M.G., F. Kapteijn, and J. Gascon, *Fascinating chemistry or frustrating unpredictability: observations in crystal engineering of metal–organic frameworks.* CrystEngComm, 2013. **15**(45): p. 9249-9257.

29. Hasegawa, S., et al., *Three-Dimensional Porous Coordination Polymer Functionalized with Amide Groups Based on Tridentate Ligand: Selective Sorption and Catalysis.* Journal of the American Chemical Society, 2007. **129**(9): p. 2607-2614.

30. Gascon, J., et al., *Amino-based metal-organic frameworks as stable, highly active basic catalysts.* Journal of Catalysis, 2009. **261**(1): p. 75-87.

31. Metzger, E.D., et al., *Selective Dimerization of Ethylene to 1-Butene with a Porous Catalyst.* ACS Central Science, 2016. **2**(3): p. 148-153.

32. Øien, S., et al., *Probing Reactive Platinum Sites in UiO-67 Zirconium Metal–Organic Frameworks.* Chemistry of Materials, 2015. **27**(3): p. 1042-1056.

33. Gutterød, E.S., et al., *CO2 Hydrogenation over Pt-Containing UiO-67 Zr-MOFs—The Base Case.* Industrial & Engineering Chemistry Research, 2017. **56**(45): p. 13206-13218.

34. Canivet, J., et al., *MOF-Supported Selective Ethylene Dimerization Single-Site Catalysts through One-Pot Postsynthetic Modification.* Journal of the American Chemical Society, 2013. **135**(11): p. 4195-4198.

35. Gonzalez, M., J. Oktawiec, and J.R. Long, *Ethylene Oligomerization in Metal-Organic Frameworks Bearing Nickel(II) 2,2[prime or minute]-Bipyridine Complexes.* Faraday Discussions, 2017.

36. Yuan, S., et al., *Exposed Equatorial Positions of Metal Centers via Sequential Ligand Elimination and Installation in MOFs.* Journal of the American Chemical Society, 2018. **140**(34): p. 10814-10819.

37. Madrahimov, S.T., et al., *Gas-Phase Dimerization of Ethylene under Mild Conditions Catalyzed by MOF Materials Containing (bpy)NiII Complexes.* ACS Catalysis, 2015. **5**(11): p. 6713-6718.

38. *Ethylene Global Supply Demand Analytics Service*. [cited 2020 Feb. 17]; Available from: https://www.woodmac.com/news/editorial/ethylene-global-supply-demand-analytics-service/.

39. Gao, Y., et al., *Recent Advances in Intensified Ethylene Production—A Review.* ACS Catalysis, 2019. **9**(9): p. 8592-8621.

40. Ding, J. and W. Hua, *Game Changers of the C3 Value Chain: Gas, Coal, and Biotechnologies.* Chemical Engineering & Technology, 2013. **36**(1): p. 83-90.

41. Bruijnincx, P.C.A. and B.M. Weckhuysen, *Shale Gas Revolution: An Opportunity for the Production of Biobased Chemicals?* Angewandte Chemie International Edition, 2013. **52**(46): p. 11980-11987.

42. Armor, J.N., *Key questions, approaches, and challenges to energy today.* Catalysis Today, 2014. **236, Part B**: p. 171-181.

43. IEA. *Future of petrochemicals*. 2018 [cited 2020 23.02]; Available from: https://www.iea.org/reports/the-future-of-petrochemicals.

44. Weusthuis, R.A., J.M.M.J.G. Aarts, and J.P.M. Sanders, *From biofuel to bioproduct: is bioethanol a suitable fermentation feedstock for synthesis of bulk chemicals?* Biofuels, Bioproducts and Biorefining, 2011. **5**(5): p. 486-494.

45. Bozell, J.J., *Connecting Biomass and Petroleum Processing with a Chemical Bridge.* Science, 2010. **329**(5991): p. 522.

46. IEA. *Renewables 2019*. 2019 [cited 2020 23.02]; Available from: https://www.iea.org/reports/renewables-2019.

47. Hulea, V., *Toward Platform Chemicals from Bio-Based Ethylene: Heterogeneous Catalysts and Processes.* ACS Catalysis, 2018. **8**(4): p. 3263-3279.

48. Posada, J.A., et al., *Potential of bioethanol as a chemical building block for biorefineries: Preliminary sustainability assessment of 12 bioethanol-based products.* Bioresource Technology, 2013. **135**: p. 490-499.

49. Rass-Hansen, J., et al., *Bioethanol: fuel or feedstock?* Journal of Chemical Technology & Biotechnology, 2007. **82**(4): p. 329-333.

50. Angelici, C., B.M. Weckhuysen, and P.C.A. Bruijnincx, *Chemocatalytic Conversion of Ethanol into Butadiene and Other Bulk Chemicals.* ChemSusChem, 2013. **6**(9): p. 1595-1614.

51. Zhang, M. and Y. Yu, *Dehydration of Ethanol to Ethylene.* Industrial & Engineering Chemistry Research, 2013. **52**(28): p. 9505-9514.

52. Mohsenzadeh, A., A. Zamani, and M.J. Taherzadeh, *Bioethylene Production from Ethanol: A Review and Techno-economical Evaluation.* ChemBioEng Reviews, 2017. **4**(2): p. 75-91.

53. Naik, S.N., et al., *Production of first and second generation biofuels: A comprehensive review.* Renewable and Sustainable Energy Reviews, 2010. **14**(2): p. 578-597.

54. Pujado, P.R.a.V., B. V, *Make C3-C4 olefins selectively.* Hydrocarbon Processing, 69, 1990.

55. Torres Galvis, H.M., et al., *Supported Iron Nanoparticles as Catalysts for Sustainable Production of Lower Olefins.* Science, 2012. **335**(6070): p. 835.

56. Tian, P., et al., *Methanol to Olefins (MTO): From Fundamentals to Commercialization.* ACS Catalysis, 2015. **5**(3): p. 1922-1938.

57. van Leeuwen, P.W.N.M., N.D. Clément, and M.J.L. Tschan, *New processes for the selective production of 1-octene.* Coordination Chemistry Reviews, 2011. **255**(13–14): p. 1499-1517.

58. Breuil, P.-A.R., L. Magna, and H. Olivier-Bourbigou, *Role of Homogeneous Catalysis in Oligomerization of Olefins : Focus on Selected Examples Based on Group 4 to Group 10 Transition Metal Complexes.* Catalysis Letters, 2014. **145**(1): p. 173-192.

59. Wilke, G., *Fifty Years of Ziegler Catalysts: Consequences and Development of an Invention.* Angewandte Chemie International Edition, 2003. **42**(41): p. 5000-5008.

60. Cossee, P., *Ziegler-Natta catalysis I. Mechanism of polymerization of α-olefins with Ziegler-Natta catalysts.* Journal of Catalysis, 1964. **3**(1): p. 80-88.

61. Arlman, E.J. and P. Cossee, *Ziegler-Natta catalysis III. Stereospecific polymerization of propene with the catalyst system $TiCl_3 \cdot AlEt_3$.* Journal of Catalysis, 1964. **3**(1): p. 99-104.

62. Manyik, R.M., W.E. Walker, and T.P. Wilson, *A soluble chromium-based catalyst for ethylene trimerization and polymerization.* Journal of Catalysis, 1977. **47**(2): p. 197-209.

63. Forestière, A., H. Olivier-Bourbigou, and L. Saussine, *Oligomerization of Monoolefins by Homogeneous Catalysts.* Oil & Gas Science and Technology - Rev. IFP, 2009. **64**(6): p. 649-667.

64. Speiser, F., P. Braunstein, and L. Saussine, *Catalytic Ethylene Dimerization and Oligomerization: Recent Developments with Nickel Complexes Containing P,N-Chelating Ligands.* Accounts of Chemical Research, 2005. **38**(10): p. 784-793.

65. McGuinness, D.S., *Olefin Oligomerization via Metallacycles: Dimerization, Trimerization, Tetramerization, and Beyond.* Chemical Reviews, 2010. **111**(3): p. 2321-2341.

66. Fan, L., et al., *Theoretical Study of Ethylene Oligomerization by an Organometallic Nickel Catalyst.* Inorganic Chemistry, 1996. **35**(13): p. 4003-4006.

67. Deng, L., et al., *The Role of Bulky Substituents in Brookhart-Type Ni(II) Diimine Catalyzed Olefin Polymerization: A Combined Density Functional Theory and Molecular Mechanics Study.* Journal of the American Chemical Society, 1997. **119**(26): p. 6177-6186.

68. Johnson, L.K., C.M. Killian, and M. Brookhart, *New Pd(II)- and Ni(II)-Based Catalysts for Polymerization of Ethylene and .alpha.-Olefins.* Journal of the American Chemical Society, 1995. **117**(23): p. 6414-6415.

69. Helldörfer, M., W. Milius, and H.G. Alt, *The influence of halogen substituents at the ligand framework of (α-diimine)nickel(II) catalyst precursors on their behavior in ethylene oligomerization and polymerization.* Journal of Molecular Catalysis A: Chemical, 2003. **197**(1): p. 1-13.

70. Gates, D.P., et al., *Synthesis of Branched Polyethylene Using (α-Diimine)nickel(II) Catalysts: Influence of Temperature, Ethylene Pressure, and Ligand Structure on Polymer Properties.* Macromolecules, 2000. **33**(7): p. 2320-2334.

71. Britovsek, G.J.P., et al., *Ethylene Oligomerization beyond Schulz–Flory Distributions.* ACS Catalysis, 2015. **5**(11): p. 6922-6925.

72. Young, C.T., et al., *The Mathematics of Ethylene Oligomerisation and Polymerisation.* Topics in Catalysis, 2020.

73. Stockis, A. and R. Hoffmann, *Metallacyclopentanes and bisolefin complexes.* Journal of the American Chemical Society, 1980. **102**(9): p. 2952-2962.

74. Chappell, S.D. and D.J. Cole-Hamilton, *The preparation and properties of metallacyclic compounds of the transition elements.* Polyhedron, 1982. **1**(11): p. 739-777.

75. Buchwald, S.L. and R.B. Nielsen, *Group 4 metal complexes of benzynes, cycloalkynes, acyclic alkynes, and alkenes.* Chemical Reviews, 1988. **88**(7): p. 1047-1058.

76. Dixon, J.T., et al., *Advances in selective ethylene trimerisation – a critical overview.* Journal of Organometallic Chemistry, 2004. **689**(23): p. 3641-3668.

77. Bollmann, A., et al., *Ethylene Tetramerization: A New Route to Produce 1-Octene in Exceptionally High Selectivities.* Journal of the American Chemical Society, 2004. **126**(45): p. 14712-14713.

78. Robinson, R., D.S. McGuinness, and B.F. Yates, *The Mechanism of Ethylene Dimerization with the Ti(OR')4/AlR3 Catalytic System: DFT Studies Comparing Metallacycle and Cossee Proposals.* ACS Catalysis, 2013. **3**(12): p. 3006-3015.

79. Skupinska, J., *Oligomerization of .alpha.-olefins to higher oligomers.* Chemical Reviews, 1991. **91**(4): p. 613-648.

80. Sydora, O.L., *Selective Ethylene Oligomerization.* Organometallics, 2019. **38**(5): p. 997-1010.

81. Keim, W., *Nickel: An Element with Wide Application in Industrial Homogeneous Catalysis.* Angewandte Chemie International Edition in English, 1990. **29**(3): p. 235-244.

82. Ittel, S.D., L.K. Johnson, and M. Brookhart, *Late-Metal Catalysts for Ethylene Homo- and Copolymerization.* Chemical Reviews, 2000. **100**(4): p. 1169-1204.

83. Gibson, V.C. and S.K. Spitzmesser, *Advances in Non-Metallocene Olefin Polymerization Catalysis.* Chemical Reviews, 2003. **103**(1): p. 283-316.

84. Mecking, S., *Olefin Polymerization by Late Transition Metal Complexes—A Root of Ziegler Catalysts Gains New Ground.* Angewandte Chemie International Edition, 2001. **40**(3): p. 534-540.

85. Macchioni, A., *Ion Pairing in Transition-Metal Organometallic Chemistry.* Chemical Reviews, 2005. **105**(6): p. 2039-2074.

86. Chen, E.Y.-X. and T.J. Marks, *Cocatalysts for Metal-Catalyzed Olefin Polymerization: Activators, Activation Processes, and Structure–Activity Relationships.* Chemical Reviews, 2000. **100**(4): p. 1391-1434.

87. Killian, C.M., L.K. Johnson, and M. Brookhart, *Preparation of Linear α-Olefins Using Cationic Nickel(II) α-Diimine Catalysts.* Organometallics, 1997. **16**(10): p. 2005-2007.

88. Britovsek, G.J.P., V.C. Gibson, and D.F. Wass, *The Search for New-Generation Olefin Polymerization Catalysts: Life beyond Metallocenes.* Angewandte Chemie International Edition, 1999. **38**(4): p. 428-447.

89. Bryliakov, K.P. and A.A. Antonov, *Recent progress of transition metal based catalysts for the selective dimerization of ethylene.* Journal of Organometallic Chemistry, 2018. **867**: p. 55-61.

90. Svejda, S.A. and M. Brookhart, *Ethylene Oligomerization and Propylene Dimerization Using Cationic (α-Diimine)nickel(II) Catalysts.* Organometallics, 1999. **18**(1): p. 65-74.

91. Keim, W., *Oligomerization of Ethylene to α-Olefins: Discovery and Development of the Shell Higher Olefin Process (SHOP).* Angewandte Chemie International Edition, 2013. **52**(48): p. 12492-12496.

92. Keim, W., et al., *Novel Coordination of (Benzoylmethylene)triphenylphosphorane in a Nickel Oligomerization Catalyst.* Angewandte Chemie International Edition in English, 1978. **17**(6): p. 466-467.

93. Kuhn, P., et al., *Structure–reactivity relationships in SHOP-type complexes: tunable catalysts for the oligomerisation and polymerisation of ethylene.* Dalton Transactions, 2007(5): p. 515-528.

94. Finiels, A., F. Fajula, and V. Hulea, *Nickel-based solid catalysts for ethylene oligomerization - a review.* Catalysis Science & Technology, 2014. **4**(8): p. 2412-2426.

95. Olivier-Bourbigou, H., et al., *Nickel Catalyzed Olefin Oligomerization and Dimerization.* Chemical Reviews, 2020. **120**(15): p. 7919-7983.

96. O'Connor, C.T. and M. Kojima, *Alkene oligomerization.* Catalysis Today, 1990. **6**(3): p. 329-349.

97. Corma, A. and S. Iborra, *Oligomerization of Alkenes.* Catalysts for Fine Chemical Synthesis, 2006: p. 125-140.

98. Kustov, L.M., V.Y. Borovkov, and V.B. Kazansky, *Study of Ethylene Oligomerization on Bronsted and lewis Acidic Sites of Zeolites Using Diffuse Reflectance IR Spectroscopy*, in *Studies in Surface Science and Catalysis*, P.A. Jacobs, et al., Editors. 1984, Elsevier. p. 241-247.

99. Kofke, T.J.G. and R.J. Gorte, *A temperature-programmed desorption study of olefin oligomerization in H·ZSM-5.* Journal of Catalysis, 1989. **115**(1): p. 233-243.

100. Sanati, M., C. Hornell, and S.G. Jaras, *The oligomerization of alkenes by heterogeneous catalysts*, in *Catalysis: Volume 14*. 1999, The Royal Society of Chemistry. p. 236-288.

101. Peuckert, M. and W. Keim, *Heterogenization of homogeneous nickel-based ethylene oligomerization catalysts.* Journal of Molecular Catalysis, 1984. **22**(3): p. 289-295.

102. Angelescu, E., et al., *Ethylene selective dimerization on polymer complex catalyst of Ni(4,4'-bipyridine)Cl2 coactivated with AlCl(C2H5)2.* Journal of Molecular Catalysis A: Chemical, 2004. **219**(1): p. 13-19.

103. Rossetto, E., et al., *Ethylene oligomerization using nickel-β-diimine hybrid xerogels produced by the sol–gel process.* Applied Catalysis A: General, 2013. **454**: p. 152-159.

104. Rossetto, E., et al., *Heterogeneous complexes of nickel MCM-41 with β-diimine ligands: Applications in olefin oligomerization.* Journal of Catalysis, 2015. **323**: p. 45-54.

105. Li, Z., et al., *Sintering-Resistant Single-Site Nickel Catalyst Supported by Metal–Organic Framework.* Journal of the American Chemical Society, 2016. **138**(6): p. 1977-1982.

106. Metzger, E.D., et al., *Highly Selective Heterogeneous Ethylene Dimerization with a Scalable and Chemically Robust MOF Catalyst.* ACS Sustainable Chemistry & Engineering, 2019. **7**(7): p. 6654-6661.

107. Metzger, E.D., et al., *Mechanism of Single-Site Molecule-Like Catalytic Ethylene Dimerization in Ni-MFU-4l.* Journal of the American Chemical Society, 2017. **139**(2): p. 757-762.

108. Mlinar, A.N., et al., *Selective Propene Oligomerization with Nickel(II)-Based Metal–Organic Frameworks.* ACS Catalysis, 2014. **4**(3): p. 717-721.

109. Morikawa, K., *Reactivity of lower hydrocarbons. VI. Activation of specific bonds in ethylene on catalytic surface.* Kogyo Kagaku Zasshi, 1938. **41**.

110. Sohn, J.R., W.C. Park, and D.C. Shin, *Characterization of nickel sulfate supported on SiO2 for ethylene dimerization and promoting effect of Al2O3 on catalytic activity.* Journal of Molecular Catalysis A: Chemical, 2006. **256**(1): p. 156-163.

111. Hartmann, M., A. Pöppl, and L. Kevan, *Ethylene dimerization in nickel containing MCM-41 and AlMCM-41 studied by electron spin resonance and gas chromatography*, in *Studies in Surface Science and Catalysis*, J.W. Hightower, et al., Editors. 1996, Elsevier. p. 801-809.

112. Heveling, J., A. van der Beek, and M. de Pender, *Oligomerization of ethene over nickel-exchanged zeolite y into a diesel-range product.* Applied Catalysis, 1988. **42**(2): p. 325-336.

113. Lallemand, M., et al., *Ni-MCM-36 and Ni-MCM-22 catalysts for the ethylene oligomerization*, in *Studies in Surface Science and Catalysis*, A. Gédéon, P. Massiani, and F. Babonneau, Editors. 2008, Elsevier. p. 1139-1142.

114. Martínez, A., et al., *New bifunctional Ni–H-Beta catalysts for the heterogeneous oligomerization of ethylene.* Applied Catalysis A: General, 2013. **467**: p. 509-518.

115. Lacarriere, A., et al., *Distillate-Range Products from Non-Oil-Based Sources by Catalytic Cascade Reactions.* ChemSusChem, 2012. **5**(9): p. 1787-1792.

116. Sohn, J.R., W.C. Park, and S.-E. Park, *Characterization of Nickel Sulfate Supported on SiO2–Al2O3 for Ethylene Dimerization and Its Relationship to Acidic Properties.* Catalysis Letters, 2002. **81**(3): p. 259-264.

117. Ng, F.T.T. and D.C. Creaser, *Ethylene dimerization over modified nickel exchanged Y-zeolite.* Applied Catalysis A: General, 1994. **119**(2): p. 327-339.

118. Lallemand, M., et al., *Nature of the Active Sites in Ethylene Oligomerization Catalyzed by Ni-Containing Molecular Sieves: Chemical and IR Spectral Investigation.* The Journal of Physical Chemistry C, 2009. **113**(47): p. 20360-20364.

119. Agirrezabal-Telleria, I. and E. Iglesia, *Stabilization of active, selective, and regenerable Ni-based dimerization catalysts by condensation of ethene withinordered mesopores.* Journal of Catalysis, 2017. **352**: p. 505-514.

120. Moussa, S., et al., *Heterogeneous oligomerization of ethylene to liquids on bifunctional Ni-based catalysts: The influence of support properties on nickel speciation and catalytic performance.* Catalysis Today, 2016. **277, Part 1**: p. 78-88.

121. Moussa, S., et al., *Nature of Active Nickel Sites and Initiation Mechanism for Ethylene Oligomerization on Heterogeneous Ni-beta Catalysts.* ACS Catalysis, 2018. **8**(5): p. 3903-3912.

122. Brogaard, R.Y. and U. Olsbye, *Ethene Oligomerization in Ni-Containing Zeolites: Theoretical Discrimination of Reaction Mechanisms.* ACS Catalysis, 2016: p. 1205-1214.

123. Toch, K., J.W. Thybaut, and G.B. Marin, *Ethene oligomerization on Ni-SiO2-Al2O3: Experimental investigation and Single-Event MicroKinetic modeling.* Applied Catalysis A: General, 2015. **489**: p. 292-304.

124. Andrei, R.D., et al., *Heterogeneous oligomerization of ethylene over highly active and stable Ni-AlSBA-15 mesoporous catalysts.* Journal of Catalysis, 2015. **323**: p. 76-84.

125. Ehrmaier, A., et al., *Dimerization of Linear Butenes on Zeolite-Supported Ni2+.* ACS Catalysis, 2019. **9**(1): p. 315-324.

126. Joshi, R., et al., *Evidence for the Coordination–Insertion Mechanism of Ethene Dimerization at Nickel Cations Exchanged onto Beta Molecular Sieves.* ACS Catalysis, 2018. **8**(12): p. 11407-11422.

127. Brückner, A., et al., *The role of different Ni sites in supported nickel catalysts for butene dimerization under industry-like conditions.* Journal of Catalysis, 2009. **266**(1): p. 120-128.

128. Ng, F.T.T. and D.C. Creaser, *Ethylene Dimerization: Kinetics and Selectivity for 1-Butene*, in *Studies in Surface Science and Catalysis*, K.J. Smith and E.C. Sanford, Editors. 1992, Elsevier. p. 123-131.

129. Espinoza, R.L., et al., *Catalytic oligomerization of ethene over nickel-exchanged amorphous silica-alumina; effect of the reaction conditions and modelling of the reaction.* Applied Catalysis, 1987. **29**(1): p. 175-184.

130. Li, L., R.D. Palcheva, and K.-J. Jens, *Conversion of Ethene to Propene by a Dual Function NiSO4/Re2O7/γ-Al2O3 Catalyst.* Topics in Catalysis, 2013. **56**(9): p. 783-788.

131. Kaur, G., *Optimization of UiO-67 type Metal-Organic Frameworks for Catalysis*, in *Department of Chemistry*. 2020, University of Oslo.

132. Dent, A.J., et al., *B18: A core XAS spectroscopy beamline for Diamond.* Journal of Physics: Conference Series, 2009. **190**: p. 012039.

133. Ravel, B. and M. Newville, *ATHENA, ARTEMIS, HEPHAESTUS: data analysis for X-ray absorption spectroscopy using IFEFFIT.* Journal of Synchrotron Radiation, 2005. **12**(4): p. 537-541.

134. Abdala, P.M., et al., *Scientific opportunities for heterogeneous catalysis research at the SuperXAS and SNBL beam lines.* Chimia, 2012. **66**(9): p. 699-705.

135. Muller, O., et al., *Quick-EXAFS setup at the SuperXAS beamline for in situ X-ray absorption spectroscopy with 10 ms time resolution.* Journal of Synchrotron Radiation, 2016. **23**(1): p. 260-6.

136. Clark, A.H., et al., *ProQEXAFS: a highly optimized parallelized rapid processing software for QEXAFS data.* Journal of Synchrotron Radiation, 2020. **27**(Pt 2): p. 551-557.

137. Camp, C.H., *pyMCR: A python library for multivariate curve resolution analysis with alternating regression (MCR-AR).* Journal of Research of the National Institute of Standards and Technology, 2019. **124**.

138. Martini, A., et al., *PyFitit: the software for quantitative analysis of XANES spectra using machine-learning algorithms.* Computer Physics Communication, 2020. **250**: p. 107064.

139. Guda, S.A., et al., *Optimized Finite Difference Method for the Full-Potential XANES Simulations: Application to Molecular Adsorption Geometries in MOFs and Metal–Ligand Intersystem Crossing Transients.* Journal of Chemical Theory and Computation, 2015. **11**(9): p. 4512-4521.

140. Guda, A.A., et al., *Finite difference method accelerated with sparse solvers for structural analysis of the metal-organic complexes.* Journal of Physics: Conference Series, 2016. **712**: p. 012004.

141. Mihaylov, M. and K. Hadjiivanov, *FTIR Study of CO and NO Adsorption and Coadsorption on Ni-ZSM-5 and Ni/SiO_2.* Langmuir, 2002. **18**: p. 4376-4383.

142. Hadjiivanov, K., et al., *Characterization of Ni/SiO_2 Catalysts Prepared by Successive Deposition and Reduction of Ni^{2+} Ions.* J. Catal., 1999. **185**: p. 314-326.

143. Hadjiivanov, K., H. Knozinger, and M. Mihaylov, *FTIR Study of CO Adsorption on Ni-ZSM-5.* J. Phys. Chem. B, 2002. **106**: p. 2618-2624.

144. Ganjkhanlou, Y., et al., *Incorporation of Ni into HZSM-5 zeolites: Effects of zeolite morphology and incorporation procedure.* Microporous and Mesoporous Materials, 2016. **229**: p. 76-82.

145. Zecchina, A., et al., *Surface structures of oxides and halides and their relationships to catalytic properties.* Adv. Catal., 2001. **46**: p. 265-397.

146. Gopalakrishnan, S., et al., *Unravelling the structure and reactivity of supported Ni particles in Ni-CeZrO2 catalysts.* Applied Catalysis B: Environmental, 2013. **138–139**: p. 353-361.

147. Penkova, A., et al., *Effect of the Preparation Method on the State of Nickel Ions in BEA Zeolites. A Study by Fourier Transform Infrared Spectroscopy of Adsorbed CO and NO, Temperature-Programmed Reduction, and X-Ray Diffraction.* The Journal of Physical Chemistry C, 2007. **111**(24): p. 8623-8631.

148. Borfecchia, E., et al., *Revisiting the nature of Cu sites in the activated Cu-SSZ-13 catalyst for SCR reaction.* Chemical Science, 2015. **6**(1): p. 548-563.

149. Bartholomew, C.H., *Mechanisms of catalyst deactivation.* Applied Catalysis A: General, 2001. **212**(1): p. 17-60.

150. Wulfers, M.J. and R.F. Lobo, *Assessment of mass transfer limitations in oligomerization of butene at high pressure on H-beta.* Applied Catalysis A: General, 2015. **505**: p. 394-401.

151. Mlinar, A.N., et al., *Propene oligomerization over Ni-exchanged Na-X zeolites.* Journal of Catalysis, 2012. **296**(0): p. 156-164.

152. Mlinar, A.N., et al., *Selective Propene Oligomerization with Nickel(II)-Based Metal–Organic Frameworks.* ACS Catalysis, 2014: p. 717-721.

153. Reddy, J.K., et al., *Effect of morphology and particle size of ZSM-5 on catalytic performance for ethylene conversion and heptane cracking.* Journal of Catalysis, 2012. **289**(0): p. 53-61.

154. Lu Li, S.C., Elena Groppo, Einar Sagstuen, Silvia Bordiga, Unni Olsbye, Klaus-Joachim Jens, *Characterization of the $NiSO_4$ site on a $NiSO_4$-ReOx/γ-Al_2O_3 catalyst for tandem conversion of ethylene to propylene.* Catalysis Science & Technology, 2016. **Manuscript submitted for publication**.

155. Agapie, T., J.A. Labinger, and J.E. Bercaw, *Mechanistic Studies of Olefin and Alkyne Trimerization with Chromium Catalysts: Deuterium Labeling and Studies of Regiochemistry Using a Model Chromacyclopentane Complex.* Journal of the American Chemical Society, 2007. **129**(46): p. 14281-14295.

156. Suttil, J.A. and D.S. McGuinness, *Mechanism of Ethylene Dimerization Catalyzed by Ti(OR')4/AlR3.* Organometallics, 2012. **31**(19): p. 7004-7010.

157. Kaur, G., et al., *Controlling the Synthesis of Metal–Organic Framework UiO-67 by Tuning Its Kinetic Driving Force.* Crystal Growth & Design, 2019. **19**(8): p. 4246-4251.

158. Shearer, G.C., et al., *Defect Engineering: Tuning the Porosity and Composition of the Metal–Organic Framework UiO-66 via Modulated Synthesis.* Chemistry of Materials, 2016. **28**(11): p. 3749-3761.

159. Shearer, G.C., et al., *Tuned to Perfection: Ironing Out the Defects in Metal–Organic Framework UiO-66.* Chemistry of Materials, 2014. **26**(14): p. 4068-4071.

160. Shearer, G.C., et al., *In Situ Infrared Spectroscopic and Gravimetric Characterisation of the Solvent Removal and Dehydroxylation of the Metal Organic Frameworks UiO-66 and UiO-67.* Topics in Catalysis, 2013. **56**(9): p. 770-782.

161. Øien, S., et al., *Detailed Structure Analysis of Atomic Positions and Defects in Zirconium Metal–Organic Frameworks.* Crystal Growth & Design, 2014. **14**(11): p. 5370-5372.

162. Mondloch, J.E., et al., *Vapor-Phase Metalation by Atomic Layer Deposition in a Metal–Organic Framework.* Journal of the American Chemical Society, 2013. **135**(28): p. 10294-10297.

163. Žunkovič, E., et al., *Structural study of Ni- or Mg-based complexes incorporated within UiO-66-NH_2 framework and their impact on hydrogen sorption properties.* Journal of Solid State Chemistry, 2015. **225**: p. 209-215.

164. Gonzalez, M.I., et al., *Single-Crystal-to-Single-Crystal Metalation of a Metal–Organic Framework: A Route toward Structurally Well-Defined Catalysts.* Inorganic Chemistry, 2015. **54**(6): p. 2995-3005.

165. Gutterød, E.S., et al., *Hydrogenation of CO_2 to Methanol by Pt Nanoparticles Encapsulated in UiO-67: Deciphering the Role of the Metal–Organic Framework.* Journal of the American Chemical Society, 2020. **142**(2): p. 999-1009.

166. Downie, T.C., et al., *A three-dimensional study of the crystal structure of nickel acetate tetrahydrate.* Acta Crystallographica Section B, 1971. **27**(3): p. 706-712.

167. Chen, L., et al., *One-step encapsulation of Pd nanoparticles in MOFs via a temperature control program.* Journal of Materials Chemistry A, 2015. **3**(29): p. 15259-15264.

168. Gutterød, E.S., et al., *Influence of Defects and H2O on the Hydrogenation of CO2 to Methanol over Pt Nanoparticles in UiO-67 Metal–Organic Framework.* Journal of the American Chemical Society, 2020. **142**(40): p. 17105-17118.

169. Kandiah, M., et al., *Post-synthetic modification of the metal–organic framework compound UiO-66.* Journal of Materials Chemistry, 2010. **20**(44): p. 9848-9851.

170. Larabi, C. and E.A. Quadrelli, *Titration of Zr3(μ-OH) Hydroxy Groups at the Cornerstones of Bulk MOF UiO-67, [Zr6O4(OH)4(biphenyldicarboxylate)6], and Their Reaction with [AuMe(PMe3)].* European Journal of Inorganic Chemistry, 2012. **2012**(18): p. 3014-3022.

171. Li, Z., et al., *Size effect of the active sites in UiO-66-supported nickel catalysts synthesized via atomic layer deposition for ethylene hydrogenation.* Inorganic Chemistry Frontiers, 2017. **4**(5): p. 820-824.

172. Bordiga, S., et al., *Low temperature CO adsorption on Na-ZSM-5 zeolites: An FTIR investigation.* Journal of Catalysis, 1992. **137**(1): p. 179-185.

173. Chavan, S., et al., *Response of CPO-27-Ni towards CO, N_2 and C_2H_4.* Physical Chemistry Chemical Physics, 2009. **11**(42): p. 9811-9822.

174. Sadykov, V.A., et al., *Ni-loaded nanocrystalline ceria-zirconia solid solutions prepared via modified Pechini route as stable to coking catalysts of CH_4 dry reforming.* Open Chemistry, 2016. **14**(1): p. 363-376.

175. Bloch, E.D., et al., *Reversible CO Binding Enables Tunable CO/H_2 and CO/N_2 Separations in Metal-Organic Frameworks with Exposed Divalent Metal Cations.* Journal of the American Chemical Society, 2014. **136**(30): p. 10752-10761.

176. Chavan, S., et al., *CO Adsorption on CPO-27-Ni Coordination Polymer: Spectroscopic Features and Interaction Energy.* Journal of Physical Chemistry C, 2009. **113**(8): p. 3292-3299.

177. Hu, C., et al., *Temperature-programmed FT-IR study of the adsorption of CO and co-adsorption of CO and H_2 on $NiAl_2O_3$.* Journal of Molecular Catalysis A: Chemical, 1996. **110**(2): p. 163-169.

178. Peri, J.B., *Infrared Studies of Ni Held at Low Concentrations on Alumina Supports.* Journal of Catalysis, 1984. **86**(1): p. 84-94.

179. Tada, S., et al., *N_2O Pulse Titration of Ni/α-Al_2O_3 Catalysts: A New Technique Applicable to Nickel Surface-Area Determination of Nickel-Based Catalysts.* Journal of Physical Chemistry C, 2013. **117**(28): p. 14652-14658.

180. Abdel-Mageed, A.M., et al., *Highly Active and Stable Single-Atom Cu Catalysts Supported by a Metal–Organic Framework.* Journal of the American Chemical Society, 2019. **141**(13): p. 5201-5210.

181. Braglia, L., et al., *Exploring structure and reactivity of Cu sites in functionalized UiO-67 MOFs.* Catalysis Today, 2017. **283**: p. 89-103.

182. Henry, R., et al., *Ethene oligomerization on nickel microporous and mesoporous-supported catalysts: Investigation of the active sites.* Catalysis Today, 2018. **299**: p. 154-163.

183. Bernales, V., et al., *Computationally Guided Discovery of a Catalytic Cobalt-Decorated Metal–Organic Framework for Ethylene Dimerization.* The Journal of Physical Chemistry C, 2016. **120**(41): p. 23576-23583.

184. Gadalla, A.M. and H.-F. Yu, *Thermal behavior of some NiII and FeIII salts.* Thermochimica Acta, 1990. **164**: p. 21-36.

185. De Jesus, J.C., et al., *Thermal decomposition of nickel acetate tetrahydrate: an integrated study by TGA, QMS and XPS techniques.* Journal of Molecular Catalysis A: Chemical, 2005. **228**(1): p. 283-291.

186. Mishra, S.K. and S.B. Kanungo, *Thermal dehydration and decomposition of nickel chloride hydrate ($NiCl_2 \cdot xH_2O$).* Journal of thermal analysis, 1992. **38**(11): p. 2417-2436.

187. El-Mahalawy, A.M., *Structural and optical characteristics of nickel bis(acetylacetonate) thin films as a buffer layer for optoelectronic applications.* Materials Science in Semiconductor Processing, 2019. **100**: p. 145-158.

188. Nichio, N.N., et al., *Study of the decomposition of supported nickel acetylacetonate by thermal techniques.* Thermochimica Acta, 2003. **400**(1): p. 101-107.

189. Giordanino, F., et al., *Characterization of Cu-exchanged SSZ-13: a comparative FTIR, UV-Vis, and EPR study with Cu-ZSM-5 and Cu-β with similar Si/Al and Cu/Al ratios.* Dalton Transactions, 2013. **42**(35): p. 12741-12761.

190. Øien-Ødegaard, S., et al., *UiO-67-type Metal–Organic Frameworks with Enhanced Water Stability and Methane Adsorption Capacity.* Inorganic Chemistry, 2016. **55**(5): p. 1986-1991.

7 Appendix

7.1 Additional data

7.1.1 Ni-aluminosilicates

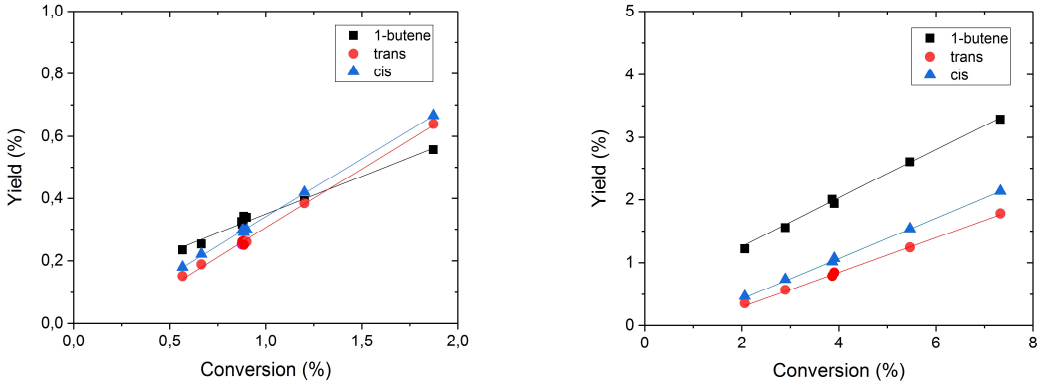

Figure A 1: Yield (%) (square: 1-butene, circle: trans-2-butene and up triangle: cis-2- butene) as a function of conversion at 4 bar ethene (left) and 18 bar ethene (right). Reaction conditions: m_{cat} = 0.200 g, contact time: 4–20 mg_{cat}·min·mL^{-1} at STP, T = 150 ◦C and P_{total} = 30 bar where P_{ethene} = 4 or 18 bar and P_{inert} = 26 or 12 bar.

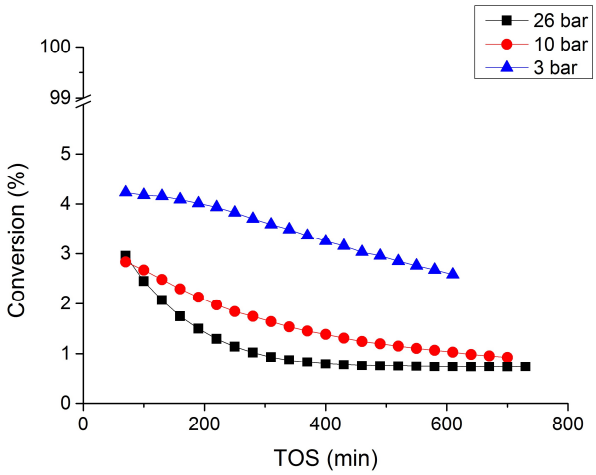

Figure A 2: Conversion as a function of TOS at different P_{ethene} for Ni-CPO-27 catalyst. Reaction conditions: 0.100 g catalyst, contact time: 3.4 mg_{cat}·min·mL^{-1} at STP, 30 bar total pressure, T = 180 °C.

7.1.2 Ni-MOFs

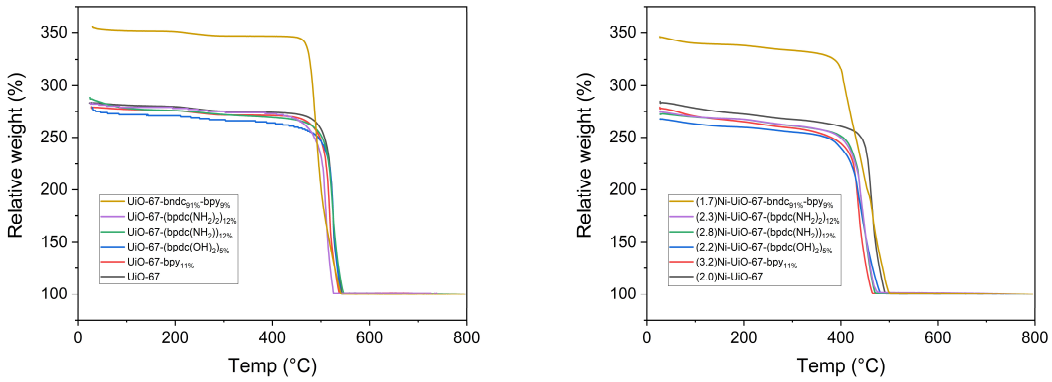

Figure A 3: TG of parent mixed-linker MOFs (left) and $Ni(OAc)_2{\cdot}4H_2O$ functionalized mixed-linker MOF catalysts. The samples were heated from 25 to 800 °C, 5 °C/min in a flow of synthetic air.

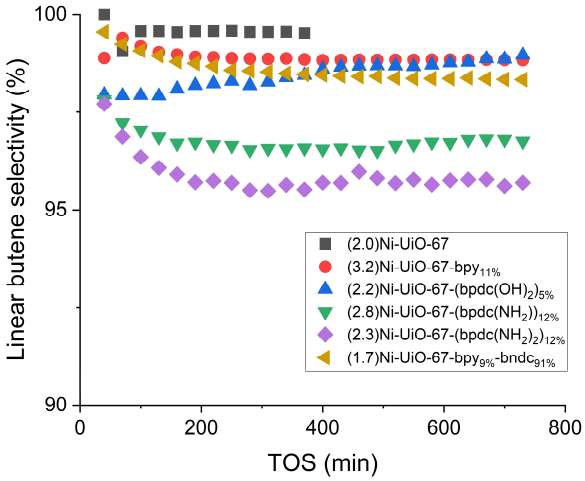

Figure A 4: Linear butene selectivity vs TOS for $Ni(OAc)_2{\cdot}4H_2O$ functionalized mixed-linker MOF catalysts.

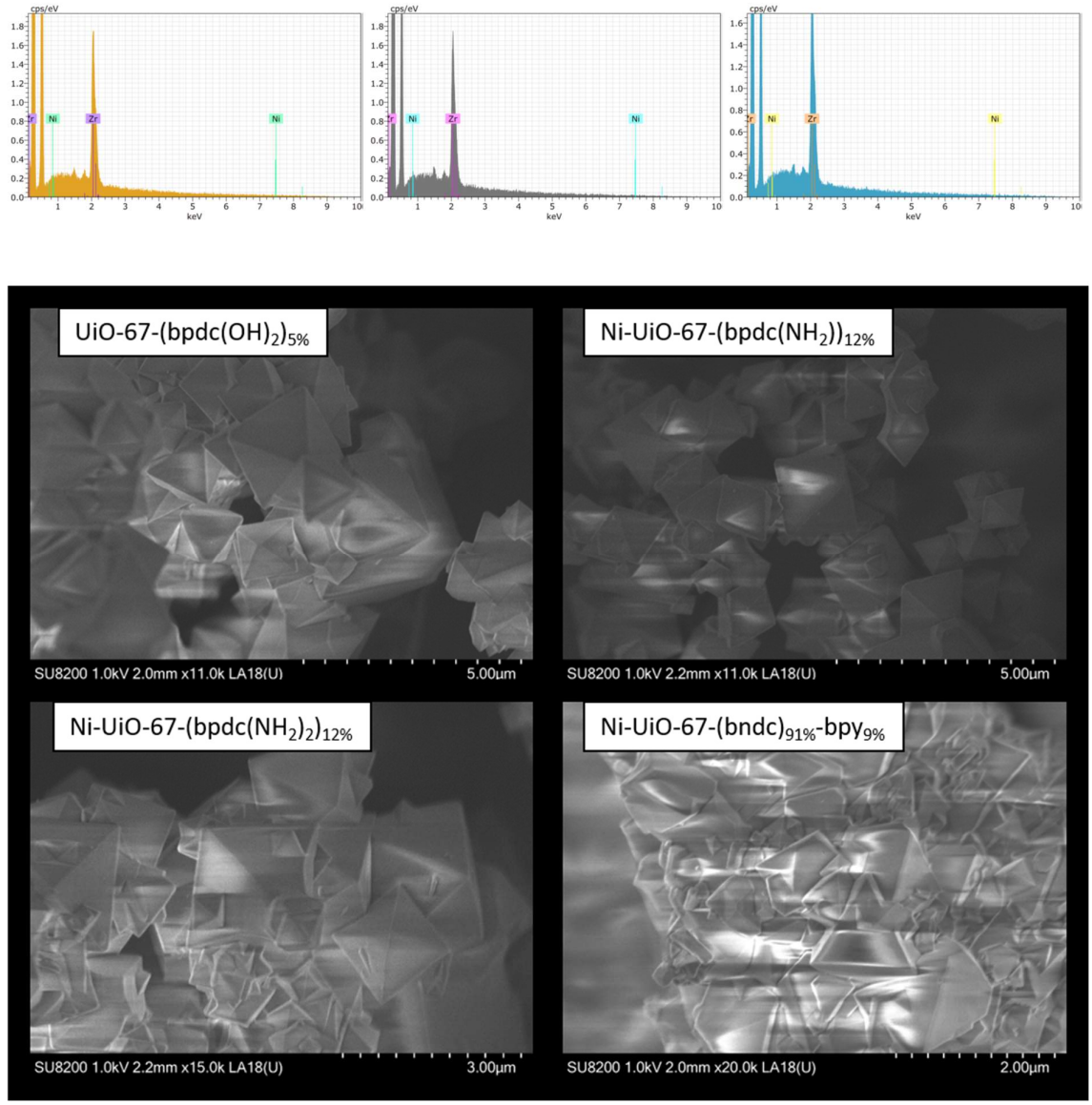

Figure A 5: EDS measurements (top) from left to right for (2.8)Ni-UiO-67-(bpdc(NH_2))$_{12\%}$, (2.3)Ni-UiO-67-(bpdc(NH_2)$_2$)$_{12\%}$ and (2.2)Ni-UiO-67-(bpdc(OH)$_2$)$_{5.1\%}$ and SEM images (bottom) of pristine $Ni(NO_3)_2{\cdot}6H_2O$ functionalized Ni-MOFs.

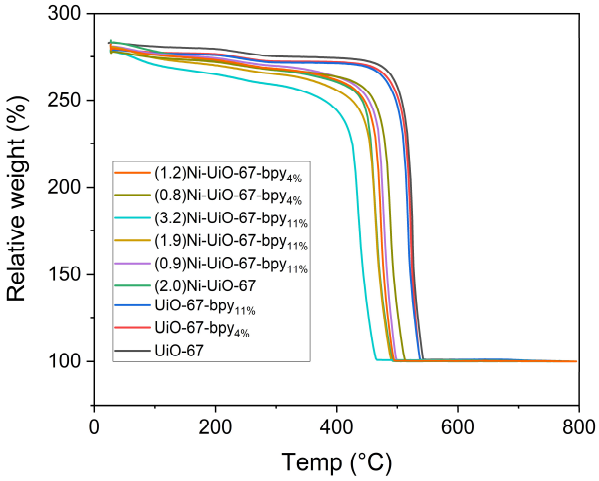

Figure A 6: TG curve of parent and $Ni(OAc)_2{\cdot}4H_2O$ functionalized MOF catalysts. The samples were heated from 25 to 800 °C, 5 °C/min in a flow of synthetic air.

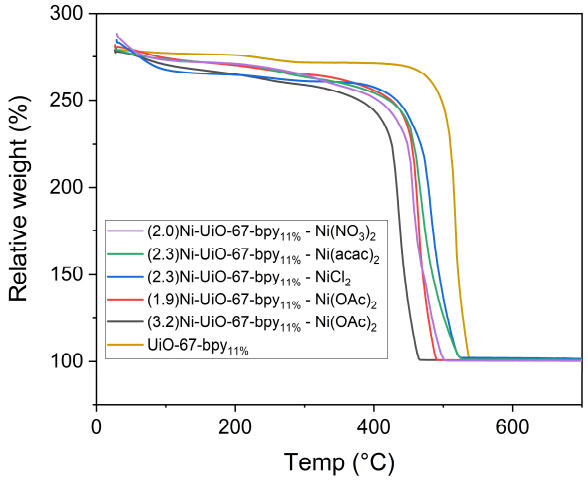

Figure A 7: TG curve of parent and MOF catalysts functionalized with various Ni precursors. The samples were heated from 25 to 800 °C, 5 °C/min in a flow of synthetic air.

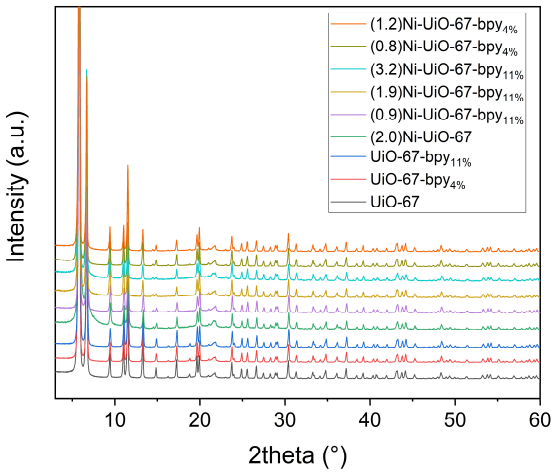

Figure A 8: XRD of parent and $Ni(OAc)_2{\cdot}4H_2O$ functionalized MOF catalysts.

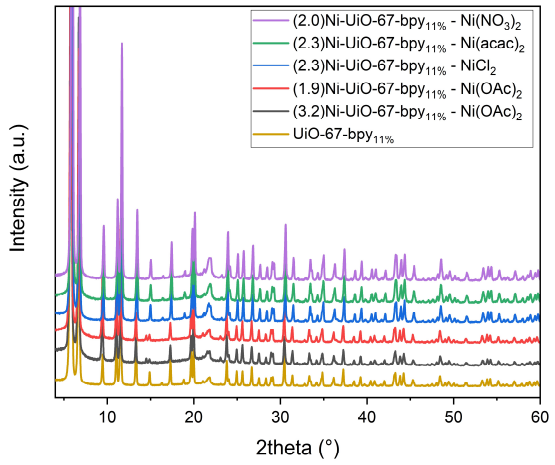

Figure A 9: XRD of parent MOF and catalysts functionalized with different Ni precursors.

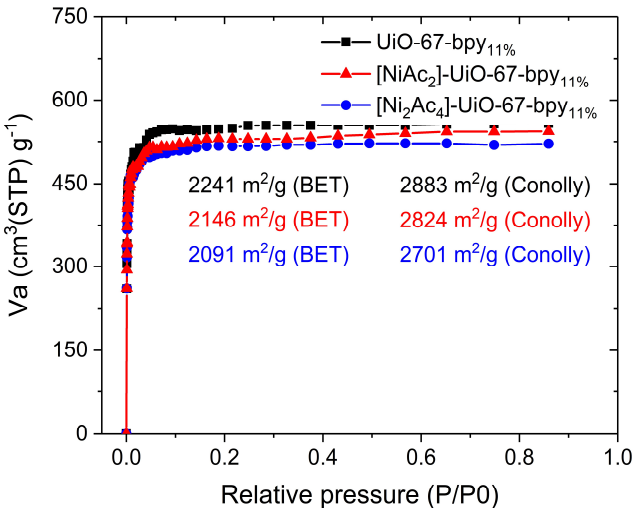

Figure A 10: Simulated isotherms for UiO-67, $[Ni(OAc)_2]$-UiO-67-$bpy_{11\%}$ (Ni:bpy mol = 1) and $[Ni2(OAc)_4]$-UiO-67-$bpy_{11\%}$ (Ni:bpy mol = 2).

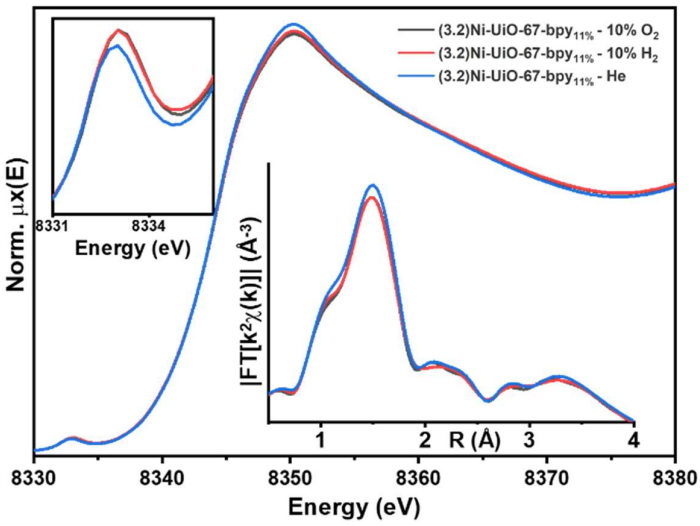

Figure A 11: Ni K-edge XANES of (3.2)Ni-UiO-67-$bpy_{11\%}$ after activation at 300 °C for 360 min under different atmosphere. The bottom inset shows the corresponding phase-uncorrected FT-EXAFS spectra, obtained transforming the k^2-weighted $k^2\chi(k)$ curves in the 2.4-14.0 $Å^{-1}$ range.

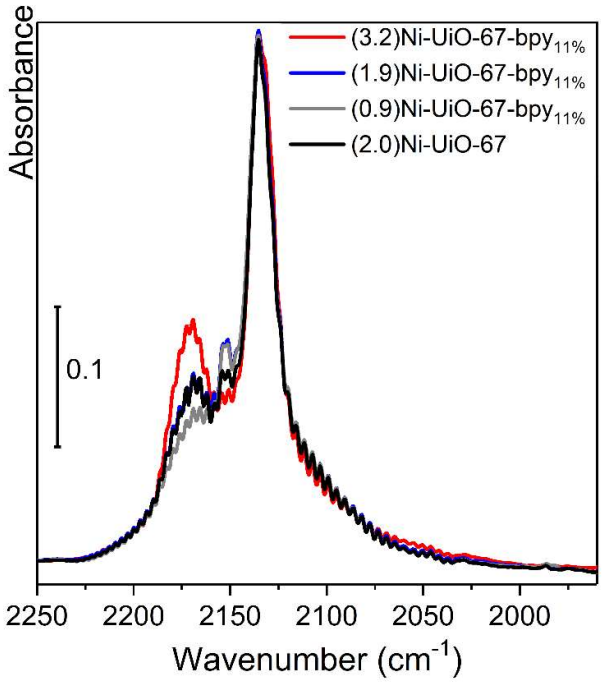

Figure A 12: CO FTIR spectra at LNT of UiO-67-bpy$_{11\%}$ samples with different Ni(OAc)$_2$ concentration and (2.0)Ni-UiO-67 after activation for 6h at 300 °C in 10% O_2 and testing under reaction conditions for 12h, except (2.0)Ni-UiO-67 which was tested for 6h. The plotted spectra represent the maximum coverage of CO after the subtraction of the spectra at minimum coverage (θ_{min}). The spectra are then normalized with respect to the peak at 2135 cm–1 (physisorbed CO), which considers not only the total amount of CO that is dosed but also the pellet thickness.

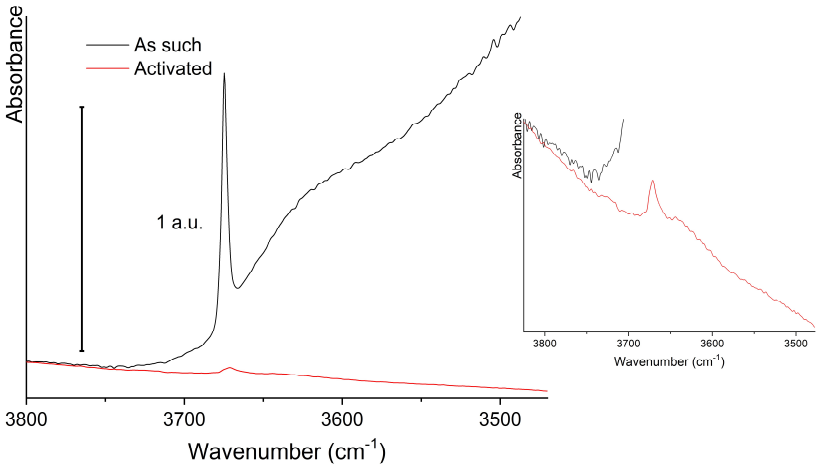

Figure A 13: FTIR spectra collected prior to and after thermal pretreatment, in the 4000-3500 cm^{-1} range, for *ex situ* activated (1.9)Ni-UiO-67-$bpy_{11\%}$ (inset: zoom on the activated catalyst).

Table A 1: Fractional distribution of butenes in the effluent in 1-butene isomerization experiments over UiO-67-$bpy_{11\%}$. By-pass measurement is included as 0 min TOS to show the presence of trans and cis-2-butene impurities in the feed. Reaction conditions: 0.150 mg UiO-67-$bpy_{11\%}$, contact time: 5.0 mg·min/mL at STP, temperature = 250 °C, 1 bar total pressure where $P_{1\text{-butene}}$ = 0.03 bar.

TOS (min)	1-butene	Trans-2-butene	Cis-2-butene
0	0.996	0.002	0.002
60	0.993	0.004	0.003
120	0.996	0.002	0.002
180	0.995	0.003	0.002

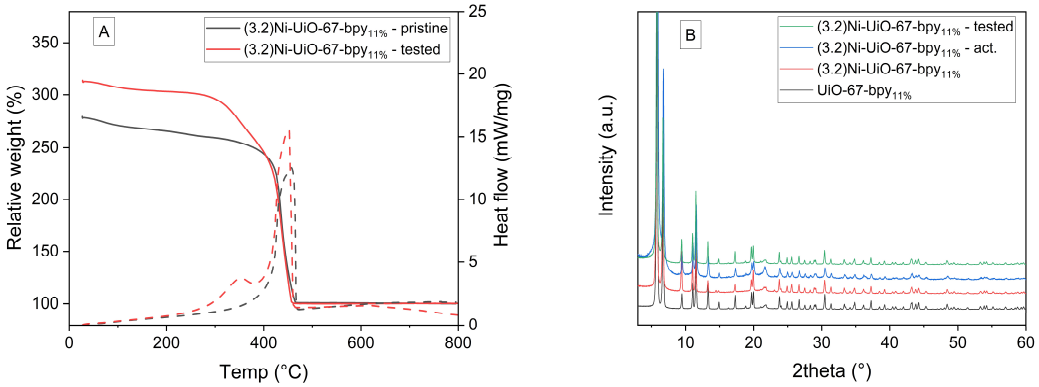

Figure A 14: A) TG curve (solid lines) and DSC (dashed lines) of the pristine and tested (3.2)Ni-UiO-67-$bpy_{11\%}$. The samples were heated from 25 to 800 °C, 5 °C/min in a flow of synthetic air (25 mL/min). B) XRD pattern of pristine, activated and tested (3.2)Ni-UiO-67-$bpy_{11\%}$

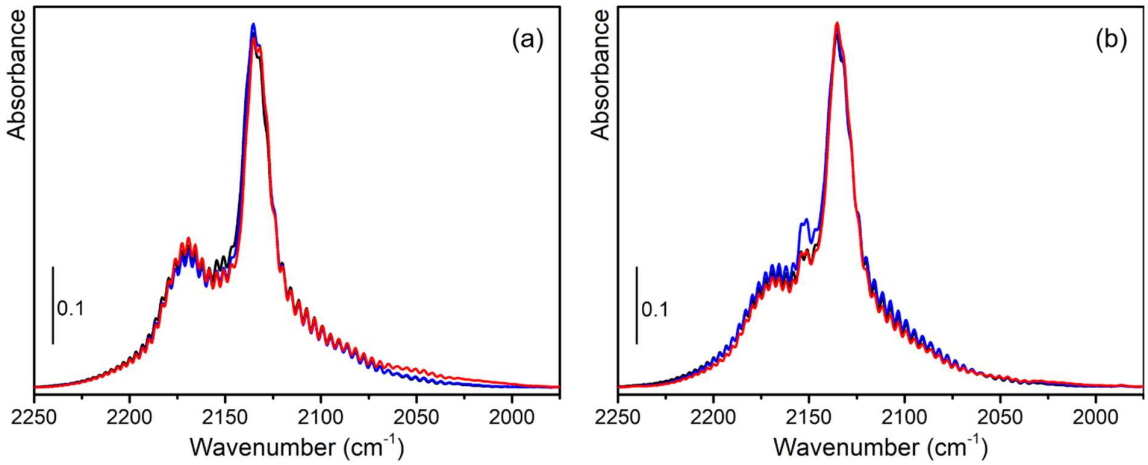

Figure A 15: CO FTIR spectra, in the 2252-1950 cm–1 range, for samples (3.2)Ni-UiO-67-bpy$_{11\%}$ (a) and (1.9)Ni-UiO-67-bpy$_{11\%}$ (b). The activated, 100 min tested, and 720 min tested catalysts are represented by black, blue, and red curves, respectively. The plotted spectra represent the maximum coverage of CO after the subtraction of the spectra at minimum coverage (θ_{min}). It is possible to notice that 720 min tested (3.2)Ni-UiO-67-bpy$_{11\%}$ display the typical feature for CO chemisorbed on metallic Ni nanoparticles (centered at 2050 cm–1), even if it has a much lower intensity than the one relative to Ni^{2+} species. The spectra are then normalized with respect to the peak at 2135 cm–1 (physisorbed CO), which considers not only the total amount of CO that is dosed but also the pellet thickness.

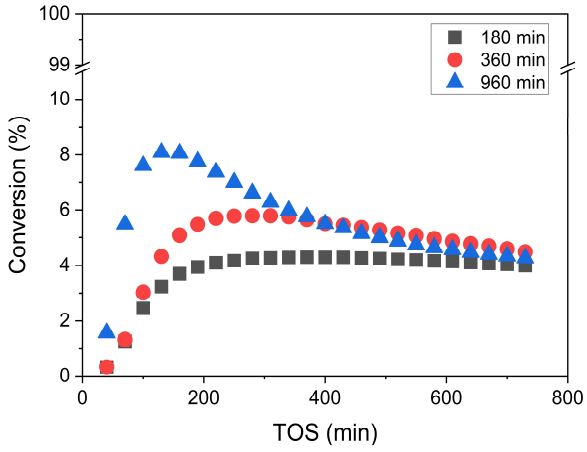

Figure A 16: Ethene conversion vs TOS for (3.2)Ni-UiO-67-bpy$_{11\%}$ after various activation duration. Activation conditions: 3 °C/min up to 300 °C, 180, 360 and 960 min @ 300 °C in 10 % O_2 in He (5 mL/min O2, 45 mL/min He). Reaction conditions: m_{cat} = 0.150 g, 30 bar total pressure where P_{ethene} = 26 bar and P_{inert} = 4 bar, temperature = 250 °C and contact time = 5.0 mg_{cat}·min·mL^{-1} at STP.

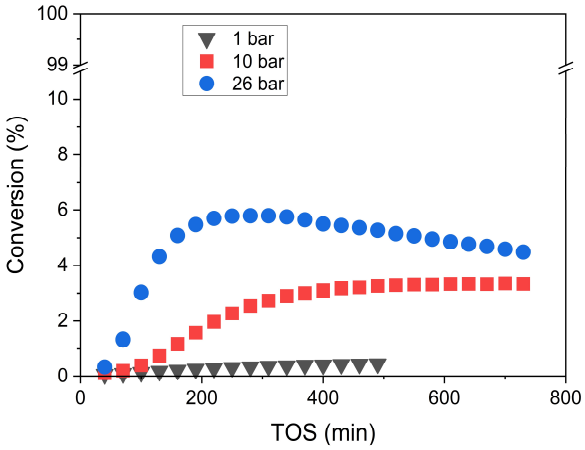

Figure A 17: Ethene conversion vs TOS for (3.2)Ni-UiO-67-bpy$_{11\%}$ under atmospheric conditions (1 bar ethene) and 10 bar and 26 bar ethene where P_{total} = 30 bar. Reaction conditions: m_{cat} = 0.150 g, T = 250 °C and contact time = 5.0 and 15 mg·min·mL^{-1} at STP at P_{total} = 30 bar and P_{total} = 1 bar, respectively.

Table A 2: Coordination number (*N*), average distance (<*R*>), and Debye-Waller parameter (σ^2) obtained from the first-shell EXAFS analysis.

	N	**<*R*>**	**σ^2**
red	5.8(5)	2.03(1)	0.009(2)
blue	3.9(3)	1.98(1)	0.011(1)
green	5.6(7)	1.97(2)	0.014(3)

Papers I - III

I

Catalysis Today 299 (2018) 154–163

Contents lists available at ScienceDirect

Catalysis Today

journal homepage: www.elsevier.com/locate/cattod

Ethene oligomerization on nickel microporous and mesoporous-supported catalysts: Investigation of the active sites

Reynald Henry[a], Mustafa Komurcu[a], Yadolah Ganjkhanlou[c], Rasmus Y. Brogaard[a], Li Lu[b], Klaus-Joachim Jens[b], Gloria Berlier[c,*], Unni Olsbye[a,*]

[a] Department of Chemistry, University of Oslo, P.O. Box 1033, Oslo 0315, Norway
[b] Faculty of Technology, University College of Southeast Norway, P.O. Box 203, Porsgrunn 3901, Norway
[c] University of Turin, Department of Chemistry, Via P. Giuria 7, Turin 10125, Italy

ARTICLE INFO

Keywords:
Ethene oligomerization
Nickel-based catalysts
Low temperature FTIR-CO
Beta zeolite
Active nickel sites

ABSTRACT

Nickel-containing mesoporous (using Al_2O_3 or SiO_2-Al_2O_3 support) and microporous (using nano- or micro-crystalline Beta zeolite support) catalysts were prepared by ion exchange and characterized by XRD, SEM, N_2-adsorption, MP-AES and FTIR. The samples were subjected to testing as ethene oligomerization catalysts at T = 120 °C, P_{total} = 29 bar, P_{ethene} = 11.6–25.1 bar. All catalysts were active for ethene oligomerization, and linear butenes were the main gaseous products. However, catalyst deactivation due to retained long-chain alkenes was observed. Ethene partial pressure variation experiments showed that the reaction order in ethene for butene formation was 1.5–1.7 for the mesoporous, and 2.0 for the microporous catalysts. Contact time variation experiments carried out with the microporous catalysts at P_{ethene} = 18 bar showed that product selectivity was independent of ethene conversion, and suggested that 1-butene and 2-butenes are primary products. This result is consistent with the Cossee-Arlman mechanism. The nature of the active sites was investigated with FTIR spectroscopy with CO as probe molecule. The results point to Ni^{2+}-counterions as the preeminent active sites, while we suggest that Ni-sites grafted on silanol groups and NiO particles are spectators.

1. Introduction

The world is currently seeing a gradual shift from oil as the dominating source for transportation fuels and chemicals production to other alternative sources, such as natural gas, biomass and coal [1]. Traditionally, naphtha reforming has been the major source of low carbon olefins (C_2–C_6 alkenes), but the recent shift towards ethane cracking favors ethene production over the C_3–C_6 fraction. In addition, the demand for propene and butenes has increased more rapidly than the demand for ethene [2]. This led to a growing interest in selective oligomerization of ethene to C_4–C_8 products [3,4]. Ethene is among the most important base chemicals and has a worldwide production capacity over 130 million tons [2]. It is raw material for a wide range of products; reactions of ethene include oxidation, oligomerization and polymerization [4]. The commercial processes for ethene oligomerization utilize homogeneous catalysts (transition metal catalysts in organic solvents [5]). In these processes, a co-catalyst such as $Al(C_2H_5)_3$ is required to start the catalytic cycle. The mechanism of alkene oligomerization with homogeneous catalysts has been reviewed by McGuinness [5] and the two widely recognized mechanisms, metallacycle and Cossee-Arlman, are shown in Scheme 1.

In recent years, significant effort has been made to develop heterogeneous catalysts for the ethene oligomerization reaction, as they potentially offer a more environmentally friendly alternative to the homogeneously catalyzed process [4].

Nickel containing inorganic porous materials such as amorphous silica-alumina [6,7], ordered mesostructured materials [8–10] and Ni-zeolites [11–13] are regarded as the most promising candidates among the reported catalysts. Notably, all these catalysts are active without the use of a co-catalyst. The mesoporous catalysts are reported to perform better than microporous catalysts, which typically suffer from rapid deactivation due to blocking of micropores by alkenes formed during the reaction [12]. An exception is the nanocrystalline Ni-H-Beta zeolite, investigated at 120 °C and P_{ethene} = 26 bar, which was resistant to deactivation. The Ni-H-Beta catalysts were prepared by ion exchange of protons with Ni^{2+}. For these catalysts, the activity was reported to increase linearly with increasing Ni loading until almost all of the acid sites were exchanged. Furthermore, for catalysts with Ni content ≤ 2% (i.e. with significant amounts of Brønsted acid sites remaining), approximately 93% selectivity towards even numbered alkenes with

* Corresponding authors.
E-mail addresses: gloria.berlier@unito.it (G. Berlier), unni.olsbye@kjemi.uio.no (U. Olsbye).

http://dx.doi.org/10.1016/j.cattod.2017.04.029
Received 5 December 2016; Received in revised form 28 February 2017; Accepted 13 April 2017
Available online 28 April 2017
0920-5861/

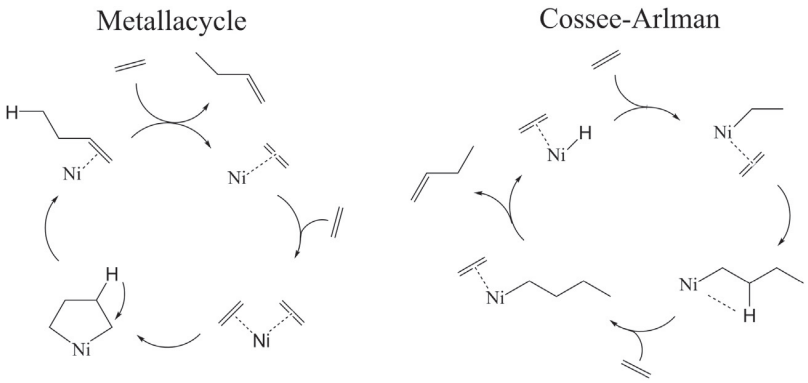

Scheme 1. The two widely recognized reaction mechanism for the homogeneously catalyzed oligomerization of ethene.

Schulz-Flory type distribution was observed, suggesting that the acid sites have negligible activity for oligomerization under these conditions. However, the observed branching among the even numbered products was ascribed to the acid sites [13].

A detailed kinetic study of the ethene oligomerization reaction was recently published by Toch et al. [14] who investigated Ni-SiO_2-Al_2O_3 catalyst between 170 and 230 °C and P_{ethene} from 1.5 to 3.5 bar. They observed that the catalyst was resistant to deactivation during 8 h on stream and due to the absence of strong acid sites, they concluded the catalytic activity to be solely from the nickel ion sites. The catalyst showed a Schulz-Flory type product distribution with about 90% selectivity towards butenes, while thermodynamic distribution was observed among the linear butenes. By combining experimentally obtained data with single event microkinetic modelling, they concluded the Cossee-Arlman mechanism to be more likely than the metallacycle mechanism because of the Schulz-Flory product distribution, without excluding the metallacycle mechanism completely [14].

Recently, Brogaard and Olsbye utilized molecular modelling to investigate the reaction mechanism of ethene oligomerization catalyzed by Ni-SSZ-24 zeolite, as well as the formation of the active site. After comparing three possible catalytic cycles, they concluded the most probable reaction path to be the Cossee-Arlman mechanism and that the support could be involved in the active site formation [15].

The metallacycle mechanism has recently been proposed for ethene oligomerization by Andrei et al. over Ni-AlSBA-15. The authors suggested two types of mechanisms: the metallacycle mechanism for oligomerization of ethene and a second mechanism based on acid catalysis for isomerization of products. The Cossee-Arlman mechanism was concluded as unlikely because of the absence of co-catalysts in these reactions [16].

The aim of the current study was to compare the performance of Ni-based catalysts based on zeolite supports and dense, mesoporous supports, respectively, under similar reaction conditions. A further aim of the study was to characterize the active sites of zeolite-based catalysts by FTIR spectroscopy and elucidate mechanistic details of the ethene oligomerization reaction through contact time variation experiments.

2. Experimental

2.1. Catalyst preparation

Microcrystalline NH_4-Beta zeolite ((Si/Al) = 19) was obtained from Zeolyst (CP-814C). The NH_4-Beta sample was calcined at 550 °C for 6 h using a heating rate of 1.5 °C/min to obtain the protonated form. The resulting material is denoted H-Beta(m).

Nanocrystalline Na-Beta zeolite (Si/Al = 13) was obtained from PQ. The Na-Beta sample was calcined at 550 °C for 3 h using a heating rate of 1 °C/min (denoted Na-Beta(n)) before ion exchange. The catalyst was subjected to three consecutive ion exchanges with 1 M NH_4NO_3 at 70 °C for 2 h using a liquid to solid ratio of 20 cm^3/g, then dried overnight. The exchange was then followed by calcination at 550 °C for 8 h, using a heating rate of 5 °C/min to obtain the protonated form. The resulting material is denoted H-Beta(n).

The nickel ion exchanged zeolite samples were prepared as described by Martinez et al. [13]. The zeolite sample was subjected to four consecutive ion exchanges with intermediate drying steps at 100 °C. The exchanges were carried out with 0.1 M aqueous solution of Ni $(NO_3)_2$ at 70 °C for 4 h using a liquid-to-solid-ratio of 10 cm^3/g. Subsequently, the material was calcined at 550 °C for 3 h using a heating rate of 1 °C/min. The material obtained by ion exchange and calcination of H-Beta(m) is denoted Ni-H-Beta(m). The material obtained by ion exchange and calcination of Na-Beta(n) is denoted Ni-H(Na)-Beta(n)(2), while the material obtained by ion exchange and calcination of H-Beta(n) is denoted Ni-H-Beta(n) and Ni-H-Beta(n)(2) with 2 and 4 wt% Ni, respectively.

2 wt.% $NiSO_4$-SiO_2-Al_2O_3 and 2 wt.% $NiSO_4$-Al_2O_3 catalysts were prepared as previously described in detail by Lu et al. [17]. SiO_2-Al_2O_3 and γ-Al_2O_3 supports were impregnated with an aqueous solution of nickel sulfate ($NiSO_4$) followed by drying over night at 105 °C and calcination in air at 400 °C for 2 h.

2.2. Catalyst characterization

The phase identification of the zeolite samples was performed by X-ray powder diffraction (PXRD) measurements. A Bruker D8 Discover diffractometer was employed, using Cu K_α radiation (λ = 1.5406 Å). The textural properties of the samples were derived from N_2 adsorption isotherms, measured at −196 °C, using a BELSORP-mini II instrument. All samples were outgassed in vacuum for 1 h at 80 °C and 3 h at 300 °C, and then measured. The catalyst pore volumes and surface areas were determined using the t-plot and BET methods. Scanning electron microscopy (SEM) was performed by using a Hitachi SU8230 microscope; the characterization parameters are included in the images. Elemental analysis was performed on Agilent 4100 MP-AES instrument after dissolving the catalyst in 1 mL 15 wt% HF.

The nature of the active sites was investigated by FTIR spectroscopy. The experiments were carried out in transmission mode using a Nicolet 6700 FTIR spectrometer (Thermo Scientific) equipped with a mercury cadmium telluride (MCT) cryodetector working with 2 cm^{-1} resolution. Thin self-supporting wafers of each sample (H-Beta(m) and Ni-H-Beta(m)) were placed inside a flow IR cell designed to allow high temperature treatment under gas flow and ex-situ low-temperature IR measurements. Prior to adsorption experiments, samples were thermally treated in He flow (50 mL/min) up to 300 °C and left at this temperature for 3 h, in order to mimic the activation conditions used in the catalytic tests. In order to investigate the role of Ni sites in the oligomerization reaction, in one experiment Ni-H-Beta(m) sample was

Table 1
Textural properties and elemental composition for all catalysts.

	S_{BET} (m^2/g)	V_{micro} (cm^3/g)	V_{meso} (cm^3/g)	Si/Al	Ni/Al	Ni (wt.%)	BAS mmol/g	LAS mmol/g
H-Beta(m)	677	0.28	0.08	19.7	–	–	0.55	0.49
Ni-H-Beta(m)	651	0.28	0.17	24.0	1.2	2.2	0.19	0.92
Na-Beta(n)	712	0.27	0.76	13.5	–	–		
H-Beta(n)	677	0.19	0.80		–	–	0.65	0.68
Ni-H-Beta(n)	570	0.18	0.58	17.4	0.83	2.1	0.29	1.20
Ni-H(Na)-Beta(n)(2)	616	0.23	0.73	17.5	1.76	4.2	0.42	1.37
Ni-H-Beta(n)(2)	620	0.22	0.69	15.8	1.73	4.6	0.26	1.41
$NiSO_4$-Al_2O_3	193	0.01	0.66	–	–	2.0		
$NiSO_4$-SiO_2-Al_2O_3	454	0.03	0.55	–	–	2.0		

subsequently cooled down to 150 °C, and then contacted with a flow of ethene (20 mL/min) and helium (50 mL/min) for 30 min. After activation, the cell was moved to the IR instrument (in controlled atmosphere) to carry out measurements at low temperature (liquid nitrogen temperature, LNT). Activated samples were kept in He (or He/C_2H_4) atmosphere (slight overpressure) until connection to the vacuum line. Before CO dosage the catalysts were then outgassed at room temperature (RT) to remove He or He/C_2H_4 atmosphere.

CO adsorption experiments were carried out at LNT by sending 30 Torr of CO on the zeolites activated as described above, followed by stepwise decrease of the pressure. For all samples, the spectrum before CO dosage was used as reference to obtain the subtracted spectra reported in the CO stretching region (νCO). For comparison spectra were normalized by employing the fingerprint region of silicate frameworks in the 1750–2100 cm^{-1} region (overtone and combination modes of framework vibrations).

The concentration of acid sites was investigated with FTIR spectroscopy using pyridine as probe molecule. The measurements were performed in transmission mode on a Bruker Vertex 80 instrument with a Mercury Cadmium Telluride (MCT) detector. For this purpose, a quartz cell with KBr windows was employed. Catalysts were prepared as thin wafers supported in a gold envelope and pre-treated in vacuum ($< 10^{-5}$ mbar) for 3 h: 1 h at 150 °C followed by 2 h at 300 °C. The adsorption of pyridine was done by exposing the pellets to pyridine vapor. After equilibration at room temperature, the catalysts were degassed at 200 °C for 2 h. The final spectrum was recorded at RT and the integrated area of the bands at 1545 and 1455 cm^{-1} with molar extinction coefficients of 0.73 and 0.64 were used to determine the amounts of Brønsted and Lewis acid sites, respectively.

2.3. Catalytic testing

Catalytic tests were carried out in a continuous flow, fixed bed, stainless steel reactor. Before each experiment, the catalyst was pressed, crushed and sieved to 240–420 μm grain size. The catalyst mass (100–200 ± 5 mg) was adjusted to obtain partial conversion (below 20%). The catalyst was loaded in the reactor and was activated in-situ at 300 °C for 16 h under 1 bar of helium. The total pressure was then increased in He (up to 30 bar) and controlled by a back-pressure regulator (Bronkhorst P-702CV). During reaction, the partial pressures were controlled by adjusting individual flows. The desired mixture of ethene (provided by AGA, 2.5 grade), inert and internal standard (10% Ne in He, provided by AGA, 2.5 grade) was fed through the reactor, keeping the total pressure constant, but varying the partial pressure of ethene. Typical reaction conditions were: 120 °C with a total pressure of 29 bar and with a contact time of 0.0068 $min*g_{cat}*mL^{-1}$ or 0.0034 $min{\cdot}g_{cat}{\cdot}mL^{-1}$ (at STP). The experiments used the following reference condition: T = 120 °C, P(total) = 29 bar where P_{ethene} = 25.1 bar and P_{inert} = 3.9 bar. Each experiment started under reference conditions and then returned to reference conditions between each change of conditions. The reference conditions were then used to simulate a deactivation model and to correct for the deactivation (see Figure SI 1 for an example). In this contribution, such correction was only employed in the partial pressure variation experiments (Section 3.3.3), since the conversion level under reference conditions was rather constant in the contact time variation experiments (Section 3.3.4).

A small portion of the reactor effluent, about 4 mL/min, was led through heated lines to an online gas chromatograph (Agilent 7890B) equipped with three columns: CP-Molsieve 5A (50 m × 0.53 mm × 50 μm) connected to TCD, GS-Gaspro (60 m × 0.32 mm) and DB-1 (40 m × 0.10 mm × 0.20 μm) both connected to FID. The three channels were used for detection of neon, light hydrocarbons up to butenes and heavier hydrocarbons, respectively. This made it possible to analyze all effluent products simultaneously (without the need to condense the heavy products), while the presence of Ne as an internal standard allowed for calibration to obtain accurate mass balances.

Ethene conversion and product selectivity were calculated by using the following formulas:

$$Conversion\,(\%) = (1 - \frac{[Ethene_{out}]}{[Ethene_{in}]} * \frac{V_{out}}{V_{in}}) \cdot 100 \quad (1)$$

Where $[Ethene_{in}]$ is determined by feed analysis and V_{out}/V_{in} is determined by $[Ne_{in}]/[Ne_{out}]$.

$$Selectivity\,(i)(\%) = \frac{[Product\,(i)]}{\sum_n [Product\,(n)]} \quad (2)$$

3. Results and discussion

3.1. Catalyst characterization

The main physical properties of the catalysts are summarized in Table 1. X-ray Diffractograms of the zeolite samples are shown in Fig. 1. Scanning Electron Microscopy images of two representative samples (Ni-H-Beta(m) and Ni-H-Beta(n)(2)) are shown in Fig. 2.

Looking first at Fig. 1, the XRD patterns confirmed that all zeolite samples belong to the BEA framework. No changes in the intensity or the position of the diffraction peaks were observed after calcination and/or ion exchange, assessing the absence of degradation during preparation. Martinez et al. [13] reported diffraction peaks at 37.2° and 43.3° for Ni-impregnated, nanocrystalline Beta samples and ascribed them to crystalline nickel oxide (NiO). However, no such peaks were observed in the samples prepared in the present study. Considering next the results presented in Fig. 2, the SEM images confirmed the micro- and nanocrystalline size of Ni-H-Beta(m) and Ni-H-Beta(n)(2), respectively. The particle size distribution of Ni-H-Beta(n)(2) was narrow and below 50 nm, while the particle size for Ni-H-Beta(m) ranged from 100 to 700 nm. The nickel distribution in each sample was investigated by mapping different regions of the samples. For Ni-H-Beta(m), Ni-containing particles with less than 20 nm diameter were observed on the zeolite surface, ascribed to NiO. These nanoparticles were not observed with XRD most probably due to the low amount present in the sample. No NiO particles were detected for Ni-H-Beta(n)(2) (see Figure SI 2 for

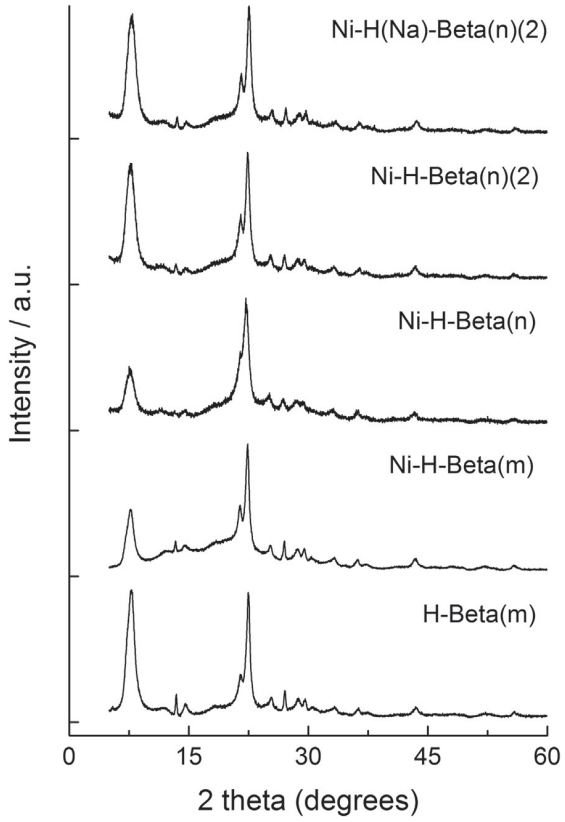

Fig. 1. X-ray diffraction patterns for zeolite catalysts.

backscattered electron images).

In Table 1, it can be observed that all zeolite samples had high and similar specific surface areas (S_{BET}), as expected for such highly crystalline structure. All nanocrystalline samples (n) exhibited one order of magnitude higher mesoporous volume (V_{meso}) compared to the microcrystalline samples (m). Comblor et al. [18] have shown that decreasing the crystal size increases the mesoporous volume observed in adsorption isotherms, and assigned this effect to inter-particular space and to agglomeration. On the right side of the table, the elemental analysis shows that, for all measured zeolite samples, the silicon to aluminum ratio increased slightly after ion exchange, suggesting that aluminum was lost during the treatment. This is most likely extra-framework aluminum that was washed away during ion exchange, as further supported by FT-IR (see below).

The amount of Brønsted and Lewis acid sites (BAS and LAS, respectively) for the zeolite catalysts was determined by FT-IR-pyridine and is shown in Table 1. The parent samples contained both BAS and

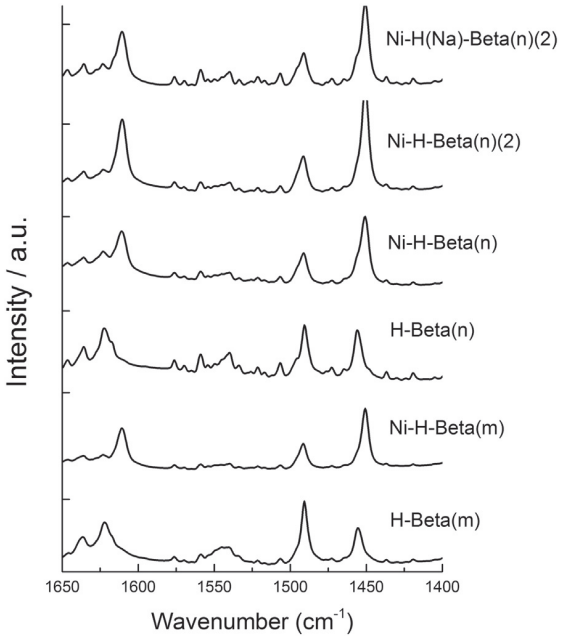

Fig. 3. Spectra of the pyridine region after pyridine desorption at 200 °C.

LAS; the LAS were possibly due to extra-framework Al species. Upon ion exchange with Ni^{2+}, the amount of BAS decreased, compared to the parent micro- and nanocrystalline H-Beta catalysts, indicating that Ni^{2+} is exchanged with the Brønsted acid sites. Furthermore, the LAS were shifted towards lower frequencies and increased in abundance upon Ni^{2+} exchange. This shift is illustrated in Fig. 3, where in addition to the band at 1622 cm^{-1} ascribed to pyridine coordinated to aluminum species, a new band at 1610 cm^{-1} is observed. This band is only present in the Ni-exchanged catalysts and is attributed to pyridine coordinated to Ni^{2+} cations [19,20]. However, the Ni/Al ratio of some of the catalysts was above 1, suggesting that Ni is also present in another form, such as NiO observed on the surface of Ni-H-Beta(m) with SEM (Figure SI 2) or Ni^{2+} sites grafted to defective silanol groups [43]. Even though no NiO was observed for nanocrystalline catalysts, we cannot discard its presence completely. As a final note, a sample denoted Ni-H(Na)-Beta(n)(2) was prepared by ion exchange of the calcined Na-Beta (n) sample. The aim was to compare a sample containing Ni sites but not proton sites, to the Ni- and proton-containing samples. Surprisingly, the pyridine adsorption experiments revealed that the amount BAS of Ni-H(Na)-Beta(n)(2) was higher than in Ni-H-Beta(n)(2). This result indicates that during Ni-exchange, sodium is not only exchanged with nickel, but also with protons. Similar results have been reported for Y zeolite, where the introduction of divalent cations (Ca^{2+}, Mg^{2+}, Ni^{2+}) also introduced BAS [21]. Thus, with these catalysts, isolating and

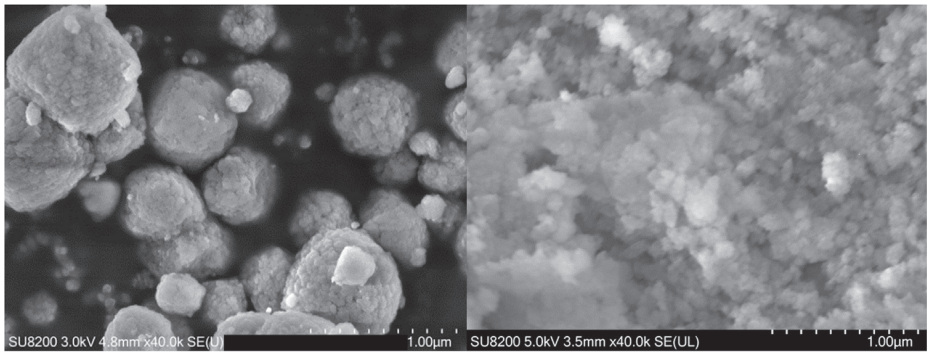

Fig. 2. Scanning Electron Microscopy images of Ni-H-Beta(m) (left) and Ni-H-Beta(n)(2) right. Identical scaling was used to highlight the difference in crystal size between the samples.

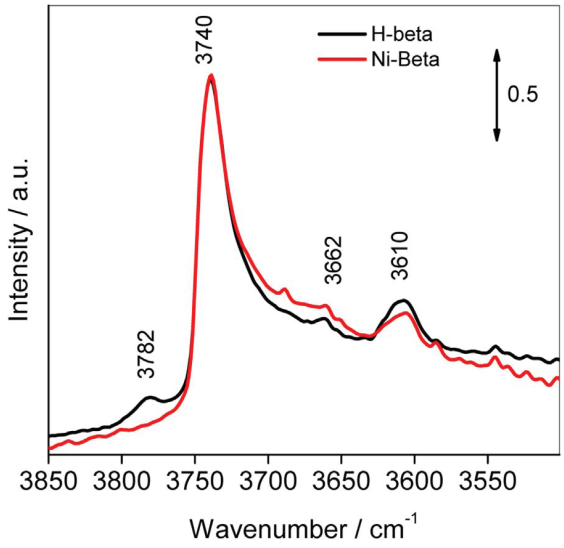

Fig. 4. IR spectra in the νOH region of dehydrated H-Beta(m) and Ni-H-Beta(m) samples.

studying nickel in BAS free catalyst would require a different procedure.

3.2. FTIR: pursuing the active site(s)

FTIR spectroscopy was employed to gain insight about the active site(s) on the catalyst. We initially characterized the different Ni sites present in the pristine catalysts. The catalysts were characterized again after reaction with ethene, leading us to propose both active and spectator sites.

3.2.1. νOH region: ion exchange of nickel sites

The νOH vibrational region of activated H-Beta(m) and Ni-H-Beta (m) samples is shown in Fig. 4. In both spectra, absorption bands at 3740, 3662 and 3610 cm^{-1} are observed, while H-Beta(m) also shows a weak band at 3782 cm^{-1}. The band at 3745 cm^{-1} is related to isolated silanol groups on the external zeolite surface. The two components at 3782 and 3662 cm^{-1} are typical of OH groups related to extraframework Al atoms [22], even if features in the 3720–3620 cm^{-1} range have also been observed in defective Al-free silicalites, and assigned to internal silanols in different environments [23]. Noticeably, after Ni exchange the band at 3782 cm^{-1} specifically assigned to OH groups on tricoordinated Al atom partially linked to the framework [22], disappears. This is in agreement with the increase of Si/Al ratio observed by elemental analysis (Table 1). The typical νOH band of Si(OH)Al Brønsted sites is found at 3610 cm^{-1}. After Ni exchange, the relative intensity of the band related to Brønsted acid sites decreased, as expected. However, ion exchange is not complete, and a significant fraction of Brønsted sites is still present, as confirmed by pyridine adsorption experiments.

3.2.2. Adsorbed species after ethene contact

As described in experimental section, Ni-H-Beta(m) sample was contacted with ethene at 150 °C for 30 min. The IR spectra after and before ethene contact are shown in Fig. 5. Bands related to CH_3 and CH_2 groups could be observed in both stretching (2956, 2927, 2873 and 2856 cm^{-1}) and bending (1406, 1380 and 1366 cm^{-1}) regions. Other weak bands are observed at 1503 and 1534 cm^{-1}. Bands in similar positions have been assigned to unsaturated carbocations [24]. Coke analysis of the spent catalysts (Figure SI 4) showed no aromatics detected by GC–MS, even after dissolution of the materials in HF. These results suggest that the adsorbed compounds are mainly aliphatic hydrocarbons.

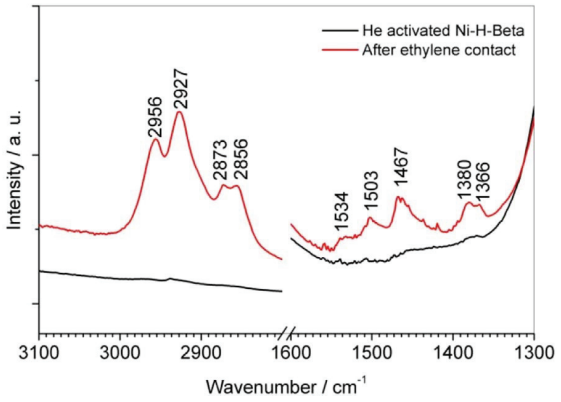

Fig. 5. Adsorbed species formed on Ni-H-Beta(m) sample after contact with ethene/He mixture at 150 °C for 30 min.

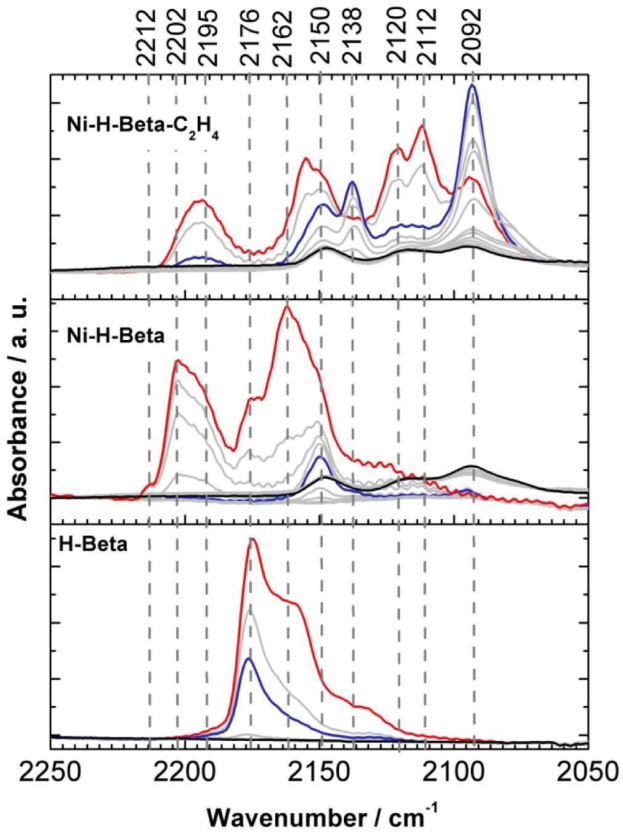

Fig. 6. Low coverage CO spectra measured at LNT on: top) Ni-H-Beta(m) sample activated in He/ethene flow at 150 °C; middle) Ni-H-Beta(m) sample activated in He flow at 300 °C and bottom) H-Beta(m) sample activated in He flow at 300 °C. Red curves correspond to the highest CO pressure (0.1 mbar), blue curves to intermediate coverage allowing to appreciate spectra evolution (0.01–0.005 mbar), black spectra were measured under dynamic vacuum (residual pressure 1 10^{-4} mbar). (For interpretation of the references to colour in this figure legend, the reader is referred to the web version of this article.)

3.2.3. Ni species: active and spectator sites

Infrared spectroscopy of CO adsorbed at low temperature (LNT, around −196 °C) was utilized to investigate the different types of Ni surface sites available before and after ethene contact (Fig. 6). Data obtained on H-Beta(m) sample are also reported for comparison. Low temperature experiments were carried out according to Martinez et al. [13], who reported that upon room temperature CO contact Ni^{2+} sites could be reduced to Ni^{+}, thus affecting the interpretation. However our

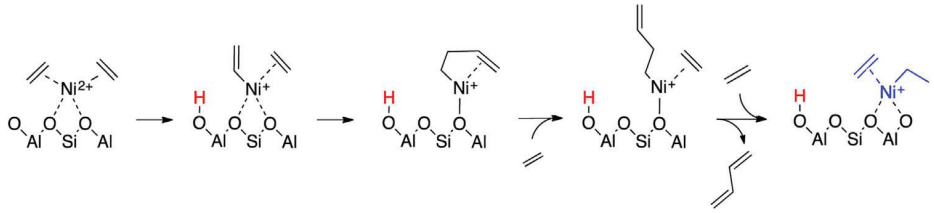

Scheme 2. Formation of the active site.

recent investigations on Ni-containing ZSM-5 [25] showed that if Ni content is low (less than 2%), reduction of Ni^{2+} by CO at room temperature does not occur.

High coverage CO spectra (not shown) were characterized for all samples by the typical bands related to CO adducts with Brønsted sites (2176 cm^{-1}), silanols (2157 cm^{-1}) and by the typical band of physisorbed CO ('liquid-like', 2141 cm^{-1}) [25,26]. These are the only ones present on Ni-free sample (H-Beta, bottom panel of Fig. 6). For the sake of brevity, only the spectra measured at relatively low CO coverage (θ_{CO}) are reported and discussed, since they provide most information about the nature of Ni sites. These are reported in Fig. 6 for Ni-H-Beta (m) sample activated in He/ethene or He flows (top and middle, respectively) and for on H-Beta(m) activated in He (bottom), for comparison. In all panels of Fig. 6 the spectra measured at the highest considered θ_{CO} (0.1 mbar) are reported in red; blue spectra are related to intermediate coverage, allowing to better appreciate spectra evolution with pressure (0.01–0.005 mbar); finally, black curves were measured while outgassing the sample under dynamic vacuum (residual pressure $1*10^{-4}$ mbar).

Concentrating on He activated Ni-H-Beta(m) sample (middle panel), new features are observed at high frequency at 2212 (weak), 2202 and 2195 cm^{-1} (shoulder), which gradually decrease with θ_{CO}. These are in the typical region of CO adducts on Ni^{2+} sites and were assigned to complexes formed on two distinct Ni^{2+} counterions (2212 and 2202 cm^{-1}) and on grafted Ni^{2+} sites (2195 cm^{-1}) [25,27–29]. Moving to lower frequency, the band at 2150 cm^{-1}, disappearing upon θ_{CO} decrease, was observed upon CO adsorption on low surface area NiO particles, suggesting the presence of small (not detected by XRD, see above) nickel oxide particles [30]. Bands at lower frequency are in the spectral region typical of CO adducts on Ni^{+} ions and Ni^{0} particles [13,25,31,32]. More in detail, at intermediate coverage (blue spectrum) very weak features are observed at 2138 and 2095 cm^{-1}. Under dynamic vacuum (black curve) broad bands are formed with maxima at 2148, 2116 and 2092 cm^{-1}, with a broad tail extending to lower wavenumbers. The nature of these bands will be discussed in more detail later on. For now, it is sufficient to mention that they indicate that some reduction of Ni^{2+} upon activation in inert He atmosphere has occurred, as observed elsewhere [25].

The top panel of Fig. 6 shows the CO spectra measured in similar conditions on Ni-H-Beta(m) sample after ethene contact. First, we note the decrease in intensity of the bands at 2176 and 2162 cm^{-1}, related to CO adducts on BAS and silanols, indicating an interaction of ethene with these sites. Concerning the bands assigned to Ni ions, we note that the bands related to Ni^{2+} counterions (2202 and 2215 cm^{-1}) are no longer present, as opposed to those related to grafted Ni^{2+} sites and NiO small particles. Additionally, an increase in the intensity of the bands related to reduced Ni sites (2157, 2138, 2120, 2112 and 2092 cm^{-1}) is observed. While the bands at 2157, 2120 and 2112 cm^{-1} decrease in intensity, the couple at 2138 and 2092 cm^{-1} first increases (maximum intensity at 0.01 mbar, blue curves) and then decreases. This transformation could be explained by a $Ni^{+}(CO)_3$ to $Ni^{+}(CO)_2$ transformation, as reported by Penkova et al. on reduced Ni-Beta [32]. The same authors reported the occurrence of an equilibrium between $Ni^{+}(CO)_2$ and $Ni^{+}(CO)$ adducts when the experiment was carried out at RT, with the latter giving a band at 2113 cm^{-1}. The reported results clearly show a reductive effect of ethene, with formation of highly coordinatively unsaturated Ni^{+}, which are thus likely to be present as counterions. Noticeably, even if a small amount of $Ni^{+}(CO)_2$ complexes could be inferred also on the sample activated in He (middle panel, blue curve, bands at 2138 and 2092 cm^{-1}), in that case we could not exclude the formation of Ni^{0} particles, as suggested by the broad tail below 2100 cm^{-1}, increasing when reducing CO pressure, as often observed in the presence of metal particles [31]. This suggests that the reduction mechanism in the presence of inert atmosphere and ethene is different.

It remains elusive how ethene reduces exchanged Ni^{2+} to Ni^{+}; it is insufficient to explain it by an electron transfer from ethene to Ni, as it does not take into account how the excess zeolite framework charge is compensated for. Based on our recent theoretical work [24], we suggest an alternative explanation: what appears to be a reduction of exchanged Ni^{2+} to Ni^{+} ions on the basis of IR data, could instead be related to active sites formed by reaction of ethene with the Ni^{2+} ions (Scheme 2) [24]. When the cell is evacuated after contact with ethene, excess ethene and alkyl groups are removed, reducing these Ni^{2+} sites to isolated Ni^{+} ions analogously to how zeolite supported $[Cu(II)\text{-}OH]^{+}$ is reduced to Cu^{+} in vacuum [33]. Summarizing, the results may be explained by a mechanism where ethene reacts with Ni^{2+} counter ions to form Cossee-Arlman oligomerization sites, while Ni sites grafted and on the surface of small NiO particles are spectator species. We acknowledge the recent results by Moussa et al., who proposed a higher activity for Ni sites on the surface of NiO particles, on samples with relatively high Ni content (5%) [16]. However, in conjunction with previous work [13] our results indicate that NiO particles can be considered 'spectators' in the ethene oligomerization reaction.

3.3. Catalytic testing

3.3.1. Influence of active site. Ni-H-Beta(m) versus H-Beta(m)

The nickel ion exchanged samples contain two different types of active sites; nickel (oxidation state 0, +I or +II) and Brønsted acid sites. These sites have been reported to show different activity and selectivity for the ethene oligomerization reaction under identical reaction conditions [11]. To elucidate the respective roles of nickel and proton sites under the conditions used in the present study, experiments were carried out with Ni-H-Beta(m) and H-Beta(m). Ethene conversion and linear butene selectivity obtained over the two samples at 120, 200 and 300 °C are shown in Fig. 7. Over H-Beta(m), the initial ethene conversion was 5% at 120 °C, i.e. the standard reaction temperature in the present study, and 4% at 200 °C. Over Ni-H-Beta(m), the initial ethene conversion was 22% at 120 °C and 34% at 200 °C. These results show that the initial activity of the proton sites for ethene oligomerization is low compared to the nickel sites under the conditions studied here.

Considering product selectivity, it should be noted that not all products formed are gaseous: some carbon-containing products were not detected by GC-FID, but were quantified from mass balance (denoted retained hydrocarbons, R-HC). Small amounts of gaseous hexene (below 5% selectivity in the gas phase) were also detected; for clarity, this amount was lumped with the R-HC fraction. For example, with H-Beta(m), the selectivity towards gaseous products was below 1%

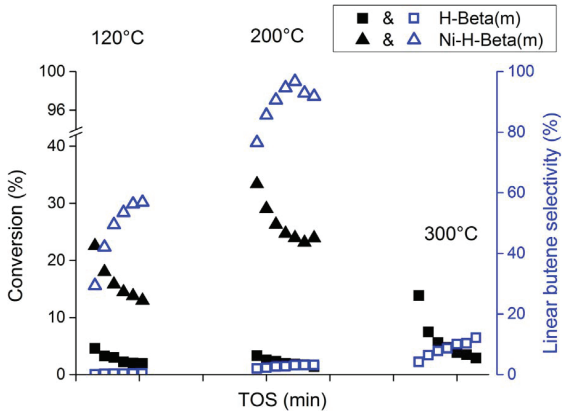

Fig. 7. Ethene conversion (solid symbols) and linear butene selectivity (hollow symbols) at 120–200–300 °C versus time on stream. Reaction conditions: m_{cat} = 0.200 g, contact time: 0.0067 g*min*mL^{-1} at STP, 29 bar total pressure where P_{ethene} = 21.2 bar and P_{inert} = 7.8 bar for H-Beta(m) and P_{ethene} = 25.1 bar and P_{inert} = 3.9 bar for Ni-H-Beta (m).

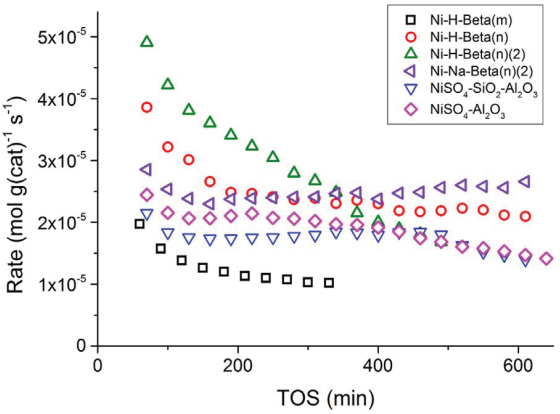

Fig. 8. Rate of ethene oligomerization versus time on stream for all catalysts. Reference reaction conditions: 29 bar total pressure where P_{ethene} = 25.1 bar and P_{inert} = 3.9 bar and T = 120 °C.

at 120 °C, and around 20% at 200 °C (see Figure SI 3 for selectivity versus time on stream).

In terms of linear butenes selectivity over the two samples, the initial selectivity was 27% over Ni-H-Beta(m), and less than 1% over H-Beta(m) at 120 °C. At 200 °C, this increased to 76% and 2%, respectively. While the by-products of Ni-H-Beta(m) were exclusively longer, linear, even carbon-numbered alkenes, the effluent of H-Beta(m) included a variety of linear, branched alkanes and alkenes, mostly between C_3 and C_6. The selectivity towards these products is consistent with the presence of acid sites in the zeolite, catalyzing oligomerization reactions as well as proton transfer, isomerization and cracking reactions [34].

To highlight the differences in selectivity over the two materials, the integrated yields of linear and branched C_4 products during 1260 min on stream are shown in Table 2. Over H-Beta(m), the production of linear and branched alkenes are of the same order of magnitude, at both temperatures. This observation is in agreement with literature data: Brønsted acid sites are expected to promote the carbenium ion mechanism, favoring the production of branched aliphatic products [35]. In addition to butenes, the selectivity towards iso-butane was significant, at approximately 20%, suggesting the presence of hydrogen transfer on the Brønsted acid sites [36].

Over Ni-H-Beta(m), the integrated yield of branched alkenes and alkanes is negligible compared to the production of linear butenes. The results obtained show that the Ni sites dominate as ethene oligomerization sites on Ni-H-Beta(m) under the conditions used in the present study.

3.3.2. *Influence of support topology and morphology. Ni-H-Beta(m), Ni-H-Beta(n), Ni-H(Na)-Beta(n) and $NiSO_4$-(SiO_2)-Al_2O_3*

Initial ethene conversion rates obtained over the Ni-containing catalysts under standard conditions (120 °C, P_{ethene} = 25.1 bar) are plotted versus time on stream in Fig. 8.

The zeolite catalysts showed rapid initial deactivation, followed by a period of slower deactivation. Such behavior is typical of processes where product deposition is responsible for catalyst deactivation [37]. The lower conversion rate of Ni-H-Beta(m) compared to Ni-H-Beta(n) is mainly ascribed to the particle size as the amount of nickel, BAS and LAS are similar in the two materials (Table 1). Larger crystallites (Ni-H-Beta(m)) present a longer diffusion path. Transport of the reactant and products between the active sites and the surface is limited [38], leading to build-up of larger products inside the pores and finally deactivation. Comparing Ni-H-Beta(n) with 2 wt% Ni to Ni-H-Beta(n)(2) and Ni-H(Na)-Beta(n)(2) with 4 wt% Ni shows that the conversion rate is almost unaffected by the nickel amount. This result suggests that different nickel species are present in the catalyst and that only nickel in certain environment/configuration is active for ethene oligomerization as previously reported by Martinez et al. [13].

After a short period of deactivation, around 120 min, the activity of the mesoporous catalyst ($NiSO_4/Al_2O_3$ and $NiSO_4/SiO_2$-Al_2O_3) increased for several hours before subsequently decreasing again. Such behavior is typical of systems where active sites are initially formed or gradually become accessible for the reactants at a higher rate than the rate of deactivation, until deactivation dominates, in this case after approximately 200 and 500 min on stream for $NiSO_4/Al_2O_3$ and $NiSO_4/SiO_2$-Al_2O_3, respectively. This pattern has already been observed in propene oligomerization by Mlinar et al. [39]. In that work, the authors argue that the activation period is due to the migration of nickel ions in the lattice of faujasite; this interpretation cannot be directly applied to the $NiSO_4$-containing catalysts used in this study as they do not present the same microporous structure. Another possible explanation is that the initiation period is due to the slow build-up of active sites, which may involve formation of Ni-C bond and breakage of Ni-O bond [15,40].

The linear butene selectivity observed during the initiation period is reported in Fig. 9. The data were obtained during the same tests shown in Fig. 8, i.e. with deactivating catalysts. All catalysts showed high linear butene selectivity, while only traces of alkanes and odd carbon number products were formed, indicating that acid-catalyzed side reactions are not occurring to a significant extent. Furthermore, no trace of iso-butene was observed. The hydrocarbons R-HC retained in Ni-H-Beta(n) were characterized, and were found to consist of long chained even-numbered alkenes (see Figure SI 4 for GC–MS analysis of the spent catalysts). The absence of odd numbered products in R-HC further supports that the acid sites are not active to a significant degree.

Concentrating first on the four zeolite-based catalysts (Fig. 9, left panel), butene selectivity steadily decreased with conversion. This

Table 2
Integrated yield (mg) of linear and branched butenes produced during 1260 min time on stream. Reaction conditions: m_{cat} = 0.200 g, contact time = 0.0067 g *min*mL^{-1} at STP, 29 bar total pressure where P_{ethene} = 21.2 bar and P_{inert} = 7.8 bar for H-Beta(m) and P_{ethene} = 25.1 bar and P_{inert} = 3.9 bar for Ni-H-Beta(m).

	$T_{reaction}$ = 120 °C		$T_{reaction}$ = 200 °C	
	Linear-$C_4^=$ (mg)	Branched $C_4^=$ (mg)	Linear-$C_4^=$ (mg)	Branched $C_4^=$ (mg)
H-Beta(m)	0.4	0.3	21	43
Ni-H-Beta (m)	490	0.4	1250	3.4

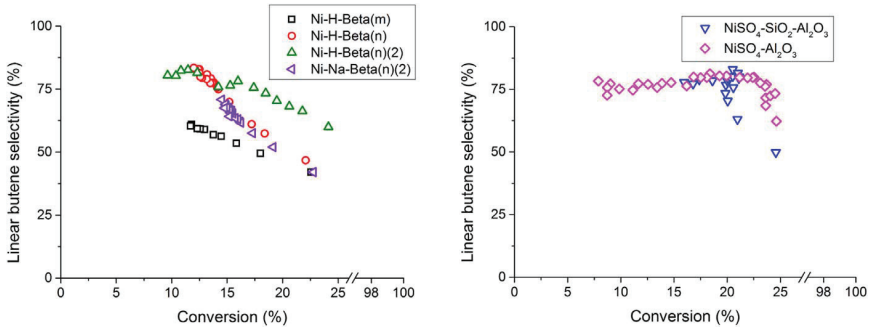

Fig. 9. Linear-$C_4^=$ selectivity versus conversion for zeolite (left) and $NiSO_4$-containing (right) catalysts. Reference reaction conditions: 29 bar total pressure where P_{ethene} = 25.1 bar and P_{inert} = 3.9 bar and T = 120 °C.

result may suggest that not only ethene, but also product butene and possibly higher alkenes, may adsorb and be converted on the active sites of the catalyst. However, it could also mean that the active sites are changing with deactivation. At any given conversion, butene selectivity was lower for microcrystalline Ni-H-Beta(m) than for nanocrystalline Ni-H-Beta(n), hence the selectivity towards heavier products, including R-HC, is higher. This difference may be explained again by the difference of particle size. Because of the longer diffusion path in larger particles (Ni-H-Beta(m)), the transport of the primary product, butene, from the active sites to the external bulk phase is hindered [42]; this longer residence time in the pores likely favors secondary reactions and formation of longer chains. The longest of these secondary products are permanently stuck in the pores, as the relatively fast deactivation rate and the GC–MS analyses of the spent catalysts suggest. Secondly, larger particles (Ni-H-Beta(m)) have significantly lower external surface, and the selectivity of the external nickel sites is expected to yield formation of smaller products than inside the pores, because of the absence of stabilization of longer aliphatics.

Concentrating next on the mesoporous catalysts (Fig. 9, right panel), a different pattern was observed: an increase in butene selectivity was observed during the activation period for each catalyst. This observation suggests that not only the amount, but also the nature of the active sites change during the activation period [43]. During the subsequent period of deactivation, no change in butene selectivity was observed upon decreasing conversion. This result is in accordance with data published by Toch et al. for a Ni/SiO_2-Al_2O_3 catalyst [14]. They observed that product selectivity is independent of ethene conversion, leading to a Schulz-Flory type product distribution [44].

Likewise, the difference observed between the microporous (left panel) and mesoporous (right panel) catalysts may be due to a different reaction mechanism, or to the enhanced diffusion restrictions in the microporous catalyst, which is likely to increase the abundance of secondary reactions.

To further elaborate on selectivity differences between the materials, 1-butene/total butene ratio versus ethene conversion is shown in Fig. 10. The plots are divided into two groups: first, the 1-butene/total butene ratio over zeolite catalysts increased steadily with decreasing conversion, suggesting initially high rate for isomerization of 1-butene or high initial formation of 2-butenes. The other group comprises the two mesoporous catalysts, $NiSO_4/Al_2O_3$ and $NiSO_4/SiO_2$-Al_2O_3. Over these catalysts, the 1-butene/total butene ratio was lower than for zeolite catalyst and increased only slightly with decreasing conversion. Under these conditions, the equilibrium 1-butene/total linear butene ratio is approximately 0.07 [45]. The mesoporous catalysts are closer to thermodynamic equilibrium and this suggests a much higher isomerization rate compared to the ethene oligomerization rate over these catalysts. The evolution of butene selectivities with conversion for the zeolite catalysts will be discussed further in Section 3.3.4

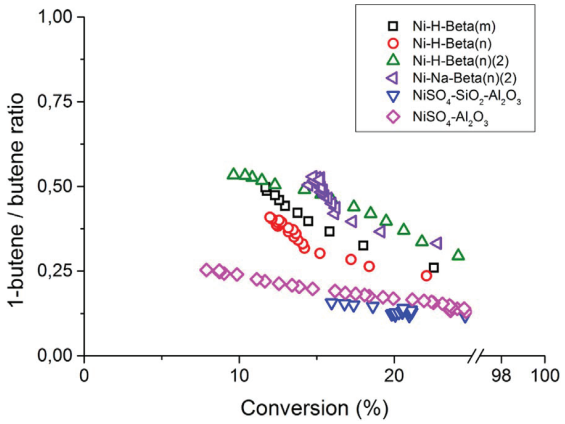

Fig. 10. 1-butene/(1- and 2-butene) ratio versus conversion for all catalysts. Reference reaction conditions: 29 bar total pressure where P_{ethene} = 25.1 bar and P_{inert} = 3.9 bar and T = 120 °C.

3.3.3. *Partial pressure variation experiments*

To further elucidate the effect of catalyst topology, the five catalysts were subjected to ethene partial pressure variation tests at 120 °C in order to derive the reaction order of ethene in the rate of consumption of ethene. Distinct differences were observed between the microporous and mesoporous catalysts. The ethene oligomerization reaction was second order over the microporous catalysts, while it was closer to one (1.2 and 1.4) over the mesoporous catalysts. The latter agrees reasonably well with previous work of Toch et al., who observed a first order dependency on P_{ethene} on Ni/SiO_2-Al_2O_3, for P_{ethene} between 1.5–3.5 bar [14].

Next, we focus on the reaction order of ethene in the rate of production of butenes, in order to obtain mechanistic insight in the dimerization reaction. The results are reported in Fig. 11 and summarized in Table 3. It is instructive to consider the mechanistic implication of the reaction order depending on the catalyst topology. Considering first the Cossee-Arlman mechanism of Scheme 1, theoretical work from Brogaard and Olsbye found that [Ni-alkene-alkyl] species have quite similar stability in the SSZ-24 microporous zeolite [24]. This means that in the Cossee-Arlman mechanism, the resting state of the catalyst can easily change from [Ni-ethene-ethyl], giving a reaction order of 0, to a [Ni-alkene-alkyl] species resulting in a reaction order of 2 in ethene for the rate of butene production. It is reasonable to expect a higher reaction order in the microporous zeolites, where alkyl chains are significantly stabilized, than on mesoporous catalysts where such stabilization is significantly less. This is consistent with the higher reaction orders obtained experimentally with the Beta zeolites, around 2, than on the $NiSO_4$-containing materials, between 1.5 and 1.7 (the uncertainties being high, as the conversion at P_{ethene} = 9 bar is below 5%). However, a similar change in reaction order could also be consistent with the metallacycle mechanism, for the same reason:

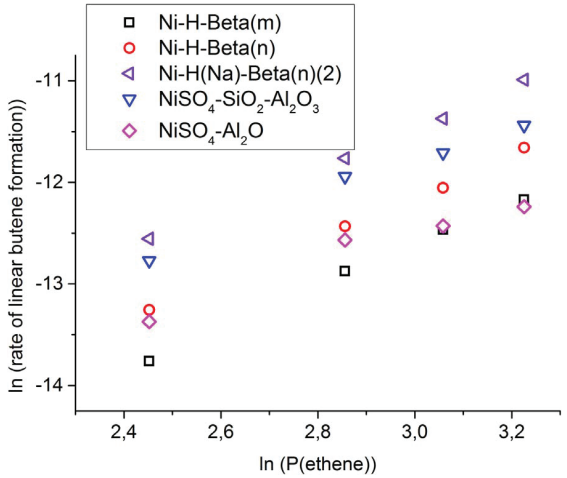

Fig. 11. Logarithm plot of butenes production rate for all catalysts, as a function of logarithm of partial pressure of ethene at T = 120 °C.

Table 3
Reaction order with respect to ethene for the rate of production of butenes, for the investigated catalysts. Reaction conditions: T = 120 °C, 29 bar total pressure where P_{ethene} = 25.1–11.6 bar and P_{inert} = 3.9–17.4 bar.

Catalyst	Ethene consumption	Butene formation
Ni-H-Beta(m)	2.0	2.0
Ni-H-Beta(n)	2.0	2.0
Ni-H(Na)-Beta(n)(2)	2.0	2.0
$NiSO_4$–Al_2O_3	1.2	1.5
$NiSO_4$–SiO_2–Al_2O_3	1.4	1.7

longer alkenes adsorb on the Ni sites in the micropores, leading to a second order dependence in ethene for butene production, which could decrease towards first (zeroth) order on a catalyst without stabilization from pores, having a Ni-ethene (dimer) species as resting state.

3.3.4. Steady state performance

It was discussed in Section 3.3.2 that the selectivities among butenes vary with conversion during the initiation phase. The evolution of yields as a function of ethene conversion, obtained by contact time variation under steady state conditions, can give us a better insight into the primary and secondary products, as well as into the potential presence of different active sites. A new series of experiments was therefore carried out with the Ni-H-Beta(m), Ni-H-Beta(n), Ni-H-Beta(n)(2) and Ni-H(Na)-Beta(n)(2) catalysts at lower ethene partial pressure (P_{ethene} = 17.4 bar and P_{inert} = 11.6 bar, T = 120 °C). 1-butene and 2-butenes selectivities during the initial deactivation period (insets) and in steady state (main plots) is shown in Fig. 12. Overall, the trends are very similar among the four catalysts.

The initial performance for all catalysts changed in a similar manner as observed in the tests at P_{ethene} = 26 bar: 1-butene yield increases with deactivation, which may suggest that the nature of the active sites changes through time, or that some secondary reaction sites producing 2-butenes from 1-butene, such as Brønsted acid sites, deactivate.

On the other hand, the steady state plots suggest that all butene yields follow a straight line going through the origin. This indicates that all three linear butenes are primary products; hence only one type of active site is involved in the conversion of ethene to butenes, at least after the first deactivation period. This observation is in best agreement with the Cossee-Arlman mechanism: which accounts for the formation of 2-butenes through isomerization prior to elimination [46], whereas the metallacycle mechanism produces exclusively 1-butene (Scheme 1).

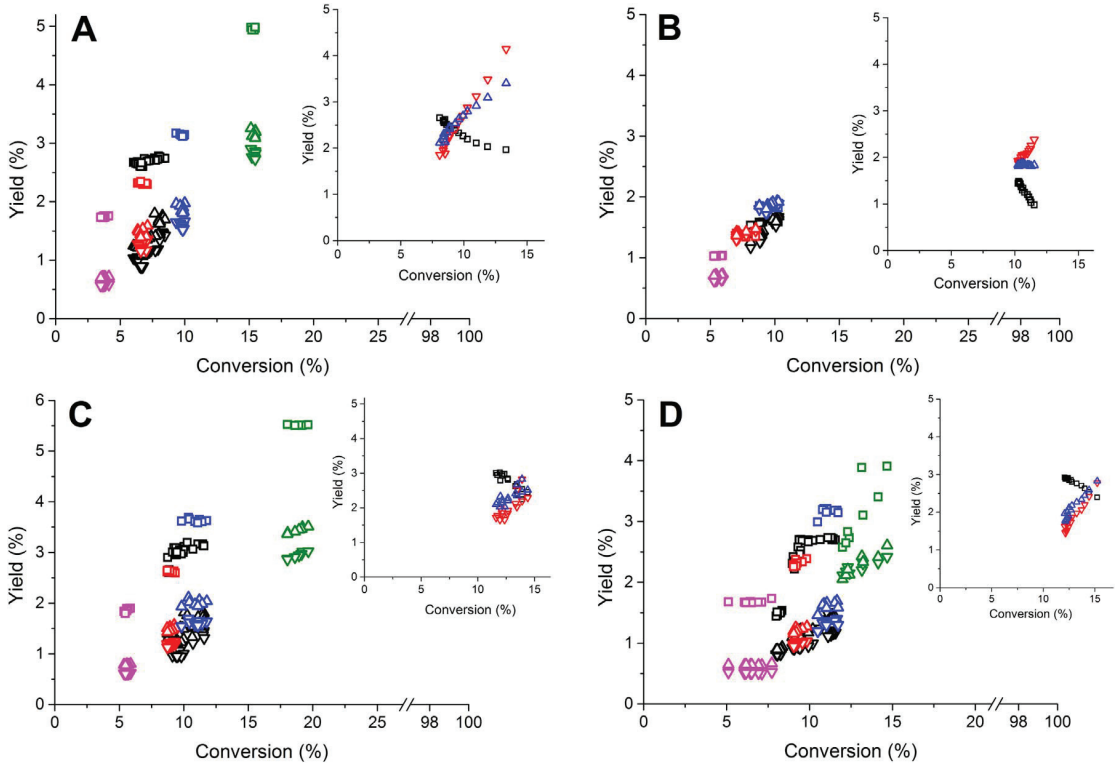

Fig. 12. Yield (%) (square: 1-butene, up triangle: *cis*-2-butene, down triangle: *trans*-2-butene) as a function of conversion during the initial deactivation period (insets) and in steady state (main plot) for a) Ni-H-Beta(m), b) Ni-H-Beta(n), c) Ni-H-Beta(n)(2), d) Ni-H(Na)-Beta(n)(2). Reaction conditions: 29 bar total pressure where P_{ethene} = 17.4 bar and P_{inert} = 11.6 bar, T = 120 °C. Contact time varied between 0.002–0.008 for nanocrystalline and between 0.004–0.016 g_{cat}*min*mL^{-1} for microcrystalline catalysts, the results from each contact time measurement are represented by a different colour.

4. Conclusion

Nickel-containing mesoporous ($NiSO_4$-SiO_2-Al_2O_3/$NiSO_4$-Al_2O_3) and microporous (microcrystalline Ni-H-Beta and nanocrystalline Ni-H/Na-Beta) catalysts were prepared by ion exchange of commercial catalysts. Characterization of the materials by N_2 sorption showed predictably that the Beta zeolites have a much higher microporous volume than the amorphous supports. Moreover, SEM and elemental analysis revealed that the amount of nickel present was 2–4 wt.% depending on the sample. One sample (Ni-H-Beta(m)) showed notably presence of nickel oxide clusters.

Ethene oligomerization tests were performed at 29 bar and 120 °C in a plug flow fixed bed reactor. Significant differences were identified between the catalysts in terms of activity, selectivity and reaction order. These results depended especially on porosity and particle size. First, the results obtained with the different zeolite samples emphasized the role of nickel as the active site for oligomerization of ethene as the amount of ethene converted at Brønsted acid sites was found to be negligible. Another finding is that crystal size has a large impact on deactivation, because of diffusion limitations associated with the formation of long chain products eventually leading to the build-up of products inside the pores. Secondly, the mesoporous catalysts presented a period of activation, attributed to the formation of the active sites by contact of $NiSO_4$ with the reactant. Also, the product selectivities were quite different from the zeolites; stable $C_4=$ selectivity with deactivation was rapidly achieved. Furthermore, the 1-butene to total butene ratio was closer to thermodynamic equilibrium over these catalysts than over the microporous catalysts.

The initial change in product selectivity during deactivation of the zeolite catalysts indicates that they initially had more than one active site, but only one active site was remaining after the initial deactivation period. Based on contact time variation experiments, all three linear butenes were found to be primary products, in accordance with the Cossee-Arlman mechanism.

FTIR spectroscopy confirmed the presence of a variety of Ni species in sample Ni-H-Beta(m), including two distinct Ni^{2+} counterions, grafted Ni^{2+}, small NiO particles and possibly a very small amount of Ni^0 particles. Measurements carried out to probe the sites accessible to the CO probe after interaction with ethene showed that only ion exchanged nickel, under +II oxidation state, and Brønsted acid sites allow adsorption and reaction of ethene in the described conditions, ruling out the participation of NiO or grafted nickel in the process.

Acknowledgment

This research was funded by the Research Council of Norway through the OLIGOM project (224980).

Appendix A. Supplementary data

Supplementary data associated with this article can be found, in the online version, at http://dx.doi.org/10.1016/j.cattod.2017.04.029.

References

[1] IEA's Key World Energy Statistics, (2015).
[2] Jacob A. Moulijn, Michiel Makkee, Annelies E. van Diepen, Chemical Process Technology, 2nd edition, John Wiley and Sons, 2013, 2017.
[3] P.-A.R. Breuil, L. Magna, H. Olivier-Bourbigou, Role of homogeneous catalysis in oligomerization of olefins: focus on selected examples based on group 4 to group 10 transition metal complexes, Catal. Lett. 145 (1) (2014) 173–192.
[4] A. Finiels, F. Fajula, V. Hulea, Nickel-based solid catalysts for ethylene oligomerization – a review, Catal. Sci. Technol. 4 (8) (2014) 2412–2426.
[5] D.S. McGuinness, Olefin oligomerization via metallacycles: dimerization, trimerization, tetramerization, and beyond, Chem. Rev. 111 (3) (2010) 2321–2341.
[6] J.R. Sohn, W.C. Park, S.-E. Park, Characterization of nickel sulfate supported on SiO2–Al2O3 for ethylene dimerization and its relationship to acidic properties, Catal. Lett. 81 (3) (2002) 259–264.
[7] J. Heveling, C.P. Nicolaides, M.S. Scurrell, Catalysts and conditions for the highly efficient: selective and stable heterogeneous oligomerisation of ethylene, Appl. Catal. A: Gen. 173 (1) (1998) 1–9.
[8] V. Hulea, F. Fajula, Ni-exchanged AlMCM-41—an efficient bifunctional catalyst for ethylene oligomerization, J. Catal. 225 (1) (2004) 213–222.
[9] M. Lallemand, et al., Continuous stirred tank reactor for ethylene oligomerization catalyzed by NiMCM-41, Chem. Eng. J. 172 (2–3) (2011) 1078–1082.
[10] R.D. Andrei, et al., Heterogeneous oligomerization of ethylene over highly active and stable Ni-AlSBA-15 mesoporous catalysts, J. Catal. 323 (2015) 76–84.
[11] J. Heveling, A. van der Beek, M. de Pender, Oligomerization of ethene over nickel-exchanged zeolite y into a diesel-range product, Appl. Catal. 42 (2) (1988) 325–336.
[12] M. Lallemand, et al., NiMCM-36 and NiMCM-22 catalysts for the ethylene oligomerization: effect of zeolite texture and nickel cations/acid sites ratio, Appl. Catal. A: Gen. 338 (1–2) (2008) 37–43.
[13] A. Martínez, et al., New bifunctional Ni–H-Beta catalysts for the heterogeneous oligomerization of ethylene, Appl. Catal. A: Gen. 467 (2013) 509–518.
[14] K. Toch, J.W. Thybaut, G.B. Marin, Ethene oligomerization on Ni-SiO2-Al2O3: experimental investigation and single-event MicroKinetic modeling, Appl. Catal. A: Gen. 489 (2015) 292–304.
[15] R.Y. Brogaard, U. Olsbye, Ethene oligomerization in Ni-containing zeolites: theoretical discrimination of reaction mechanisms, ACS Catal. 2016 (2016) 1205–1214.
[16] S. Moussa, et al., Heterogeneous oligomerization of ethylene to liquids on bifunctional Ni-based catalysts: the influence of support properties on nickel speciation and catalytic performance, Catal. Today 277 (Part 1) (2016) 78–88.
[17] L. Li, R.D. Palcheva, K.-J. Jens, Conversion of ethene to propene by a dual function NiSO4/Re2O7/γ-Al2O3 catalyst, Top. Catal. 56 (9) (2013) 783–788.
[18] M.A. Camblor, A. Corma, S. Valencia, Characterization of nanocrystalline zeolite Beta, Microporous Mesoporous Mater. 25 (1–3) (1998) 59–74.
[19] A. Brückner, et al., The role of different Ni sites in supported nickel catalysts for butene dimerization under industry-like conditions, J. Catal. 266 (1) (2009) 120–128.
[20] M.I. Vázquez, A. Corma, V. Fornés, Characterization of NiO supported on zeolite Y: by pyridine adsorption, Zeolites 6 (4) (1986) 271–274.
[21] J.W. Ward, The nature of active sites on zeolites, J. Catal. 10 (1) (1968) 34–46.
[22] J.P. Marques, et al., Infrared spectroscopic study of the acid properties of dealuminated BEA zeolites, Microporous Mesoporous Mater. 60 (1–3) (2003) 251–262.
[23] S. Bordiga, et al., Characterisation of defective silicalites, J. Chem. Soc. Dalton Trans. 2000 (21) (2016) 3921–3929.
[24] L. Palumbo, et al., Conversion of methanol to hydrocarbons: spectroscopic characterization of carbonaceous species formed over H-ZSM-5, J. Phys. Chem. C 112 (26) (2008) 9710–9716.
[25] Y. Ganjkhanlou, et al., Incorporation of Ni into HZSM-5 zeolites: effects of zeolite morphology and incorporation procedure, Microporous Mesoporous Mater. 229 (2016) 76–82.
[26] B.-T.L. Bleken, et al., Probing the surface of nanosheet H-ZSM-5 with FTIR spectroscopy, Phys. Chem. Chem. Phys. 15 (2013) 13363–13370.
[27] M. Mihaylov, K. Hadjiivanov, FTIR study of CO and NO adsorption and coadsorption on Ni-ZSM-5 and Ni/SiO_2, Langmuir 18 (2002) 4376–4383.
[28] K. Hadjiivanov, et al., Characterization of Ni/SiO_2 catalysts prepared by successive deposition and reduction of Ni^{2+} ions, J. Catal. 185 (1999) 314–326.
[29] K. Hadjiivanov, H. Knozinger, M. Mihaylov, FTIR study of CO adsorption on Ni-ZSM-5, J. Phys. Chem. B 106 (2002) 2618–2624.
[30] A. Zecchina, et al., Surface structures of oxides and halides and their relationships to catalytic properties, Adv. Catal. 46 (2001) 265–397.
[31] S. Gopalakrishnan, et al., Unravelling the structure and reactivity of supported Ni particles in Ni-CeZrO2 catalysts, Appl. Catal. B: Environ. 138–139 (2013) 353–361.
[32] A. Penkova, et al., Effect of the preparation method on the state of nickel ions in BEA zeolites. a study by fourier transform infrared spectroscopy of adsorbed CO and NO: temperature-programmed reduction, and X-Ray diffraction, J. Phys. Chem. C 111 (24) (2007) 8623–8631.
[33] E. Borfecchia, et al., Revisiting the nature of Cu sites in the activated Cu-SSZ-13 catalyst for SCR reaction, Chem. Sci. 6 (1) (2015) 548–563.
[34] B. Xu, et al., Catalytic activity of Brønsted acid sites in zeolites: intrinsic activity, rate-limiting step, and influence of the local structure of the acid sites, J. Catal. 244 (2) (2006) 163–168.
[35] M. sanati, C. Hornell, S.G. Jaras, The oligomerization of alkenes by heterogeneous catalysts, Catalysis 14 (1999) 236–288.. The Royal Society of Chemistry.
[36] G.S. Nivarthy, et al., The role of hydride transfer in zeolite catalyzed isobutane/butene alkylation, in: F.V.M.S.M. Avelino Corma, G.F. José Luis (Eds.), Studies in Surface Science and Catalysis, Elsevier, 2000, pp. 2561–2566.
[37] C.H. Bartholomew, Mechanisms of catalyst deactivation, Appl. Catal. A: Gen. 212 (1–2) (2001) 17–60.
[38] M.J. Wulfers, R.F. Lobo, Assessment of mass transfer limitations in oligomerization of butene at high pressure on H-beta, Appl. Catal. A: Gen. 505 (2015) 394–401.
[39] A.N. Mlinar, et al., Propene oligomerization over Ni-exchanged Na-X zeolites, J. Catal. 296 (2012) 156–164.
[40] A.N. Mlinar, et al., Selective propene oligomerization with nickel(II)-based metal–organic frameworks, ACS Catal. (2014) 717–721.
[42] J.K. Reddy, et al., Effect of morphology and particle size of ZSM-5 on catalytic performance for ethylene conversion and heptane cracking, J. Catal. 289 (2012) 53–61.
[43] Lu Li, S.C. Elena Groppo, Einar Sagstuen, Silvia Bordiga, Unni Olsbye, Klaus-Joachim Jens, Characterization of the NiSO4 site on a NiSO4-ReOx/γ-Al2O3 catalyst for tandem conversion of ethylene to propylene, Catal. Sci. Technol. (2016) Manuscript submitted for publication.
[44] G.J.P. Britovsek, et al., Ethylene oligomerization beyond Schulz–Flory distributions, ACS Catal. 5 (11) (2015) 6922–6925.
[45] R.A. Alberty, C.A. Gehrig, Standard chemical thermodynamic properties of alkene isomer groups, J. Phys. Chem. Ref. Data 14 (3) (1985) 803–820.
[46] M.D. Leatherman, S.A. Svejda, L.K. Johnson, M.J. Brookhart, Am. Chem. Soc. 125 (2003) 3068–3081, http://dx.doi.org/10.1021/ja021071w.

Supporting information

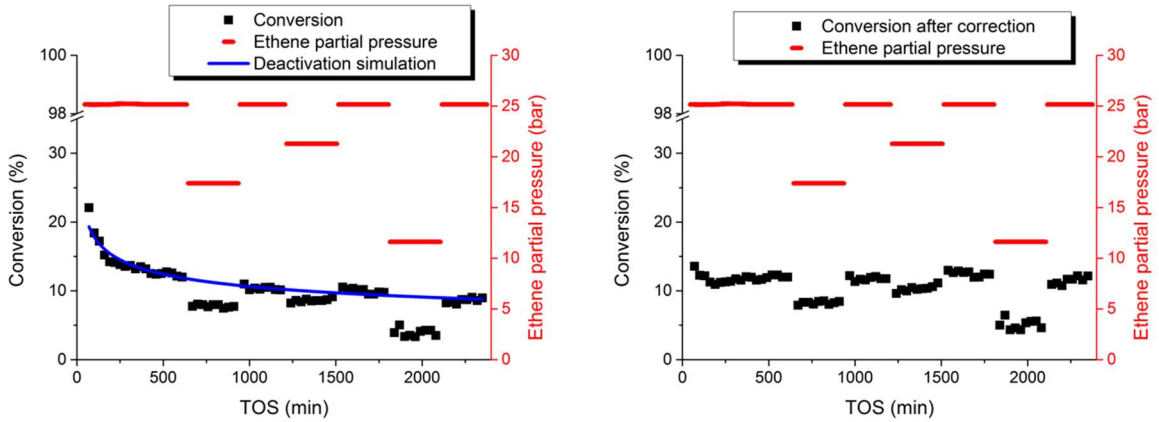

Figure SI 1: Left: Deactivation simulation based on standard condition (29 bar total pressure where P_{ethene} = 25.1 bar and P_{inert} = 3.9 bar and T = 120 °C). Right: Conversion versus TOS, after correcting for deactivation

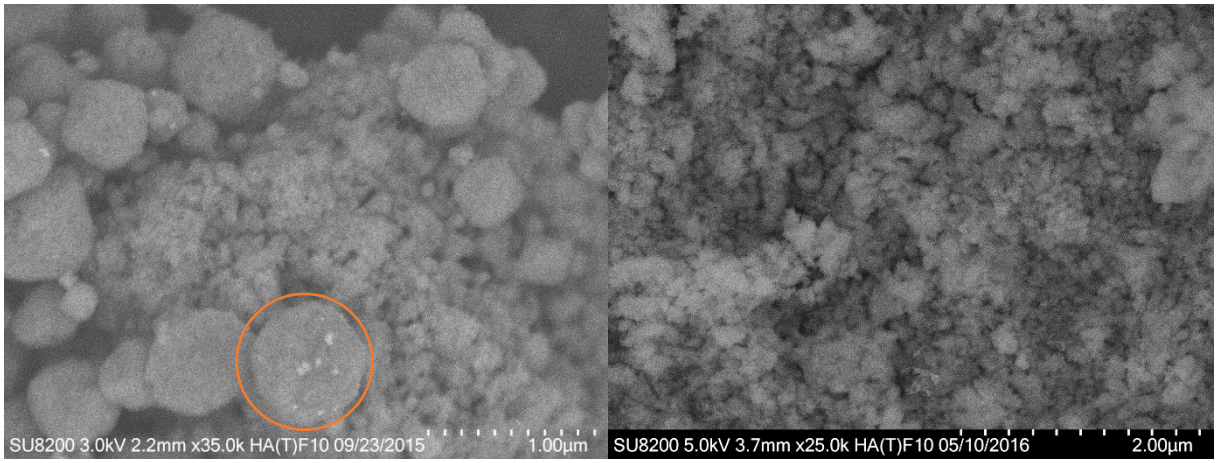

Figure SI 2: Backscattered electron picture of Ni-H-Beta(m) (left) and Ni-Na-Beta(n) (right)

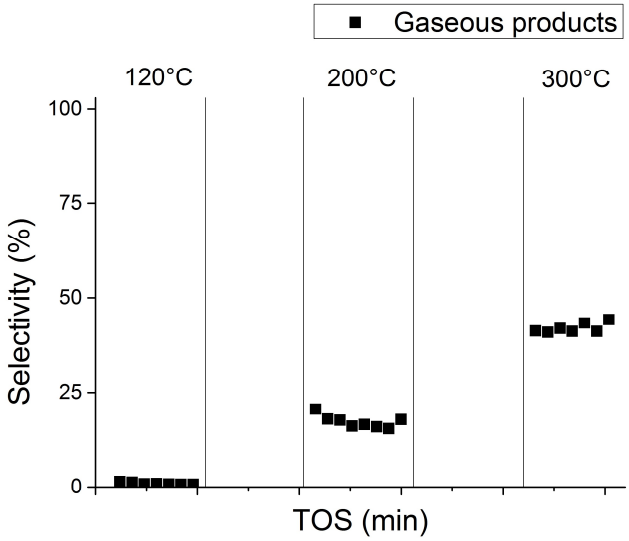

Figure SI 3: Selectivity towards gaseous products at 120, 200 and 300°C for H-Beta(m)

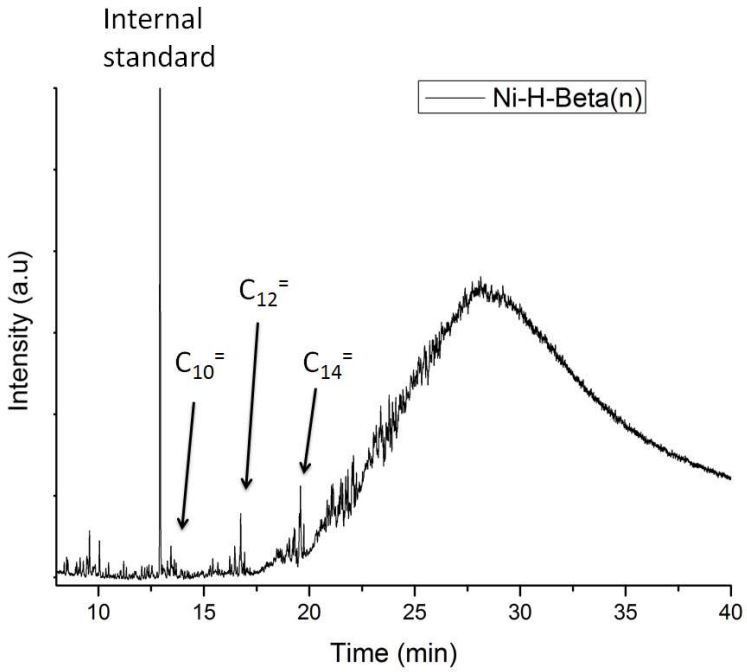

Figure SI 4: Gas chromatogram of the retained hydrocarbons in the spent Ni-H-Beta(n) catalyst, extracted in dichloromethane

II

ACS Catalysis

Letter

Cite This: ACS Catal. 2019, 9, 5645−5650

pubs.acs.org/acscatalysis

Ethene Dimerization on Zeolite-Hosted Ni Ions: Reversible Mobilization of the Active Site

Rasmus Yding Brogaard,*[,†,‡,¶] Mustafa Kømurcu,[†] Michael Martin Dyballa,[†] Alexandru Botan,[§] Veronique Van Speybroeck,[‡] Unni Olsbye,*[,†] and Kristof De Wispelaere*[,‡]

[†]Department of Chemistry, Centre for Materials and Nanoscience (SMN), University of Oslo, P.O. Box 1033, Blindern, NO-0315 Oslo, Norway

[‡]Center for Molecular Modeling (CMM), Ghent University, Tech Lane Ghent Science Park Campus A, Technologiepark 46, 9052 Zwijnaarde, Belgium

[§]Department of Physics, Centre for Materials and Nanoscience (SMN), University of Oslo, P.O. Box 1033, Blindern, NO-0315 Oslo, Norway

Supporting Information

ABSTRACT: The active site in ethene oligomerization catalyzed by Ni-zeolites is proposed to be a mobile Ni(II) complex, based on density functional theory-based molecular dynamics (DFT-MD) simulations corroborated by continuous-flow experiments on Ni-SSZ-24 zeolite. The results of the simulations at operating conditions show that ethene molecules reversibly mobilize the active site as they exchange with the zeolite as ligands on Ni during reaction. Microkinetic modeling was conducted on the basis of free-energy profiles derived with DFT-MD for oligomerization on these mobile $[(ethene)_2\text{-Ni-alkyl}]^+$ species. The model reproduces the experimentally observed high selectivity to dimerization and indicates that the mechanism is consistent with the observed second-order rate dependence on ethene pressure.

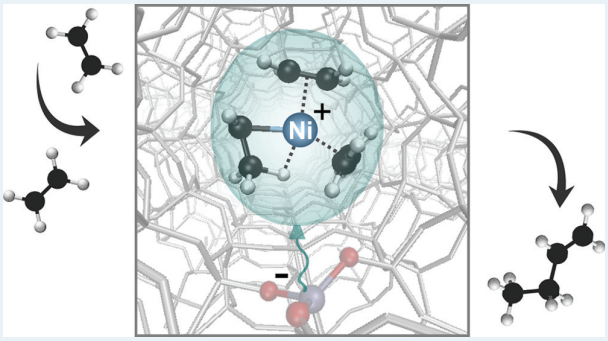

KEYWORDS: *adsorption, host−guest systems, molecular dynamics, agostic interactions, alkene oligomerization, homogeneous catalysis*

Homogeneous and heterogeneous catalysts are traditionally distinguished by the active site being either in solution or anchored on a support. However, recent works have revealed heterogeneous catalysts where the active sites are mobilized: selective catalytic reduction of nitrogen oxides with ammonia in Cu-SSZ-13 zeolite[1] and with hydrocarbons in Ag-ZSM-5 zeolite,[2] reactant-mobilized protons in methanol to hydrocarbons conversion in H-ZSM-5,[3] and ethylene dimerization/hydrogenation on Rh sites in Y zeolite.[4] In this work, we present findings on a reaction, ethene oligomerization in Ni-SSZ-24 zeolite, that indicate that the active site is reversibly mobilized and anchored to the support *during* the catalytic cycle.

There is increasing interest in selective oligomerization of alkenes, and in particular heterogeneous catalysts for ethene dimerization, as it is both a fundamentally challenging topic of catalysis and a versatile reaction for the chemical industry, such as forming butene from biobased ethylene.[5] Ni-aluminosilicates have long been known as promising heterogeneous catalysts.[6] Intriguingly, they work without the alkylaluminoxane cocatalysts required for homogeneous and metal−organic framework (MOF)-based heterogeneous catalysts.[7] Nevertheless, there is accumulating evidence provided by us and others that the reaction follows the Cossee−Arlman mechanism (Scheme 1)[8−11] known from homogeneous catalysis. The three-dimensional structure of the Ni-aluminosilicates plays a central role in alkene oligomerization: experimental results show that dimer formation is first order in alkene pressure on Ni-silicaalumina[10,12] but second order in Ni-zeolites.[12,13] 1-Butene formation is also second order in mesoporous Ni-silicaalumina at low temperatures, where it was demonstrated that condensation of ethene in the pores stabilized catalytic activity.[14] These observations suggest that surrounding molecules can have a significant influence on alkene oligomerization in Ni-aluminosilicates, an influence we for the first time elucidate with molecular simulations mimicking operating conditions.

We simulated ethene oligomerization in Ni-SSZ-24 using density-functional-theory-based molecular dynamics (DFT-MD) simulations and advanced free-energy sampling techni-

Received: February 18, 2019
Revised: May 15, 2019
Published: May 22, 2019

Scheme 1. Cossee−Arlman Catalytic Cycle of Ethene Oligomerization in Ni(II) Cationic Complexes

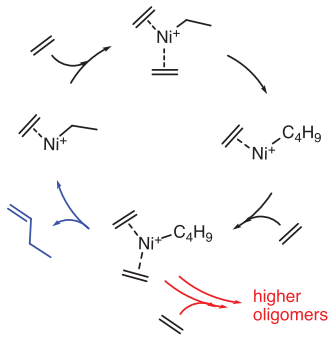

ques. Such an approach has proven to account for the complexity of catalytic reactions at operating conditions by allowing for dynamic active sites and the influence of surrounding molecules.[3,15] The latter was found to be critical to investigate the nature of the active site in the presence of multiple ethene molecules. The computational results show a remarkable resemblance between the active sites in Ni-zeolites and homogeneous catalysts for alkene oligomerization, as ethene molecules reversibly mobilize the Ni site inside the zeolite pores. Continuous-flow experiments were conducted to verify the corresponding kinetic parameters predicted from theory. This leads us to predict that the active site within the Ni-zeolite dynamically crosses the border between homogeneous and heterogeneous catalysis throughout the reaction.

The computational part of this work takes its starting point in the Cossee−Arlman cycle, shown in Scheme 1, inferring that the Ni-ethyl species initially forms in situ by reaction between Ni(II) ions and ethene (Section S1).[11] We seek to unravel the dynamics of the active site at operating conditions by simulating the catalytic cycle in Ni-SSZ-24 zeolite with DFT-MD (see details in Computational and Experimental Methods), starting from the simplest Cossee−Arlman species [ethene-Ni-ethyl]$^+$ surrounded by 2 ethene molecules in the micropore of the simulation cell (Section S2.2). This ethene loading corresponds to equilibrium at typical experimental conditions of 120 °C and 25 bar ethene pressure,[10,12] as evidenced by Grand Canonical Monte Carlo simulations (Section S3). We have investigated several reaction steps and obtain good agreement in the free-energy barriers of the few of these steps that were investigated in our previous work (Section S2.4).[8] We collected the free-energy profiles of the elementary steps that make up the most favorable pathways for ethene oligomerization in the diagram shown in Figure 1. Note that alkene adsorption/desorption in this diagram occurs from/to the zeolite pore encompassing the adsorbates. By using the equilibrium loading of two ethene molecules surrounding the [ethene-Ni-ethyl]$^+$ species, we ensure that in this state the free energy of ethene in the pore is equivalent to that of gas phase ethene at 120 °C and 25 bar.

Remarkably, the catalytic cycle of oligomerization proceeds on mobile complexes. Such a species is created from [ethene-Ni-ethyl]$^+$ by coordination of an additional ethene to Ni, thereby detaching the Ni complex from the ion-exchange position of the zeolite to create a mobile active site. The mobility is observed in the distribution of Ni−Al distances in Figure 2: the distribution is shifted toward larger values and is wider for the detached [(ethene)$_2$-Ni-ethyl]$^+$ than the anchored species. In the mobile species Ni can achieve its preferred square-planar coordination, realizing the maximal potential of the metal site by opening up a favorable pathway for C−C coupling (vide infra). Figure 2 shows the simulated free-energy profiles for coordination of ethenes on Ni-alkyl

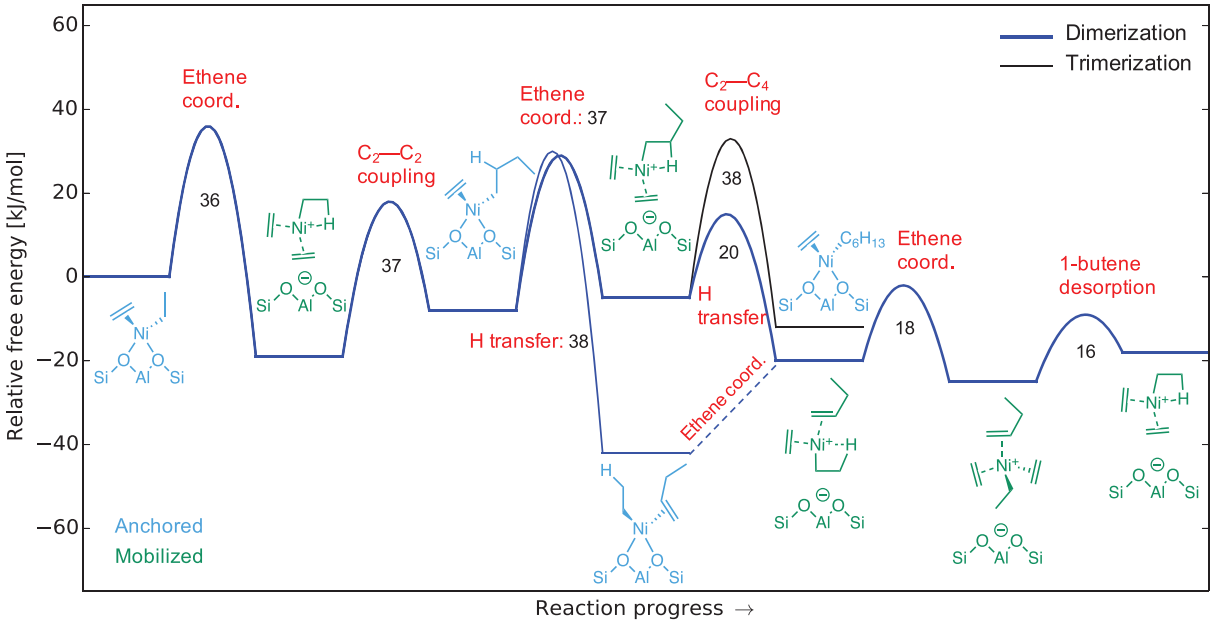

Figure 1. Free-energy diagram for ethene oligomerization pathways in Ni-SSZ-24 zeolite at 25 bar and 120 °C, based on free-energy profiles of elementary steps obtained with DFT-MD umbrella sampling simulations. The reference state is the equilibrium loading of ethene surrounding [ethene-Ni-ethyl]$^+$, as discussed in the text. The numbers indicate intrinsic free energies of activation in kJ/mol. As indicated in the diagram, the [ethyl-Ni-butene]$^+$ species can also be reached by ethene desorption; see Section S2.3 for a detailed discussion of how the diagram was constructed.

DOI: 10.1021/acscatal.9b00721
ACS Catal. 2019, 9, 5645−5650

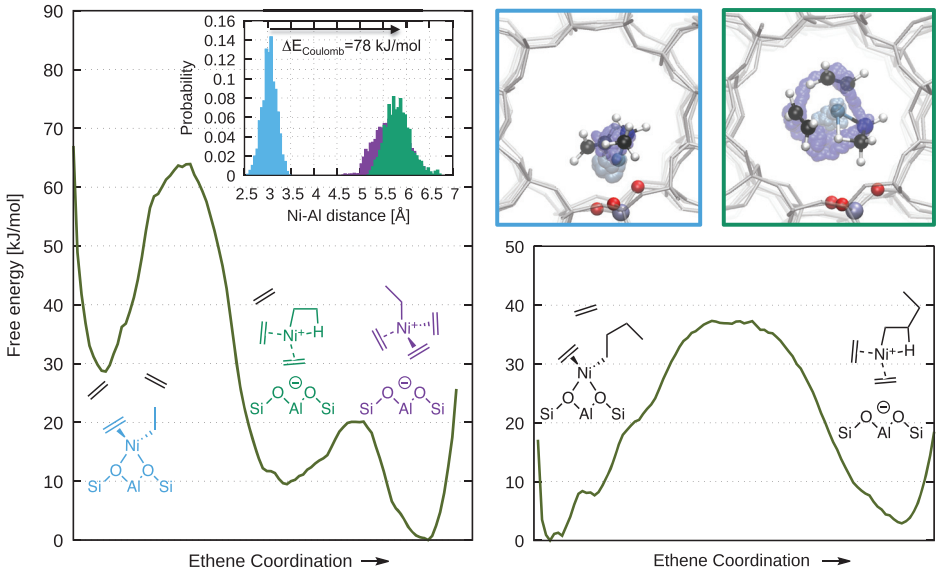

Figure 2. Free-energy profiles for ethene coordination to [ethene-Ni-ethyl]$^+$ (left) and [ethene-Ni-butyl]$^+$ (right) at 25 bar and 120 °C, derived from DFT-MD simulations. The left inset shows histograms of Ni−Al distances, illustrating that the doubly and triply ethene-coordinated Ni-ethyl species are detached from the framework and more mobile than their anchored counterpart. The associated charge-separation energy is estimated to 78 kJ/mol (Section S2.5). The right insets show snapshots from the simulations of the Ni-ethyl species, including the trajectories of the Ni (light blue) and the α alkyl C (dark blue) atoms (Figure S8 shows the butyl analogues).

Table 1. Intrinsic Free-Energy Barriers (kJ/mol) of Ethene Desorption and C−C Coupling in [(ethene)$_x$-Ni-ethyl]$^+$ Species in SSZ-24 Zeolite, Obtained from DFT-MD Simulations at 120 °C (Sections S2.7 and S2.8)

	[ethene-Ni-ethyl]$^+$	[(ethene)$_2$-Ni-ethyl]$^+$	[(ethene)$_3$-Ni-ethyl]$^+$
C−C coupling	77	37	76
ethene desorption	72	54	20

species originally anchored to the zeolite. The results show that [ethene-Ni-ethyl]$^+$ is stabilized by coordination of up to two additional ethene molecules. In [(ethene)$_2$-Ni-ethyl]$^+$, one oxygen coordination is replaced by ethene and the second by an agostic bond with a β hydrogen of the ethyl group, creating a square planar coordination of Ni (Figure 2, right inset). The same is the case for the butyl analogue (Figure S8). This square-planar geometry is preferred for Ni as a d^8 metal when coordinated to strong-field ligands,[16] such as alkyl and hydride.[17]

The mobile Ni complexes resemble a homogeneous oligomerization catalyst in solution; the noncovalent interactions with the zeolite framework parallel the nondirectional stabilization by a solvent shell. However, the positively charged complex is tethered to the zeolite framework by the negative charge of the ion-exchange site. Note that there is a potential energy gain on formation of the [(ethene)$_2$-Ni-ethyl]$^+$ detached species (28 kJ/mol, Section S2.6.1). Ethene coordination thus counteracts the energy required to separate the positive Ni ion from the framework (78 kJ/mol, Figure 2). As complex formation is also favored in free energy (19 kJ/mol, Figure 2), the entropy loss of coordinating ethene is partly compensated by the configurational entropy of the mobile [(ethene)$_2$-Ni-ethyl]$^+$ complex; translation (Figure S9) and rotation (inset of Figure 2). This rotation may also explain why ethene coordination to [ethene-Ni-butyl]$^+$ is favored in potential energy (38 kJ/mol, Section S2.6.1) but slightly disfavored in free energy (3 kJ/mol, Figure 2); the Ni-butyl species is bulkier than the ethyl analogue, limiting rotation in the zeolite micropore (Figure S8).

C−C coupling is the central reaction step in ethene oligomerization, which in the mobile species proceeds through migratory insertion of ethene in the Ni-alkyl bond. We find the intrinsic free-energy barrier in [(ethene)$_2$-Ni-ethyl]$^+$ to be significantly lower than in both the anchored [ethene-Ni-ethyl]$^+$ species and the mobile [(ethene)$_3$-Ni-ethyl]$^+$ species (Table 1). We explain this trend using Hammond's postulate[18] considering the structures shown in Figure 3; C−C coupling in [ethene-Ni-ethyl]$^+$ is an endergonic reaction (Figure S11) leading to a large activation barrier with a late transition state that resembles a [Ni-butyl]$^+$ product with a γ-agostic hydrogen bond. In [(ethene)$_2$-Ni-ethyl]$^+$, the reaction is exergonic (Figure S13), leading to a low activation barrier with an early transition state that resembles the reactant with the favorable square-planar coordination of Ni. In [(ethene)$_3$-Ni-ethyl]$^+$ the transition state (trigonal bipyramid) resembles neither the reactant (half trigonal bipyramid) nor the product ([(ethene)$_2$-Ni-butyl]$^+$, square planar) and is hence significantly higher in free energy than either state (Figure S14). The Ni-butyl analogues exhibit the same trend (Figures S11 and S13).

Following C−C coupling, the reaction proceeds from [(ethene)$_2$-Ni-butyl]$^+$ via transfer of a β hydrogen of the butyl chain to form 1-butene, which subsequently desorbs. Like for C−C coupling, the hydrogen transfer has the lowest barrier in the mobile [(ethene)$_2$-Ni-butyl]$^+$ species (20 kJ/mol, Figures 1 and S21), as hydrogen is already involved in an

DOI: 10.1021/acscatal.9b00721
ACS Catal. 2019, 9, 5645−5650

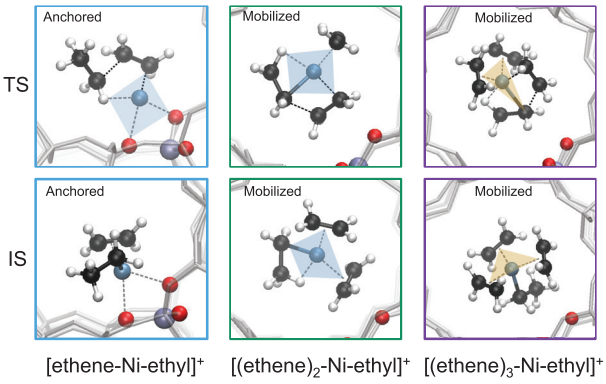

Figure 3. Snapshots from DFT-MD umbrella simulations of the initial (IS) and transition states (TS) of C−C coupling in $[(ethene)_x$-Ni-ethyl$]^+$ species in SSZ-24 zeolite. Planes of square and trigonal coordination are shown in blue and yellow, respectively.

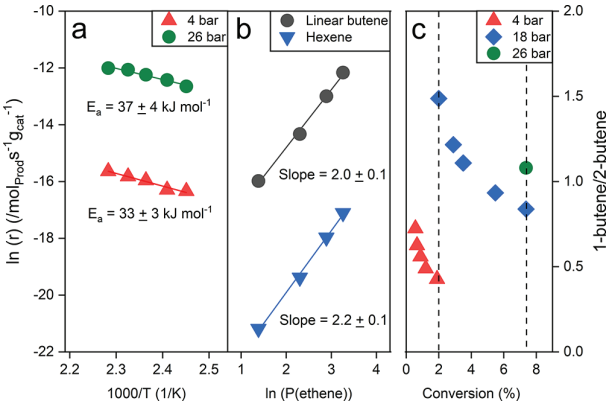

Figure 4. Results from continuous-flow experiments on ethene oligomerization in Ni-SSZ-24: (a) Arrhenius plot for butene formation at 4 and 26 bar ethene pressure, (b) reaction order of butene and hexene formation at 150 °C, and (c) butene isomer selectivity at 150 °C. All results were obtained at differential ethene conversions of 1−7%.

agostic bond to Ni prior to reaction (see Ni-ethyl analogue in Figure 3). In contrast, the anchored [ethene-Ni-butyl]$^+$ species undergoes a significant rearrangement to reach the transition state, reflected in a higher barrier (38 kJ/mol, Figures 1 and S18).

The last step toward dimerization is desorption of 1-butene. Analogously to ethene (Table 1), the 1-butene desorption barrier decreases with ethene coordination and is hence lowest in $[(ethene)_2$-ethyl-Ni-1-butene$]^+$ (Table S5). This can be explained by the late transition state of desorption: in this species, the 1-butene weakly interacts with the favored square-planar $[(ethene)_2$-Ni-ethyl$]^+$ (Figure S22). In the latter species, the catalytic cycle is closed.

In summary, we have used DFT-MD to predict that both ethene dimerization and trimerization are catalyzed by positively charged Ni complexes mobilized by ethene coordination. The transition states involved in butene formation are slightly lower in free energy than that for hexene formation (Figure 1), indicating a preference toward butene over higher oligomers. Indeed, when employing the free-energy profiles in a microkinetic model (Section S4), we obtain a rate of formation of 1-butene that is 2 orders of magnitude higher than that of 1-hexene (Section S4.3).

We now consider experimental results to verify our computational findings. Ethene oligomerization was investigated in continuous-flow experiments on Ni-SSZ-24 zeolite (see details in Computational and Experimental Methods). The catalyst achieves a selectivity of more than 98% to butenes at ethene pressures ranging from 4 to 26 bar (Section S5.3), in agreement with the computational result that the production rate of butene is 2 orders of magnitude higher than that of hexene as a representative of higher oligomers. Figure 4 shows that the rate of butene (and hexene) formation is second order in ethene pressure and that the apparent activation energy is virtually pressure-independent. These findings strongly suggest that the oligomerization mechanism is the same over a wide pressure range. The observed reaction order agrees with microkinetic modeling based on the free-energy profiles shown in Figure 1, where oligomerization occurs on mobile active sites. Note that a second order is only obtained from the model when [ethyl-Ni-alkene]$^+$ species are the most abundant adsorbates, the catalyst resting states (Table S7, Section S4.3). We note that the predicted coverage of [ethyl-Ni-alkene]$^+$ and hence the reaction order is sensitive to the free energy of these species (Table S7), which is associated with some uncertainty (Section S2.3). However, a zeolite-anchored [ethyl-Ni-alkene]$^+$ resting state is consistent with recent experimental X-ray absorption data, which indicate that in the catalyst resting state in Ni-Beta zeolite, Ni is in tetrahedral coordination with oxygens in the first coordination shell.[11] In the context of resting states it is instructive to consider the concept of *the energetic span* introduced by Kozuch and Shaik: the largest free-energy difference between an adsorbate and a transition state along the catalytic cycle, corresponding to the apparent free energy of activation.[19] While being cautious about using the free energies from Figure 1 directly (Section S2.3), we derive an energetic span for butene formation of 71 kJ/mol between the [ethyl-Ni-butene]$^+$ and the transition state of hydrogen transfer, which is in fairly good agreement with the 58 kJ/mol derived from the experiments (Section S5.3.1).

Finally, the experimental results indicate that both 1- and 2-butenes are primary products (Section S5.3), as was also observed on Ni-Beta.[11] This supports the Cossee−Arlman mechanism, as the [ethyl-Ni-butene]$^+$ species can isomerize between 1- and 2-butene through β-hydrogen elimination on the Ni site prior to desorption (Figure S17), analogously to homogeneous catalysts.[20] Note also that 1-butene selectivity increases with pressure (Figure 4), contrary to what would be expected for isomerization at Brønsted acid sites, but paralleling the results of previous work by Agirrezabal-Telleria and Iglesia on mesoporous Ni-silicaalumina.[14] Interestingly, the same work demonstrated stabilization of catalytic activity at subambient temperatures when ethene condenses in the mesopores.[14] Such conditions likely favor coordination of multiple ethene molecules to form the mobile sites described here (Section S6). These sites may be involved in the stabilization, as they facilitate butene desorption over further oligomerization.

In conclusion, we have conducted an experimental and computational investigation of ethene oligomerization in Ni-SSZ-24 zeolite. The computational results allow us to make detailed predictions about the reaction at operating conditions; two ethene molecules adsorb on Ni-alkyl species, creating mobile active sites in the zeolite pores. The mobilization is reversible, as ethene dynamically exchanges with oxygens of

DOI: 10.1021/acscatal.9b00721
ACS Catal. 2019, 9, 5645−5650

the zeolite support as ligand on Ni *during* the reaction. Microkinetic modeling based on calculated free-energy profiles reproduces the experimentally observed relative production rate of butene over higher oligomers of 10^2. The model indicates that the proposed mechanism leads to a second-order rate dependence on ethene pressure as experimentally observed here and elsewhere.[12,14] An analogous mechanism may explain the second-order rate dependence observed in 1-butene dimerization.[13] Such reactant-mobilized active sites have also been observed in selective catalytic reduction of nitrogen oxides with ammonia in Cu-SSZ-13 zeolite[1] and with hydrocarbons in Ag-ZSM-5,[2] in methanol to hydrocarbons conversion in H-ZSM-5,[3] and ethylene dimerization/hydrogenation on Rh sites in Y zeolite.[4] Together these works present materials that appear as hybrids between heterogeneous and homogeneous catalysts, highlighting an intriguing regime of catalysis[21] that likely extends beyond the examples known to date.

COMPUTATIONAL AND EXPERIMENTAL METHODS

Density functional theory (DFT)-based Molecular Dynamics (DFT-MD) simulations were carried out with CP2K,[22] versions 2.6 and 3.0.[23] Energies and forces were calculated from DFT based on a mixed Gaussian and plane wave approach[24] using the revPBE functional[25] with Grimme D3 dispersion correction.[26] DFT-MD calculations were carried out nonspinpolarized, as our previous work determined the singlet state to be the most stable for the Ni(II) species investigated here.[8] The majority of the simulations employed a super cell constructed by repeating the AFI unit cell twice along the channel direction (1 × 1 × 2) and making one Si/Al substitution (Si/Al = 47), while a larger super cell (Si/Al = 72) was used in a few simulations (Figure S23). Enhanced free-energy sampling in the DFT-MD simulations was done using umbrella sampling[27,28] with quadratic potentials by interfacing CP2K with PLUMED 2.[29] Free-energy profiles of elementary reaction steps were computed from the output of umbrella simulations along collective variables, using the Weighted Histogram Analysis Method (WHAM).[27] Monte Carlo simulations were carried out using LAMMPS,[30] while microkinetic modeling was conducted with CatMAP.[31] Graphics of molecular structures from the DFT-MD simulations were created using POV-Ray 3.6 and VMD 1.9.1.[32]

The synthesis of SSZ-24 was conducted as described in literature.[33] The zeolite was ion-exchanged five consecutive times with 0.1 M $Ni(NO_3)_2$(aq), washed and calcined to form Ni-SSZ-24, Si/Al = 80, Ni/Al = 0.34. Kinetic experiments were carried out in a continuous-flow, fixed-bed, stainless steel reactor. Standard measurement conditions were 150 °C and 30 bar total pressure, P(ethene)=26 bar, P(inert)=4 bar, with a total flow rate of 30 mL/min (contact time at STP: 6.7 $mg_{cat}\cdot min\cdot mL_{ethene}^{-1}$). A small fraction of the effluent was analyzed on an online gas chromatograph. Carbon mass balances closed witin 2%. Further computational and experimental details can be found in the Supporting Information.

ASSOCIATED CONTENT

Supporting Information

The Supporting Information is available free of charge on the ACS Publications website at DOI: 10.1021/acscatal.9b00721.

Complete body of DFT-MD results, results of Monte Carlo simulations, setup and results of microkinetic modeling, additional experimental details and results (PDF)

CatMAP files (ZIP)

AUTHOR INFORMATION

Corresponding Authors

*E-mail: rabr@topsoe.com.
*E-mail: unni.olsbye@kjemi.uio.no.
*E-mail: kristof.dewispelaere@ugent.be.

ORCID

Rasmus Yding Brogaard: 0000-0001-7882-9183
Michael Martin Dyballa: 0000-0002-8883-1145
Veronique Van Speybroeck: 0000-0003-2206-178X
Unni Olsbye: 0000-0003-3693-2857

Present Address

¶R.Y.B.: Haldor Topsøe A/S, Nymøllevej 55, DK-2800 Kgs. Lyngby, Denmark

Notes

The authors declare no competing financial interest.

ACKNOWLEDGMENTS

This research was funded in part by the Research Council of Norway through the OLIGOM (224980) and CONFINE (250795) projects. R.Y.B. thanks the University of Oslo for the Young Scientist Mobility Grant. V.V.S. and R.Y.B acknowledge funding from the European Union's Horizon 2020 research and innovation program (consolidator ERC grant agreement No. 647755 - DYNPOR (2015-2020)). The work is also supported by the Research Board of Ghent University (BOF). The Norwegian Metacenter for High Performance Computing (NOTUR) and Prof. Stian Svelle are thanked for computing resources (nn4683k). Ghent University (Stevin Supercomputer Infrastructure) and the VSC (Flemish Supercomputer Center), funded by the Research Foundation Flanders (FWO), are also thanked for computational resources. K.D.W. is a fellow funded by the FWO (FWO16-PDO-047).

REFERENCES

(1) Paolucci, C.; Khurana, I.; Parekh, A. A.; Li, S.; Shih, A. J.; Li, H.; Di Iorio, J. R.; Albarracin-Caballero, J. D.; Yezerets, A.; Miller, J. T.; Delgass, W. N.; Ribeiro, F. H.; Schneider, W. F.; Gounder, R. Dynamic Multinuclear Sites Formed by Mobilized Copper Ions in NO_x Selective Catalytic Reduction. *Science* **2017**, *357*, 898−903.

(2) Shibata, J.; Shimizu, K.-i.; Takada, Y.; Shichi, A.; Yoshida, H.; Satokawa, S.; Satsuma, A.; Hattori, T. Structure of Active Ag Clusters in Ag Zeolites for SCR of NO by Propane in the Presence of Hydrogen. *J. Catal.* **2004**, *227*, 367−374.

(3) Moors, S. L. C.; De Wispelaere, K.; Van der Mynsbrugge, J.; Waroquier, M.; Van Speybroeck, V. Molecular Dynamics Kinetic Study on the Zeolite-Catalyzed Benzene Methylation in ZSM-5. *ACS Catal.* **2013**, *3*, 2556−2567.

(4) Serna, P.; Gates, B. C. Zeolite-Supported Rhodium Complexes and Clusters: Switching Catalytic Selectivity by Controlling Structures of Essentially Molecular Species. *J. Am. Chem. Soc.* **2011**, *133*, 4714−4717.

(5) (a) Hulea, V. Toward Platform Chemicals from Bio-Based Ethylene: Heterogeneous Catalysts and Processes. *ACS Catal.* **2018**, *8*, 3263−3279. (b) Nicholas, C. P. Applications of Light Olefin Oligomerization to the Production of Fuels and Chemicals. *Appl. Catal., A* **2017**, *543*, 82−97.

DOI: 10.1021/acscatal.9b00721
ACS Catal. 2019, 9, 5645−5650

(6) Finiels, A.; Fajula, F.; Hulea, V. Nickel-based Solid Catalysts for Ethylene Oligomerization - a Review. *Catal. Sci. Technol.* **2014**, *4*, 2412−2426.
(7) (a) Canivet, J.; Aguado, S.; Schuurman, Y.; Farrusseng, D. MOF-Supported Selective Ethylene Dimerization Single-Site Catalysts Through One-Pot Postsynthetic Modification. *J. Am. Chem. Soc.* **2013**, *135*, 4195−4198. (b) Madrahimov, S. T.; Gallagher, J. R.; Zhang, G.; Meinhart, Z.; Garibay, S. J.; Delferro, M.; Miller, J. T.; Farha, O. K.; Hupp, J. T.; Nguyen, S. T. Gas-Phase Dimerization of Ethylene under Mild Conditions Catalyzed by MOF Materials Containing (bpy)Ni^{II} Complexes. *ACS Catal.* **2015**, *5*, 6713−6718. (c) Bernales, V.; League, A. B.; Li, Z.; Schweitzer, N. M.; Peters, A. W.; Carlson, R. K.; Hupp, J. T.; Cramer, C. J.; Farha, O. K.; Gagliardi, L. Computationally Guided Discovery of a Catalytic Cobalt-Decorated Metal-Organic Framework for Ethylene Dimerization. *J. Phys. Chem. C* **2016**, *120*, 23576−23583. (d) Metzger, E. D.; Comito, R. J.; Hendon, C. H.; Dincă, M. Mechanism of Single-Site Molecule-Like Catalytic Ethylene Dimerization in Ni-MFU-4l. *J. Am. Chem. Soc.* **2017**, *139*, 757−762. (e) Liu, J.; Ye, J.; Li, Z.; Otake, K.-i.; Liao, Y.; Peters, A. W.; Noh, H.; Truhlar, D. G.; Gagliardi, L.; Cramer, C. J.; Farha, O. K.; Hupp, J. T. Beyond the Active Site: Tuning the Activity and Selectivity of a Metal-Organic Framework-Supported Ni Catalyst for Ethylene Dimerization. *J. Am. Chem. Soc.* **2018**, *140*, 11174−11178.
(8) Brogaard, R. Y.; Olsbye, U. Ethene Oligomerization in Ni-containing Zeolites: Theoretical Discrimination of Reaction Mechanisms. *ACS Catal.* **2016**, *6*, 1205−1214.
(9) Forget, S.; Olivier-Bourbigou, H.; Delcroix, D. Homogeneous and Heterogeneous Nickel-Catalyzed Olefin Oligomerization: Experimental Investigation for a Common Mechanistic Proposition and Catalyst Optimization. *ChemCatChem* **2017**, *9*, 2408−2417.
(10) Toch, K.; Thybaut, J.; Marin, G. Ethene Oligomerization on Ni-SiO_2-Al_2O_3: Experimental Investigation and Single-Event Micro-Kinetic Modeling. *Appl. Catal., A* **2015**, *489*, 292−304.
(11) Joshi, R.; Zhang, G.; Miller, J. T.; Gounder, R. Evidence for the Coordination-Insertion Mechanism of Ethene Dimerization at Nickel Cations Exchanged onto Beta Molecular Sieves. *ACS Catal.* **2018**, *8*, 11407−11422.
(12) Henry, R.; Komurcu, M.; Ganjkhanlou, Y.; Brogaard, R. Y.; Lu, L.; Jens, K.-J.; Berlier, G.; Olsbye, U. Ethene Oligomerization on Nickel Microporous and Mesoporous-Supported Catalysts: Investigation of the Active Sites. *Catal. Today* **2018**, *299*, 154−163.
(13) Ehrmaier, A.; Liu, Y.; Peitz, S.; Jentys, A.; Chin, Y.-H. C.; Sanchez-Sanchez, M.; Bermejo-Deval, R.; Lercher, J. Dimerization of Linear Butenes on Zeolite-Supported Ni^{2+}. *ACS Catal.* **2019**, *9*, 315−324.
(14) Agirrezabal-Telleria, I.; Iglesia, E. Stabilization of Active, Selective, and Regenerable Ni-based Dimerization Catalysts by Condensation of Ethene within Ordered Mesopores. *J. Catal.* **2017**, *352*, 505−514.
(15) (a) Van Speybroeck, V.; De Wispelaere, K.; Van der Mynsbrugge, J.; Vandichel, M.; Hemelsoet, K.; Waroquier, M. First Principle Chemical Kinetics in Zeolites: the Methanol-to-Olefin Process as a Case Study. *Chem. Soc. Rev.* **2014**, *43*, 7326−7357. (b) De Wispelaere, K.; Ensing, B.; Ghysels, A.; Meijer, E. J.; Van Speybroeck, V. Complex Reaction Environments and Competing Reaction Mechanisms in Zeolite Catalysis: Insights from Advanced Molecular Dynamics. *Chem. - Eur. J.* **2015**, *21*, 9385−9396. (c) De Wispelaere, K.; Wondergem, C. S.; Ensing, B.; Hemelsoet, K.; Meijer, E. J.; Weckhuysen, B. M.; Van Speybroeck, V.; Ruiz-Martínez, J. Insight into the Effect of Water on the Methanol-to-Olefins Conversion in H-SAPO-34 from Molecular Simulations and in Situ Microspectroscopy. *ACS Catal.* **2016**, *6*, 1991−2002. (d) De Wispelaere, K.; Vanduyfhuys, L.; Van Speybroeck, V. *Modelling and Simulation in the Science of Micro- and Meso-Porous Materials*; Elsevier, 2017; Chapter entitled Entropy Contributions to Transition State Modelling. (e) Li, G.; Pidko, E. A. The Nature and Catalytic Function of Cation Sites in Zeolites: a Computational Perspective. *ChemCatChem* **2019**, *11*, 134−156.
(16) Gray, H. B.; Ballhausen, C. J. A Molecular Orbital Theory for Square Planar Metal Complexes. *J. Am. Chem. Soc.* **1963**, *85*, 260−265.
(17) Chatt, J.; Hayter, R. G. 167. Ligand Field Strengths of the Halide, Methyl, Phenyl, and Hydride Anions. *J. Chem. Soc.* **1961**, 772−774.
(18) Hammond, G. S. A. Correlation of Reaction Rates. *J. Am. Chem. Soc.* **1955**, *77*, 334−338.
(19) Kozuch, S.; Shaik, S. How to Conceptualize Catalytic Cycles? The Energetic Span Model. *Acc. Chem. Res.* **2011**, *44*, 101−110.
(20) Ittel, S. D.; Johnson, L. K.; Brookhart, M. Late-Metal Catalysts for Ethylene Homo- and Copolymerization. *Chem. Rev.* **2000**, *100*, 1169−1204.
(21) Shamzhy, M.; Opanasenko, M.; Concepción, P.; Martínez, A. New Trends in Tailoring Active Sites in Zeolite-Based Catalysts. *Chem. Soc. Rev.* **2019**, *48*, 1095−1149.
(22) Hutter, J.; Iannuzzi, M.; Schiffmann, F.; VandeVondele, J. CP2K: Atomistic Simulations of Condensed Matter Systems. *WIREs Comput. Mol. Sci.* **2014**, *4*, 15−25.
(23) *CP2K*, version 3.0 or higher, the CP2K developers group. CP2K is freely available from http://www.cp2k.org.
(24) VandeVondele, J.; Krack, M.; Mohamed, F.; Parrinello, M.; Chassaing, T.; Hutter, J. Quickstep: Fast and Accurate Density Functional Calculations using a Mixed Gaussian and Plane Waves Approach. *Comput. Phys. Commun.* **2005**, *167*, 103−128.
(25) (a) Perdew, J. P.; Burke, K.; Ernzerhof, M. Generalized Gradient Approximation Made Simple. *Phys. Rev. Lett.* **1996**, *77*, 3865−3868. (b) Zhang, Y.; Yang, W. Comment on "Generalized Gradient Approximation Made Simple. *Phys. Rev. Lett.* **1998**, *80*, 890−890.
(26) (a) Grimme, S.; Antony, J.; Ehrlich, S.; Krieg, H. A Consistent and Accurate Ab Initio Parametrization of Density Functional Dispersion Correction (DFT-D) for the 94 Elements H-Pu. *J. Chem. Phys.* **2010**, *132*, 154104. (b) Grimme, S.; Ehrlich, S.; Goerigk, L. Effect of the Damping Function in Dispersion Corrected Density Functional Theory. *J. Comput. Chem.* **2011**, *32*, 1456−1465.
(27) Kumar, S.; Rosenberg, J. M.; Bouzida, D.; Swendsen, R. H.; Kollman, P. A. The Weighted Histogram Analysis Method for Free-energy Calculations on Biomolecules. I. The method. *J. Comput. Chem.* **1992**, *13*, 1011−1021.
(28) Ensing, B.; Laio, A.; Parrinello, M.; Klein, M. L. A Recipe for the Computation of the Free Energy Barrier and the Lowest Free Energy Path of Concerted Reactions. *J. Phys. Chem. B* **2005**, *109*, 6676−6687.
(29) Tribello, G. A.; Bonomi, M.; Branduardi, D.; Camilloni, C.; Bussi, G. PLUMED 2: New Feathers for an Old Bird. *Comput. Phys. Commun.* **2014**, *185*, 604−613.
(30) Plimpton, S. Fast Parallel Algorithms for Short-Range Molecular Dynamics. *J. Comput. Phys.* **1995**, *117*, 1−19.
(31) Medford, A. J.; Shi, C.; Hoffmann, M. J.; Lausche, A. C.; Fitzgibbon, S. R.; Bligaard, T.; Nørskov, J. K. CatMAP: A Software Package for Descriptor-Based Microkinetic Mapping of Catalytic Trends. *Catal. Lett.* **2015**, *145*, 794−807.
(32) Humphrey, W.; Dalke, A.; Schulten, K. VMD - Visual Molecular Dynamics. *J. Mol. Graphics* **1996**, *14*, 33−38.
(33) Kubota, Y.; Maekawa, H.; Miyata, S.; Tatsumi, T.; Sugi, Y. Hydrothermal Synthesis of Metallosilicate SSZ-24 from Metallosilicate Beta as Precursors. *Microporous Mesoporous Mater.* **2007**, *101*, 115−126.

DOI: 10.1021/acscatal.9b00721
ACS Catal. 2019, 9, 5645−5650

Note: The supporting information file for **Paper II** have not been included in this document due to length restrictions.

III

ARTICLE IN PRESS

Catalysis Today xxx (xxxx) xxx

Contents lists available at ScienceDirect

Catalysis Today

journal homepage: www.elsevier.com/locate/cattod

Co-catalyst free ethene dimerization over Zr-based metal-organic framework (UiO-67) functionalized with Ni and bipyridine

Mustafa Kømurcu [a], Andrea Lazzarini [a], Gurpreet Kaur [a], Elisa Borfecchia [b], Sigurd Øien-Ødegaard [a], Diego Gianolio [c], Silvia Bordiga [a,b], Karl Petter Lillerud [a], Unni Olsbye [a,*]

[a] Department of Chemistry, University of Oslo, P.O. Box 1033, Oslo, 0315, Norway
[b] University of Turin, Department of Chemistry, Via P. Giuria 7, Turin, 10125, Italy
[c] Diamond Light Source, Harwell Science and Innovation Campus, Chilton, Didcot, OX11 0DE, UK

ARTICLE INFO

Keywords:
Ethene dimerization
Linear alkenes
Ni-MOF
Heterogeneous catalysis
Co-catalyst free

ABSTRACT

Ni functionalized metal organic frameworks (MOF) are promising heterogeneous ethene dimerization catalysts. Activities comparable to or higher than Ni-aluminosilicates have been reported in literature. However, unlike the Ni-aluminosilicates, those Ni-MOFs require a large excess of co-catalyst to initiate the dimerization process and some catalysts generate polymers which lead to catalyst deactivation. Herein, we report a series of Ni(II) and 2,2′-bipyridine-5,5′-dicarboxylate (bpy) functionalized UiO-67 MOF that catalyze the ethene dimerization reaction co-catalyst free. The catalysts were active for ethene dimerization (up to 850 mg butene $g_{cat}^{-1} h^{-1}$) after activation at 300 °C in 10 % O_2 for 360 min and subsequent exposure to flowing ethene (P(ethene) =26 bar, 250 °C) for 240 min. The catalysts yielded up to 6 % conversion with 99 % selectivity to linear 1- and 2-butenes, which formed in non-equilibrated ratios. Overall, the test data indicate that all three linear butenes are formed on a single active site, in accordance with the Cossee-Arlman mechanism. *Ex situ* XAS and CO FT-IR spectroscopy studies point towards Ni monomers or, plausibly, low-nuclearity Ni-multimers, docked at bpy linkers with Ni-Ni distances > 4 Å, as the main active site for the ethene dimerization reaction.

1. Introduction

The industrial transition from naphtha to ethane as feedstock for ethene production has led to a shorter supply of propene and butene conventionally produced from oil [1]. This change has inspired the search for alternative production processes for propene, butene and butadiene, among which ethene oligomerization is a prominent candidate. Dimerization of ethene to linear α-butene is one of a few large-scale homogeneously catalyzed reactions [2]. The reaction is carried out in organic solvents, and a co-catalyst (*e.g.* Et_2AlCl) is required to start the catalytic cycle [3]. With the intention of making the process more practical and sustainable, recent research efforts have focused on the development of heterogeneous dimerization catalysts.

For a long time, Ni-aluminosilicates have been considered the most promising heterogeneous ethene oligomerization catalyst. The important upsides of Ni-aluminosilicate catalysts compared to the traditional homogeneous Ni-complexes is that they do not require a co-catalyst and they may be regenerated by heating in an oxidative atmosphere at elevated temperature to burn off reaction products deposited on the catalyst [4]. Recently, metal-organic framework (MOF) based ethene oligomerization catalysts are appearing [4,5]. Metal–organic frameworks are crystalline, porous materials where the three-dimensional structure consists of metal ions or clusters connected by organic linkers. The synthetic diversity of these materials enables control over density of active sites and pore size, and the ability to incorporate sophisticated chemical functionalities as part of the framework [6,7]. This strategy includes installing homogeneous catalysts onto the organic ligands [8,9], on the metal clusters [10–12] or encapsulating metal particles [13]. The ability to create well-defined active sites on porous solids, opens up the possibility for tailoring MOFs for ethene dimerization reaction.

Notably, Metzger et al. [10] prepared a catalytically active material, Ni-MFU-4 l, by exchanging one of the five Zn^{2+} ions in the MOF cluster with Ni^{2+}. Ni-MFU-4 l achieved the highest activity reported so far for

* Corresponding author.
E-mail address: Unni.olsbye@kjemi.uio.no (U. Olsbye).

https://doi.org/10.1016/j.cattod.2020.03.038
Received 31 October 2019; Received in revised form 8 March 2020; Accepted 17 March 2020
Available online 19 March 2020

MOF catalysts (TOF = 41500 mol(ethene) mol(Ni)$^{-1}$ h^{-1}) while retaining > 90 % selectivity towards 1-butene. Another method for utilizing the MOF nodes was reported by Madrahimov et al. [11] where nickel grafted 2,2′-bipyridine (bpy) was grafted on the free Zr-OH sites in the NU-1000 cluster. NU-1000-bpy-$NiCl_2$ was shown to be catalytically active with an intrinsic activity for butenes that was an order of magnitude higher compared to the molecular bpy-Ni^{2+} catalyst. In a more recent study, Gonzales et al. [9] utilized the Ni^{2+} functionalized bpy for ethene oligomerization. The bpy linker was reported to be exchanged with the biphenyl linkers of UiO-67 and functionalized with Ni^{2+}. This catalyst was active for ethene oligomerization and products ranging from C_4 – C_{18} was observed. Control experiments showed that Ni^{2+} functionalized UiO-67 was active for ethene oligomerization reaction without the bpy-Ni^{2+} moiety with similar TOF. The authors suggested that the activity originated most likely from excess nickel coordinated to water and hydroxide ligands on the zirconium cluster. Overall, the challenge with product separation and catalyst regeneration, because of polymer formation, persists in most reported Ni-MOF catalysts [9,11,12].

Importantly, most Ni-MOF catalysts published to date are tested as liquid-phase oligomerization catalysts where the use of solvent and co-catalyst, such as diethylaluminum chloride (Et_2AlCl) or methylaluminoxane (MAO), is required in large excess [8–11,14,15]. These compounds are highly flammable, and avoiding their use would have strong impact on process safety. To the best of our knowledge, the only Ni-MOF that has been reported as ethene oligomerization catalyst without a co-catalyst is Ni-CPO-27 [16]. This catalyst was tested using a continuous flow fixed-bed reactor and was active for propene and ethene dimerization at 5 bar and 180 °C. The two major drawbacks of Ni-CPO-27 were the low conversion and the rapid deactivation (conversion < 1 % for propene and 2 % for ethene after 400 min TOS, reaction condition: 5 bar propene, 453 K, WHSV =64 h^{-1}).

The reaction mechanism in Ni-MOFs and Ni-aluminosilicates have been examined both experimentally and computationally in recent publications. Similar to homogeneous catalysts, the Ni-MOFs are generally concluded to operate through the Cossee-Arlman mechanism [8,9,17–19]. Here, the co-catalyst is hypothesized to generate the active metal-alkyl intermediate where oligomerization proceeds by insertion of ethene into a metal-alkyl bond. Since Ni-aluminosilicates do not require a co-catalyst, the active site formation and reaction mechanism have proven difficult to determine and both metallacycle and Cossee-Arlman mechanism have been suggested [20–24]. However, recent experimental and theoretical investigations further support the Cossee-Arlman mechanism. Specifically, Gounder et al. [25] evaluated the ethene dimerization activity of Ni^{2+} sites in Ni-Beta zeolite (0.01–1 kPa, 453 K, WHSV = 0.01–10 h^{-1}) after suppressing contributions from the H^+ sites on the support. Continued formation of 2-butenes on Ni^{2+} -derived active sites, together with ethene assisted formation of [Ni(II)-H]$^+$ intermediates (based on H_2 co-feed and H/D isotopic scrambling experiments) were found to be consistent with the Cossee-Arlman mechanism. Furthermore, Brogaard et al. performed Density Functional Theory (DFT) calculations of ethene oligomerization in another microporous zeolite-based catalyst, Ni-SSZ-24, and found that the Cossee-Arlman mechanism is energetically favored compared to the metallocycle mechanism in this catalyst. Moreover, the computational results suggested that the ethene oligomerization mechanism is initiated by proton transfer to the zeolite, leading to Ni-H and, furthermore, Ni-alkyl formation as the most abundant intermediate, without the addition of a co-catalyst [20]. Very recently, Brogaard et al. addressed another peculiar observation of ethene oligomerization over microporous Ni-aluminosilicates catalysts, *i.e.*; the second order reaction in P (ethene). DFT-based molecular dynamics simulations were combined with continuous-flow experiments and microkinetic modeling of the same Ni-SSZ-24 zeolite [26]. The authors found that the second order reaction is consistent with a Cossee-Arlman mechanism in which the (Ni-ethyl-ethene)$^+$ complex is solvated in the zeolite pore by the addition of another ethene molecule. Moreover, it was found that such solvatisation dramatically reduces the activation energy of reaction. The excellent C_4 selectivity of the catalyst was ascribed to the entropic penalty of a solvated (Ni-butyl-ethene$_2$)$^+$ complex compared to the smaller (Ni-ethyl-ethene$_2$)$^+$ complex [25].

The main goal of the current contribution is to elucidate the potential of Ni-MOFs as co-catalyst free, ethene dimerization catalysts that maintain high linear butene selectivity. One of the MOFs that have shown remarkable chemical, thermal and mechanical stability is the UiO-67 belonging to the UiO Zr-MOF series. The UiO-67 framework consist of 12 coordinated $Zr_6(\mu^3\text{-}O)_4(\mu^3\text{-}OH)_4$clusters connected by biphenyl-4,4′-dicarboxylic acid (bpdc) to yield a microporous three-dimensional framework with both tetrahedral and octahedral cavities with diameters of 12 Å and 16 Å, respectively [6] (Fig. 1).

Herein, we report a series of UiO-67 Zr-MOFs where part of the biphenyl linkers was replaced by bipyridine, as grafting sites for Ni ions. Butene yields up to 1850 mg g_{cat}^{-1} h^{-1} were obtained in gas phase without the use of a co-catalyst. Detailed characterization of fresh and used catalyst (SEM-EDS, N_2 adsorption, XRD, TGA, FTIR, XAS) was performed to identify the active site and to verify the structural stability of the catalyst under reaction conditions.

2. Experimental

2.1. Synthesis

UiO-67-bpy was synthesized via a simple one-pot reaction in dimethylformamide (DMF) at 130 °C, using benzoic acid and water as modulators. 135 g of zirconium chloride (1 eq) was added to a 3 L reactor, containing 63 mL distilled water (6 eq) and 2243 mL DMF (50 eq) at room temperature on a stirring plate. This solution was heated and 212 g of benzoic acid (3 eq) was added, and left until completely dissolved. Subsequently, 14 g of [2,2′-bipyridine]-5,5′-dicarboxylic acid (bpy) was added, followed by 126 g of [1,1′-biphenyl]-4,4′-dicarboxylic acid (bpdc). The solution was left at 130 °C, overnight with stirring under reflux. The resulting product was filtered and washed with hot DMF and acetone, followed by drying at 150 °C, overnight. A white powder was obtained which was filtered and washed with hot DMF (three times with 20 mL) and acetone (three times with 20 mL), followed by drying of product at 150 °C, overnight.

The post synthetic metalation of the MOFs was carried out in EtOH with Ni(acetate)$_2$*4H_2O as the metal source. All MOFs were dried at 196 °C in air prior to metalation. The required amount of Ni salt for various Ni:bpy (mol/mol) ratios was dissolved in EtOH (10 mL_{EtOH}/g_{cat}) and mixed with the catalyst in a HDPE bottle. The slurry was sonicated for 30 min, capped and heated overnight at 65 °C. The resulting slurry was washed three times with 10 mL_{EtOH}/g_{cat} and dried in air overnight at 65 °C. The nickel functionalized samples were denoted xNi-UiO-67-bpy$_y$, where x is the Ni wt % determined by EDS analysis and y stands for the mol % bpy relative to (bpy + bpdc) determined by ^{1}H-NMR.

2.2. Characterization

The bpy content of UiO-67-bpy was determined by liquid-phase ^{1}H-NMR, after digestion of the MOF in a NaOH/ D_2O solution. 20 mg of dry sample was weighed in a centrifuging tube and 1 mL of 1 M NaOH (in D_2O) was added. The tube was shaken properly to obtain a homogeneous suspension and kept overnight for digestion. After centrifuging the digested suspension for 15 min, 600 µL solution was pipetted to an NMR tube. Liquid ^{1}H NMR spectra were obtained with a Bruker AVII 400 NMR Spectrometer (400 MHz). The relaxation delay (d1) was set to 20 s with 64 scans.

Powder X-ray diffraction (PXRD) patterns of the MOF samples before and after metalation and after reaction were obtained using a Bruker D8 Discover diffractometer with Cu K_α radiation ($\lambda = 1.5406$ Å).

The textural properties of the samples were derived from N_2

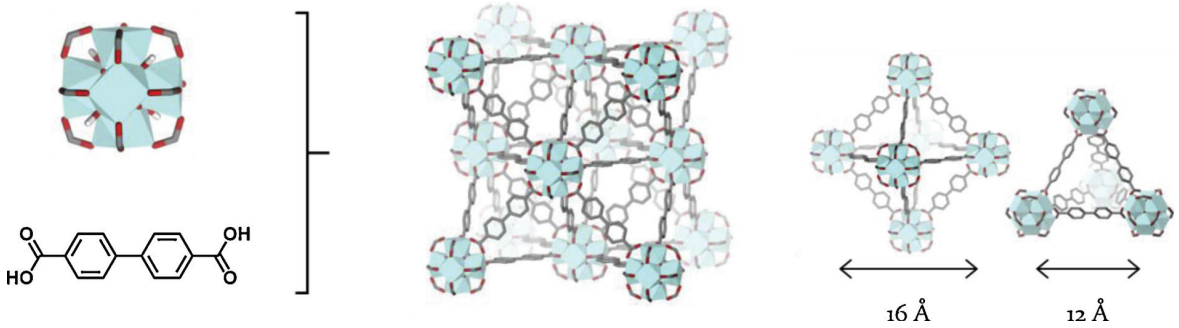

Fig. 1. The $Zr_6(\mu^3\text{-}O)_4(\mu^3\text{-}OH)_4(COO)_{12}$ clusters that are connected by bpdc linkers to form the three-dimensional microporous framework of UiO-67 with tetrahedral and octahedral cages. Atom color: black, C; red, O; blue, Zr. Adopted from [27]. (For interpretation of the references to colour in this figure legend, the reader is referred to the web version of this article).

adsorption isotherms, measured at −196 °C, using a BELSORP-mini II instrument. Unless specified otherwise, all samples were outgassed in vacuum for 1 h at 80 °C and 3 h at 300 °C, and then measured. The catalyst pore volumes and surface areas were determined using the t-plot and BET methods.

The elemental composition, specifically Ni/Zr ratio, was determined by energy-dispersive X-ray (EDS) spectroscopy at 10 kV accelerating voltage utilizing a X-flash 6|10 detector. The stability of the catalysts in synthetic air, as well as the amount of retained hydrocarbons after reaction was determined by thermogravimetric analysis (TGA) on a Netzsch STA 449 F3-Jupiter instrument. Approximately 20 mg of catalyst was heated under a flow of synthetic air (25 mL/min) to 800 °C at a rate of 5 °C/min.

FT-IR measurements with CO probing at 77 K were performed in transmission mode using a Vertex80 spectrometer from Bruker, equipped with a liquid nitrogen cooled MCT detector. Each spectrum was obtained averaging 64 scans with a resolution of 2 cm^{-1}. The pure sample in powder form was pressed into a thin self-sustained pellet and placed in a gold envelope sample holder. The sample holder was then inserted in an evacuable cell, with IR transparent KBr windows, for pretreatment at 250 °C for 3 h. Afterwards, around 20 mbar of CO was dosed to the sample at RT; the cell was then closed and cooled using liquid nitrogen to favor the interaction of the probe with the samples. Once full coverage of CO on the sample surface was achieved, the probe was gradually removed through volume expansions, with the help of a vacuum line, while IR spectra were collected at each step of desorption. Once it was not possible anymore to appreciate variations in the spectral features, dynamic vacuum at 77 K was used to remove the remaining CO.

Ni K-edge XAS data were collected at the B18 beamline [28] of the Diamond Light Source (UK). XAS spectra were collected in transmission mode, using a fixed-exit double crystal water-cooled Si(111) monochromator and Pt-coated mirrors. A pair of smaller plane mirrors was used for rejection of higher harmonics. The incident (I_0) and transmitted ($I_{1,2}$) X-ray intensities were detected using ionization chambers filled with different mixtures of He and Ar (30 mbar Ar for I_0 and 230 mbar Ar for $I_{1,2}$) to result in ca. 10 % and 70 % absorption respectively. The third ionization chamber (I_2) was used for the simultaneous collection of the XANES spectrum of a Ni metal foil for the energy calibration of each spectrum [29]. Ni-functionalized MOF samples, in their as-prepared state and recovered after catalytic tests were measured at RT in air, in the form of self-supporting pellets, with optimized weights in the 80−90 mg for 1.3 cm^2 area pellets, resulting in edge jumps $\Delta\mu x$ in the 0.2–0.5 range for a total absorption after the edge of $\mu x = 2.5$. The selected model compounds (NiO, $Ni(OH)_2$, $Ni(OAc)_2(H_2O)_4$, $Ni(OAc)_2(H_2O)_2(bpy)$) were also measured in the form of self-supporting pellets, with optimized weights for transmission-mode XAS, using BN as diluent when necessary to obtain a robust enough pellet. XAS spectra were acquired in Quick-EXAFS mode in the 8133–9333 eV range (up to $k_{max} \sim 16$ $Å^{-1}$), with a constant energy step of 0.3 eV in the whole energy range. Each scan required 3 min. To characterize each pelletized sample, we collected five consecutive scans, and averaged the corresponding μx(E) curves after checking for signal reproducibility. All the XAS spectra were normalized to unity edge jump and aligned in energy using the Athena software from the Demeter package [30]. The χ(k) EXAFS functions were also extracted by using the Athena program. Fourier-transform (FT) EXAFS spectra were obtained by transforming the $k^2\chi(k)$ functions in the (2.4–14.0) $Å^{-1}$ range.

XANES linear combination fit (LCF) analysis of the spectra of (1.8)Ni-UiO-67-$bpy_{11\%}$, (3.1)Ni-UiO-67-$bpy_{11\%}$ and (1.1)Ni-UiO-67-$bpy_{6\%}$ was performed using the Athena software from the Demeter package [30], in the 8324–8384 eV energy range. The experimental XANES, μ^{EXP} (E) were fitted to a linear combination of two reference XANES spectra, μ_i^{REF} (E), *i.e.*: μ^{LCF} (E) = Σ_i w_i μ_i^{REF} (E), i = 1,2, optimizing the weights w_i for each reference spectrum. We employed as references the XANES spectra of the extremal samples in the investigated compositional series, namely (2.0) Ni-UiO-67 (representative of bpy-free Ni^{2+} species) and (0.9) Ni-UiO-67- $bpy_{11\%}$ (representative of bpy-coordinated Ni^{2+} species) LCF was performed by setting the total sum of the weights to unity, $\Sigma_i w_i = 1$. The LCF R-factor (calculated as Σ_j $[\mu^{EXP}{}_{,j}$ (E) − $\mu^{LCF}{}_{,j}$ (E)$]^2$/ Σ_j $[\mu^{exp}{}_{,j}$ (E,)$]^2$, where *j* indicates each experimental point in fitted energy range) was always $< 1 \times 10^{-4}$, indicating a very good LCF quality.

2.3. Catalytic testing

Catalytic tests were carried out in a continuous flow, fixed bed, stainless steel reactor (I.D. 8.3 mm). Before each experiment, the catalyst was pressed (0.5 tons), crushed and sieved to 240–420 μm grain size. 150–300 mg catalyst was loaded in the reactor and was activated *in situ* at 300 °C for 6 h in a flow of 10 % O_2 in He (total flow of 50 mL*min^{-1}) unless specified otherwise. The total pressure was then increased in He (up to 30 bar) and controlled by a back-pressure regulator (Bronkhorst P-702CV). During reaction, the partial pressures were controlled by adjusting individual flows. The desired mixture of ethene (3.5 grade), inert and internal standard (10 % Ne in He, 2.5 grade) was fed through the reactor, keeping the total pressure constant, but varying *e.g.* the partial pressure of ethene. Standard reaction conditions were 250 °C and 30 bar where P(ethene) =26 bar and P(inert) =4 bar and with a total flow rate of 30 mL/min (contact time at STP: 5.0 mg_{cat} min mL^{-1}_{ethene}).

A fraction of the reactor effluent, about 10 mL/min, was led through heated lines to an on-line gas chromatograph (Agilent 7890B) equipped with three columns: CP-Molsieve 5A (50 m ×0.53 mm ×50 μm) connected to TCD, GS-Gaspro (60 m ×0.32 mm) and DB-1 (40 m ×0.10 mm ×0.20 μm) both connected to FID. The three channels were used for detection of neon, light hydrocarbons up to butenes and heavier hydrocarbons, respectively. The carbon mass balance closed within ± 2 %.

3. Results and discussion

3.1. Material synthesis and characterization

Three series of catalysts with varying bpy concentration were prepared; UiO-67, UiO-67-bpy$_{6\%}$ and UiO-67-bpy$_{11\%}$ (Fig. SI 1). Ni was subsequently grafted onto the three parent materials with varying concentration. The main physical properties of the catalysts are presented in Table 1. The Ni content in the UiO-67-bpy$_{11\%}$ series varied between 0.9–3.1 wt % corresponding to Ni:bpy molar ratios from 0.5 to 1.6. Two catalysts with 0.8 and 1.1 Ni wt % were prepared for the UiO-67-bpy$_{6\%}$ series, corresponding to Ni:bpy mole ratios of 0.9 and 1.4, respectively. Ni-UiO-67, without bpy, was used as reference catalyst. Its metal concentration was determined to be 2 wt % Ni. The X-ray diffractograms of the catalysts are shown in Fig. SI 2. The XRD patterns show that all catalysts have the UiO-67 structure. No additional crystalline phase was identified, especially, the absence of diffraction peaks corresponding to NiO or Ni particles suggests that Ni is highly dispersed in the samples.

Thermogravimetric analysis (Fig. SI 3) of the three parent materials show very similar temperature stability with a decomposition temperature ~ 500 °C. Combination of solution ^{1}H-NMR and TGA measurements of the parent materials showed that their Zr node:linker ratio was between 5.1–5.4 (Table SI 1) suggesting similar defect concentration [31]. For the Ni metalated catalysts, the decomposition temperature decreased with increasing Ni concentration, independent of bpy concentration. The decomposition temperature was ~ 420 °C for the catalyst with highest concentration of Ni. In xNi-UiO-67-bpy$_{y\%}$, this difference could result from strain induced by Ni coordination to bpy linkers [32]. However, Ni might also catalyze the combustion of organic linkers, in line with the reduced stability of (2.0)Ni-UiO-67.

All parent materials had similar, high specific surface areas (S_{BET}) close to the theoretical value of 2800 m^2/g for UiO-67 [7]. Introduction of 2 wt % Ni to UiO-67 reduced the S_{BET} from ~2350 to 1540 m^2/g. Similarly, in the UiO-67-bpy$_{11\%}$ and UiO-67-bpy$_{6\%}$ series, the S_{BET} of the catalysts were found to decrease with increasing Ni loading. There were no appreciable increase in mesopore volume with increasing Ni concentration, showing that the Ni-treatment did not partially destroy the crystals to create mesopores. Prior contributions have reported that metal complexes coordinate to the bpy linker to form isolated [metal-bpy] complexes inside the MOF, and only a slight decrease in S_{BET} was reported by Gonzalez et al. [9] for (2.3)Ni-UiO-67-bpy$_{14\%}$, and by Gutterød et al. for Pt functionalized UiO-67-bpy$_{6\%}$ [13]. Molecular dynamics simulations were performed to investigate whether the loss of specific surface area with increasing Ni concentration could result from the gradual formation of a [bpy-Ni$_2$Ac$_4$] complex inside the pores, rendering the pores inaccessible for N_2 during measurement. Simulations show that the loss of specific surface area was insignificant compared to what was observed experimentally (Fig. SI 5). This result may suggest that Ni complex grafting leads to blocking of pore mouths, or to local structure distortions in the material.

Table 1
Physicochemical properties of the parent materials and Ni functionalized catalysts.

	Nickel wt. %[a]	S_{BET} (m^2/g)	V_{micro} (cm^3/g)	V_{meso} (cm^3/g)	Ni:bpy (mol/mol)
UiO-67	–	2350	0.93	0.06	–
UiO-67-bpy$_{6\%}$	–	2404	0.94	0.07	–
UiO-67-bpy$_{11\%}$	–	2431	0.97	0.06	–
(2.0)Ni-UiO-67	2.0	1540	0.62	0.10	–
(0.9)Ni-UiO-67-bpy$_{11\%}$	0.9	2146	0.83	0.07	0.5
(1.8)Ni-UiO-67-bpy$_{11\%}$	1.8	1834	0.75	0.10	1.0
(3.1)Ni-UiO-67-bpy$_{11\%}$	3.1	1549	0.68	0.10	1.8
(0.8)Ni-UiO-67-bpy$_{6\%}$	0.8	2281	0.91	0.09	0.8
(1.1)Ni-UiO-67-bpy$_{6\%}$	1.1	2156	0.88	0.09	1.5

[a] Nickel weight percent was determined by EDS analysis based on Ni/Zr ratio.

The catalysts were further analyzed with SEM to investigate the possibility of crystal degradation. SEM images of UiO-67-bpy11 %, (3.1) Ni-UiO-67-bpy$_{11\%}$, UiO-67 and (2.0)Ni-UiO-67 are shown in Fig. 2. Among the catalysts containing both bpy and Ni, crystal morphology was maintained from the parent to functionalized material. Deposition on top of the MOF crystals of (2.0)Ni-UiO-67 were observed, suggesting that the nickel acetate is either not diffusing into the pores, or diffused towards the outer surface during drying. In contrast, no deposits were observed on the surface of the highest Ni- and bpy- containing catalyst, (3.1)Ni-UiO-67-bpy$_{11\%}$ (Fig. 2B). This result suggests that bpy plays a key role in directing nickel into the pores of xNi-UiO-67-bpy$_{y\%}$, in accordance with prior literature reports [9,13]. However, for catalysts with Ni:bpy mol ratio > 1, it is evident that Ni has to form other complexes in addition to the isolated [Ni^{2+}-bpy] complex. The nature of Ni in the MOFs is further discussed in Section 3.2.

Overall, the material characterization suggests that the MOF lattice is intact after Ni functionalization, but local distortions cannot be excluded.

3.2. Catalytic testing

3.2.1. Influence of Ni and bpy concentration

The evolution of catalyst turn-over rates for ethene dimerization with time on stream under standard reaction conditions is shown in Fig. 3A. Fig. 3B and C highlight the influence of Ni:bpy ratio and bpy content in the catalysts on the ethene dimerization rate after 360 min on stream. Focusing first on Fig. 3B, UiO-67-bpy without Ni showed no conversion under the conditions used, clearly pointing to Ni as the active site. Similarly, the UiO-67-Ni catalyst without bpy linker (Ni:bpy = ∞) showed negligible conversion rate (Fig. 3 B–C), hence demonstrating the essential role of bpy linkers for grafting and activation of the Ni acetate complex.

Concentrating next on the time evolution of catalysts that contained both Ni and bpy, and focusing on the Ni-UiO-67-bpy$_{11\%}$ series, the catalysts showed an initiation period where the rate of reaction increased with TOS. This observation is consistent with a rather slow formation of the active catalyst state after the on-set of reaction. Within the Ni-UiO-67-bpy$_{11\%}$ series, the initiation period was shortest for the catalyst with high Ni content and the duration increased with decreasing Ni amount. Furthermore, the more active (3.1)Ni-UiO-67-bpy$_{11\%}$ catalyst deactivated gradually with TOS after 360 min on stream, whereas the less active catalysts had not yet reached their activity maximum after 360 or 720 min on stream (*i.e.*; the test duration), respectively. Moving next to the Ni-UiO-67-bpy$_{6\ \%}$ catalysts, it is very interesting to note that the transient behavior after on-set of reaction, as well as the turn-over rate per Ni in the catalyst at a given time on stream, were generally very similar for catalysts having the same Ni:bpy ratio, while total Ni and bpy content individually had less impact on catalyst performance (Fig. 3A–C). Fig. 3B clearly shows that the activity per Ni site increased with increasing Ni:bpy ratio, in particular for Ni:bpy ratios above 1. This result suggests that the presence of two adjacent Ni acetate complexes either facilitates the formation of the active Ni species, or creates a particularly active Ni site. It is further interesting to note that the activation and deactivation does not correlate with ethene conversion (Fig. SI 6), but with Ni:bpy mol ratio.

Turning next to product selectivity, linear butenes represented 99 % of the products in the reactor effluent, over all tested catalysts, in the studied conversion range (≤ 6 % conversion). Longer chained alkenes, denoted C_{6+}, with selectivity ~1 % were also identified. Considering the $C_4^=$ product distribution, the 1-butene : trans-2-butene : cis-2-butene ratio was 41:26:32 (Fig. SI 7). Importantly, the distribution was very similar in all catalysts, irrespective of conversion level, and far from the equilibrium distribution at the reaction temperature (see dotted lines in Fig. SI 7).

The butene isomer distribution could be primary, because of butyl

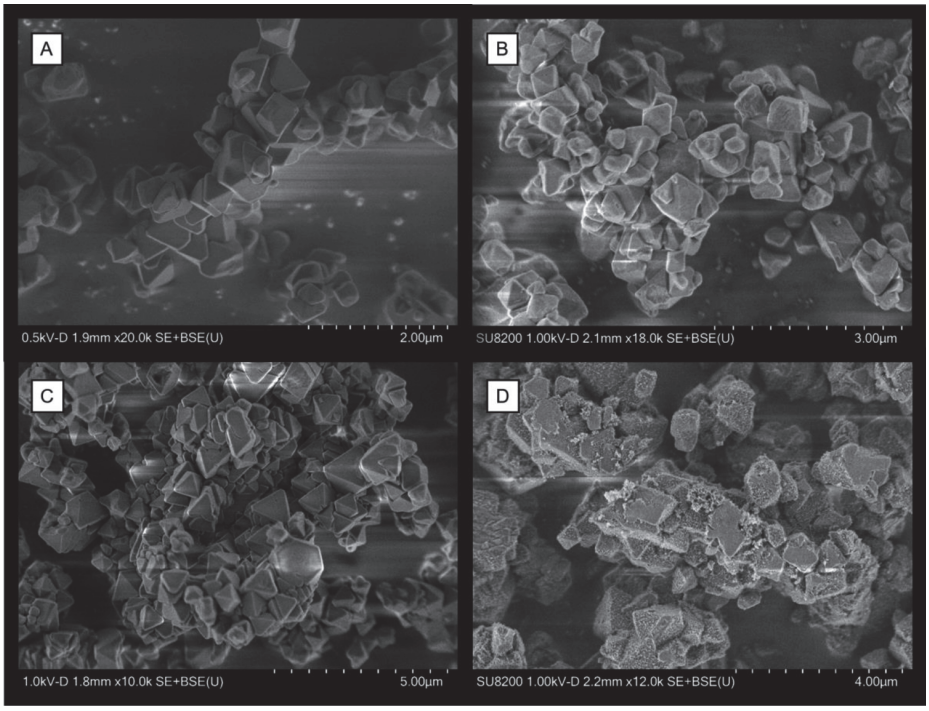

Fig. 2. SEM images of A) UiO-67-bpy$_{11\%}$, B) (3.1)Ni- UiO-67-bpy$_{11\%}$, C) UiO-67 and D) (2.0)Ni-UiO-67.

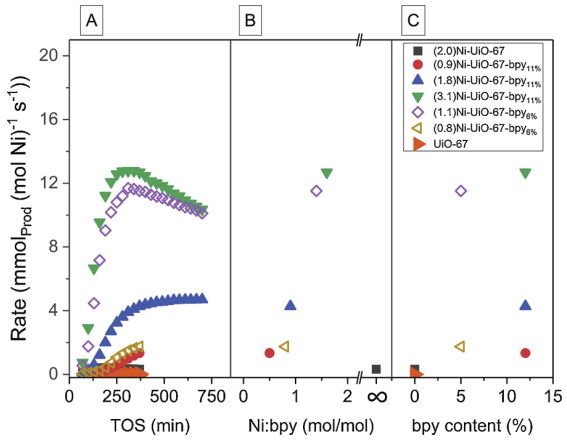

Fig. 3. A) Ethene dimerization rate vs TOS. B) Ethene dimerization rate vs Ni:bpy (mol/mol) ratio and C) vs bpy content (%) after 370 min TOS. The conversion at 370 min TOS for each catalyst shown in the legend was 0.1 %, 0.2 %, 1.1 %, 5.8 %, 1.9 %, 0.2 %, in descending order, respectively. Reaction conditions: m_{cat} =0.150 g, 30 bar total pressure where P_{ethene} =26 bar and P_{inert} =4 bar, temperature =250 °C and contact time =5.0 mg·min/mL at STP.

isomerization on the active site before desorption of the 1- or 2-butene product, or it could be secondary, due to isomerization at the Ni site or at a support site, after re-adsorption of a butene molecule. In zeolites, isomerization is mainly catalyzed by Brønsted acid sites in the zeolite lattice [23,33,34]. For this reason, we decided to investigate whether *e.g.* the μ_3-OH sites on the Zr nodes in UiO-67-bpy might catalyze the isomerization reaction, 1-butene was fed over UiO-67-bpy$_{11\%}$ at 250 °C, 1 bar total pressure. No conversion to the 2-butene isomers (or to other products) was observed (Table SI 2).

The rate of a secondary reaction is expected to depend on the concentration of the primary product. We observe that the product distribution was unaffected by change in ethene conversion, further supporting that all butenes are primary products. Together, the test data suggest that the butene isomer distribution is primary in nature, resulting from butyl isomerization on the Ni site before desorption of the butene products. The high butene selectivity and non-equilibrated butene isomer distribution point to shape selectivity as a dominant parameter in the Ni-UiO-67-bpy catalysts. Similar to what observed in Ni-SSZ-24 zeolite (Table SI 2).

These results are in accordance with the Cossee-Arlman (degenerate polymerization) mechanism, as previously suggested for other heterogeneous Ni-based ethene oligomerization catalysts [8,9,17,18]. In contrast to the metallacycle mechanism, typical of homogeneous Ni catalysts [35], the Cossee-Arlman mechanism enables isomerization of the formed butyl species before desorption from the active site. As a final note, the similar product selectivity observed for all Ni-UiO-67-bpy catalysts in this study, points to a single Ni site, positioned in a similar, well-defined, confined environment, being responsible for the activity of all catalysts. This conclusion further points to a direct correlation between the turn-over frequency of each catalyst and the fraction of Ni sites that reaches an active state after the on-set of reaction.

A comparison between the most active catalyst reported in this study, (3.1)Ni-UiO-67-bpy$_{11\%}$, and other ethene oligomerization catalysts reported in literature, shows that a higher temperature is required to achieve similar activity over Ni-UiO-67-bpy compared to silica-alumina based materials such as Ni-SSZ-24 and Ni-Beta (Table 2). Further studies are needed to establish whether the difference is due to a lower fraction of active sites, higher activation energy, or both. In either case, the disparity in reaction temperature between the two catalyst classes could arise from the difference in electron charge density on Ni as a result of varying electron donation ability of the two types of support. For homogeneous Ni catalysts, a more electrophilic metal center have been suggested to lead to an increase in the rate of ethene oligomerization, especially in the ethene insertion step (C—C coupling) [36]. Contrary to bpy ligands in UiO-67-bpy that can act as σ donors as well as π acceptors with d metals, the electron withdrawing function of zeolites may lead to a more electrophilic metal center, thus lead to an increased dimerization rate. Interestingly, both Ni-MOF and Ni-aluminosilicate

Table 2
Co-catalyst free heterogeneous catalysts for ethene dimerization in gas phase.

Catalyst	Ni (wt %)	T (°C)	P(ethene) (bar)	Conversion (%)	TOF (h^{-1})	C4 sel. (%)	Ref
Reaction in batch mode							
Ni-MFU-4l	1.0	25	50		41500	97	[10]
Ni@(Fe)-MIL-101	2.8	10	15		6300	95	[8]
Ni-MCM-48	0.5	150	35		47380	55	[38]
Ni-SBA-15	2.6	150	35		14150	54	[22]
Reaction in flow mode							
Ni-UiO-67- $bpy_{11\%}$	3.1	250	26	6	41	99	This work
Ni-SSZ-24	0.4	150	26	7	330	99	[26]
Ni-Beta	1.7	120	26	27	70	85	[34]
Ni-Beta	4.6	120	25	10	77	80	[23]
Ni-SBA-15	2.6	150	30	91	733	58	[22]

catalysts are suggested to operate through the Cossee-Arlman mechanism.

The Ni-aluminosilicate catalysts are generally operated at a rather low temperature (< 200 °C) to avoid secondary reactions such as cracking and isomerization that can take place on remaining Brønsted acid sites [23,33,34] and are active even at sub-ambient temperatures (−15 °C) [37].

The literature studies reported in Table 2 further show that testing in a continuous flow fixed-bed reactor gives significantly lower activity (TOF) compared to catalysts tested under batch conditions (Table 2). This discrepancy in activity may be a result of difference in testing conditions, evidenced by the up to 20-fold increase in activity over Ni-SBA-15 tested under similar reaction conditions when changing from flow to batch mode. Among heterogeneous Ni catalysts, Ni-MOFs are the better dimerization catalyst both in terms of activity and selectivity, but require co-catalyst in large excess.

Selectivity comparisons between the catalyst classes are complicated by the difference in reported conversion levels. However, comparing Ni-UiO-67-bpy to the 1-dimensional Ni-SSZ-24 zeolite shows very similar selectivity at similar conversion. On the other hand, the 3-dimensional Ni-Beta, that contains channel intersections that surpass the size of the Ni-SSZ-24 channels, gives substantially lower butene selectivity at comparable conversion; the main by-product being long-chain alkenes [23]. This result suggests a higher abundance of secondary reactions in those intersections, gradually blocking the pores. However, the effect of pore size is not isolated between these two materials and other properties such as acid site density and strength can play a significant role in the ethene dimerization reaction [4].

3.2.2. Catalyst stability

A major drawback of Ni-MOF catalysts associated with ethene dimerization reaction is deactivation and the complex regeneration protocol required to avoid structural damage to the framework [5]. The most common deactivation pathway reported for these catalysts is the formation of polyethylene during reaction, eventually rendering the active site inaccessible [9,11]. In the current study, deactivation over (3.1)Ni-UiO-67-$bpy_{11\%}$ with TOS was observed and this catalyst was investigated further to elucidate the deactivation pathway. Thermogravimetric analysis of the pristine and used catalyst showed that the mass of tested catalyst increased by approximately 15 % compared to the pristine catalyst, suggesting that product deposition is a reason for deactivation (Fig. 4B). In accordance with this result, the N_2 adsorption isotherm of pristine, activated and tested catalyst showed that the specific surface area of the catalyst was not notably changed after activation (Table 3). Conversely, the spent catalyst had a substantially lower specific surface area, which may best be explained by pore blocking or by MOF decomposition (Table 3).

X-ray diffractograms of pristine, activated and tested catalyst showed that the MOF catalyst was crystalline in all stages of the experiment and that the MOF framework was intact after testing (Fig. 4A). Hence, pore blocking by hydrocarbon deposits is the most probable reason for deactivation of Ni-UiO-67-$bpy_{11\%}$. Interestingly, TG-DSC analysis of pristine and tested catalyst in synthetic air revealed that prior to the framework decomposition at ~ 450 °C, the tested catalyst underwent a

Table 3
BET surface area of pristine, activated and tested catalyst determined with N_2 – adsorption. Prior to the measurement, the samples were outgassed 1 h at 80 °C and 3 h at 250 °C.

	S(BET) (m^2/g)
(3.1)Ni-UiO-67-$bpy_{11\%}$ - synthesized	1549
(3.1)Ni-UiO-67-$bpy_{11\%}$ - activated	1525
(3.1)Ni-UiO-67-$bpy_{11\%}$ - tested	503

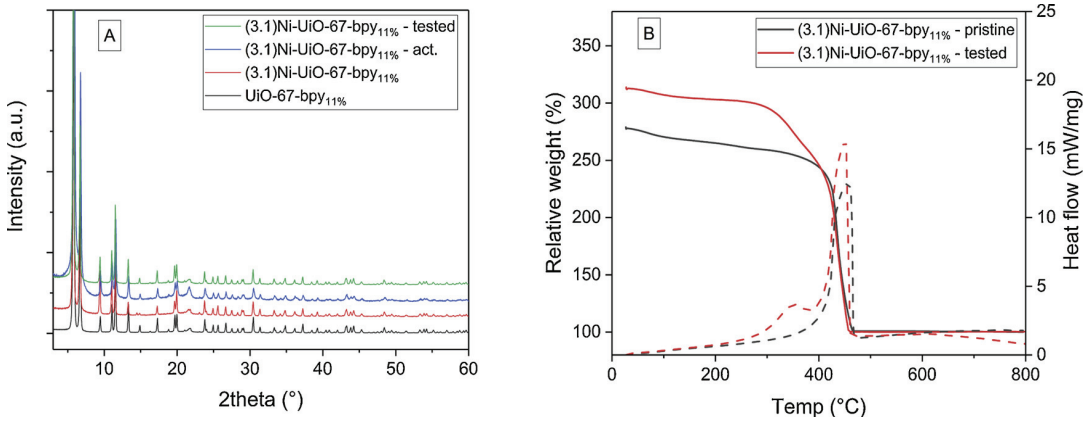

Fig. 4. A) XRD pattern of pristine, activated and tested (3.1)Ni-UiO-67-$bpy_{11\%}$. B) TG curve (solid lines) and DSC (dashed lines) of the pristine and tested (3.1)Ni-UiO-67-$bpy_{11\%}$. The samples were heated from 25 to 800 °C, 5 °C/min in a flow of synthetic air (25 mL/min).

combustion process occurring around 350 °C (Fig. 4B). The heat signal indicates that this process is exothermic, as expected from a combustion process, in contrary to what we would expect if reactions such as cracking took place during the TGA. This result indicated that the deposits are mainly lighter hydrocarbons, and that catalyst regeneration methods might be developed that enable use of the catalyst through multiple test-regeneration cycles. However, such optimization is beyond the scope of this contribution, and was not explored further.

The nature of the adsorbed products was investigated with FT-IR. Fig. 5 shows that the byproducts deposited on the porous material are predominantly linear short chain alkenes. The inset of the figure compares the residual products of reaction with the spectrum of 1-octene [39] and it is possible to observe that they possess the typical spectral features of ν_{CH2} and ν_{CH3}. Especially the presence of -CH_3 moiety let us exclude the presence of a large amount of longer oligomers of polyolefins, for whom -CH_2 is the prominent chemical species. It is difficult to completely exclude the formation of 1-octene oligomers, whose IR spectrum is very similar to the one of the monomer [40]. However, in addition to the TG and FT-IR results, XRD of the used catalyst does not show any indication either for crystalline or for amorphous polyethylene formation. Taken together with the fact that the catalysts show 99 % selectivity towards C_4 alkenes, we find long chain hydrocarbon formation very unlikely. Therefore, identification of medium chain hydrocarbons as the main carbonaceous deposit in Ni-UiO-67-bpy$_{11\%}$ further supports the strong shape selectivity of this catalyst.

3.3. FT-IR and XAS: active and spectator Ni sites

Probe molecule-assisted FT-IR is one of the simplest and most used techniques to detect and characterize active sites in heterogeneous catalysis [41]. Carbon monoxide is widely used to determine the speciation of acid sites (both Brønsted- and Lewis-type, *i.e.* acidic protons and isolated metal ions, respectively) on metal oxides, zeolites and MOFs; furthermore, it is commonly used as a probe for metal nanoparticles, due to its efficient coordination to their surfaces. All these properties make CO a perfect candidate to detect all the species that are possibly present inside our Ni-functionalized MOF catalysts. However,

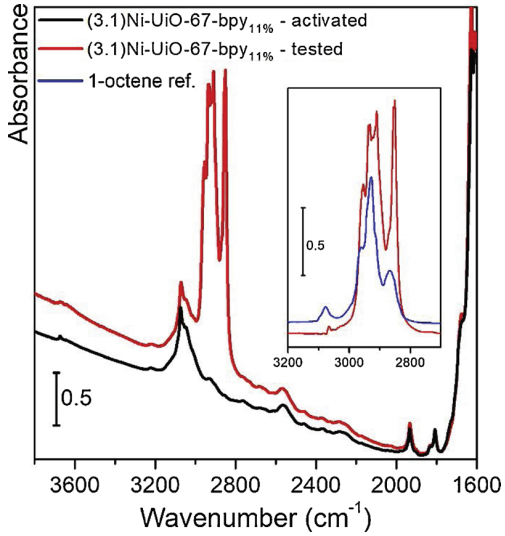

Fig. 5. FT-IR spectra of (3.1)Ni-UiO-67-bpy$_{11\%}$ sample activated for 360 min at 300 °C in 10 % O_2 (black curve), activated for 360 min and tested for 720 min (red curve). Inset shows the tested sample, after background compensation and subtraction of the only activated sample, in comparison with 1-octene FT-IR spectrum (from NIST chemistry web book [39]). (For interpretation of the references to colour in this figure legend, the reader is referred to the web version of this article).

we will begin describing the main IR features of UiO-67 (Fig. 6A). Starting from the high frequency part, we observe a tiny sharp band at 3670 cm^{-1}, related to the residual Zr-μOH at the cornerstones remaining after the thermal treatment for water removal [42,43]. ν(C-H_{arom}) stretching, belonging to the biphenyl and bipyridine linkers are arising in 3200−3000 cm^{-1} interval [42,43]. The region in which ν(C═O) from carboxylates is present (1600-1250 cm^{-1}) is excluded, since the signal is so intense as to be out of scale. In the region between 1250 and 700 cm^{-1} all the different bending modes from C-H_{arom} of the linkers are present. The most important evidence obtained from Fig. 6A is that all samples maintain the same chemical bonding typical of UiO-67 MOFs after the activation in O_2 for 360 min independently from the Ni loading present.

All samples show three evident IR bands: i) an intense band at 2135 cm^{-1}, assigned to CO physisorbed inside the material porosities [44–46]; ii) a signal at 2150 cm^{-1}, due to the interaction of CO with the residual hydroxyls terminating the Zr clusters in the MOF [46]; iii) a feature centered at 2170 cm^{-1}, ascribable to carbon monoxide interactiong with Ni^{2+} moieties [45,47,48]. The absence of bands at frequency lower than the band due to physisorbed carbon monoxide, testify the lack of metal nano-particles, for which we could expect components between 2100 and 2000 cm^{-1} [46,49–51]. We note that the intensity of the peak at 2170 cm^{-1}, assigned to CO···Ni^{2+} correlates perfectly with the total amount of Ni^{2+} moieties present in the catalysts: (*i.e.* from the one containing 3.1 wt % Ni (corresponding to Ni:bpy molar ratio of 1.6; part B) to the one having only 0.9 wt % Ni (corresponding to Ni/bpy molar ratio of 0.5; part D). Moreover we observe that Ni^{2+} is also present in the sample that does not contain bpy (part E).

We can also make the assumption that, with the given bpy concentration, we should have a good distribution of bpy across the whole MOF structure (1 linker out of 10 is a bpy, considering that UiO-67 unit cell has 6 linker molecules we have less than 1 Ni anchoring point per unit cell). Stated that, we can easily assess that Ni species are well distributed inside the MOF framework. Another variation that is possible to observe is relative to the signal at 2150 cm^{-1}; however, this can be easily correlated with slight differences in the dehydration level of Zr cornerstones of UiO-67 structure.

CO was also used to monitor the state of Ni with the specific idea to verify if Ni species had any propensity to aggregate and clustering. We decided to probe the (3.1)Ni-UiO-67-bpy$_{11\%}$ sample tested for 720 min after being activated for 360 min or 960 min, respectively, at 300 °C in 10 % O_2 (Fig. SI 8 for catalytic test and Fig. SI 9 for CO@FT-IR). Proceeding with a careful observation, it is possible to notice that the tested samples display the typical feature for CO chemisorbed on metallic Ni nanoparticles (centered at 2050 cm^{-1}), even if it has a much lower intensity than the one relative to Ni^{2+} species. A longer activation period led to a faster increase in ethene conversion, a higher conversion maximum and a more rapid deactivation. Both catalyst activated for 360 min and 960 min reached steady-state after 400 min TOS and the conversion and deactivation rates over both catalysts converged. At this point, the catalysts are hypothesized to be in similar state *i.e.* same relative concentration of the active nickel species. The curves corresponding to tested (3.1)Ni-UiO-67-bpy$_{11\%}$ samples activated for 360 min (violet) or 960 min (green) perfectly overlap along the whole spectral region, displaying an identical amount of Ni^{2+} able to chemisorb CO. The only appreciable difference, highlighted in the inset of Fig. SI 9, concerns the amount of Ni nanoparticles present in the sample.

The spectrum of the sample only activated for 360 min did not display any sign of Ni or NiO nanoparticles, eliminating the possibility of nanoparticle formation during the activation process. Considering that nanoparticles were not observed on the other catalysts, Ni and NiO nanoparticles can be ruled out as the active site, leaving Ni^{2+} as the most likely active site for ethene dimerization. Furthermore, nickel aggregation to form nanoparticles suggests that nickel is mobile and may be a secondary deactivation path.

Ni K-edge XAS provided complementary information on the average Ni-speciation and local coordination environment in Ni-functionalized

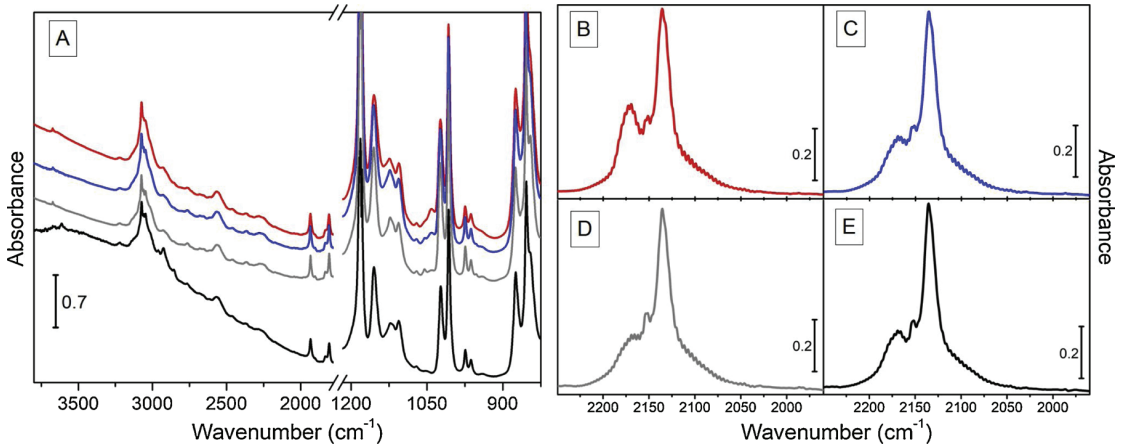

Fig. 6. A) FT-IR spectra of UiO-67-bpy$_{11\%}$ samples with different Ni(OAc)$_2$ content (3.1 wt % - red curve; 1.8 wt % - blue curve; 0.9 wt % - grey curve) and of (2.0)Ni-UiO-67 (black curve) after activation for 360 min at 300 °C in 10 % O_2. The carboxylates spectral region (1700-1250 cm^{-1}) is excluded since it is out of scale. CO@77 K FT-IR spectra of UiO-67-bpy$_{11\%}$ samples with different Ni(OAc)$_2$ content (3.1 wt % - part B; 1.8 wt % - part C; 0.9 wt % - part D) and of (2.0)Ni-UiO-67 (part E). All the plotted spectra in parts B-C-D-E represent the maximum coverage of CO (θ_{MAX}) after the subtraction of the spectra at minimum coverage (θ_{min}). The spectra are then normalized with respect to the peak at 2135 cm^{-1} (physisorbed CO), which takes into account not only the total amount of CO that is dosed but also the pellet thickness. (For interpretation of the references to colour in this figure legend, the reader is referred to the web version of this article).

MOF catalysts, in their as-prepared state as well as after activation and reaction.

These evidences can be rationalized in line with the compositional characteristics of the two extremal samples. Indeed, (2.0) Ni-UiO-67 is representative of Ni^{2+} ions incorporated in the UiO-67 MOF environment in the absence of privileged anchoring points at bpy-linkers. The intense WL in its XANES spectra closely resemble what is observed in the Ni(OAc)$_2$(H$_2$O)$_4$ precursor. Nonetheless, we note a slight shift to higher energy of the WL peak in the XANES of (2.0) Ni-UiO-67 with respect to what is observed in the model compound, together with certain differences in the 2−4 Å range in FT-EXAFS. Such deviations suggest that the MOF could play an active role – although to a minor extent in the absence of bpy - in directing the incorporation of Ni-species from the Ni(OAc)$_2$(H$_2$O)$_4$ precursor. Ni(OAc)$_2$(H$_2$O)$_4$ deposits at the outer crystal surfaces, observed by SEM for (2.0) Ni-UiO-67, could coexist with different Ni^{2+} moieties inside the MOFs scaffold, possibly interacting with defects at the UiO-67 nodes.

Conversely, (0.9) Ni-UiO-67- bpy$_{11\%}$, with Ni:bpy (mol/mol) = 1:2, provides a large excess of bpy linkers with respect to Ni ions, resulting in almost exclusive presence of bpy-coordinated Ni^{2+} moieties inside the MOF scaffold: comparing the (0.9) Ni-UiO-67- bpy$_{11\%}$ XAS data with the ones obtained for a series of well-characterized bpy-OAc Ni^{2+} complexes, we found the best agreement in both the XANES and EXAFS region with a Ni(OAc)$_2$(H$_2$O)$_2$(bpy) model complex, structurally characterized by single crystal XRD (see Fig. SI 10).

We were able to properly model the XANES of the remaining three catalysts, namely (1.8)Ni-UiO-67-bpy11 %, (3.1)Ni-UiO-67-bpy$_{11\%}$ and (1.1)Ni-UiO-67-bpy$_{6\%}$, as linear combinations of the spectra collected for the two extremal materials. Linear combination fit (LCF) analysis resulted in R-factors lower than 1×10^{-4}, corroborating the validity of the adopted model. As illustrated by the pie charts in Fig. 7A, an increased Ni:bpy ratio translates in the progressive increase of bpy-free

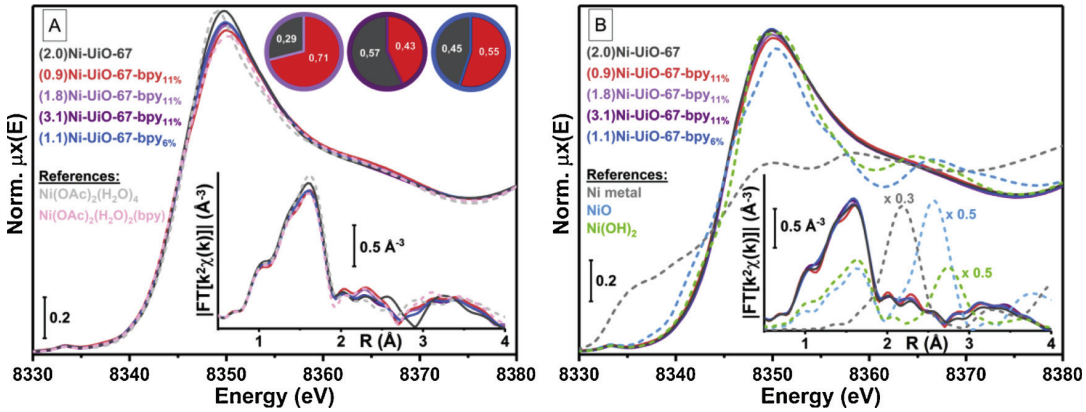

Fig. 7. (A) Ni K-edge XANES of as-prepared Ni-functionalized MOF catalysts. The bottom inset shows the corresponding phase-uncorrected FT-EXAFS spectra, obtained transforming the k^2-weighted k$^2\chi$(k) curves in the 2.4-14.0 Å^{-1} range. Pie charts illustrate Ni-speciation in samples (1.8)Ni-UiO-67-bpy$_{11\%}$ (light purple), (3.1)Ni-UiO-67-bpy$_{11\%}$ (purple) and (1.1)Ni-UiO-67-bpy$_{6\%}$ (blue) estimated from XANES LCF analysis using as references the spectra of the (2.0) Ni-UiO-67 (grey) and (0.9) Ni-UiO-67- $_{bpy11\%}$ (red), representative of Ni^{2+} species incorporated into bpy-free UiO-67 and Ni^{2+} species coordinated to bpy linkers in UiO-67-bpy MOFs, respectively. LCF errors on reported Ni fractions are of ± 0.02 in all cases. XANES and FT-EXAFS spectra of relevant model compounds are also reported as dashed lines, including Ni(OAc)$_2$(H$_2$O)$_4$ (light grey) and Ni(OAc)$_2$(H$_2$O)$_2$(bpy) (pink). (B) As part (A) but for Ni-functionalized MOF catalysts recovered after catalytic tests. XANES and FT-EXAFS spectra of bulk Ni metal (grey), NiO (light blue) and Ni(OH)$_2$ (green) are also reported as dashed lines, scaled by appropriate factors in the FT-EXAFS for an easier comparison with the spectra of the Ni-functionalized MOF catalysts. (For interpretation of the references to colour in this figure legend, the reader is referred to the web version of this article).

Ni^{2+} moieties at the expenses of bpy-coordinated Ni^{2+} species. Interestingly, we observe a very similar fractional distribution among bpy-free and bpy-coordinated Ni^{2+} species in as-prepared (3.1)Ni-UiO-67-$bpy_{11\%}$ and (1.1)Ni-UiO-67-$bpy_{6\ \%}$, close in both cases to 50 % total Ni for each component: this falls in line with the equivalent rates observed for the ethene dimerization reaction over the two catalysts (Fig. 3).

From Fig. 7A it is also clear that no large metallic or oxidic aggregates are detectable in the as-prepared catalysts: in agreement with the CO FT-IR and PXRD results, Ni-speciation is dominated by well-dispersed Ni^{2+} species. Most importantly, the same conclusion can be reached after activation and reaction. With this respect, Fig. 7B reports a direct comparison between the XAS spectra of Ni-functionalized MOFs recovered after catalytic tests and of Ni metal, NiO and $Ni(OH)_2$ model compounds.

The XANES line shape remains similar to the one observed in the as-prepared materials, diagnostic for (pseudo)-octahedral Ni^{2+} species. However, we note a global broadening and dampening in the WL, accompanied with a general reduction of the differences discussed above between the different catalysts in the series, in both the XANES and EXAFS regions. Albeit subtle, such modifications with respect to the as-prepared materials underpin reorganization of Ni-species during activation and catalysis, likely involving interaction between the dehydrated form of bpy-coordinated and bpy-free Ni^{2+}-species discussed before. These phenomena will be addressed in more detail in future, with dedicated XAS studies carried out under *in situ* and *operando* conditions.

Exposure to the atmosphere after testing is expected to result into a prompt coordination of H_2O molecules to exposed Ni sites generated after activation, thus restoring an octahedral environment around the metal centers. Nonetheless, if metal or oxide/hydroxide phases would have formed under activation and/or reaction conditions, these should be detectable by XAS at the adopted experimental conditions. In this respect, no traces of the characteristic fingerprints of Ni metal, NiO or Ni $(OH)_2$ are observed in the XANES. In parallel, in the EXAFS, well-defined scattering features in the 2−3 Å range (phase uncorrected), characteristic of Ni-Ni contributions in the considered aggregate phases, are absent, within the detection limits of the technique (typically, 5 % total Ni). In substantial agreement with FT-IR results, XAS points to dispersed Ni^{2+} species as the active sites for the ethene dimerization reaction. These could include Ni-monomers or, plausibly, low-nuclearity Ni-multimers, docked at bpy linkers with Ni-Ni distances > 4 Å, eluding an efficient detection by EXAFS.

4. Conclusion

The results obtained in this study confirm the potential of co-catalyst free Ni-UiO-67-bpy as ethene dimerization catalysts. Spectroscopic investigations point to well-distributed Ni^{2+} sites, probably in the form of low-nuclearity Ni-multimers docked at bpy linkers, as the main active site for the ethene dimerization reaction. Those sites, and the surrounding UiO-67 lattice, impose strong shape selectivity on the reacting species, leading to exceptionally high selectivity (99 %) to linear 1- and 2-butenes in the gas phase, and to medium chain hydrocarbons as the dominant deposits in the catalyst after deactivation. Notably, all linear butenes were primary in nature and the selectivity was controlled by kinetic factors, providing an opportunity to tune the selectivity of the reaction towards the α-olefin, 1-butene. The high versatility of MOFs in terms of both their extraordinary degree of variability and the potential control over the active site opens up the possibility for tailored MOF ethene dimerization catalysts in the future.

CRediT authorship contribution statement

Mustafa Kømurcu: Conceptualization, Investigation, Formal analysis, Writing - original draft, Writing - review & editing. **Andrea Lazzarini:** Investigation, Formal analysis, Writing - original draft, Writing - review & editing. **Gurpreet Kaur:** Investigation, Formal analysis, Writing - original draft. **Elisa Borfecchia:** Investigation, Formal analysis, Writing - original draft. **Sigurd Øien-Ødegaard:** Investigation, Formal analysis. **Diego Gianolio:** Investigation, Formal analysis. **Silvia Bordiga:** Formal analysis, Writing - original draft, Supervision. **Karl Petter Lillerud:** Supervision. **Unni Olsbye:** Conceptualization, Data curation, Writing - original draft, Writing - review & editing, Supervision, Project administration.

Declaration of Competing Interest

The authors declare that they have no known competing financial interests or personal relationships that could have appeared to influence the work reported in this paper.

Acknowledgements

The Research Council of Norway is acknowledged for financial support of this work through project no. 250795 (CONFINE). We acknowledge Diamond Light Source for time on Beamline B18 under Proposal SP21713-1.

Appendix A. Supplementary data

Supplementary material related to this article can be found, in the online version, at doi:https://doi.org/10.1016/j.cattod.2020.03.038.

References

[1] J.N. Armor, Key questions, approaches, and challenges to energy today, Catal. Today 236 (Part B) (2014) 171–181.
[2] P.-A.R. Breuil, L. Magna, H. Olivier-Bourbigou, Role of homogeneous catalysis in oligomerization of olefins : focus on selected examples based on group 4 to group 10 transition metal complexes, Catal. Letters 145 (1) (2014) 173–192.
[3] D.S. McGuinness, Olefin oligomerization via Metallacycles: dimerization, trimerization, tetramerization, and beyond, Chem. Rev. 111 (3) (2010) 2321–2341.
[4] A. Finiels, F. Fajula, V. Hulea, Nickel-based solid catalysts for ethylene oligomerization - a review, Catal. Sci. Technol. 4 (8) (2014) 2412–2426.
[5] V. Hulea, Toward platform chemicals from bio-based ethylene: heterogeneous catalysts and processes, ACS Catal. 8 (4) (2018) 3263–3279.
[6] J.H. Cavka, et al., A new zirconium inorganic building brick forming metal organic frameworks with exceptional stability, J. Am. Chem. Soc. 130 (42) (2008) 13850–13851.
[7] S. Øien-Ødegaard, et al., UiO-67-type metal–organic frameworks with enhanced water stability and methane adsorption capacity, Inorg. Chem. 55 (5) (2016) 1986–1991.
[8] J. Canivet, et al., MOF-supported selective ethylene dimerization single-site catalysts through one-pot postsynthetic modification, J. Am. Chem. Soc. 135 (11) (2013) 4195–4198.
[9] M. Gonzalez, J. Oktawiec, J.R. Long, Ethylene Oligomerization in Metal-Organic Frameworks Bearing Nickel(II) 2,2[prime or minute]-Bipyridine Complexes, Faraday Discussions, 2017.
[10] E.D. Metzger, et al., Selective dimerization of ethylene to 1-butene with a porous catalyst, ACS Cent. Sci. 2 (3) (2016) 148–153.
[11] S.T. Madrahimov, et al., Gas-phase dimerization of ethylene under mild conditions catalyzed by MOF materials containing (bpy)NiII complexes, ACS Catal. 5 (11) (2015) 6713–6718.
[12] Z. Li, et al., Sintering-resistant single-site nickel catalyst supported by metal–organic framework, J. Am. Chem. Soc. 138 (6) (2016) 1977–1982.
[13] E.S. Gutterød, et al., CO2 hydrogenation over Pt-containing UiO-67 Zr-MOFs—the base case, Ind. Eng. Chem. Res. 56 (45) (2017) 13206–13218.
[14] B. Liu, et al., Postsynthetic modification of mixed-linker metal–organic frameworks for ethylene oligomerization, RSC Adv. 4 (107) (2014) 62343–62346.
[15] S. Yuan, et al., Exposed equatorial positions of metal centers via sequential ligand elimination and installation in MOFs, J. Am. Chem. Soc. 140 (34) (2018) 10814–10819.
[16] A.N. Mlinar, et al., Selective propene oligomerization with nickel(II)-Based metal–organic frameworks, ACS Catal. 4 (3) (2014) 717–721.
[17] E.D. Metzger, et al., Mechanism of single-site molecule-like catalytic ethylene dimerization in Ni-MFU-4l, J. Am. Chem. Soc. 139 (2) (2017) 757–762.
[18] V. Bernales, et al., Computationally guided discovery of a catalytic cobalt-decorated metal–organic framework for ethylene dimerization, J. Phys. Chem. C 120 (41) (2016) 23576–23583.
[19] E.J. Arlman, P. Cossee, Ziegler-Natta catalysis III. Stereospecific polymerization of propene with the catalyst system TiCl3 AlEt3, J. Catal. 3 (1) (1964) 99–104.

[20] R.Y. Brogaard, U. Olsbye, Ethene oligomerization in Ni-containing zeolites: theoretical discrimination of reaction mechanisms, ACS Catal. (2016) 1205–1214.
[21] K. Toch, J.W. Thybaut, G.B. Marin, Ethene oligomerization on Ni-SiO2-Al2O3: experimental investigation and single-event MicroKinetic modeling, Appl. Catal. A Gen. 489 (2015) 292–304.
[22] R.D. Andrei, et al., Heterogeneous oligomerization of ethylene over highly active and stable Ni-AlSBA-15 mesoporous catalysts, J. Catal. 323 (2015) 76–84.
[23] R. Henry, et al., Ethene oligomerization on nickel microporous and mesoporous-supported catalysts: investigation of the active sites, Catal. Today 299 (2018) 154–163.
[24] A. Ehrmaier, et al., Dimerization of linear Butenes on zeolite-supported Ni2+, ACS Catal. 9 (1) (2019) 315–324.
[25] R. Joshi, et al., Evidence for the coordination–insertion mechanism of ethene dimerization at nickel cations exchanged onto Beta molecular sieves, ACS Catal. 8 (12) (2018) 11407–11422.
[26] R.Y. Brogaard, et al., Ethene dimerization on zeolite-hosted Ni ions: reversible mobilization of the active site, ACS Catal. 9 (6) (2019) 5645–5650.
[27] S. Øien-Ødegaard, Preparation, structure and reactivity of functionalized zirconium metal-organic frameworks, Oslo (2016).
[28] A.J. Dent, et al., B18: a core XAS spectroscopy beamline for diamond, J. Phys. Conf. Ser. 190 (2009) 012039.
[29] S. Bordiga, et al., Reactivity of surface species in heterogeneous catalysts probed by in situ X-ray absorption techniques, Chem. Rev. 113 (3) (2013) 1736–1850.
[30] B. Ravel, M. Newville, ATHENA, ARTEMIS, HEPHAESTUS: data analysis for X-ray absorption spectroscopy using IFEFFIT, J. Synchrotron Radiat. 12 (4) (2005) 537–541.
[31] G. Kaur, et al., Controlling the synthesis of metal–organic framework UiO-67 by tuning its kinetic driving force, Cryst. Growth Des. 19 (8) (2019) 4246–4251.
[32] M.I. Gonzalez, et al., Single-crystal-to-single-crystal metalation of a metal–organic framework: a route toward structurally well-defined catalysts, Inorg. Chem. 54 (6) (2015) 2995–3005.
[33] M. Sanati, C. Hornell, S.G. Jaras, The oligomerization of alkenes by heterogeneous catalysts, in: Catalysis, vol. 14, The Royal Society of Chemistry, 1999, pp. 236–288.
[34] A. Martínez, et al., New bifunctional Ni–H-beta catalysts for the heterogeneous oligomerization of ethylene, Appl. Catal. A Gen. 467 (2013) 509–518.
[35] F. Speiser, P. Braunstein, L. Saussine, Catalytic ethylene dimerization and oligomerization: recent developments with nickel complexes containing P,N-chelating ligands, Acc. Chem. Res. 38 (10) (2005) 784–793.
[36] S.A. Svejda, M. Brookhart, Ethylene oligomerization and propylene dimerization using cationic (α-Diimine)nickel(II) catalysts, Organometallics 18 (1) (1999) 65–74.
[37] I. Agirrezabal-Telleria, E. Iglesia, Stabilization of active, selective, and regenerable Ni-based dimerization catalysts by condensation of ethene withinordered mesopores, J. Catal. 352 (2017) 505–514.
[38] M. Lallemand, et al., in: R. Xu (Ed.), Ethylene Oligomerization Over Ni-Containing Mesostructured Catalysts With MCM-41, MCM-48 and SBA-15 Topologies, in Studies in Surface Science and Catalysis, Elsevier, 2007, pp. 1863–1869.
[39] O. Atkins, Weller Rourke, Armstrong, Inorganic Chemistry, OUP Oxford, 2009.
[40] T.C. Chung, Functionalized polyolefins via copolymerization of borane monomers in Ziegler-Natta process, in: J.C. Salamone, J.S. Riffle (Eds.), Advances in New Materials, Springer US, Boston, MA, 1992, pp. 323–331.
[41] C. Lamberti, et al., Probing the surfaces of heterogeneous catalysts by in situ IR spectroscopy, Chem. Soc. Rev. 39 (12) (2010) 4951–5001.
[42] S. Chavan, et al., H2storage in isostructural UiO-67 and UiO-66 MOFs, J. Chem. Soc. Faraday Trans. 14 (5) (2012) 1614–1626.
[43] M. Kandiah, et al., Post-synthetic modification of the metal–organic framework compound UiO-66, J. Mater. Chem. 20 (44) (2010) 9848–9851.
[44] S. Bordiga, et al., Low temperature CO adsorption on Na-ZSM-5 zeolites: an FTIR investigation, J. Catal. 137 (1) (1992) 179–185.
[45] S. Chavan, et al., Response of CPO-27-Ni towards CO, N_2 and C_2H_4, J. Chem. Soc. Faraday Trans. 11 (42) (2009) 9811–9822.
[46] V.A. Sadykov, et al., Ni-loaded nanocrystalline ceria-zirconia solid solutions prepared via modified Pechini route as stable to coking catalysts of CH_4 dry reforming, Open Chem. 14 (1) (2016) 363–376.
[47] E.D. Bloch, et al., Reversible CO binding enables tunable CO/H_2 and CO/N_2 separations in metal-organic frameworks with exposed divalent metal cations, J. Am. Chem. Soc. 136 (30) (2014) 10752–10761.
[48] S. Chavan, et al., CO adsorption on CPO-27-Ni coordination polymer: spectroscopic features and interaction energy, J. Phys. Chem. C 113 (8) (2009) 3292–3299.
[49] C. Hu, et al., Temperature-programmed FT-IR study of the adsorption of CO and co-adsorption of CO and H_2 on $NiAl_2O_3$, J. Mol. Catal. A Chem. 110 (2) (1996) 163–169.
[50] J.B. Peri, Infrared studies of Ni held at low concentrations on alumina supports, J. Catal. 86 (1) (1984) 84–94.
[51] S. Tada, et al., N_2O pulse titration of Ni/α-Al_2O_3 catalysts: a new technique applicable to nickel surface-area determination of nickel-based catalysts, J. Phys. Chem. C 117 (28) (2013) 14652–14658.

Supporting info

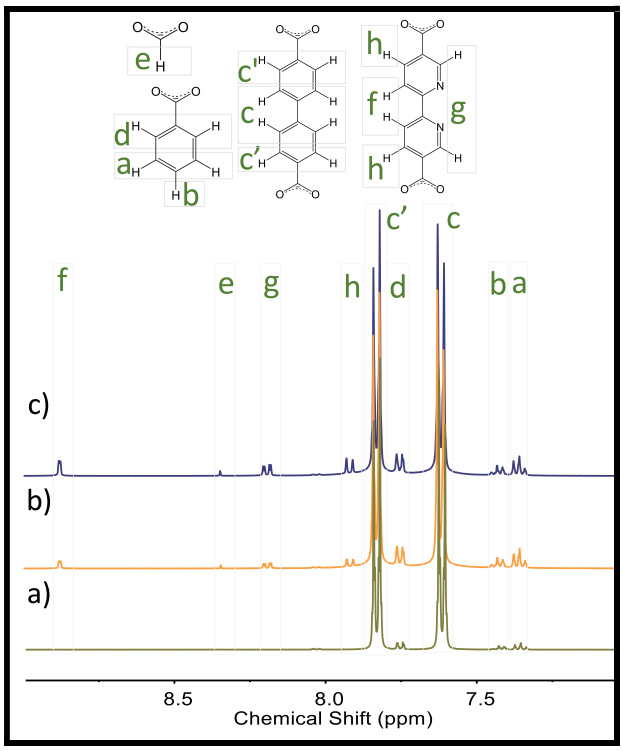

Figure SI 1: ^{1}H NMR spectra of the digested MOF for a) UiO-67, b) UiO-67-bpy$_{6\%}$ and c) UiO-67-bpy$_{11\%}$.

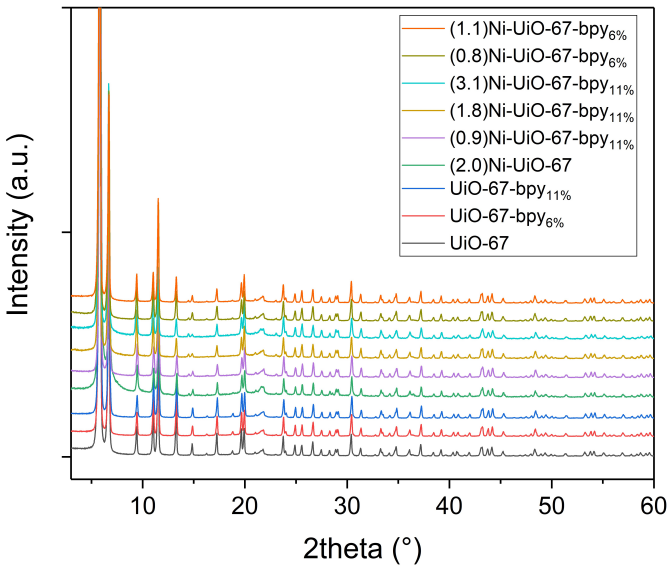

Figure SI 2: XRD patterns of parent and Ni functionalized MOF catalysts.

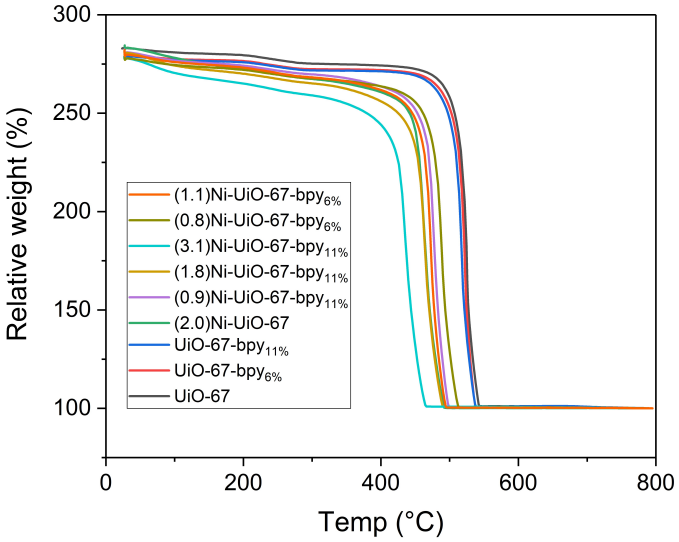

Figure SI 3: TG curve of parent and Ni functionalized MOF catalysts. The samples were heated from 25 to 800 °C, 5 °C/min in a flow of synthetic air.

Table SI 1: Defectivity of UiO-67, UiO-67-bpy$_{6\%}$ and 3. UiO-67-bpy$_{11\%}$ estimated from solution state ^{1}H-NMR and TGA. (BPDC+BPY):Zr cluster (node) = 6 in the perfect UiO-67 system.

MOF	Wt %$_{400\,°C}$	Bpdc:Node	Bpy:Node	BA:Node	FA:Node	Linker:Node
UiO-67	274	5.40	0	0.31	0	5.40
UiO-67-bpy$_{6\%}$	272	4.90	0.22	0.83	0.05	5.12
UiO-67-bpy$_{11\%}$	271	4.70	0.56	0.48	0.09	5.26

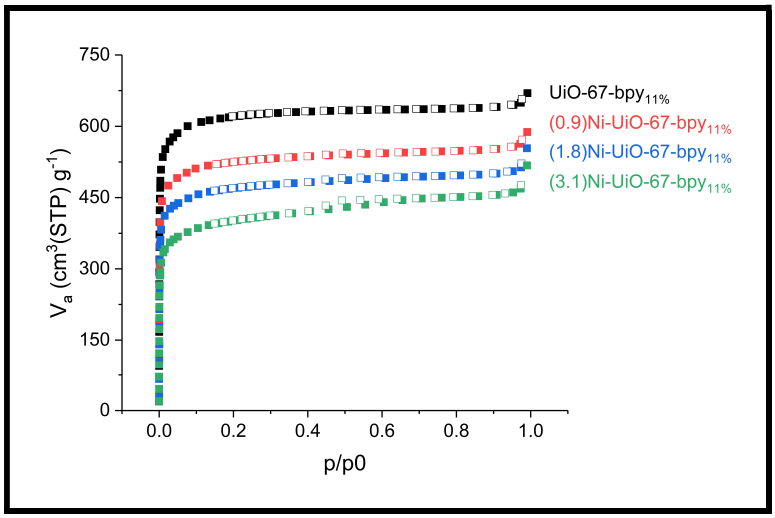

Figure SI 4: N_2 adsorption isotherms of UiO-67-bpy$_{11\%}$ with 0 – 3.1 % Ni.

Simulated isotherms are calculated with the Sorption tool in Materials Studio version 2019. The adsorption isotherm is calculated by performing a series of 50 fixed pressure calculations at pressure from 0.01 to 100 kPa with a N_2-molecule as the adsorbate. The quality setting is "Medium" to reduce the computational cost, this will underestimate the surface area slightly, but relative differences are realistic. Surface area was also calculated with the "Volume calculation" tool in Materials Studio. This method is based on calculations of Connolly surfaces with a 1.85Å probe to simulate the N_2 molecule. This method overestimate the surface area but give the same relative difference.

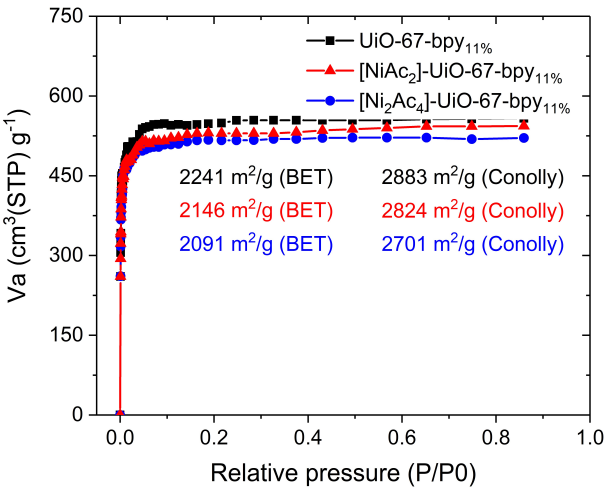

Figure SI 5: Simulated isotherms for UiO-67, [NiAc$_2$]-UiO-67-bpy$_{11\%}$ (Ni:bpy mol = 1) and [Ni$_2$Ac$_4$]-UiO-67-bpy$_{11\%}$ (Ni:bpy mol = 2).

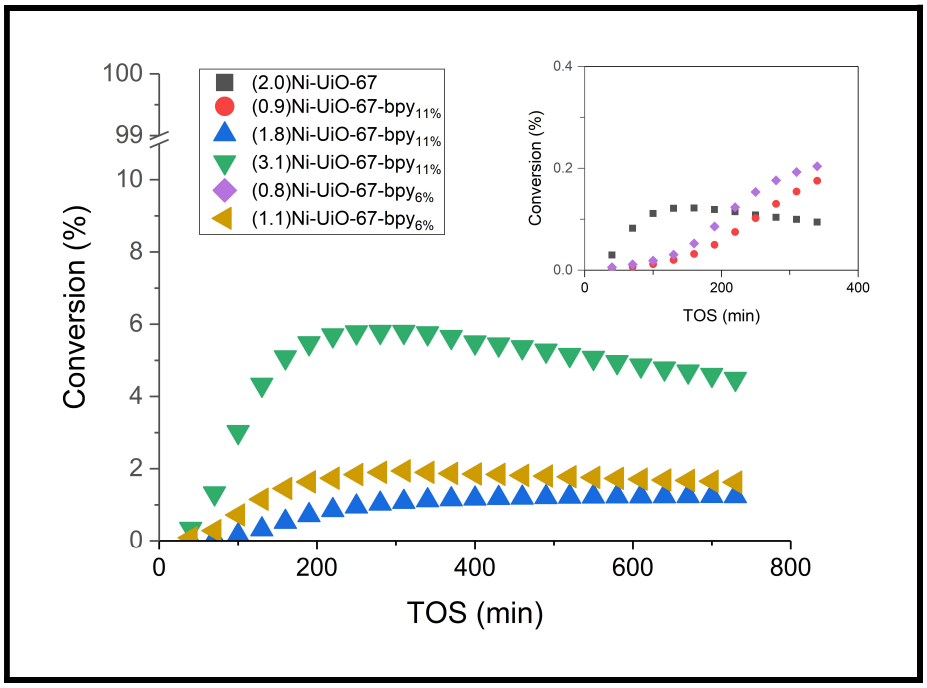

Figure SI 6: Conversion vs TOS over Ni-functionalized MOF catalysts. Reaction conditions: m_{cat} = 0.150 g, 30 bar total pressure where P_{ethene} = 26 bar and P_{inert} = 4 bar, temperature = 250 °C and contact time = 5.0 mg·min/mL at STP

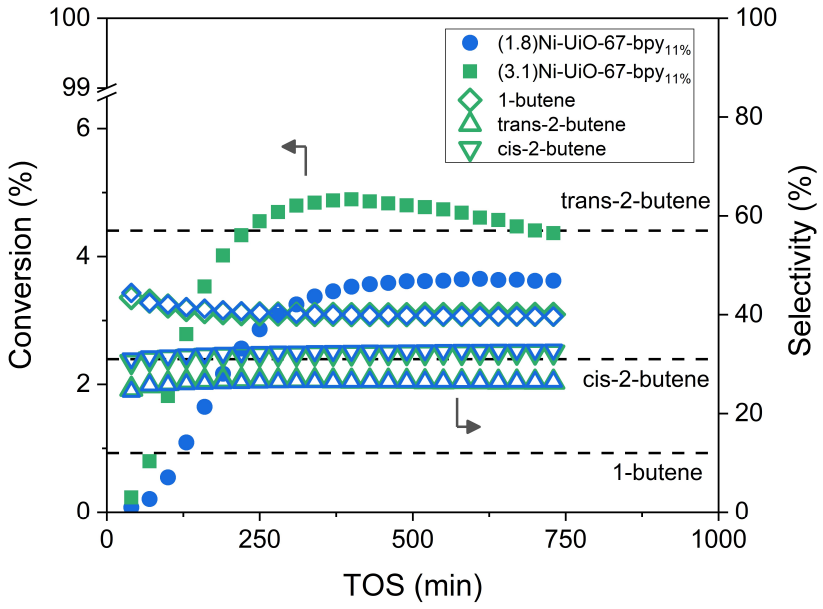

Figure SI 7: Ethene conversion (solid symbols) and product selectivities (hollow symbols) for (3.1)Ni-UiO-67-bpy$_{11\%}$ (green symbols) and for (1.8)Ni-UiO-67-bpy$_{11\%}$ (blue symbols) versus time on stream. The dashed lines show the linear butene selectivities at equilibrium distribution at 250 °C. Reaction conditions: m_{cat} = 0.150 g and 0.300 g for (3.1)Ni-UiO-67-bpy$_{11\%}$ and (1.8)Ni-UiO-67-bpy$_{11\%}$,, respectively, 30 bar total pressure where P_{ethene} = 26 bar and P_{inert} = 4 bar, temperature = 250 °C and contact time = 5.0 and 10 mg·min/mL at STP.

Table SI 2: Fractional distribution of butenes in the effluent in 1-butene isomerization experiments over UiO-67-bpy$_{11\%}$. By-pass measurement is included as 0 min TOS to show the presence of trans and cis-2-butene impurities in the feed. Reaction conditions: 0.150 mg UiO-67-bpy$_{11\%}$, contact time: 5.0 mg·min/mL at STP, temperature = 250 °C, 1 bar total pressure where $P_{1\text{-butene}}$ = 0.03 bar.

TOS (min)	1-butene	Trans-2-butene	Cis-2-butene
0	0.996	0.002	0.002
60	0.993	0.004	0.003
120	0.996	0.002	0.002
180	0.995	0.003	0.002

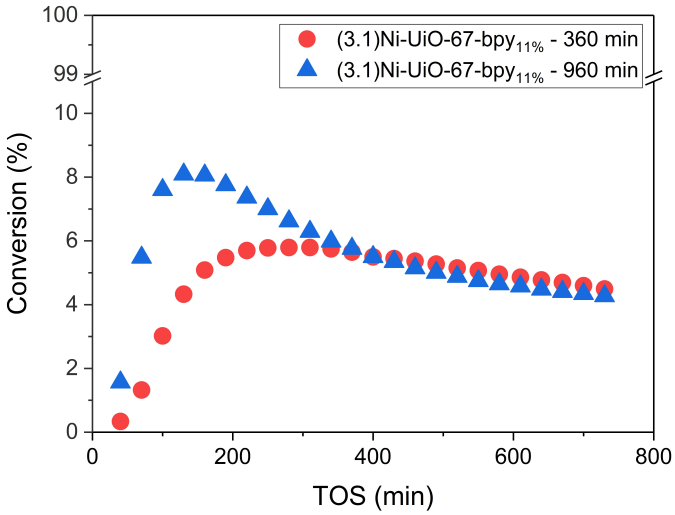

Figure SI 8: Ethene conversion vs TOS for (3.1)Ni-UiO-67-bpy$_{11\%}$ after various activation duration. Activation conditions: 3 °C/min up to 300 °C, 360 and 960 min, respectively, @ 300 °C, 10 % O_2 in He (5 mL/min O_2, 45 mL/min He). Reaction conditions: m_{cat} = 0.150 g, 30 bar total pressure where P_{ethene} = 26 bar and P_{inert} = 4 bar, temperature = 250 °C and contact time = 5.0 mg·min/mL at STP.

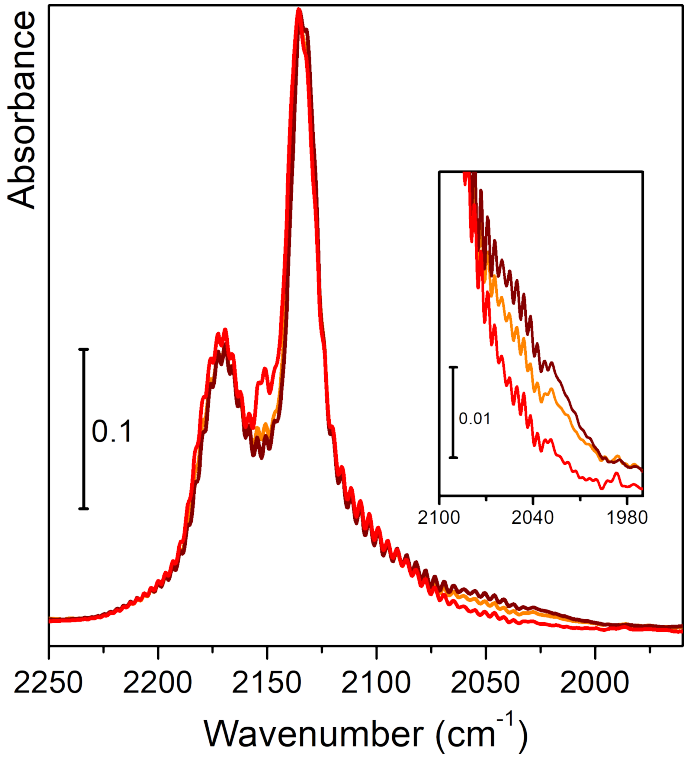

Figure SI 9: CO@77K FT-IR spectra of (3.1)Ni-UiO-67-bpy$_{11\%}$ sample activated for 360 min at 300°C in 10% O_2 (red curve), activated for 360 min and tested for 720 min (orange curve), activated for 960 min and tested for 720 min (maroon curve). All the plotted spectra represent the maximum coverage of CO (θ_{MAX}) after the subtraction of the spectra at minimum coverage (θ_{min}). The spectra are then normalized with respect to the peak at 2135 cm^{-1} (physisorbed CO), which takes into account not only the total amount of CO that is dosed but also the pellet thickness.

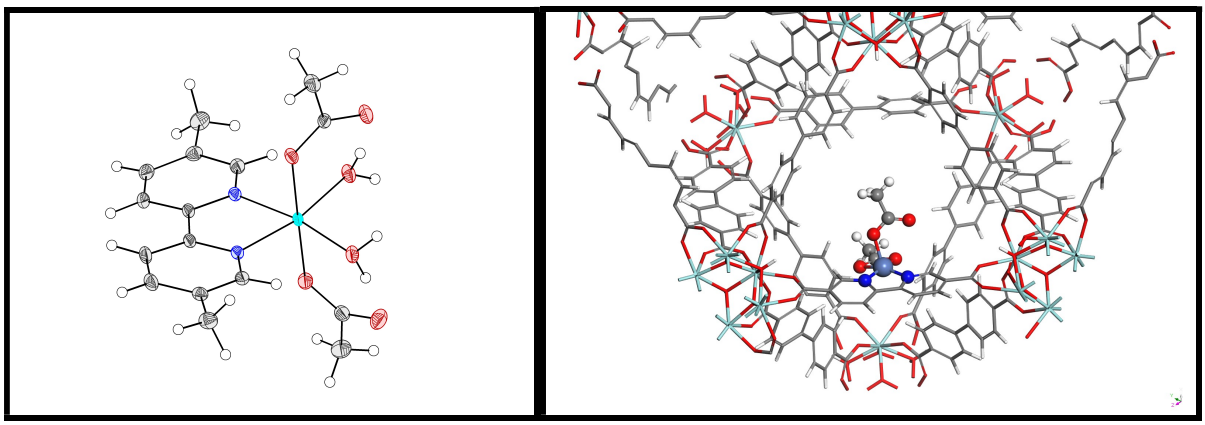

Figure SI 10: Structural representation of isolated Ni(OAc)$_2$(H$_2$O)$_2$(bpy) model complex (left) and Ni(OAc)$_2$(bpy) in UiO-67 (right).